Untersuchung von Werkstoffen für die Katalyse mit Elektronentomographie

---

Investigation of materials for catalysis with electron tomography

vorgelegt von

Diplom-Physiker
Roman Grothausmann

von der Fakultät III – Prozesswissenschaften
der Technischen Universität Berlin
zur Erlangung des akademischen Grades

Doktor der Naturwissenschaften
- Dr. rer. nat. -

genehmigte

Dissertation

durchgeführt am Institut für
Angewandte Materialforschung,
Helmholtz-Zentrum Berlin für Materialien und Energie

Promotionsausschuss:
Vorsitzender: Prof. Dr. H. Schubert
Gutachter: Prof. Dr. J. Banhart
Gutachter: Dr. C. Kübel

Tag der wissenschaftlichen Aussprache: 9. Mai 2011

Berlin, im Januar 2011

D 83

Kurzfassung/Abstract

Untersuchung von Werkstoffen für die Katalyse mit Elektronentomographie

Elektronentomographie mit dem Transmissionselektronenmikroskop (TEM) ermöglicht die Erstellung dreidimensionaler Darstellungen (Tomogramme) von Proben in der Größenordnung von einigen Nanometern bis hin zu einigen Mikrometern. Im Rahmen dieser Arbeit wurden verschiedene auf Ruthenium basierende Werkstoffe für die Katalyse in Brennstoffzellen untersucht. Die Tomographie liefert, im Gegensatz zu gewöhnlichen TEM Bildern (Projektionen), Aufschluss über die Verteilung und Erreichbarkeit der Katalysatorpartikel auf bzw. in dem Trägermaterial. Es konnte gezeigt werden, dass neben qualitativen Vergleichen der Verteilung der Rutheniumpartikel auf/in dem Kohleträgermaterial verschieden hergestellter Proben auch detaillierte quantitative Analysen möglich sind. Da die Katalyse an heterogenen Katalysatoren an der Oberfläche des Katalysators stattfindet, spielen neben der Größe der Oberfläche auch die unterschiedlichen Koordinationszahlen verschieden orientierter Facetten der Katalysatorpartikel eine Rolle. Dazu wurde erstmalig ein Algorithmus entwickelt, der es erlaubt, viele verschiedene Partikel in dreidimensionalen Datensätzen automatisch hinsichtlich Facettierung zu analysieren. Durch die teilweise Einbettung der Katalysatorpartikel in das Trägermaterial ist eine Unterscheidung der bedeckten und unbedeckten Oberfläche nötig, da nur der unbedeckte Teil der Katalysatoroberfläche von den Reaktanten erreicht werden kann. Neben dieser unbedeckten Oberfläche ist durch die teilweise Einbettung auch die Ausrichtung der Katalysatorpartikel in Bezug zur lokalen Oberfläche des Trägers bedeutsam, da so statistische Untersuchungen der unbedeckten Facettentypen möglich werden. Zu den durchgeführten Charakterisierungen wie: Partikelverteilung innerhalb des Trägers, Größenverteilung, Oberflächen, Volumina, Formanalyse und der lokalen Ausrichtung, wurden Erkenntnisse gewonnen, die es erlauben, den untersuchten Katalysatortyp während der Herstellung weiter zu optimieren. Es konnte zudem gezeigt werden, dass die entwickelten Bildanalysemethoden sich auch auf tomographische Datensätze anderer Messmethoden wie z.B. Neutronen- und Focused Ion Beam-Tomographie anwenden lassen.

Investigation of materials for catalysis with electron tomography

Electron tomography with a transmission electron microscope (TEM) enables creation of three-dimensional representations (tomograms) of samples in the range of a few nanometres to a few micrometres. In the frame of this thesis different ruthenium-based materials for catalysis in fuel cells were investigated. Tomography, in contrast to common TEM images (projections), yields information about the distribution and accessibility of the catalyst particles on or in the support material. It was shown that in addition to qualitative comparisons of the distribution of ruthenium particles on/in the carbon support material of differently manufactured samples, quantitative analyses are also possible. Since catalysis on heterogeneous catalysts takes place at the surface of the catalyst, the amount of surface area matters as do the coordination numbers of differently oriented facets of the catalyst particles. For this purpose a new algorithm was developed that allows to automatically analyse faceting of many different particles in a three-dimensional dataset. Due to the partial embedding of the catalyst particles into the support material only the uncovered fraction of the catalyst surface is accessible to the reactants and therefore a differentiation between the covered and uncovered catalyst surface is necessary. Apart from this uncovered surface, the orientation of the catalyst particles relative to the local support surface is also important since this allows statistical investigation of the uncovered facet types. In addition to the conducted characterizations such as: particle distribution within the support, size distribution, surface areas, volumes, shape analysis and the local orientation, new insights were gained which allow optimization of the examined catalyst during production. Furthermore, it could be shown that the developed image analysis methods can be applied to tomographic datasets from other measurement techniques such as neutron and focused ion beam tomography.

Contents

Chapter 1

Introduction

In the past decades, two new fields of research have developed. They are the fields of 'nanotechnology' and 'renewable energy' research [109]. Nanotechnology research concentrates on the development of 'nanoscale' materials which exhibit properties that can be markedly different from the corresponding bulk materials [166; 28]. The increased surface area of nanomaterials is often regarded as the source for this, but studies showed that e.g. surface structures of nanocrystals differ from those of bulk crystalline surfaces [71]. Nanotechnology research is interdisciplinary, including physics (e.g. cluster physics), chemistry (e.g. colloidal solutions, gold ink), biology (e.g. hydrophobia of lotus leafs), medicine (e.g. contrast agents for imaging). The term 'renewable energies' is generally used for energy resources alternative to fossil fuels and other chemical energy converted by combustion causing environmental damage and pollution. Devices that are able to convert renewable energies into electric energy range from solar cells to wind turbines. Different methods and devices for energy storage are needed because renewable energies cannot be stored as easily as liquid or solid fossil fuels, e.g. petroleum or coal. Two promising candidates for portable energy storage and conversion to electricity are batteries and fuel cells (FC) combined with a fuel tank. The more complicated system FC + tank has a higher energy storage density than lithium-ion batteries [42; 43; 44]. However, FCs need catalysts such as platinum on both the cathode and the anode side. Due to the high price of platinum, alternatives are sought. The use of metal nanoparticles finely dispersed on carbon black, i.e. nanotechnology, increases the catalytic activity and reduces the necessary amount of platinum [164]. To further reduce costs, ruthenium as a cheaper and more reliable alternative to platinum was suggested as catalyst for the oxygen reduction reaction (ORR) at the cathode side of polymer-electrolyte fuel cells (PEFC) [6; 171; 149]. Ruthenium-based ORR electrocatalysts modified with selenium even feature a superior methanol tolerance [191; 186] for the use in compact mixed reactant geometry (CMR-DMFC) [137; 34]. Significant research on $RuSe_x$-catalysts has been performed [137; 34; 130; 5; 32], but their ORR activity is still limited to 70% compared to platinum-based reference materials [5; 32; 192; 45].

The optimization of electro-catalysts for oxygen reduction can be brought down to the necessity to tailor a three-phase boundary between the Nafion®-component (supply

of H^+), the conductive carbon support (for e^- replenishment) and the catalytically active surface of the transition metal as the centre of the catalytic reaction [42; 43; 44]. Hence, there is an increasing interest in characterization techniques capable not only of estimating the overall active surface area of the metallic nanoparticles but also of accounting for particle sizes and shapes, spatial particle distributions and the porosity of the catalyst support.
Many characterization methods are necessary to assess these properties of the material on a *macroscale*. Since the material consists of nanoparticles, transmission electron microscopy (TEM) combined with tomography can be used to investigate all these 'nano properties' of a very small amount of material with a single method. Realizing that many (unusual) properties and processes originate from the 'nano world' created a high interest in investigations based on TEM tomography not only in physics but also chemistry, biology and medicine [121; 55; 160; 13; 11; 75; 74; 35; 113; 87; 110; 179; 128]. TEM tomography provides fields of view that are large enough to cover the sizes of structural characteristics of most nanomaterials and to explain their functionality. At the same time the fields of view are sufficiently small to obtain a spatial resolution that provides insight into the details needed to understand their function. TEM tomography results can be extrapolated for larger amounts of the material as used during production of FCs. This is only possible because the relevant properties result from nanoscale characteristics rather than from macroscopic features. For example, the determination of the density of a material by investigation of a very small amount by TEM tomography would be inappropriate if the density of the bulk material was significantly influenced by macroscopic pores or other inclusions.
Electron tomography is a powerful characterization technique [52; 14] for heterogeneous solid samples [90; 55; 122]. It is mostly followed by a qualitative evaluation [124; 184; 66] or carried out manually [151; 62] depending on the personal judgement of the operating scientist. Next-generation equipment and sophisticated data evaluation extend the field of applications of this technique [159; 150] and make it even more attractive for the investigation of heterogeneous catalysts [92; 181]. Carbon-supported transition metal catalysts are a highly suited system to such investigations since the contrast between the supporting carbon matrix and the catalytically active metals is sufficiently large [55; 65]. However, quantitative evaluations need digital image processing and analysis. Tomographic data is digital and three dimensional and therefore difficult to inspect with 2D reprojections or slices on PC screens or printouts. Evaluations only based on this restricted view do not make use of the full extent of the data, i.e. the complete information available in a dataset.

The field of digital image processing and analysis (DIPA) is far reaching and not restricted to tomography in science [14; 134; 133]. It is very much driven by medical applications [189; 76; 155; 49; 8; 1] but is used in a wide range of applications beyond medicine. 3D applications which originate from magnetic resonance imaging (MRI) and medical CT led to the creation of the versatile and powerful software ITK and VTK[2;3]. Other applications of DIPA range from recognition of car license plates and other imaged text, generally referred to as optical character recognition (OCR) [162; 20; 37; 161], optical music recognition (OMR) [139] and multiple choice

test and lottery evaluations [163]. Security is nowadays also based on computer-aided recognition, ranging from detection of insecure devices and substances by body and luggage scanners to recognition and comparison of biometric data. Geology also uses DIPA to e.g. categorize landscapes in photographs and to create maps [162]. Industry uses DIPA for product quality control and automated sorting [48; 19]. A new and very challenging field of DIPA is computer vision of various shapes in images taken under unoptimized conditions, i.e. brightness gradients, shadows and reflections [48; 173].

The aim of this thesis

Discover the poodle's core (des Pudels Kern erkennen)

The aim of this study is to contribute to the understanding of an important class of catalyst by analysing its characteristics with TEM tomography. Therefore, characteristic such as the size and shape distribution of ruthenium nanoparticles as well as their spacial distribution on the carbon support and their accessibility by reactants were evaluated in the tomograms (Chap. 5), see e.g. Fig. 1.1. One step towards a better understanding of the investigated catalysts lies in realizing that these characteristics can be ranked according to their influence on catalysis. Since catalysis takes place on the surface of catalytic active material the most important quantity is the uncovered catalytic surface. Any influence of shape or facettation of catalytic nanoparticles on the overall catalytic activity has no relevance if the catalytic sites are not reachable by the reactants. The aid of computers is needed in order to quantify and to measure these important 3D characteristics of the digital tomographic representation of the sample. Software was developed (Chap. 3) to create a set of tools/programs to automate the process of evaluating thousands of particles. These programs were designed with a special emphasis on bringing down the image analysis parameters to very basic properties of the measurements, therefore minimizing the influence of personal judgement on the analyses. Such an emphasis on the reduction of personal judgement and improvement of reproducibility is less commonly reported in the literature than manual measurements probably due to the high additional (programming) effort these evaluations demand. However, automated measurements are worth the effort as shown by the developed automated facet analysis,

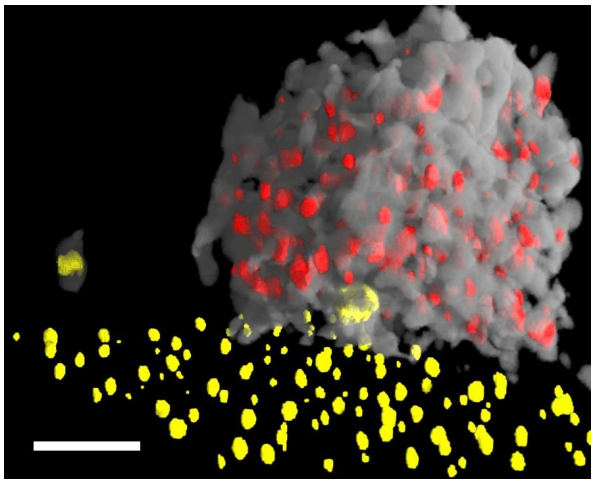

Figure 1.1: Ruthenium-based catalyst

Volume-rendered tomogram of a ruthenium based catalyst corresponding to Fig. 5.8. The ruthenium nanoparticles are coloured red, the carbon support grey and the gold marker yellow. The carbon support foil on which the markers reside is not rendered. The scale bar corresponds to 20 nm.

which revealed a property of the ruthenium nanoparticles that would have been extremely hard to recognize by manual inspection (Sec. 5.3.4.6). Automated facet analysis also has a great potential for characterizing other tomographic data containing faceted geometries as will be demonstrated in Sec. 3.4.2.

The studies of this thesis not only enabled me to characterize the given system and to contribute to the understanding of the fundamental chemical and physical processes (Chap. 6) but also to suggest further procedures during production that could improve the catalytic properties of the investigated catalysts. For example, the use of carbon supports with less micro porosity in order to avoid formation of ruthenium particles deep inside pores where they are barely accessible by reactants or to introduce an etching process during production that removes thin films covering the ruthenium surface.

Chapter 2

Aspects of electron (TEM) tomography

Tomography is a method to reconstruct digital 3D representations of samples from 2D projections. The method is described in great detail in the literature (see e.g. [29; 14; 52; 142]). Reconstruction is based on images of the sample taken at different orientations. In TEM tomography the sample is rotated around a nominally fixed axis. The resulting series of images is often called a tilt series [55; 52] and is stored in a 3D digital image *stack* where the z-coordinate corresponds to the number of the image in the series. If the image number is proportional to the acquisition angle, a cross section of the stack perpendicular to the rotation axis represents a *sinogram* or Radon transform [29; 14] which is used for digital tomographic reconstruction. Restricted space and experimental setup in a TEM generally restrict tilt angles to around $\pm 70°$ [55; 120] unless special, needle-shaped samples can be prepared [120]. The missing range of tilt angles causes a 'missing wedge' [141] in Fourier space and leads to 'missing wedge' artefacts. These and other artefacts lead to direction-dependent resolutions in TEM tomograms and are further described below.

It is often stated that an image signal used for tomographic reconstructions must conform to the 'projection requirement' which states that the projected signal must be a strictly monotonic function of a projected physical quantity [90; 120; 67]. In conventional electron microscopy, the depth of focus (DOF) is sufficiently large that to a good approximation the recorded image can be regarded as a projection [179; 120]. However, this is not at all obvious and is rarely discussed [67]. The depth of focus is discussed further below. In addition, there are many competing contrast mechanisms all of which, to varying approximations, obey the projection requirement [120; 67].

For amorphous materials conventional bright-field TEM (BF-TEM) contrast arises from changes in specimen density or thickness [146; 120]. The carbon support particles of the studied samples can be regarded as (quasi) amorphous material as described in Sec. 5.1. The projection criterion is not fulfilled for BF-TEM images of strongly scattering crystalline materials, where diffraction contrast typically dominates the image formation [90]. Although the ruthenium nanoparticles are crystalline, they are small (⌀ ranging from below 1 nm to about 10 nm) and therefore diffraction contrast in the

BF-mode does not dominate the image formation and can be largely neglected [55]. The observation that orientation, i.e. diffraction condition, dependent contrast does not strongly effect the tomographic reconstruction can be rationalized by the fact that diffraction contrast is only present in a few images of the tilt series, while tomography averages over a much larger number of images [55, sec. 2.4]. However, diffraction contrast contributes to reconstruction artefacts as can be expected for all contributions to contrast that do not fulfil the 'projection requirement'. The carbon support foil used for the TEM tomography presented in Chap. 5 can be regarded as a weakly scattering object (i.e. fulfilling the weak phase-object approximation with a thickness around 8 nm) [146]. Phase-contrast effects can be observed e.g. in Fig. 2.1. Phase contrast is normally generated in the TEM by a small defocus[1)], using the objective lens to transfer phase information to variations in amplitude [120]. This work does not depend on phase-contrast for tomographic reconstruction (i.e. no contrast transfer function (CTF)-correction was applied). Phase contrast effects can cause violations of the 'projection requirement' since phase contrast is not a monotonic function due to the oscillation of the CTF. However, the CTF is largely monotonic in the range of spatial frequencies that are imaged in tilt series of this study. Anyhow, these violations can be largely neglected because phase contrast effects decrease with increasing specimen thickness owing to the attenuation of the incident-wave amplitude [146].

Scattering contrast describes the image intensity at low and medium magnifications, where phase contrast effects normally do not have to be considered unless a highly coherent electron beam and large defocusing are employed [146].[2)] However, using a FEG and a defocus of around $\Delta f \approx -1$ µm to $\Delta f \approx -3$ µm (as generally the case in this study) phase contrast effects contribute to the contrast in images. This can be seen when comparing image regions of a tilted sample, which are therefore at different defocus e.g. in Fig. 2.1. Although the image resolution[3)] estimation based on image frequencies in Fig. 2.1 is highest around $\Delta f \approx 0$ µm (region c in Fig. 2.1), a resolution estimation that also takes contrast dynamics into account, would be at an optimum in the region of underfocus (left of c) towards region a. Imaging in overfocus should be avoided due to the inverted phase contrast transfer (right of c).[4)]

It is hard to say how much phase contrast in regard to scattering contrast contributes for thicker sample regions, such as the actual particle to be reconstructed. As stated above, phase contrast effects decrease with increasing specimen thickness owing to the attenuation of the incident-wave amplitude [146]. This reduction of phase contrast can be seen in regions β and γ in Fig. 2.1 where the resolution seems to be similar despite the defocus difference of $\Delta f \approx 300$ nm. Therefore, the main contrast mechanism used for tomographic reconstruction in this work is scattering contrast [146] which is

[1)] In this work, underfocus is expressed by negative defocus values as done in e.g. Ref. [185]. However, Reimer and Kohl [146] use the opposite convention.

[2)] Scattering contrast can be incorporated in the more general phase-contrast theory if complex scattering amplitudes are used [146].

[3)] Resolution in this work generally refers to image resolution, i.e. limit of image interpretability and not to the resolution limit of the TEM used, i.e. not the information limit of the TEM.

[4)] It should be noted that the whole sample particle shown in Fig. 2.1 is in underfocus, only the carbon foil extends into overfocus. The imaging conditions are depicted in the schematic Figure 4.3.

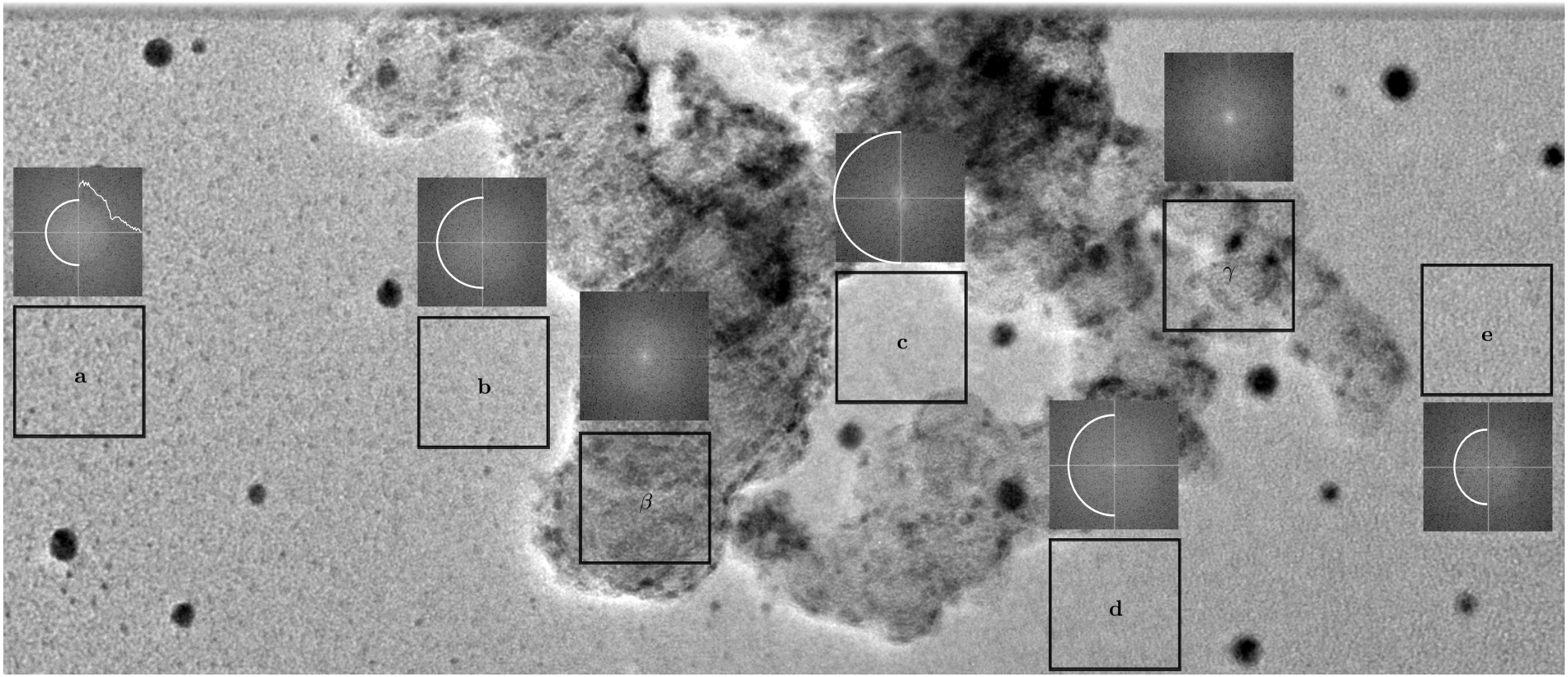

Figure 2.1: DOF and local resolution estimation by FFT

The figure shows a stripe of the image at -65° tilt angle of the series corresponding to Fig. 5.11.The labelled regions each mark a 128x128 pixel area (128 pixel correspond to about 33 nm) of the carbon support foil. The foil is about 8 nm thick (evaluated from the tomogram) and therefore can be regarded as a thin amorphous film. However, within the regions it covers a depth of about 72 nm. The corresponding FFT is shown beside each region. Regions a ($\Delta f_a \approx -600$ nm) and b are in underfocus, i.e. negative defocus, while d and e ($\Delta f_e \approx +500$ nm) are in overfocus. Region c is roughly at the position of the Gaussian focal plane, i.e. $\Delta f_c \approx 0$ nm. Regions β and γ correspond to roughly the defoci of region b and c. Despite the noise, the approximate position of the first minimum of the effective transfer function (eCTF) can be evaluated (see radial profile plot [7;19] in FFT of region a) and is marked by a half ellipse. Only region d and e exhibit astigmatism, i.e. a to c are marked with a half circle. According to e.g. Shindo and Hiraga [157]; Edington [40] the (approximate) image resolution δ corresponds to the radius of this circle, a,e: $\delta \approx 10$ Å, b,d: $\delta \approx 7$ Å, c: $\delta \approx 5$ Å. Therefore, the resolution increases from a to c and then decreases again. This is the expected behaviour for a thin foil that exceeds the DOF due to its tilt (see e.g. 'stack of 1D-FT' in [146, Fig. 6.14, p. 214] and [141; 145]).

This result demonstrates how the local resolution in the acquired image varies dependent on the z-position of the region in the TEM. This shows that the sample region imaged (at -65°) exceeds the DOF defined by the settings of the imaging system used for acquisition.

dependent (apart from other quantities) on the mass thickness $d_m = \rho d$ [146, p. 198] (ρ: density, d: thickness). The specimen is represented by its mass-density distribution $\rho(x, y, z)$ [146, p. 259] and the projection in z-direction (mass thickness distribution): $\int \rho(x, y, z)dz = d_m(x, y)$ [146, p. 260] (therefore d is the thickness in z-direction). With the transmission $T(\alpha_o) = \exp(-d_m/d_k(\alpha_o))$ [146, p. 198] the image intensity at position x,y is given by [146, p. 260]:

$$I(x, y) = I_0 \exp(-d_m(x, y)/d_k)$$

The contrast thickness $d_k(\alpha_o)$ dependent on the size of the objective aperture α_o is given by [146, p. 198]:

$$\frac{1}{d_k(\alpha_o)} = \frac{4}{Zx_{el}} \left(\frac{Z-1}{4(1+(\alpha_o/\theta_0)^2)} + \ln \sqrt{1+(\alpha_o/\theta_0)^2} \right)$$

with the atomic number Z and the characteristic angle θ_0 at which the differential elastic cross section falls to a quarter of the value at $\theta = 0$ [146, p. 151]. The dependence of the mean free path x_{el} on the total cross section σ_{el} and many other quantities is given in [146, eq. 6.2, p. 197].

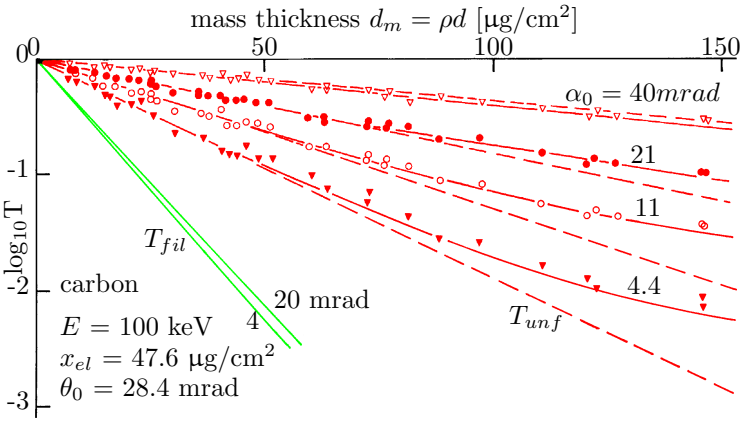

Figure 2.2: Transmission and mass thickness

Figure and caption based on [146, Fig 6.1, p. 198] showing that the projected signal, i.e. transmission T, is a monotonic function of mass thickness d_m. A mass thickness of 150 µg/cm^2 corresponds to 600 nm to 750 nm for the density of graphite ρ_C ranging from 2.0 g/cm^3 to 2.5 g/cm^3 [93]. Semilogarithmic plot of the transmission T of carbon films as a function of mass thickness d_m for different objective apertures α_o (E = 100 keV). The full curves were calculated using a multiple-scattering integral with the constants x_{el} = 47.6 µg/cm^2 and θ_0 = 28.4 mrad, obtained from a best fit of the initial slopes at small d_m. The straight lines T_{fil} (green) correspond to measurements of zero-loss-filtered transmission. The straight lines T_{unf} (red) correspond to unfiltered transmission.

This shows that the projected signal, i.e. transmission T, is a monotonic function of mass thickness d_m and therefore fulfils the 'projection requirement'. T further depends on the element specific contrast thickness d_k which in turn depends on the energy of the electrons.

According to Fig. 2.2 the contrast thickness $d_k(\alpha_o)$ shows a significant dependence on the size of the objective aperture α_o. The contrast variations in an image caused by scattering contrast increase with decreasing α_o. Therefore, a small objective aperture is generally used for BF-TEM tomography. An objective aperture reduces the occurrence of displaced diffracted images and also the spatial resolution [55, sec. 2.4].

Due to the very restricted working space within the polepiece gap (2 to 5 mm) [120] and the need for high tilts for TEM tomography, typically ±70°, a high-tilt sample holder

and a suitably prepared sample have to be used [55, sec. 2.3]. The high-tilt sample holder allows for tilting of the specimen to high angles in the microscope without touching the objective lens pole piece or the objective aperture blade [55, sec. 2.3]. However, the conditions in the used TEM (described in Sec. 4.2) allowed only a tilt upto ±45° with an inserted objective aperture despite the use of the high-tilt sample holder[5)] (see Ref. [193; 195; 46] for specifications). This tilt range is insufficient for TEM tomography and therefore no objective aperture (OA) was used for TEM tomography leading to an unknown α_o (above 50 mrad, which is about the highest α_o selectable with the OAs in the used TEM, see [195]). To improve the quality of the images and the resulting tomogram, 'zero-loss' (ZL-TEM, see e.g. [146; 120]) images were acquired and used for ZL-TEM tomography. By zero-loss filtering, the contribution of the inelastically scattered electrons can be removed and the transmission becomes [146, p. 205]:

$$T_{fil} = \exp\left(\frac{-d_m}{x_{el}}\left(\frac{1}{1+(\alpha_o/\theta_0)^2}+\nu\right)\right), \nu = \frac{x_{el}}{x_{inel}} \simeq 20/Z \text{ [146, eq. 5.94, 5.66]}$$

As Fig. 2.2 shows, the different contrast thickness $d_k(\alpha_o)$ for ZL-images shows less dependence on the size of the objective aperture α_o. Additionally, the contrast variations in an image are much more pronounced than for BF-TEM (compare curves for T_{fil} in respect to curves for T_{unf}). This can be seen in Fig. 2.3. However, the ZL-filtering reduces the signal intensity and thereby the signal-to-noise ratio (SNR). To maintain a fixed SNR, the acquisition time has to be increased in regard to BF-TEM.

The difference between ZL-TEM and BF-TEM is much less for ruthenium due to the difference between $\nu_C \simeq 3$ and $\nu_{Ru} \simeq 0.5$. The gain of contrast for zero-loss filtering by the higher sensitivity to small variations in mass thickness and by the avoidance of chromatic aberration is therefore largest for carbon-containing specimens [146, p. 205]. This can be expected to have a positive effect on the reconstruction of carbon-supported ruthenium nanoparticles since the attenuation caused by the ruthenium nanoparticles is already high compared to that of the carbon support [95].

A variety of other imaging modes of a TEM can be used for tomography as well, e.g. (high-angle-annular-dark-field) scanning transmission electron microscopy (HAADF) STEM, energy-filtered TEM (EF-TEM), more can be found in the literature [55; 90; 120; 81]. The restrictions, given by the used TEM and the functionality of available software, limited the choice of imaging techniques to BF-TEM, ZL-TEM, STEM and EF-TEM. Test experiments showed that, due to contamination sensitivity, only BF-TEM and ZL-TEM could be used for the samples studied, although (HAADF) STEM tomography is often used for non-biological samples [184; 90; 123; 55].

[5)] According to Zeiss LIBRA experts and M. Wollgarten.

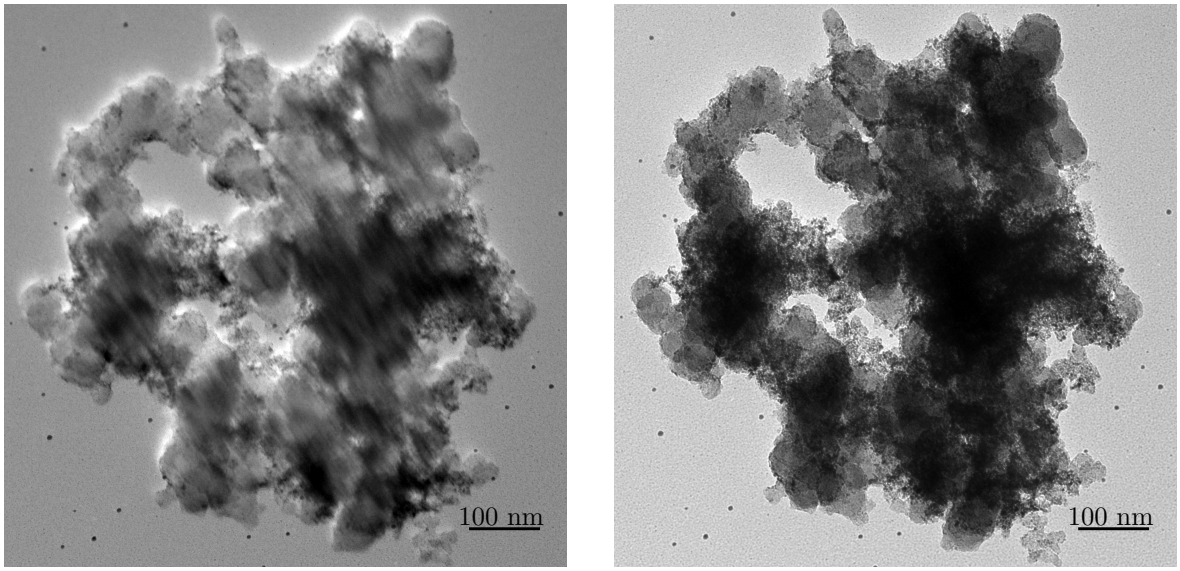

Figure 2.3: BF- and ZL-image
On the left a BF-image and on the right a ZL-image of a $RuVC_{um}$-particle (see Chap. 5 for a description) with same acquisition times are shown. Its depth (around 1 µm) is about twice its width. Although the SNR in the ZL-image is lower, the resolution of the ZL-image is better in regions where the sample is up to about a few 100 nm thick. This is because ZL-filtering avoids the otherwise significant chromatic error resulting from energy losses in thick specimens due to multiple inelastic scattering [146]. In very thick regions (above about 500 nm) the attenuation is so high that these areas are nearly opaque.

Resolution

Kübel et al. [90]; Midgley and Dunin-Borkowski [122] report a limit on feature size for tomography with conventional TEM of around 1 nm. STEM tomography is expected to yield a higher spatial resolution because of a stronger contrast dependence on the atomic number (Z-contrast) and less influence from artefacts caused e.g. by Bragg-reflections [55; 90; 124]. However, STEM tomograms show less detail in the representations of carbon support (see Fig. 5.7 and Ref. [55]). Test experiments showed that STEM also leads to much stronger local contamination for the studied samples than TEM because of the focused beam [64]. The procedure to determine the overall resolution is not well-defined for tomograms created by electron tomography [55].

To avoid switching coordinate systems, I generally use the coordinate system implied by the aligned image stack, i.e. that of the reconstruction. There, the x-axis is perpendicular to the rotation and optical axis. The y-axis is in the direction of the rotation axis and the z-axis approximately in the opposite beam-direction (see e.g. Fig. 4.5).

Assuming perfect alignment, the resolution along the rotation axis (y-axis) δ_y is equal to the resolution in the original micrographs δ (e.g. TEM images) [123; 55]. The resolution in the direction perpendicular to the rotation and optical axis (x-axis) is determined by the number of projections, N, and the diameter, D, of the reconstructed volume (Crowther criterion, [36]):

$$\delta_x = \pi D/N \tag{2.1}$$

The resolution in the direction of the optical axis (z-axis) is further affected by the 'missing wedge' [141] and can be estimated from the maximum tilt angle α as follows [141][6]:

$$\delta_z = \delta_x \sqrt{\frac{\alpha + \sin\alpha\cos\alpha}{\alpha - \sin\alpha\cos\alpha}} \tag{2.2}$$

According to Friedrich et al. [55], resolutions better than predicted by the Crowther criterion have been obtained but not understood. Reimer and Kohl [146] call eq. 2.1 a "rule of thumb". Other measures for the quality of a tomogram, i.e. related to its resolution, are outlined in the following sections.

Resolution estimation in 2D images

The resolution of a tomogram does not only depend on the reconstruction algorithm used and the reconstruction artefacts introduced. First of all, the resolution in a tomogram depends on the resolution of each individual image of the tilt series. The resolution of 2D images can be determined in different ways.

One method is to check whether a structure of known dimensions is obviously resolved in the 2D image (e.g. crystal lattice or biological structures such as cell molecules). This is an object-dependent resolution estimation. An object-defined (gold lattice) resolution for aberration-corrected TEM below 0.05 nm was reported by Freitag and Kisielowski [54].

The Young's fringe method is often used to determine the information limit of a TEM [102; 54; 153; 154; 61; 50; 51]. Depending on the acceleration voltage, the Young's fringe method is not the best method [15]. The theoretical resolution limit or information limit (of around 0.08 nm for the latest high-resolution TEMs, HRTEM, [15; 154]) is limited by the temporal coherence which depends on the energy spread of the electron source, the fluctuations of the accelerating voltage and the objective-lens current fluctuations [15; 89]. Additionally, the information limit in a particular image is further limited by the spatial coherence depending on the defocus chosen [89]. Methods to estimate image resolution in 2D images are [104]: Fourier Ring Correlation (FRC), Q-factor, S-factor, Spectral Signal-to-Noise Ratio (SSNR).

For amorphous samples, the resolution limit, taking into account chromatic aberration and beam convergence, can be evaluated from a diffractogram obtained e.g. by FFT (see [157, p. 8 and sec. 4.5.2.1, p. 163] or [40, sec. A12.3, p. 31ff]). This evaluation is not related to the Young's fringe method and is used in Fig. 2.1 and Fig. 4.4.

[6] α in radians was used –although nowhere specified and surrounded by angle specifications in degrees [141; 52]– because the formula originates from an integral, see [141, App. A2]

This variety of resolution estimation methods shows that there is no established criterion that defines the actual resolution in a 2D image. Therefore, the same problem exists in 3D images.

Depth of field

It should be noted that the resolution in 2D TEM images is also dependent on the extent of the sample along the beam direction, i.e. the depth of field (DOF).[7)] As stated by Vanhecke et al. [179, sec. 1.3, p. 315], it is possible to tilt the object and record sharp projections at different tilt angles, since the entire object is always in focus (due to the large depth of field). According to Ref. [179, sec. 4, p. 320], it is striking that the high depth of field of electromagnetic lenses is exactly what makes electron tomography possible in the first instance: the fact that the entire object is always projected in focus.

Much of TEM theory assumes a weak-phase object (i.e. fulfilling the weak-phase object approximation [146]) of a thickness (of a few nm) which generally lies within the DOF. However, the latest TEMs, that achieve resolution limits in the sub-Å region, have a DOF below 1 nm [21]. Anyway, when the object is rotated for TEM tomography, the imaged region of the object may exceed the region of the DOF depending on the chosen acquisition parameters [70]. The importance of the DOF concerning TEM tomography can be realized when comparing parallel beam STEM tomography [22] with a practically unlimited DOF and confocal STEM 'tomography' [70; 120] with a DOF below 1 nm [21].

In the STEM mode operated with a convergent beam, the DOF is easily determined by the convergence angle of the focused beam (see e.g. [22]). In the TEM mode, the determination of the actual DOF is more complicated since it depends on the collection angle, the magnification and the image resolution set by the pixel size of the CCD chip (or the grain of photographic film) [146; 185; 148]. Furthermore, under different circumstances, the limiting angle is defined by the illumination aperture or by the objective aperture [185]. Altogether, this is the reason why DOFs ranging from a few nm to a few µm are reported [148; 179; 146; 185].

A formula given by Ref. [146; 185] to estimate the DOF is:

$$DOF < \delta_s/\alpha_0 = \delta_{im}/M/\alpha_0$$

Here, δ_s is the smallest distance that can be resolved in the specimen plane and δ_{im} in the image plane. Since no defined objective aperture can be used during tomography in the used TEM, the DOF for e.g. $\alpha_0 > 50$ mrad (largest objective aperture of the used TEM) would be between 1.7 nm to 15 nm for the magnifications used in this study (20 kX to 180 kX) and a detector pixel size of about 15 µm [57]. However, during reconstruction only spatial frequencies up to the first minimum of the effective transfer

[7)] The depth of field (sometimes called depth of focus [146, sec. 4.4.4 p. 108]) must not be mistaken by depth of image (sometimes also called depth of focus [185, sec. 6.7 p. 110]).

function (eCTF) actually contribute to the tomogram. The minimum of the eCTF in the presented studies lies around a spatial frequency of $\nu \approx 0.1$ Å^{-1} (corresponding to a directly interpretable 2D resolution of $\delta_s \approx 10$ Å). The contribution of spatial frequencies above this value can be neglected due to the rapidly changing oscillations of the CTF within the defocus range covering the sample thickness. Therefore, the effective collection half angle α_0 can be estimated to $\alpha_0 = \arcsin(\lambda\nu) \approx 2.5$ mrad for the investigations of this study. The resulting DOF evaluates to $DOF < \delta_s/\alpha_0 \approx 400$ nm. This is about the thickness of the samples studied. Regions in the images of the tilt series that exceed the DOF do not fulfil the projection criterion. The corresponding regions in the reconstructed tomogram should therefore suffer from artefacts and resolution loss.

Resolution estimation in 3D images

The resolution of the final tomographic reconstruction is not only dependent on the aspects mentioned above concerning 2D resolution estimates and DOF but also on the quality of alignment of the tilt series before reconstruction (see e.g. [25]), i.e. the resolution δ_y cannot equal the resolution in the original micrographs δ if the misalignment is larger than δ. This can easily happen since the specimen changes during data collection due to beam damage. Consequently, the total electron dose used to record a tilt series must be kept as low as possible (see e.g. [198]). This however decreases the SNR and in turn limits the resolution in the tomogram due to noise.

Apart from using object-determined tomogram resolutions, as it is often possible for biological samples (see e.g. [35]), there are correlation methods to gain a quality measure expressed by a figure of merit (FOM) [25; 52; 107]. One of the most common method is the Fourier shell correlation (FSC) [120; 177; 104]. FSC is described e.g. in Ref. [177] and [104, p. 770]. It measures the normalised cross-correlation coefficient between two reconstructions over corresponding shells in Fourier space (i.e., as a function of spatial frequency). It is the generalization of the Fourier Ring Correlation (FRC) to 3D.

FSC and other methods such as e.g. DPR and SSNR (see Sec. 6.3 and App. A.2) depend on a threshold criterion for the determination of the actual resolution. Many different criteria are proposed and discussed (see, e.g. [177; 104; 52; 33]) but lead to very different resolution estimates. These resolution estimates generally do not account for the influence of reconstruction artefacts (as discussed in Sec. 6.3) which can have an influence on analysis (see e.g. [90]). Apart from the missing wedge artefact, the tomograms of the samples studied often suffered from streak artefacts [29; 14; 65] (also called ray or fan artefacts [52; 120]) arising from materials with high attenuation coefficients (e.g. ruthenium) [29] for each projection direction. The so-called 'banana' artefacts (see e.g. [25]) originate from improper alignment and play no significant role when fiducial markers are used [25; 52]; only the 'remainder' of the 'banana' artefacts. These are cross like, i.e. two global directions in roughly each maximum tilt projection direction (see e.g. [52; 111]). Changes of the sample during acquisition, e.g. contamination, lead to artefacts as well.

Specimen damage by electron irradiation

Since tomographic reconstruction builds on many images, any change of the sample during acquisition of tilt series also influences the resolution of resulting tomograms. Specimen damage by electron irradiation, i.e. beam damage, has different origins. Most of the energy dissipated in energy losses is converted into heat [146, Chap. 11]. Hydrocarbon molecules condensed from the vacuum of the microscope or deposited on the specimen during preparation and storage can form a contamination layer due to cracking of the hydrocarbon into non-gaseous compounds that cross-link to the sample surface forming a carbon-rich, polymerized film [146, Sec. 11.4]. In competition with this contamination, reactions with activated, adsorbed H_2O, O_2 or N_2 molecules cause etching of carbonaceous material. Depending on specimen preparation, partial pressures, specimen temperature, specimen surface structure and irradiation conditions, growth of either sign (positive for contamination and negative for etching) may prevail [146; 64]. The rise in specimen temperature and the extent of contaminated regions can be limited by keeping the illuminated area small. However, when only a small specimen area is irradiated, the hydrocarbon molecules are particularly likely to diffuse on the specimen and be cracked and fixed by the electron beam [146; 64].

Chapter 3

Developed image filter and analyses

Tomographic data often contains so much information, due to the three dimensions, that it is difficult to recognize all its properties. When a property is recognized it is still a challenge to extract this information in a meaningful way since three dimensions allow many degrees of freedom. My aim is to gain insight of the overall system the tomogram represents. Therefore, I decided to average variations and express overall properties by statistics. The faith in the interpretation of such statistics is dependent on the number of statistical events. In order to achieve a high number of statistical events in a reasonable time, e.g. to measure an individual property of many thousand particles, the help of a computer is needed. However, the computer needs to be told how to evaluate the given data. Therefore, my work was to define for the computer how to analyse the tomographic data. I only give a detailed description of three of the approx. 60 programs, that I created for the image processing of the data to achieve the results presented, because these three represent/execute my ideas that are essential for the further understanding of the analysis of the tomograms in Chap. 5.[1)] The description comprises three main tasks (and an introduction to point densities on a sphere):

- Particle shape analysis achieved by fitting ellipsoids to individual particles to analyse e.g. the deviation from spherical shape,
- Specialized watershed separation (that is optimized with respect to the reduction of subjective influences) to split particles at defined connections,
- Fully automated facet analysis for multiple particles in tomographic datasets to characterize particles by the orientations and sizes of their facets.

Theses programs were designed for the applications described in Chap. 5. Three example applications of the facet analysis program on tomographic data from other methods are presented at the end of this chapter. There is also a short introduction to the evaluation of weighted point densities restricted to the surface of a unit sphere, because different solutions to this problem will be needed in the following text.

[1)] The other programs are not further described either because the task they full fill is described elsewhere or because my achievement lies in the field of informatics; e.g. some programs had to be optimized to use less virtual memory or to finish faster (i.e. within less than a year).

3.1 Fitting ellipsoids to particles

In Sec. 5.3.4.3 ellipsoids are fitted to ruthenium particles to evaluate their deviation from spherical shape. The procedure used to fit ellipsoids to particles is outlined below.

The program described in this section calculates parameters to define ellipsoids that approximate each label (i.e. particle) of a 3D label image. A label image consists of marked regions of the foreground of a binary image. A unique value is assigned to each region by a given criterion (explained in more detail in App. A.1). The program fits ellipsoids to labels such that they equal in volume and that the orientations and the ratio of their main axes equal those of the label. Ellipsoids are a more general approximation than spheres of equal volume and therefore can be used to evaluate the orientations of the corresponding labels and their deviation from spherical symmetry. Since ellipsoids represent a more general shape, additional parameters are necessary to define an ellipsoid unambiguously. The moment of inertia as a tensor allows to calculate these. The ellipsoid axes can then be scaled uniformly in all directions such that the ellipsoid equals the particle in volume or surface area. I chose the volume because it is less prone to error than the estimated surface area of the discrete representation (see App. A.1). It is also a requisite for my definition of the quantity that I call ellipsoidity. The task of this program, referred to as ellipsoid fitting, is to yield a list of values that define the 'fit-ellipsoid' unambiguously for each label within an input image. This list of values can then be used for further evaluations or to draw the fit-ellipsoids.

Moment of inertia and image moments

The components of the moment of inertia tensor for the label j can be determined in discrete space using the following expression [132, p. 236]:

$$\mathbf{I}_j = \begin{pmatrix} \sum_{i=1}^{N_j} m_i(y_i^2+z_i^2) & -\sum_{i=1}^{N_j} m_i(x_i y_i) & -\sum_{i=1}^{N_j} m_i(x_i z_i) \\ -\sum_{i=1}^{N_j} m_i(y_i x_i) & \sum_{i=1}^{N_j} m_i(x_i^2+z_i^2) & -\sum_{i=1}^{N_j} m_i(y_i z_i) \\ -\sum_{i=1}^{N_j} m_i(z_i x_i) & -\sum_{i=1}^{N_j} m_i(z_i y_i) & \sum_{i=1}^{N_j} m_i(x_i^2+y_i^2) \end{pmatrix}$$

No mass inhomogeneity within the label nor between different labels is regarded since each foreground voxel is expected to represent the same material, therefore $m_i \stackrel{!}{=} 1$. The summation is only over all the voxels of the label j, i.e. N_j: # of voxels of the label, x_i, y_i, z_i are the voxel coordinates relative to the centroid, ie particle centre.

After carrying out a principal axis transformation on $\mathbf{I}_j$ the eigenvectors point in the direction of the ellipsoid axes and the eigenvalues $(\tilde{I}_{xx}; \tilde{I}_{yy}; \tilde{I}_{zz})$ correspond to the axes lengths as follows:

$$a \widehat{=} \sqrt{\frac{5}{2}\tilde{I}_{yy} + \tilde{I}_{zz} - \tilde{I}_{xx}};\ b \widehat{=} \sqrt{\frac{5}{2}\tilde{I}_{zz} + \tilde{I}_{xx} - \tilde{I}_{yy}};\ c \widehat{=} \sqrt{\frac{5}{2}\tilde{I}_{xx} + \tilde{I}_{yy} - \tilde{I}_{zz}}$$

In image analysis the so called 'image moments' are used for these calculations [101; 136]. The zero order moment equals the number of voxels N_j that make up the label j which is the same as its voxel volume. The normalized image moments of first order yield the centroid $\vec{c} = \frac{1}{N}\sum_{i=1}^{N}\vec{r}_i$ which can be regarded as the centre of mass of the label. The normalized second order (cross) moments correspond to the entries in $\mathbf{I}_j$ [101; 136].

With theses values[2)] it is now possible to create meshes representing the ellipsoids. A (3D) mesh –comparable to 2D vector graphics– consists of points, edges (connected points) and flat polygons (connected edges, often triangles) that define a discrete surface not bound to a grid (contrary to the voxel image representation). These mesh ellipsoids translated by their centroids yield a construct as shown in Fig. 5.25.

Sphericity and Ellipsoidity

The sphericity is a measure for the deviation of particles from spherical symmetry. In image analysis, it is often defined as $c_p = 6\sqrt{\pi}\quad V/S^{3/2}, c_p \in [0;1]$ and has no unit.[3)] For a sphere $c_p = 1$ and for any other shape $c_p < 1$ since a sphere is the shape with the highest volume enclosed by the smallest surface.

Analogously, I introduced the 'ellipsoidity' as a measure for the degree of deviation of particles from an ellipsoidal shape to quantify how well each fit-ellipsoid approximates its particle. I defined the ellipsoidity η as the ratio of the surface area of the fit-ellipsoid A_e to the surface area of the corresponding label (often representing particles) A_p: $\eta = A_e/A_p$. This relation only makes sense if both have the same volume, $V_e = V_p$. The surface A_e can be easily calculated e.g. from the mesh of the ellipsoid used for visualization by adding up the polygon areas. The error in this estimation of A_e is neglectable compared to the error of A_p and V_p. I will use the ellipsoidity under the assumption that the following statement holds: The ellipsoidity $\eta = A_e/A_p$ equals unity for an object that already resembles an ellipsoid, $A_p = A_e$. However, a label, i.e. a voxel object, can never be an ellipsoid because of the discrete nature of the voxel representation. A deviation of the label from ellipsoidal shape increases the surface area, $A_p > A_e$. Therefore, η decreases as the shape of the label deviates from an ellipsoid.[4)]

[2)] At the time, ITK[2] with the contribution of Lehmann [101]; Padfield and Miller [136] was the only reliable tool to gain access to these values. The quantification pack of Avizo gave completely wrong values and MAVI was not able to calculate these values at all.

[3)] The sphericity can also be defined differently: let $\gamma = 36\pi V^2/S^3$ then the sphericity can be defined as $\Psi = \sqrt[3]{\gamma}$ [180] or as $c_p = \sqrt{\gamma}$ [99]; γ, Ψ, $c_p \in [0;1]$ and $\gamma = \Psi = c_p = 1$ for a sphere.

[4)] My definition of ellipsoidity (not ellipticity) might not be an unambiguous characterization quantity. However, under the given conditions, i.e. the surface is a manifold and closed, I could not find any counterexample.

Figure 3.1: Particles badly approximated by their fit-ellipsoids
Two example particles that are badly approximated by their fit-ellipsoids, $\eta \approx 0.62$ and $\eta \approx 0.24$ respectively (see also Fig. 5.19). The ellipsoids shown are created as described in 3.1. A watershed separation splits the particle at constrictions. The resulting particles are then much better approximated by ellipsoids (see Fig. 3.2).

3.2 Watershed separation of particles

A common problem when dealing with datasets containing multiple particles is that two or more particles are connected in the binary image representation although they should be treated separately during an analysis due to additional knowledge about the system. For example, the creation of a label image for ellipsoid fitting: If the criterion for label creation consists of only the interconnectivity of foreground voxels, multiple connected particles are identified as one single label. This leads to 'ginger' shaped labels that are badly approximated by ellipsoids (Fig. 3.1 and Fig. A.6). The connection between particles can originate from inappropriate thresholding, insufficient resolution, reconstruction artefacts or a 'gluing' of the particles during the sample preparation. Therefore, prior knowledge is necessary to define if and where these connections should be separated.

In the particular case of ruthenium particles (Chap. 5), the origin for the 'gluing' (in the sense of spatial connection by the same virtual 'material') of particles is unclear. Reconstruction artefacts are definitely involved and are dominant –concerning the 'gluing' of ruthenium particles– in WBP and SIRT reconstructions of the samples. Even though the DIRECTT reconstruction has a better spatial resolution than WBP or SIRT there still seem to be particles 'glued' together if they are very close to each other (Fig. 3.1). Considering crystallographic intergrowth or an actual 'gluing' during the preparation procedures, the connection of particles is real. However, the crystalline ruthenium particles are expected to be fragments of hexagonal bipyramids [45; 131] that appear spherical or more generally ellipsoidal if the spatial resolution is insufficient to image the crystal facets. Therefore, a watershed separation was applied to the binary image of the ruthenium segment to separate the particles where they were most likely intergrown or 'glued'. Such positions can be identified by constrictions, often

referred to as concavities[5)], but not any constriction should lead to a separation.

The watershed separation is a well known technique to separate connected particles in image analysis. The basic idea is to calculate a distance map of the binary image inside the segment in which separations should take place. Then a watershed transformation (see App. A.1 for the explanation of the difference between watershed separation and transformation) is done on this distance map [18, sec. 8.1]. Therefore, the watershed separation is a filter chain (for more details on the definitions see App. A.1). Its output result is generally a label image.

However, this technique can only yield completely convex labels and therefore is only appropriate if the separated particles are all expected to be convex. Should the dataset contain particles that are supposed to have constrictions, then common watershed separations lead to unwanted separations often referred to as over-segmentation [162; 76; 52]. This is also the case for the ruthenium particles. They should only be separated at significant constrictions, not at constrictions below the resolution limit.

3.2.1 Controlling over- and under-segmentation

Over-segmentation can be controlled by parameters of additional filters inserted in the filter chain or modified watershed transformation algorithms ([18; 25] and [129, sec. II.5, p. 2588 f.]), e.g. minimal depth or size of the surface of a pool (for a detailed description see App. A.1). It should be pointed out that pools are one dimension higher than the (labelled) region they mark, which is basically the surface of the pool, the depth/height being perpendicular to the surface. Therefore, the pools of a watershed transformation of a 3D grey scale image are 4D and their 3D 'surface' marks a 3D region in the grey scale image. The parameters are constrictions that make the resulting labels reach up to a defined extent. However, under-segmentation can now occur depending on the (manually) chosen parameters. Therefore, the filter parameters should be calculated from general properties of the input image, e.g. its resolution, to avoid trial-and-error optimization of the degree of segmentation.

Additional filter parameters often introduce further case-to-case decisions. I tried to create a filter chain which depends on as few subjective parameters as possible. For this, I introduced a second distance map into the filter chain which allowed me to calculate the additional parameters from a set of basic parameters. I was able to relate these basic parameters to general properties of the input data: The minimum distance necessary to separate two points (separation error) and the position uncertainty of an edge (edge error) which both relate to the resolution limit. The remaining parameters (e.g. voxel connectivity, introduction of watershed walls, described in Sec. 4.3 and App. A.1) have little influence on the result and can be chosen to suite the needs of further image processing.

[5)] Münch et al. [129] use the word concavity. However, constriction better describes the condition for the watershed separation presented here: E.g. arrow A in Fig. 3.2b) marks a constriction whereas arrow B marks only a concavity which is therefore not separated.

The separation error is determined from the minimal distance[6] between two particles to be regarded as separated. The edge error arises from the uncertainty of the position of an edge (2D) or surface (3D, i.e. transition from ruthenium to carbon or vacuum). There is a lower limit for the separation and the edge error, introduced when changing from real space to discrete (digital) space.

The uncertainty introduced by discretization of an edge in a binary image is at least the size of a pixel. This adds up to the uncertainties that are introduced through the limited resolution of the tomogram and artefacts introduced by the reconstruction algorithm which lead to an uncertainty of the threshold position for the binarization [91; 92]. The minimum distance to distinguish two particles in discrete space is at least twice the pixel size since there has to be one background pixel between two foreground pixel. This consideration requires a definition of 'between' which is provided by the mathematical concept of connectivity.

The two errors relate to two different constraints on the watershed separation:
Firstly, the edge error value corresponds to a minimum degree of constriction that must be reached to initiate separation.
Secondly, the separation error corresponds to the minimum distance between two particle centres such that the program separates them.
These two constraints prevent over- and under-segmentation. This filter chain not only separates the ruthenium particles appropriately but also combines them in a single label if they are so close to each other that they cannot be distinguished within the error limits.

Fig. 3.2 shows the 3D watershed separation result of the 'ginger-like' particle from Fig. 3.1 and the fit-ellipsoids of the separated particles. The orange particle (see arrow B in Fig. 3.2a) is not separated although it seems to have an obvious constriction.
This illusion is caused by the analysis of the constriction only in 2D (because the picture is a projection). Viewing the same particle from the right (Fig. 3.2b) shows no sufficiently pronounced constriction considering an edge error of 2. Since *only* the shortest distance in *any* 3D-direction is recorded in the distance map there exists no minimum right of arrow B in Fig. 3.2b that could initiate a separation in this case. On the contrary, the position marked by arrow A has a sufficient pronounced constriction in Fig. 3.2a *and* Fig. 3.2b.[7]

[6] It is important to remember that the maximum value of the distance map between two particle centres corresponds to only half the distance that separates them!

[7] Making the computer evaluate here as a human does would be very complicated. The computer would first need to recognize the shape of the particle. Depending on the shape it would need to find distinct projection directions in which a 2D watershed separation would separate the particle. Finally it would need to decide depending on all distinct projection directions whether there should be a separation in 3D or not.
This shows a controversy: Would there be a constriction at arrow B in Fig. 3.2a but a broadening at arrow B in Fig. 3.2b then a separation in 3D would even seem inappropriate for a human. This decision problem does not arise in the 3D watershed separation the computer does.

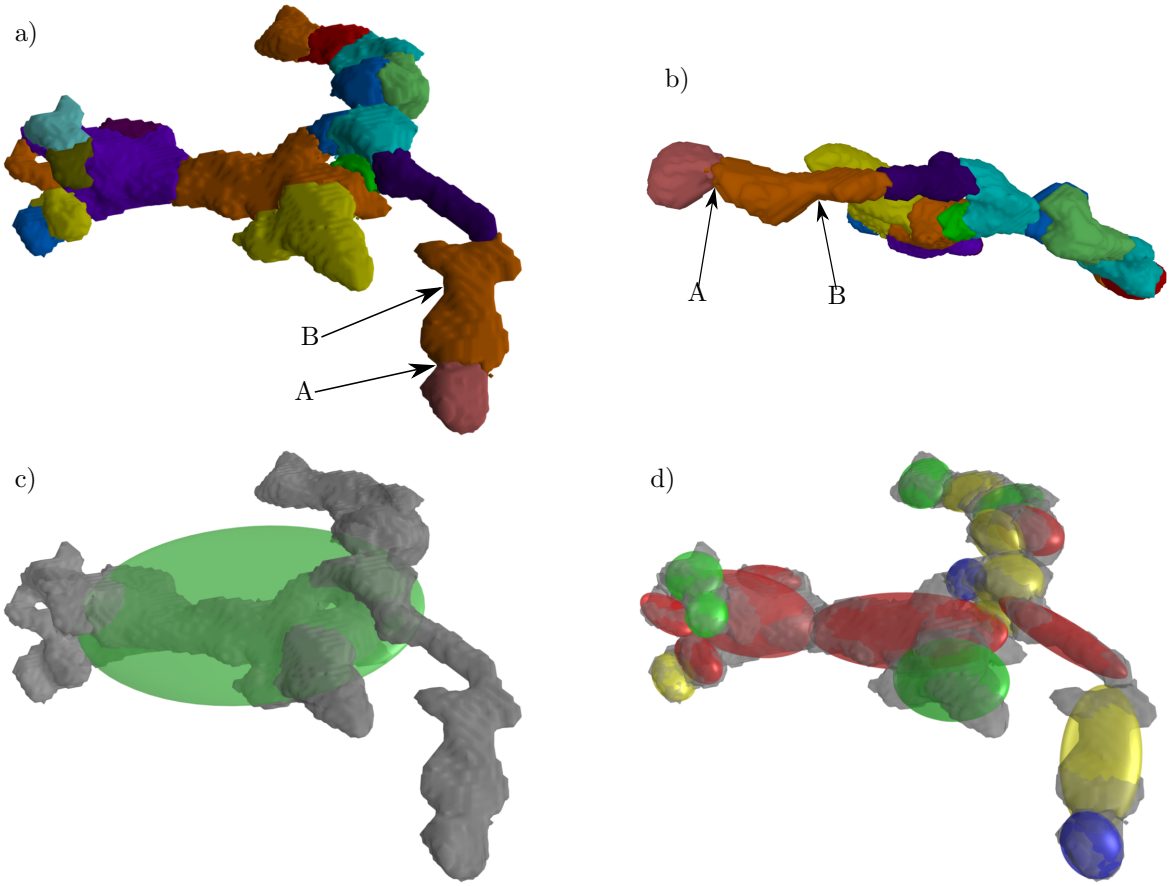

Figure 3.2: 3D watershed separation

The result of the watershed separation (top images, b) shows a) seen from the right) with a second distance map is demonstrated on a 'ginger-shaped' particle. An edge error of 2 and a separation error of 6 were assumed The fitting ellipsoids before (c) and after (d) the watershed separation are rendered in the bottom images. The ellipsoidal approximation of the particles is obviously much better after watershed separation (quantified in Sec. 5.3.4.4). The meaning of the colours of the ellipsoids is explained in Sec. 5.3.4.3.

3.2.2 Watershed separation with an additional distance map

In this section I describe how the additional distance map mentioned above is incorporated into the filter chain of the watershed separation. The additional distance map introduces an additional separation criterion which is related to the separation error and is described below.

First, a Signed Danielson Distance Map[8)] (SDDM, [76, sec. 6.8, p. 216 ff] and [162; 39], see Fig. 3.3.b) is generated from the ruthenium binary image (Fig. 3.3.a). A signed distance map is used to regard not only the distances inside particles but also distances between particles (which correspond to outside, i.e. positive distances in the SDDM, see Fig. 3.3.f). The local minima[9)] of this map are then filled to a specified height h1. Height here corresponds to a difference in the intensity value of different voxels.

[8)] There are more exact and more efficient implementations available now to generate a distance map (e.g. [17, sec. 4.2 p. 5]), but the accuracy of the SDDM (yielding floating point values of approx. Euclidean distances) seemed sufficient in this case and therefore the evaluation was not redone.

[9)] The evaluation of local minima needs a connectivity definition (i.e. 4|8 or 6|26, see Sec. 4.3).

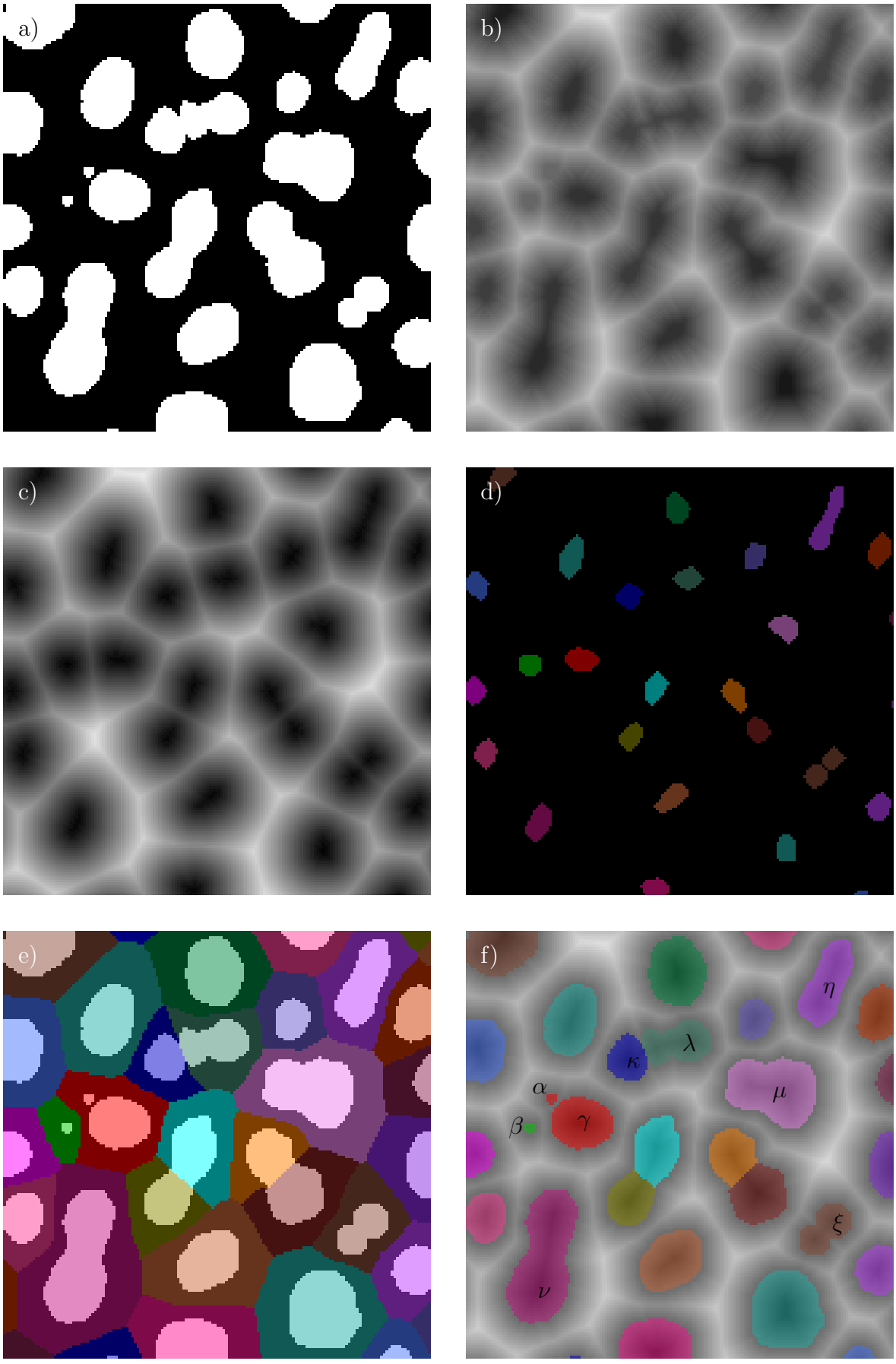

Figure caption on the opposite page

This height relates to half the edge error and the filling prevents over-segmentation otherwise caused by insignificant or uncertain constrictions.

However, multiple significant constrictions can appear close to each other. To avoid over-segmentation in these cases, a second Danielson Distance Map (DDM) is generated from the previously evaluated local minima (Fig. 3.3.c). Again, the minima of this DDM are filled up to a specified height h2. This combines particle centres that are closer to each other than half the separation error.

The remaining local minima are labelled (Fig. 3.3.d) according to a defined connectivity (i.e. 4|8 or 6|26). These labels then serve as markers (wells) for the watershed transformation on the SDDM (Fig. 3.3.e). Finally, the resulting labels are masked by the ruthenium binary image (Fig. 3.3.f). The whole procedure is referred to as the watershed separation in the rest of the text.

3.3 Local weighted point densities on a sphere

The evaluation of Local Weighted Point Densities (LWPD) of N points on the surface of a sphere (see e.g. Fig. 3.4a) is needed in four different applications of my thesis (first in the next section):

1. The facet analysis 3.4.1
2. The shape analysis 5.3.4.3
3. The global orientation analysis 5.3.4.5
4. The local orientation analysis 5.3.6.2

I found three different methods for the evaluation of LWPD, which are described in the sections where they are used such that the direct application eases the understanding. A short description of each method with its advantages and disadvantages follows to make it easier to understand why a single method is not appropriate for all applications.

Figure 3.3: Watershed separation with an additional distance map in 2D

Intermediate images from the watershed separation filter chain of a 2D example. The parameters are: h1= 2, h2= 3, always 8-connectivity, no walls.

a: binarized image of some blobs with constrictions.
b: SDDM of a), see f) for the distinction of positive and negative regions.
c: DDM of the local minima of b) filled up to a specific height $h1$.
d: Labelled local minima of c) filled up to a specific height $h2$.
e: Watershed transformation of d) overlaid by the blob mask a).
f: SDDM overlaid with the final masked watershed transformation to visualize the inner (-, coloured) and outer (+, grey) parts of the SDDM.
Although α and β do not differ in shape α is assigned the same label as γ because the distance between their centres is less than 6.
The blobs λ, η, μ, ν are not separated into sub-parts because their constrictions are not sufficient pronounced considering an edge error of 4, the constriction between κ and λ however is.
The blob ξ is not separated although there are two centres because the labelling assumed 8-connectivity and the centres are just about 6 pixel apart.

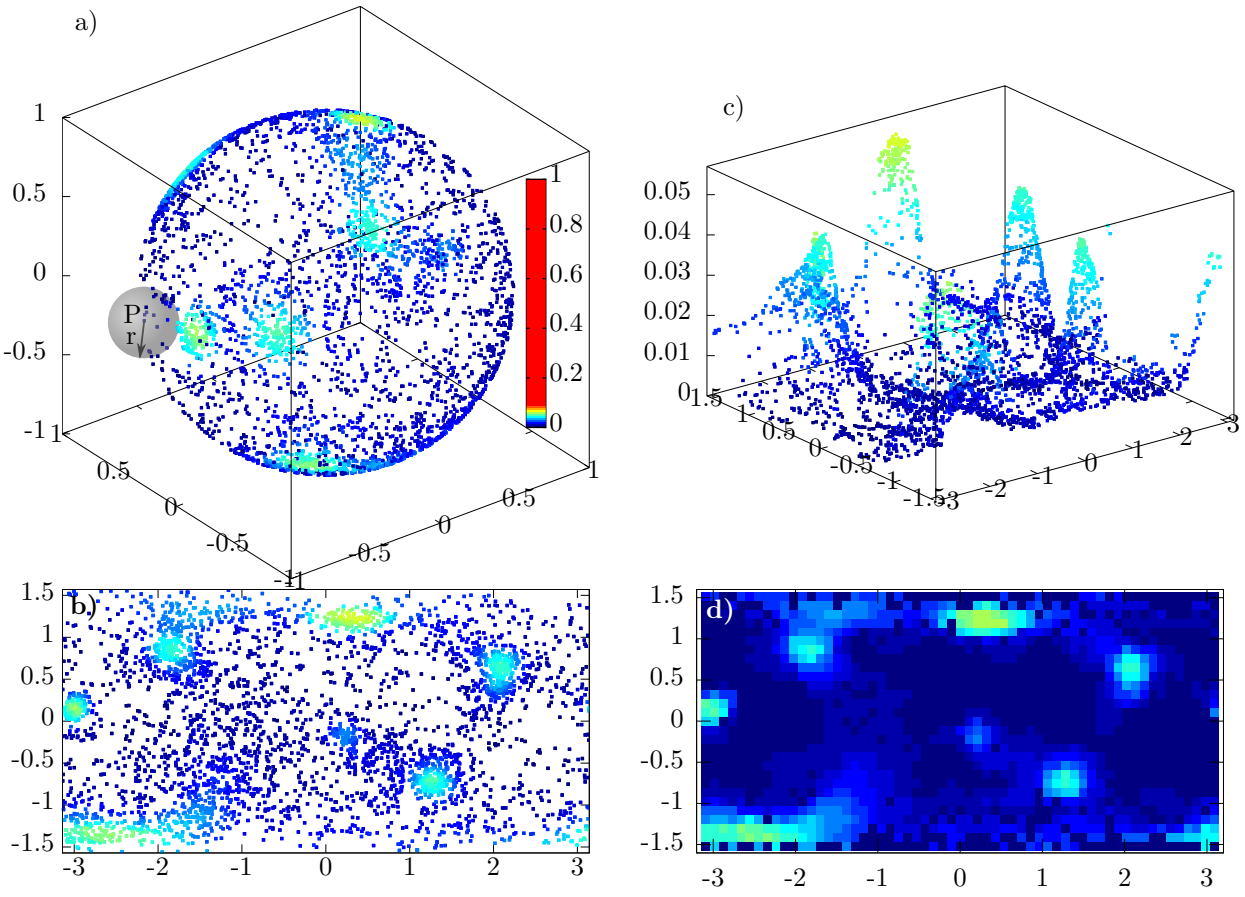

Figure 3.4: Weighted point densities evaluated by local sphere sampling

Figure visualizing the evaluation of the Local Weighted Point Density (LWPD) by local sphere sampling (LSS). The point density distribution used here for demonstration is taken from the intermediate state of the facet analysis of the smoothed particle from Fig. 3.5. The computation time of LSS is proportional to N^2; N being the total number of points, in this case 3944; one point for each triangle normal.

a: Point distribution on the unit sphere. The colouring of a point P is according to the sum of the weights of the other points found within a local sphere ($r < 1$) centred at P. (The colour bar was chosen such that a relative facet size above 1/8 would be red.)

b: Equirectangular projection of a), angles in radians.

c: b) plotted with colour values as heights to visualize the distinct peaks and the low background.

d: b) converted into a field depiction by *averaging* the LWPDs of points lying in the same field.

1. **Gaussian Splatter** (GS, as described in 3.4.1 **4.**)) is best for the facet analysis since its computation effort is proportional only to the number of points N (not N^2) and it accounts for the uncertainties of the orientations (i.e. the positions of the points on the sphere).

2. **Projection of the Points into a Plane** (PPP, as described in 5.3.4.3) can be used if the point distribution on the sphere is limited to a region whose boundaries align with the fields of a 2D histogram after a projection (i.e. a spherical triangle). The use of this method is only reasonable if the distortion introduced by the projection is negligible for the projected region. The computation effort is again proportional to N.

3. **Local Sphere Sampling** (LSS, as described in Sec. 5.3.4.5) yields the exact LWPD within a solid angle. However, the computation time is proportional to N^2. After the evaluation of the LWPD on the sphere the points can be projected into a plane for further analysis and unambiguous visualization (Fig. 3.4).

The important difference between PPP and LSS is that in PPP the projection is done before evaluation of the point density in contrast to LSS which evaluates first and then projects. Also, PPP evaluates the density within squares (generalized to parallelograms) whereas LSS evaluates within a solid angle. Only for PPP the sum of all calculated LWPDs equals the sum of all weights, because the histogram fields do not overlap, contrary to GS and LSS.

3.4 Facets of particles

Crystalline particles are mostly faceted. These facets are ideally plane faces. However, due to discretization the digital representations are generally uneven to some degree. The problem of defining a measure for the degree of roughness and the threshold for a nearly even surface to be regarded as a facet is described further on. During formation of a crystal, it grows faster on some facets depending on the corresponding lattice orientation. In some cases the relative surface areas of facets (in regard to the total surface) change during growth, some facets even vanish. Therefore, the orientations and (relative) sizes of facets can give information about the growth state of a crystal. Nucleation induced by impurities or along edges often leads to imperfect crystal growth. Imperfect crystals exhibit very irregular growth and distortion resulting in seemingly unfaceted regions if the resolution of the imaging technique is insufficient to reveal the fine facettation. I refer to this effect with the term ‘degree of facettation’. The classification of the crystal shape depending on the actual facet orientations is expressed by the term ‘type of facettation’.

Different facet orientations also have different catalytic properties (see Sec. 6.2. To improve catalysts, it is therefore important to investigate possible influences of differently formed facets and their sizes. Beside chemical characterization, electron tomography can be used to directly analyse the degree and type of facettation.

The most common evaluation of facets of digital representations is the manual determination of angles of a few selected particles (e.g. [151; 62]). This procedure leads to a subjective selection of ‘good’ particles. The manual determination of angles between nearly even faces in 3D by a 2D projection is prone to error and manual measurement of the surface area of nearly even facet is even more difficult.

The motivation to develop this facet analysis originated from the idea of checking the ruthenium particle datasets for existence of facets which play an important role during catalysis. Particular interest lay in samples with ruthenium particles on the outside of the support where the ruthenium crystals could grow unhindered during production. However, the few particles checked manually did not show distinct facets. They either

were actually not faceted because of their small size, as it is known for some nano clusters[10)], or the resolution of the reconstructions was too low to reveal the facets. The only way to search for facettation was to check all approximately 9000 particles. To achieve this, automation was needed. The developed facet analysis program (referred to as 'the facet analysis') differs in that it is fully automated, versatile and extendible. Other programs, concerning facet, orientation or structure analyses, represent computer aided analysis with user interaction often designed for very specific problems [38; 77; 156]. The facet analysis described below is applicable to any tomographic dataset (see 'Application examples of the facet analysis' 3.4.2) and runs without the need of any user interaction. The results of the analysis for ruthenium particles are presented in 5.3.4.6.

I developed the software using the ITK[2] and VTK[3] libraries in conjunction with octave[5]. It avoids user interaction and allows statistics of many particles to be gathered. A polygon mesh that resembles the original particle shape is created from a voxel representation for each label of a tomographic dataset. Then, the surface normal orientation of each polygon of the mesh is calculated. The surface normal vector is regarded as a normalized point vector whose tip lies on the unit sphere. Depending on the degree of facettation of the label, the local density of the point distribution will vary (see for example Fig. 3.4.a). A surface region of the label mesh consisting of many similar aligned triangles will lead to a maximum in the local point density (visualized by the colour gradient in Fig. 3.4). The next step defines an extent around each local maximum to identify the points close to the maximum. Such a region around the maximum is necessary since most facets will be uneven due to the former discretization causing a spread of the points around the maximum density (visible in Fig. 3.4.b). The spread of points can be regarded as an uncertainty in the evaluated orientation of the facet. This uncertainty arises from the error in the tomographic reconstruction, the introduction of artefacts and through the smoothing of the mesh. However, smoothing is necessary because of the discrete nature of the tomogram and will be described in the following section. The facet analysis program that performs the evaluation takes a label image as input and outputs a list of facet characteristics and a mesh with the identified facets for each label.

The exemplary particle used for the demonstration of the stages of the analysis is taken from a 3D dataset created by Focused Ion Beam (FIB) slicing. The sample consists of spinel crystals ($MgAl_2O_4$) whose composition might vary. As the analysis will reveal later (Sec. 3.4.2.1), the example particle has not the most typical shape of spinel crystals which is an octahedron. Until then, I will still refer to the shape as an 'octahedron' instead of the more generalized 'fractions of an asymmetric square bipyramid'.

After the outline of the facet analysis method a few applications examples from different fields of image analysis are presented that demonstrate strengths and limitations of the method and show its application on general tomographic datasets.

[10)] Private communication with S. Fiechter

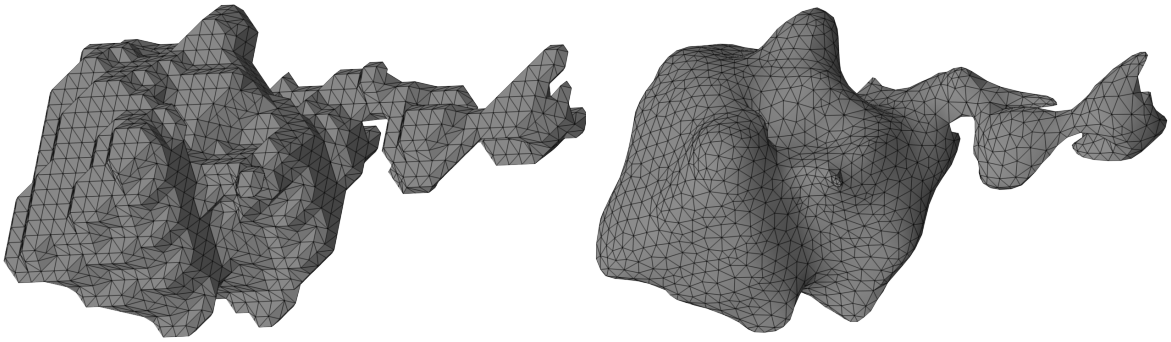

Figure 3.5: Marching cubes mesh: raw and smoothed
The left image shows an unmodified (raw) marching-cubes-sruface (of a spinel particle). The same mesh but smoothed by a windowed sinc filter (20 iterations) is rendered in the right image. The triangle sizes differ but the surface discretization is reduced and the overall shape is better visible.

3.4.1 Facet detection and analysis

The following sections describe the processing steps in the facet detection and analysis program. An image containing labelled particles (see A.1) is assumed as the starting point. The whole process is subdivided in the following three sections:

- Preprocessing
- Facet detection
- Facet analysis

Preprocessing

1.) Mesh creation A mesh of each label is created by the marching-cubes algorithm[11)] (described in Ref. [106] and [155, p. 166-171] and discussed in Sec. 6.2). The resulting mesh (or surface) consists only of triangles of similar sizes (left image in Fig. 3.5). In 3D, there can only be 26 orientations according to the 26 different nearest neighbours of a voxel.

2.) Smoothing The marching-cubes-surface needs to be smoothed to adjust the orientation of the triangles to be also related to neighbours further away. This is done by a windowed sinc smoothing filter ([170], recommended by B. Lorensen) that adjusts the vertices to relax the surface mesh. This process leads to quasi-continuous orientations and transforms regions with periodic steps into areas that are nearly flat (right image in Fig. 3.5, compare analysis of smoothed: Fig. 3.4 and raw: Fig. A.11). The remaining roughness is accounted for by the orientation uncertainty that the further evaluation considers.

3.) Area and normal calculation The last preprocessing step is to calculate the area and the orientation of the surface normal of each triangle [119; 58] [155, p. 340 f].

[11)] A better choice might be the algorithm of Mueller [127] (which was not available at the time).

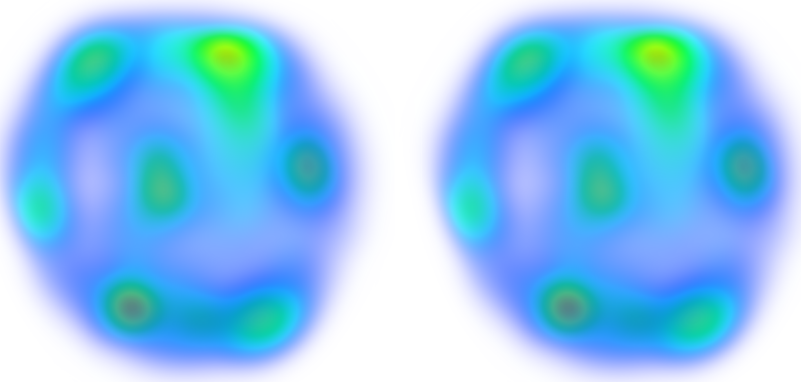

Additive Gaussian splats, volume rendered as a pair of stereo images. The grey values are mapped to a hue colour map to visualize the seven dense regions. Each of these represents a possible facet of the particle, its position corresponds to the facet orientation. The upper right dense region has an extension towards the missing 8th position.

Figure 3.6: Facet probability distribution of the spinel particle (Fig. 3.5)

Facet detection

The detection of facets can be realized by an evaluation of a weighted point density distribution on a unit sphere (as described in 3.3). The best method for facet detection of those mentioned in Sec. 3.3 is the 'Gaussian Splat' (GS) method –a discretized kernel density plot (see [178, sec. 3.1, p. 207], [172] extended to 3D)– since it is very computation efficient and accounts for uncertainties in the point positions.

4.) The Gaussian splat method 3D Gaussian splats are summed up at each point on the unit sphere to create a facet probability distribution, see Fig. 3.6. A Gaussian splat is a discrete sampled Gaussian probability distribution function $w \cdot \exp(\frac{|r-p|^2}{2\sigma^2})$ up to a limiting radius R [155, p. 355 ff]. The contribution of each splat is added to the previous result. A Gaussian distribution was chosen since it accounts appropriately for the uncertainty of the calculated orientation. This orientation uncertainty is represented by the standard deviation σ of the distribution function.

The angular uncertainty of the orientation $\Delta\alpha$ relates to σ (the parametric bandwidth): $\sigma = \sin(\Delta\alpha/180 \cdot \pi)$. I chose $\Delta\alpha$ and not σ as an input parameter to the filter since $\Delta\alpha$ is the more intuitive property which can be easier estimated for a given dataset.

Each splat is weighted by the corresponding relative triangle area w such that the maximum of the Gaussian function has the value of the relative weight. The relative weight w is the ratio of the triangle area to the total area of all triangles of the particle. Weighting ensures that facets consisting of only a few but big triangles leads to the same result as a subdivided version of this mesh.

The limiting radius R was chosen to be as big as 2σ. Approximately 95% of the overall probability of the Gaussian function is covered up to this distance.[12)].

[12)] 3σ would cover even 99% but the increase in accuracy comes with a high increase in computation time. Tests showed that a sampling radius of 2σ is sufficient for the analysed tomograms and results in a reasonable computation time: 2565 particles in a tomogram of size 1350x950x660 with

Figure 3.7:
Local minima regions

Explanatory images for a filter that marks the regions that belong to each distinct local minimum of a grey-level image. The left image shows an exemplary 2D input image. The right image visualizes the regions that belong to a distinct local minimum. All grey values that are lower than the value of the lowest adjacent saddle point are covered by the labelled regions.

5.) Inversion of the 3D probability distribution The resulting image of the splatter process (Fig. 3.6) resembles a 3D probability distribution. For the further evaluation of the regions of its local maxima it has to be inverted such that the maxima become minima. Then the regions of high probability density can be found by a specialized watershed segmentation.

6.) Identification of local minima The local minima have to be identified. Only those that have at least a depth of D are considered to discard insignificant minima. The constraint D corresponds to a minimum amount of similar oriented triangles that are necessary to form what is later regarded as a facet. This can be seen as a minimum relative size that a possible facet has to have to actually be regarded as a facet.

7.) Definition of the extent of local minima A vicinity to each local minimum has to be constructed. Triangle orientations lying within this vicinity will be regarded as part of the facet.
Constructing this vicinity is a delicate problem. One simple solution is to apply a watershed filter on the distribution image with pools originating from the identified local minima. This way each triangle is assigned to a facet. There will be no unfaceted areas because the pools and the dams grow until all space is flooded (left image in Fig. 3.8). However, in most cases a classification is needed that divides the particle into faceted and unfaceted regions.

One possibility to define distinct areas that do not extend over all space is to stop the pools from rising further at the point when a dam would be introduced. In 2D this corresponds to the problem of finding the extent of a local minimum up to the lowest surrounding saddle point. This is illustrated in Fig. 3.7. According to Richard Beare[13] this cannot be achieved by a combination of standard operations but only by a modified watershed algorithm or with the concept of component trees (see e.g. Ref. [100]).

Therefore, another approach was chosen to define a distinct area, i.e. label, around each minimum. The idea is to let the area reach up to the steepest gradient magnitude

an angle resolution of $\approx 1.13°$ (corresponding to a sample volume of 101x101x101 voxel) and an angle uncertainty of 10° (corresponding to a radius of ≈ 30 pixel) were analysed within a day

[13] ITK mailing list communications

2D slices from 3D watershed filter results. The label originate from local minima of the Gaussian splat image (Fig. 3.6). The left image shows the result of an unrestricted watershed filter introducing a wall (black), the right image the output of a restricted watershed filter (the wall is allowed to grow as well).

Figure 3.8: Unrestricted and restricted watershed filter

of the basin, i.e. grey scale valley containing the minimum.[14)] This can be achieved by using the result of the watershed filter described above and a second watershed transformation. An algorithm that introduces walls [18; 118] has to be used in the first run, left image of Fig. 3.8. This wall is then used as a marker from which an additional pool originates in the second watershed transformation. The second transformation is applied to the gradient image of the distribution. The resulting labels then only extend up to the steepest gradient and can be used as markers in a third watershed transformation applied to the second derivative of the distribution image. The result, right image of Fig. 3.8 and Fig. 3.9, are labelled areas that are bigger than those of the second watershed result (not shown). The regions/label now extend as far as the maximum curvature of the local distribution function that lies farther away from a local minimum than the steepest gradient. This idea is from Beare and Lehmann [18, 8.2 page 21].

The resulting labels identify the extent of the facets and the number of labels corresponds to the amount of facets the particle has considering:

- The angular uncertainty of the surface normal orientation,
- The minimum amount of triangles a facet has to have,
- The angular resolution of the probability distribution.

Facet analysis

Now that the facets are detected they can be analysed in respect to these properties:

- Size of each facet (relative and absolute),
- Orientation of each facet,
- Angle between any two facet normals of a label (interplanar angles),
- Angle weight depending on the sizes of the two corresponding facets.

8.) Construction of the facet labels The point of each surface normal vector on the unit sphere is sampled into an empty 3D image (all values 0) with the same dimensions

[14)] This allows the extents of a label to vary in size which is important to identify very flat facets (small extend) and rough facets (large extend). Just using a local sphere of a fixed radius as the extent, positioned at each local maximum in the probability distribution, leads to inappropriate facet detections and to a wrong analysis.

A pair of stereo images visualizing the detected maxima regions from the facet probability distribution shown in Fig. 3.6 by a restricted watershed filter (right image of Fig. 3.8). The slice shown in the left image of Fig. 3.8 is rendered at its actual position.

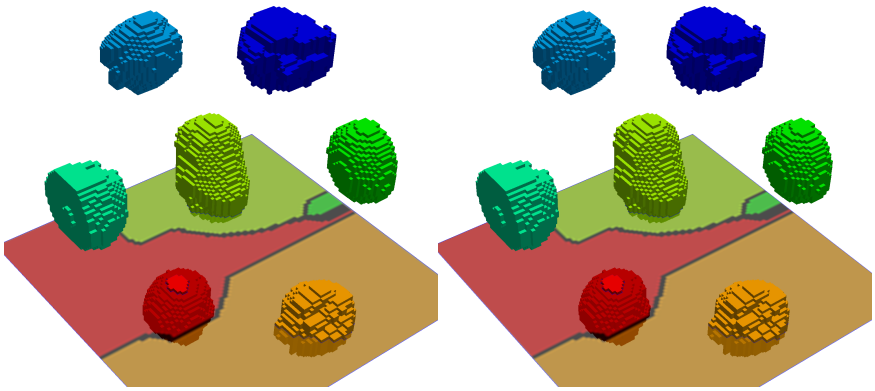

Figure 3.9: Detected facet regions from the facet probability distribution

A pair of stereo images showing the sampled triangle orientation points on the unit sphere within the labels of Fig. 3.9. The grey values, corresponding to the additive point weights w, are mapped to a hue colour map to visualize the dominant orientation within a facet.

Figure 3.10: Triangle orientation points sampled within the detected facet labels

as the probability distribution image. This is achieved by assigning the voxel closest to the point position a grey value relating to the relative area of the corresponding triangle. The grey value is the same as the weight w used in the Gaussian splatter process. Again, each point contribution is added to the previous result, see Fig. 3.10.

9.) Analysing the labels The result is passed to a label analyser [101]. The labels are the result of the facet detection described above. The analyser sums up all voxel values within a label. This yields the relative size of the facet. The analyser also computes the centroid which is regarded as the orientation of the corresponding facet. The centroid seems to be an appropriate estimate of the facet orientation since it ensures that larger areas of the face with the same orientation have a higher influence on the orientation than smaller areas with slightly different orientation.[15)] The centroid is a 3D point vector and in most cases does not lie on the unit sphere because it is an average of points on a curved surface, e.g. an even distribution of points on the whole unit sphere would lead to a zero vector since the centroid would lie at the origin. The more dispersed points the centroid averages the farther it will be away from the surface of the unit sphere. Therefore the inverse length of the centroid vector can be used as a measure of how dispersed the points of a label are and hence how distinct a facet is.

[15)] Other possible values for the facet orientation could be the unweighed centroid or the value of the maximum of the label.

10.) Calculation of the interplanar angles A list of all the angles between any two facet normals (facet angle) can now be computed. These angles are often called interplanar angles although the angles do *not* lie between two planes but between the *normals* of two planes. A weight can be assigned to each angle which characterizes the balance in size of the two corresponding facets. I chose the harmonic mean of the two relative facet sizes as weight because this is the smallest of the Pythagorean means for two different values. This seems to be an appropriate weight for an angle between the normals of a very big facet and a very small facet.

11.) Kernel density plot The list of angles can then be plotted as a frequency distribution of occurring interplanar angles either weighted or unweighted (see Fig. 3.12). A 1D kernel density plot ([79, sec. 13.2.2, p. 258] and [172]) accounts best for the angle uncertainty since it is the equivalence of the Gaussian splatter in 3D, i.e. the sum of overlapping 1D Gaussian functions. The variance of the Gaussian functions (also called the parametric bandwidth of the kernel) can be chosen to reflect the angle uncertainty of the facet analysis.

12.) Visualization The result of the analysis can be used to colour the triangles of the mesh according to the facet label they belong. If the analysis distinguished faceted and unfaceted regions (i.e. double or triple watershed instead of single watershed, see point **7.)**), I rendered unfaceted regions grey (see Fig. 3.11). A colouring according to the four-colour theorem[16)], which also holds for many none flat 2D surfaces [183], was not implemented. Instead, a colour lookup table (LUT) with 10 colours is used such that a colour repetition only appears on particles with more than 10 facets.

[16)] The four-colour theorem [9; 10] states that any map in a 2D plane can be coloured, using only four different colours, in such a way that regions sharing a common boundary (other than a single point) do not share the same colour.

3.4.2 Application examples of the facet analysis

In the following sections three exemplary applications of the described facet analysis (referred to as 'the facet analysis') are presented. First, the analysis results of the exemplary particle from Sec. 3.4.1 is given. This is followed by a demonstration of filtering particles according to the properties of their facets. Finally, the facet analysis is used to characterize dominant orientations of magnetic domain walls.

3.4.2.1 Determination of crystal geometry by interplanar angles

It is possible to conclude about the geometry of a crystal if the angles between its facet normals (interplanar angles) are known. Since the developed facet analysis gives access to these angles for all analysed labels, in this case single particles which are mostly distorted crystals, statistics about the angles can be collected. This can be plotted as a histogram from which predominant interplanar angles can be found. These angles can then be related to the crystal structure. Although not all interplanar angles might be exact, the strength of this method is to analyse thousands of particles which creates a statistic, within which these discrepancies are not significant.

Also a single particle facet analysis can be meaningful if the resolution of the tomographic data is high enough to reveal not only shape but also facets. Taking the spinel particle from Fig. 3.5 as an example: Its edges are only about 15 voxel long, but this is already sufficient to form unambiguous facets. The material (spinel, cubic structure, $MgAl_2O_4$) generally crystallizes as an octahedron formed by $\{1\,1\,1\}$ facets. However, the composition of particles may vary locally. This can lead to crystals of different shape. The imperfect example particle has seven distinguishable disconnected facets. On one side (left column in Fig. 3.11, $[0\,0\,1]$ pointing up) it resembles a square pyramid with an oriented intergrowth. One of the sides ($(0\,\overline{1}\,1)$ plane in the coordinate system shown in Fig. 3.11) is distorted and can not be regarded as a facet. The other side (left column in Fig. 3.11, $[0\,0\,1]$ pointing down) can be idealized as an extruded square pyramid or parallel intergrowth. Additionally, the particle has some unfaceted tail attached to the distorted side. This might be faceted as well but the resolution of the tomogram is not sufficient to resolve facets here.

The facet analysis on this particle yields the results which are visualized in Fig. 3.11 depending on the chosen filter parameter. These are described in the figure caption. The connectivity of detected facets is not checked, which means, that facets of similar orientation have the same label (e.g. green facet in rows 0-3). This is appropriate for most applications.

All seven facets are detected for an angular uncertainty $\Delta\alpha$ of up to 15° despite the imperfection of the crystal. From 15° onwards, the roundness of the edges (originating from the smoothing and the low resolution) causes detected facets to merge (Fig. 3.11, row 3). At $\Delta\alpha = 24°$ only the lower and upper part can still be distinguished, because the roughness of the facets and the round corners cause all other facets to merge at this high angular uncertainty.

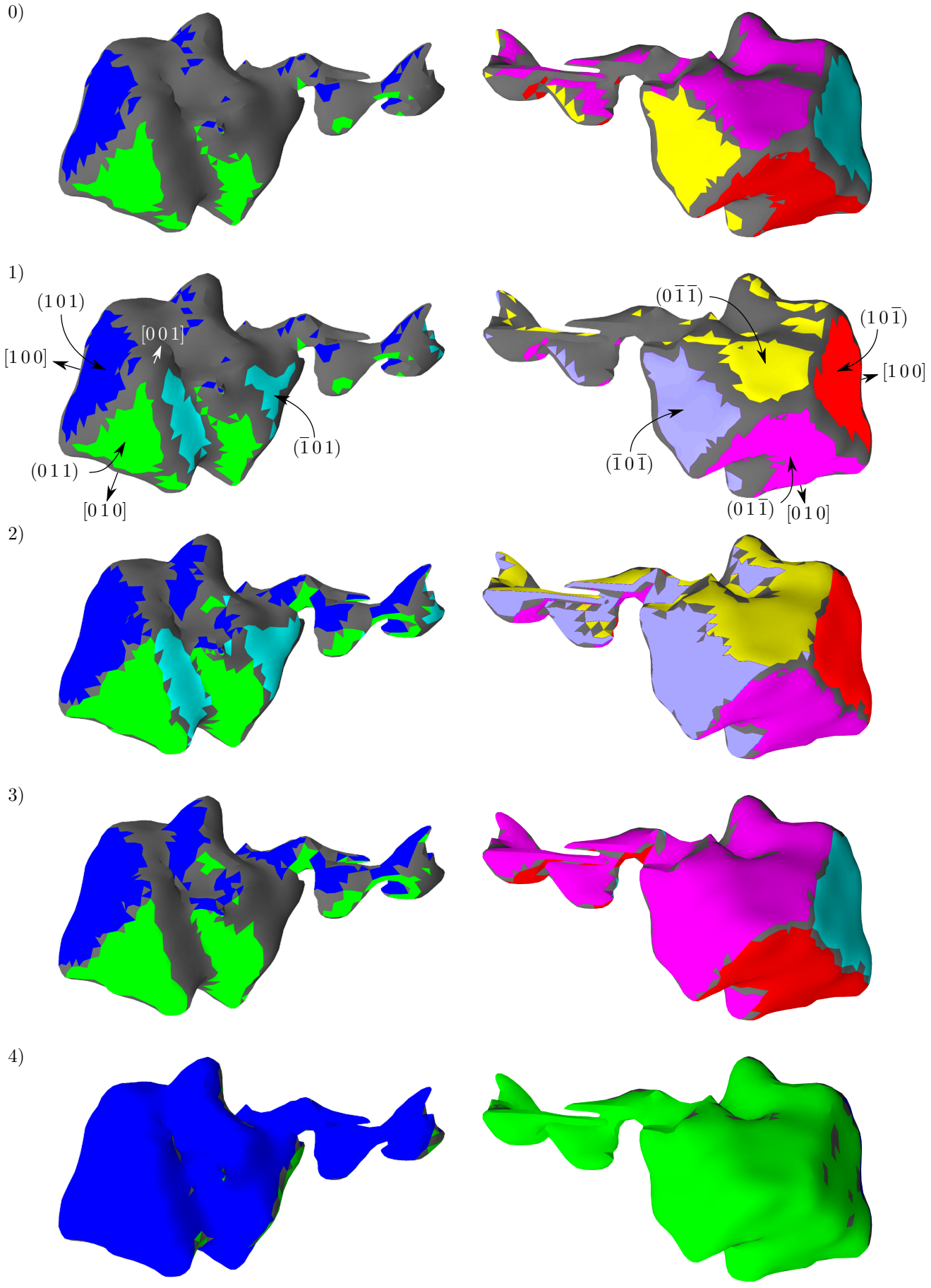

Figure caption on the opposite page

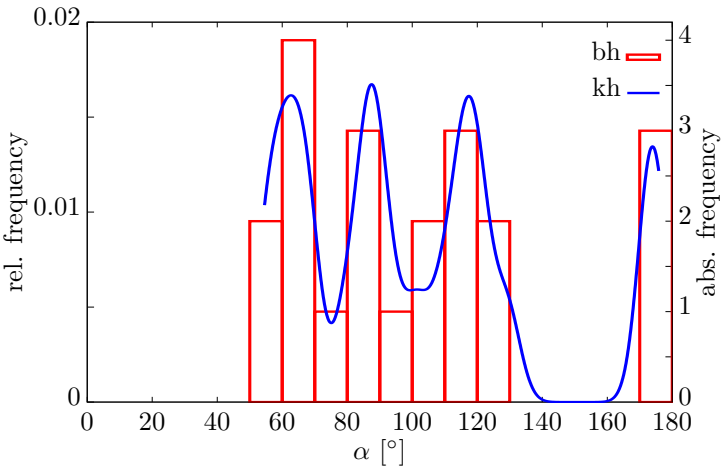

Figure 3.12: Interplanar angle frequency plot of a single label

The plot shows the frequency of the interplanar angles α (the angle between the normals of two facets) of the example particle from Fig. 3.5. The distinct peaks of the kernel density plot (kh) correspond well to the geometry of the particle. The bar histogram (bh) enables the estimation of the frequency ratios (see text).

The interplanar angle statistic (obtained by the facet analysis with an angular uncertainty of $\Delta\alpha = 10°$) is plotted as an angle histogram in Fig. 3.12. There are only 21 angles (corresponding to seven facets) in this single particle analysis so the bar histogram (bh) is very inexact. Nevertheless, the bar histogram allows the absolute number of angles found in each range to be relate to the relative frequency, which the kernel density histogram (kh) is related to. The kernel density plot is a more appropriate displaying method (as described in 3.4.1 **11.)**). The variance σ of the additive Gaussian functions can be adjusted to reflect the angular uncertainty used in the facet analysis (in the plot $\sigma = 4 \mathrel{\widehat{=}} \text{FWHM} \approx 10°$). The peaks of kh in Fig. 3.12 do not match the expected 18 angles (considering only seven facets) between all adjacent {1 1 1} facets (namely 70.5°). The three 180° angles for opposite faces are correct but of little information. Therefore, the presented crystal has not the geometry of an octahedron. Checking tables of cubic interplanar angles (e.g. [Tab. 3.8.5B 78, p. 120 f] yields {1 1 0} planes with 60°, 90°, 120°, 180°, which fit the data. With the absolute scale of the bar histogram it is now possible to estimate how often these angles occurred (moving the bar centre of bh to the peak of kh):

Figure 3.11: Facet analysis results for different angle uncertainties

Image pairs visualizing the effect of different angle uncertainties ($\Delta\alpha$) on the facet detection of the spinel particle from Fig. 3.5 (shown from two sides). The mesh triangles belonging to a facet are coloured according to their label. All mesh triangles not belonging to a facet are grey. Facets are not checked for disconnections which causes the crystal inset to have the same facet labels as the main crystal. The analysis was done with an angular resolution of about 1.13° (corresponding to a sample volume of 101x101x101 voxel) and a minimum facet size of 10 (except the first row 0). This means a facet is only detected if it has at least the area of about 10 pixel.

row 0 ($\Delta\alpha = 10°$): Only six facets are found if the minimum facet size is set to 50. The size of the smallest facet (row 1: cyan) is about 40.

row 1 ($\Delta\alpha = 10°$): Seven facets are found. The facets are not extending up to the particle edges. This is because of the roundness of the edges which was introduced by the smoothing.

row 2 ($\Delta\alpha = 14°$): The seven facets are now bigger in size because the higher angular uncertainty allows to incorporate more triangle orientations towards the particle edges.

row 3 ($\Delta\alpha = 15°$): Two facets cannot be differentiated any more (magenta) at this angular uncertainty and the smallest facet (row 1: cyan) is not detected any more (now grey).

row 4 ($\Delta\alpha = 24°$): The angular uncertainty is now so large that only the sharp edge of the jolted octahedron suffices to distinguish two sides.

interplanar angle α	α measured	# ideally	# measured
$\measuredangle\,(1\,0\,1)(0\,1\,1) = 60°$	62°	6	6
$\measuredangle\,(1\,0\,1)(\bar{1}\,0\,1) = \measuredangle\,(1\,0\,1)(1\,0\,\bar{1}) = 90°$	88°	6	4
$\measuredangle\,(1\,0\,1)(0\,\bar{1}\,\bar{1}) = \measuredangle\,(1\,0\,1)(0\,1\,\bar{1}) = 120°$	118°	6	5
$\measuredangle\,(1\,0\,1)(\bar{1}\,0\,\bar{1}) = 180°$	174°	3	3

Table 3.1: Interplanar angles for a single spinel particle (measured values are approx.)

The values of Tab. 3.1 match well considering the low resolution of the particle. This means that the crystal evaluated here is not made up of $\{1\,1\,1\}$ facets but of $\{1\,1\,0\}$ facets. It can be constructed from a rhombic dodecahedron (containing all $\{1\,1\,0\}$ faces, reported to appear naturally, see e.g. [3]) by removal of the $(1\,1\,0)$, $(\bar{1}\,1\,0)$, $(1\,\bar{1}\,0)$ and $(\bar{1}\,\bar{1}\,0)$ faces followed by a shrinkage of the remaining faces until the surface is closed again. This evaluation demonstrates how reliably the presented facet analysis is and what a powerful tool it is to characterize any tomographic dataset containing faceted labels.

It is possible that the seemingly round edges might not be smoothing artefact but could instead originate from very thin faces, see Fig. 3.13. These would be $\{1\,0\,0\}$ and $\{1\,1\,2\}$ faces, which are also reported to appear naturally [3] and would replace the edges of $\{1\,1\,0\}$. Their size would have to be below the resolution limit because they are not obvious in the mesh representation of the particle.

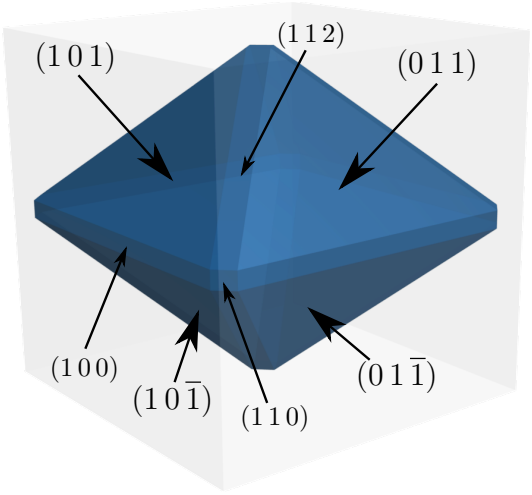

Figure 3.13: Bipyramid of $\{1\,1\,0\}$ faces
Perfect construct of a $\{1\,1\,0\}$-bipyramid within the $\{1\,0\,0\}$ cube showing the idealized shape of the particle from Fig. 3.11 with possible facets replacing the $\{1\,1\,0\}$-edges.

A minimum resolution for facet detection in regard to voxel can be estimated by the following method: A facet has to have at least an area of about 10 pixel for it to be reliably detected.[17] For comparison, the facets of a 3x3x3 voxel cube have only an area of about 1 pixel when meshed with the marching cubes algorithm and smoothed with a windowed sinc-filter. A 5x5x5 voxel cube is just about big enough such that its facets are resolved if it is aligned with the coordinate system. If that is not the case it needs to be slightly bigger (about 6x6x6) because the faces will only become flat through the smoothing filter.

3.4.2.2 Filtering objects according to facet characteristics

The facet analysis filter characterizes every single label. Its results can be used to filter out labels which do not fulfil a set criterion on any of the characteristics the facet analysis yields. That is:

[17] This suggests a value ≥ 10 for the minimum facet size parameter of the analysis filter.

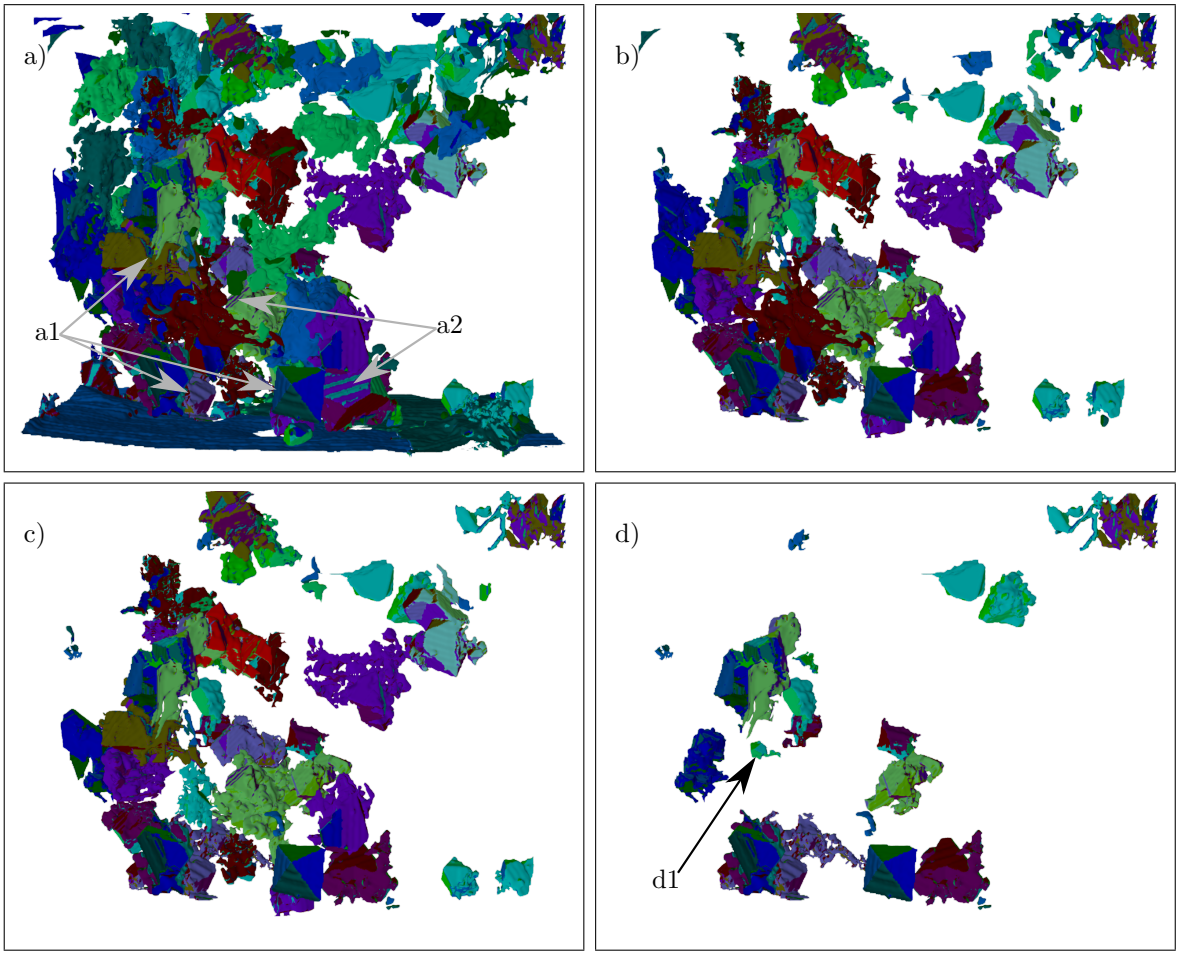

Figure 3.14: Labelled objects filtered according to their facet characteristics
Figure showing the effects of filtering the spinel particles according to different facet characteristics.
a: The result of the facet analysis of the separated and labeled particles. The facets are coloured differently (not the separated particles).
b: Only labels with at least three facets per label.
c: Only labels with at least one facet bigger than 10% of the label surface and no facet above 40%.
d: Labels were removed which might have a facet originating from the FIB-slicing, i.e. labels that have a facet whose z-component of the facet normal vector is larger in magnitude than 0.8. Since this criterion was not additionally bound to the facet size it caused quite a few more labels to be removed.

- Number of facets of each label,
- Size of each facet (relative and absolute),
- Orientation of each facet,
- Angle between any two facets of a label,
- Angle weight depending on the sizes of the two corresponding facets.

These can be used to check, e.g., if either faceted or unfaceted particles favour a special position in the walls of metal foams, thereby either type might be more suitable to stabilize foam walls during the foaming. This property filtering is demonstrated on the spinel particles from the FIB dataset, see surface render in Fig. 3.14. The usual shape of spinel crystals is octahedral. In this dataset the crystals often exhibit intergrowth or distortions as the example particle in Fig. 3.11 (which is from this dataset, see arrow

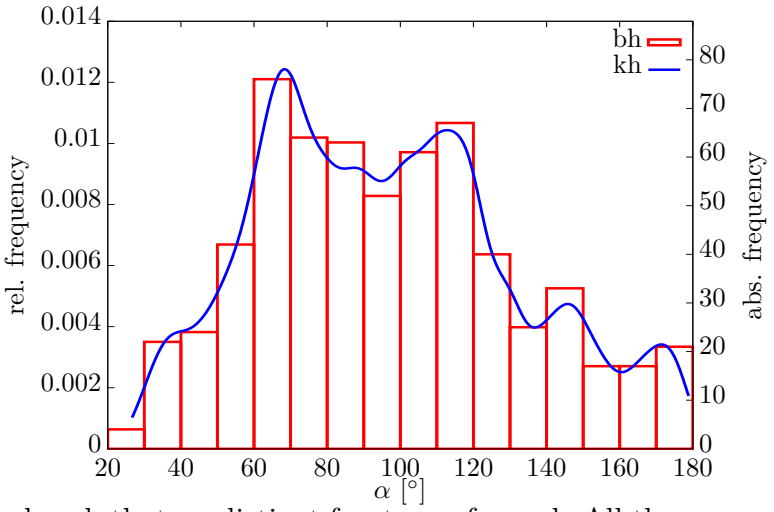

Figure 3.15: Interplanar angle frequency plot of multiple labels

The plot shows the frequency of the interplanar angles of multiple labels, in this case the crystal particles from Fig. 3.14. The distinct peaks of the kernel density plot (kh) correspond well to the most likely geometry for spinel: An octahedron formed by {1 1 1}. The bar histogram (bh) enables the estimation of the frequency ratios (see text).

d1). They can even be fully distorted such that no distinct facets are formed. All these types are visible in Fig. 3.14a. The particles were separated before the facet analysis. The facets are coloured arbitrarily, as described in 3.4.1 **12.)**. The rippled surface of some facets is caused by alignment artefacts (see arrows a1). The facet orientation uncertainty $\Delta\alpha$ was chosen such that most facets are still detected despite this uneven facet surface. In some cases, when the ripples are too pronounced, the actual facets are broken up (see arrows a2). In Fig. 3.14b-d, labels were removed by the use of successive filter criteria to demonstrate filtering based on facet analysis results. The filter parameters were not optimized since this was done only for testing.

Fig. 3.15 shows the angle frequency plot for all particles from Fig. 3.14d which do not have an obvious facet created by the FIB-slicing (21 particles, 628 angles). It shows two dominant peaks at about 70° and 110°. These angles can be assigned to those of actual octahedra formed by {1 1 1} (see [tab. 3.8.5B 78, p. 120 f]). As in Sec. 3.4.2.1 the absolute scale of the bar histogram allows for an estimation of the frequencies of these angles, Tab. 3.2.

interplanar angle α	α measured	# per oct.	tot. # measured
$\measuredangle\,(1\,1\,1)(1\,1\,\bar{1}) \approx 70°$	69°	12	140
$\measuredangle\,(1\,1\,1)(1\,\bar{1}\,\bar{1}) \approx 110°$	112°	12	130
$\measuredangle\,(1\,1\,1)(\bar{1}\,\bar{1}\,\bar{1}) = 180°$	172°	4	40

Table 3.2: Interplanar angles for multiple spinel particles (measured values are approx.)

The error of the angle between adjacent facets (i.e. facets sharing an edge, e.g. (1 1 1) and (1 1 $\bar{1}$)) adds up to the angle error between facets that only share a point (e.g. (1 1 1) and (1 $\bar{1}$ $\bar{1}$)). Therefore the error of opposite facets (e.g. (1 1 1) and ($\bar{1}$ $\bar{1}$ $\bar{1}$)) is the largest. Under these considerations the expected ratio of 12:12:4 fits roughly to the measured ratio of 140:130:40. It can be concluded that about 10 to 12 crystals in the dataset form facets corresponding to those of an actual octahedron. However, as shown in 3.4.2.1 there are exceptions. The third most common facets reported by Alijev and Jevsikova [3] are {3 1 1} which can form an angle of about 145° corresponding to e.g. (3 1 1) and ($\bar{3}$ $\bar{1}$ 1): $\measuredangle\,(3\,1\,1)(\bar{3}\,\bar{1}\,1) \approx 145°$, another peak in Fig. 3.15. The huge amount of possible combinations of different facet orientations yield a nearly continuous

spectrum of interplanar angles which creates a background in the angle frequency plot for multiple labels.

When these tests were done the facet analysis was not yet considering unfaceted regions (as it is the case in Fig. 3.11, grey areas). This causes the unfaceted parts of the labels to contribute as well. Depending on the amount of unfaceted area, this has a significant influence on the result of the filtering. Despite the filtering to extract sufficient faceted particles, as shown here, it would also be possible to identify and filter those particles that have an angle distribution as e.g. in Fig. 3.12. This would allow automated creation of the statistics for common crystal geometries of spinel, e.g. $\{1\,1\,1\}$, $\{1\,1\,0\}$ and $\{3\,1\,1\}$ as in Ref. 3.

3.4.2.3 Global orientations of magnetic domain walls

Another application for the facet analysis comes from neutron tomography. Talbot-Lau neutron tomography images magnetic domain walls within a piece of magnetic material in 3D [108]. The upper images of Fig. 3.16 show two slices of such a tomographic dataset (pixel size 30 µm) of a FeSi wedge (Si 12.8%, 7 mm ∅, 12 mm length) cut off (along ξ) from a cylinder with a small flat side (ζ). The idea is to use the facet analysis filter to evaluate the magnetic domain wall directions and size since it is expected that there is a global orientation of the domain walls with an additional size dependence.

First, the domain walls need to be extracted as a binary image. There have been various attempts at this in the group but with little success. One promising filter was created by Fabian Pucks based on partial derivatives to detect the domain walls (Bachelorarbeit). Still, all the results lack the property of creating closed domain wall representations as they are expected to be.

My approach was not to extract the domain walls but the domains themselves. A watershed segmentation is predestined for this and even creates labelled domains. Using labelled domains also circumvents the problems arising from meshing an arbitrarily oriented object that is only one voxel thick, as the domain wall representation would be.

The 'flooding' stage of the watershed segmentation is done directly on the grey value profile of the median filtered dataset, Fig. 3.16. The well of each pool is a labelled local minimum of the grey value profile. I used the watershed algorithms of MAVI[25] sec. 5.5, p. 45 and ITK[2] [76; 18; 118] that introduce watershed walls of 26-connectivity (see 4.3), since these will be needed later. They both create watershed walls where domain walls are, but not for all domain walls. The two algorithms differ in that the MAVI watershed algorithm discards regions below a minimum number of voxel (here 10000) whereas the ITK algorithm discards pools (which are one dimension higher than the marked region) below a certain depth (here 80 grey levels) before watersheds are introduced. I combined the results of both algorithms since the introduced watersheds by any of the two seemed justified concerning visual impression. This can be done by a logical AND-operation and a successive relabelling but only if both algorithms created walls. Each domain is now definitely separated from the other by a fully closed watershed

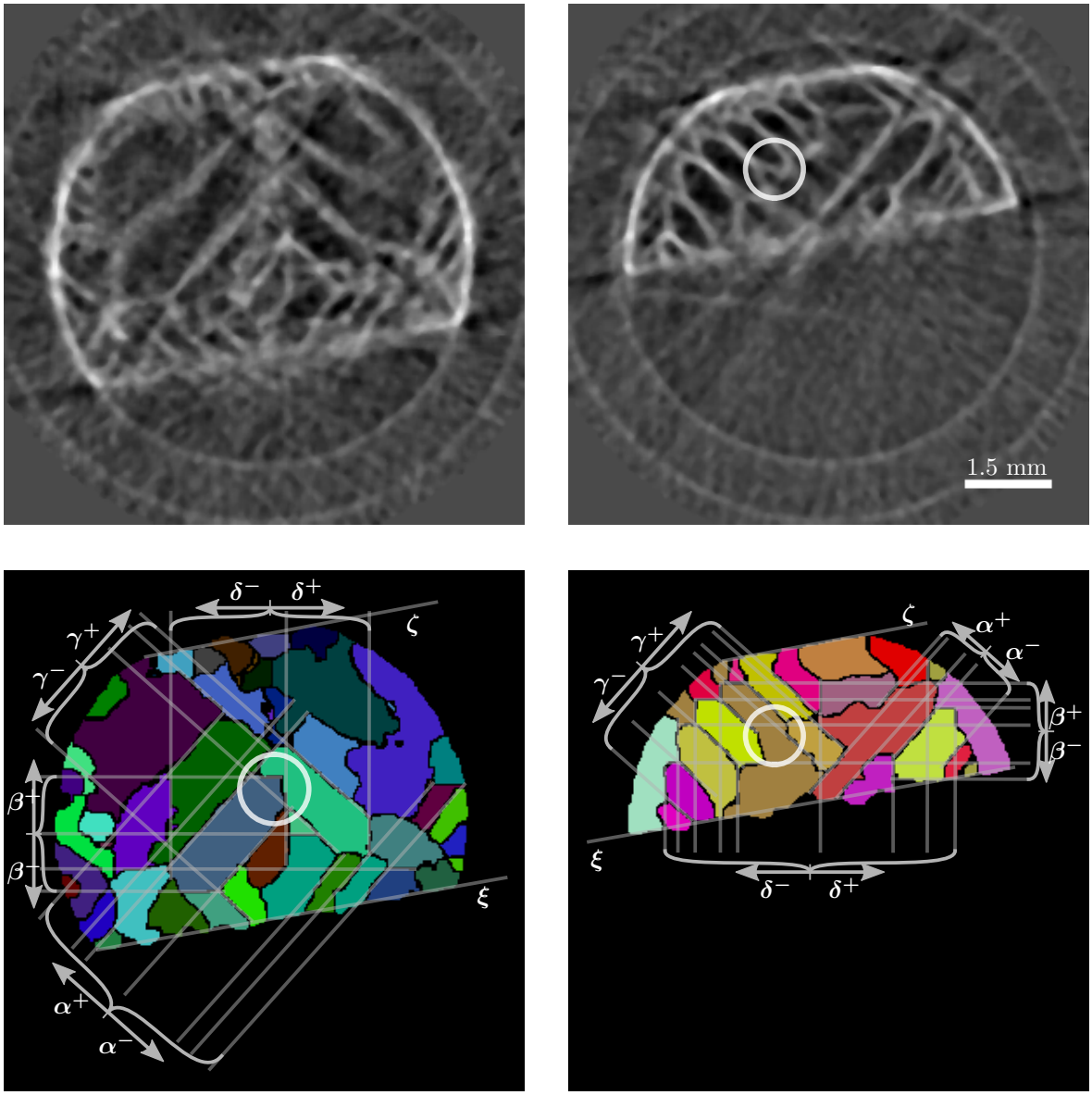

Figure 3.16: Magnetic domains labelled and masked

In the upper row are two slices through 3D-imaged domain walls. The tomogram was obtained by Talbot-Lau neutron tomography of a FeSi wedge. The dataset was already processed by a 3D-median filter with a kernel size of 5x5x5.

The two lower slices show the result after watershed segmentation and removal of everything outside the wedge. Each domain is labelled and visualized by an arbitrary colour. A 3D visualization of the wedge and its labelled domains is shown in Fig. A.13. The annotation lines point out some distinct domain wall orientations. Each set of parallel walls has two names because the domain wall normals of each domain point outward (i.e. x^+ and for opposite normal direction x^-). The names in Fig. 3.18 refer to these here. The two distinct surfaces of the wedge itself, that are not curved, correspond to ξ and ζ. They are uneven because domains smaller than 64 voxel were removed. ζ and β are not parallel.

Note, that the watershed segmentation was done in 3D but the slices only show a 2D cross section that on its own (i.e. 2D) would be segmented differently! It is the connection to the neighbouring slices that cause the result visible differ from what one might expect. For example the brown-segment is not split where a wall seems to be in the upper image (see marking circles in the right images; main text).

wall. These watershed walls are positioned where it is most likely that a domain wall was imaged in the tomogram. However, there is not necessarily a watershed wall were a domain wall appears to be. This happens if the domain wall is not fully closed in the tomogram, i.e. has a 'hole'[18]. This is the reason why there is no wall separating the brown watershed segment where there appears to be a wall in the tomogram slice (see marking circles in Fig. 3.16). It would need a specialized algorithm able to identify holes in 3D walls.[19] However, the obtained result is already sufficient for the creation of a statistical analysis of the global domain wall orientations and therefore no further refinement of the wall detection was undertaken. Two more processing steps have to be done to yield the result that can then be analysed (shown in the lower slices of Fig. 3.16). A mask of the wedge has to be created to eliminate all labels (introduced by the watershed segmentation) that are outside the wedge. Also, all domains containing less than 64 voxels need to be removed since they are likely processing artefacts and should not contribute to the analysis. If some of them were not actually artefacts their contribution to the analysis would be insignificant anyway.[20]

Finally, the facet analysis can be run on the labelled domains. An angular uncertainty $\Delta\alpha = 10°$ is a reasonable choice since the expected angles from the slices are above 20° (except the angles between β^+ and ζ, and possibly between β^- and ξ). Again, the angular resolution was set to $\approx 1.13°$ (corresponding to a sample volume of 101x101x101 voxel) and a minimum facet size of 10 pixel (corresponding to a value of about 900 μm^2). The detected facets were again coloured arbitrarily[21] for the visualisation of the filter result, see Fig. 3.17. The analysis allowed unfaceted regions which are coloured grey. It can be seen that even the domain walls making up the outer surface were all detected as facets since none of them covers an arc of more than 20°. The orientations of these outer facets will contribute as background to the global facet orientation.

The global orientations of the walls of all domains can be evaluated in a very similar way as the wall orientations of each single domain, simply by replacing the triangle orientations by the wall orientations. This is comparable to an analysis of all domains which regards them as a single label. Although this could have been done directly it would not have introduced a filtering of the domains in between the two orientation analyses, i.e. removal of the facets that make up the outer surface of the wedge. However, this possibility was not needed so far. An advantage of the second analysis is the possibility of skipping the third watershed step (as described in Sec. 3.4.1 **7.)**) to

[18] A not fully closed wall is defined here by two local minima on either side of the wall but that are not separated by higher grey values along *any* possible 3D-path between the two minima.

[19] An idea of mine for such a specialized algorithm is to impose the already found watershed walls on the original tomogram, followed by a (local) thresholding, resulting in watershed walls extended by the domain wall fragments that have holes. The result can then be handled in the same way as described in 3.2.

[20] The tomographic dataset was analysed a second time after it was rotated by 17° around the z-axis to rule out any influence possibly caused by remnants of the marching cubes triangle orientations. However the results showed no noticeable difference

[21] It would be possible to colour-code the facets according to the colours later assigned to the global orientations as in the upper images of Fig. 3.18. This was not done since another program would have to be written for this recolouring task.

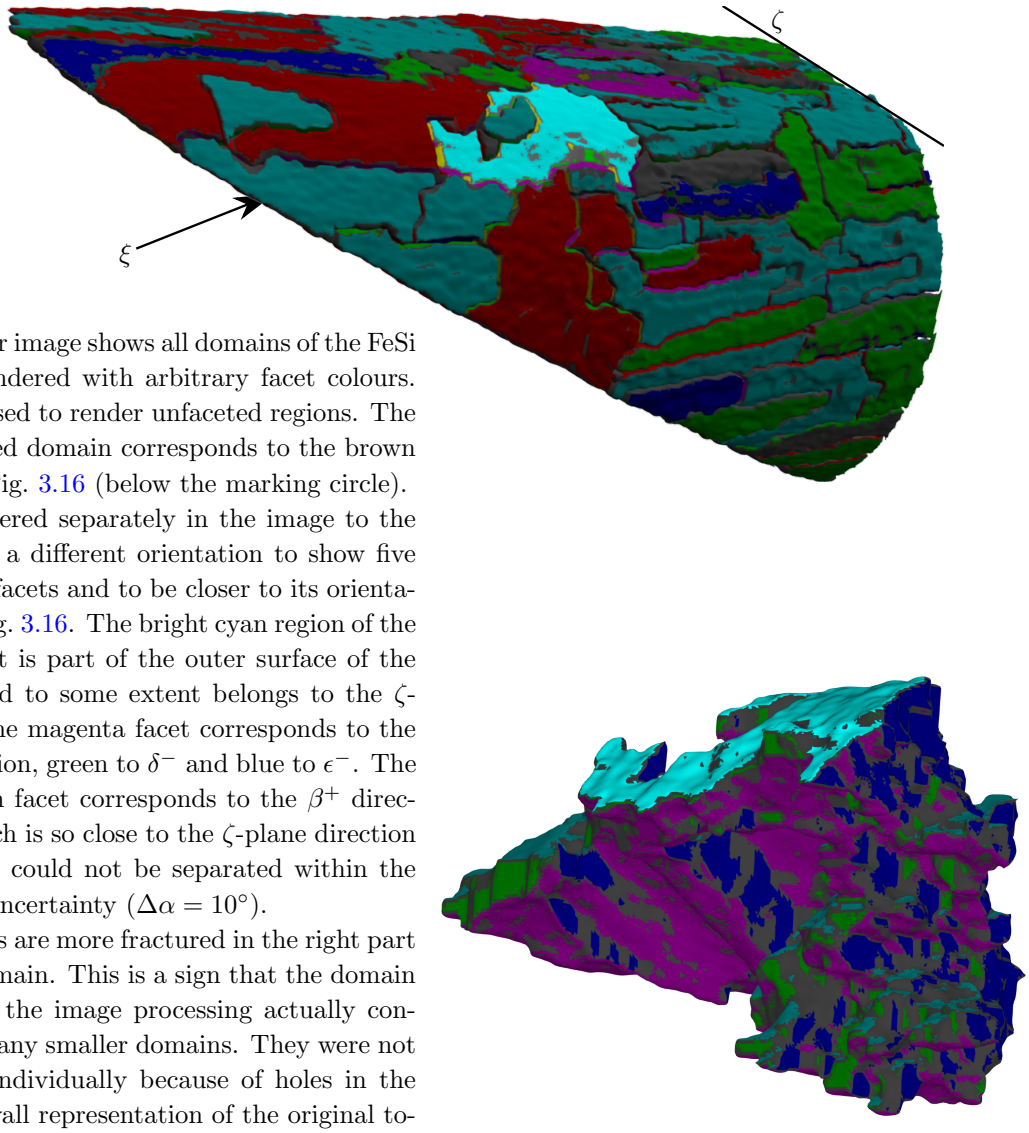

The upper image shows all domains of the FeSi wedge rendered with arbitrary facet colours. Grey is used to render unfaceted regions. The highlighted domain corresponds to the brown label in Fig. 3.16 (below the marking circle). It is rendered separately in the image to the side with a different orientation to show five different facets and to be closer to its orientation of Fig. 3.16. The bright cyan region of the cyan facet is part of the outer surface of the wedge and to some extent belongs to the ζ-plane. The magenta facet corresponds to the γ^- direction, green to δ^- and blue to ϵ^-. The dark cyan facet corresponds to the β^+ direction, which is so close to the ζ-plane direction that they could not be separated within the angular uncertainty ($\Delta\alpha = 10°$).
The facets are more fractured in the right part of the domain. This is a sign that the domain found by the image processing actually consists of many smaller domains. They were not labelled individually because of holes in the domain wall representation of the original tomogram.

Figure 3.17: Visualization of the detected magnetic domain walls

yield less broad labels. This allows for a more precise[22)] analysis of the facet orientations at the cost of less accuracy in the size measurement of each facet.

The resulting orientation probability density distribution (as described in 3.4.1 **4.)**) restricted to the unit sphere is shown in Fig. 3.18. The regions that were detected by the facet analysis as actual facets are coloured individually and labelled according to the naming convention from Fig. 3.16. Some local maxima were not detected because they are not sufficiently pronounced regarding the chosen filter parameters (e.g. β^- and ξ, they would be more distinct if a lower angular uncertainty was chosen).[23)]

The equirectangular projection of the unit sphere (Fig. 3.18) shows the centres found

[22)] The accuracy can still be increased by the use of the newly available 'Higher Order Accurate Derivative and Gradient Calculation in ITK' [117].

[23)] The filter parameters could be adjusted (to separate e.g. δ^- from its extension to the right) and labels could be removed according to their actual facet size before the second analysis is done, this however seems not necessary for the further evaluation.

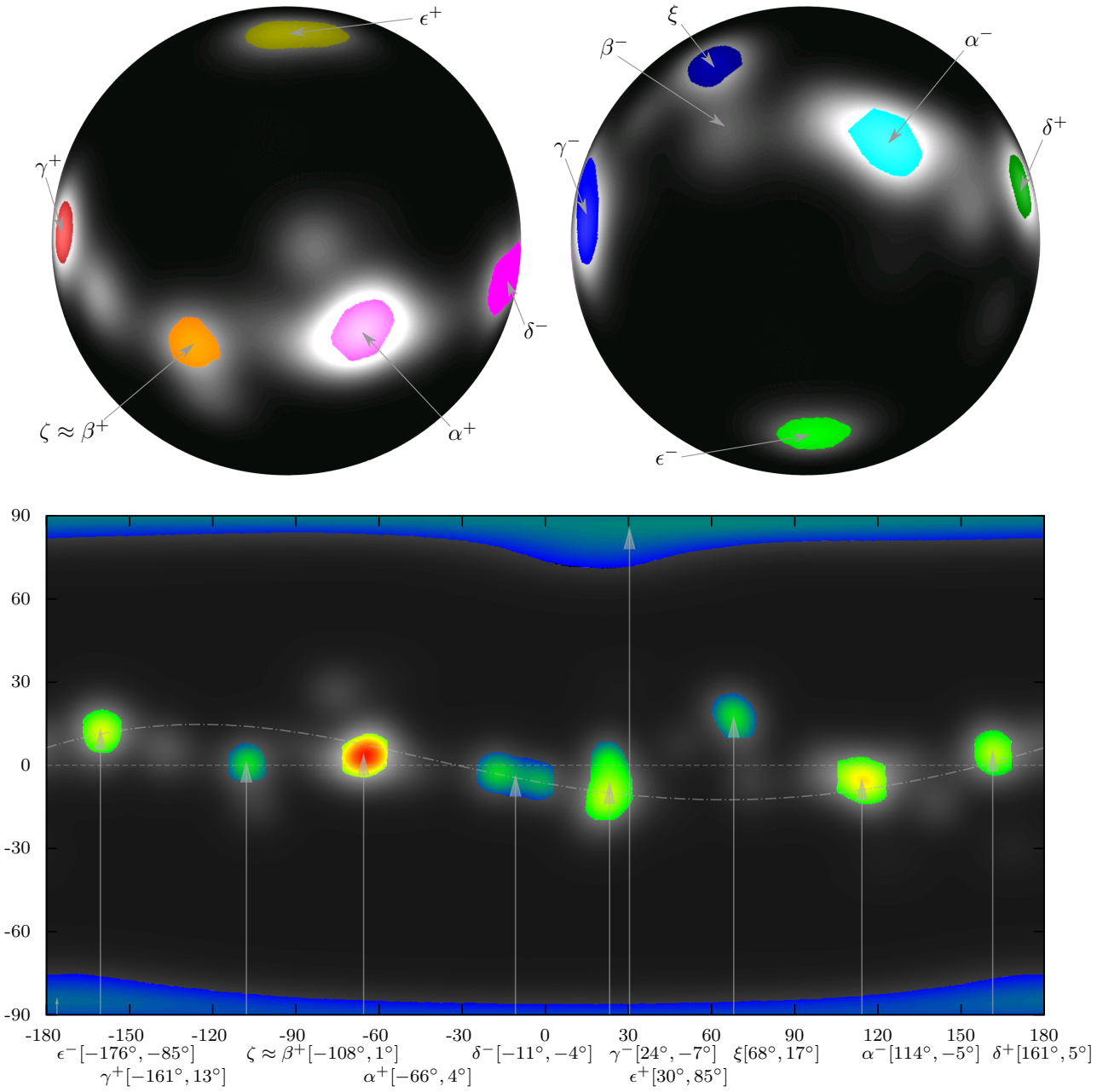

Figure 3.18: Global orientations of magnetic domains of a FeSi wedge

The upper images show the global orientation probability distribution on the unit sphere from opposite directions. The higher the probability the brighter the voxel. The regions that were detected by the facet analysis as actual facets are coloured individually and labelled according to the naming convention from Fig. 3.16. This spherical image (sample volume of 501x501x501 voxel) could be used to colour-code the facets in Fig. 3.17.

The lower image shows an equirectangular projection of the unit sphere. Here, the probability distribution within the labelled regions is globally coloured to emphasize the individual thresholds of each label and their different intensities. It can be seen that the domain wall orientations follow a slight sine trace. This shows that the domain wall orientations are not exactly perpendicular to the global z-axis of the tomogram.

by the analysis and visualizes their heights. The global colouring enables a comparison of the different centres. For example, the intensity of α^-, which relates to the facet size, is lower than that of α^+, which is obviously the most dominant domain wall direction. In accordance with the impression of the wall sizes from Fig. 3.16 the wall directions β and δ are less dominant than α and γ. β^+ and ζ are not distinguishable at this high angular uncertainty. It is likely that β^+ contributes most to this direction since the total size of ζ is very small as it is restricted to a small fraction of the outside surface (see Fig. 3.17). In contrast, the size of ξ, regarded as the facet originating from a cut that made a wedge out of a cylinder, is obviously bigger than ζ. The unique orientation makes ξ easily distinguishable from the other facet orientations and thereby provides a reference point.

The equirectangular projection also shows that the domains are nearly oriented in their length along the z-direction of the tomogram because the ϵ facets are close to the poles and the other facets near the equator. However a slight misalignment causes these facets to follow a sine trace, except β^+ which is influenced by ζ. The sine trace drawn into the projection correlates with the displacement of the ϵ facets from the poles and also with ξ. This possibly means that the asymmetry introduced by the cutting of the cylinder causes the domains to align not exactly along the cylinder axis but with a tendency in the direction of the surface normal of the cut, namely ξ.

facet	rel size [%]	abs. size [mm^2]
ϵ^-	3	7.2
γ^+	6	14.7
$\zeta \vert \beta^+$	4	8.4
α^+	10	22.8
δ^-	7	15.2
γ^-	10	23.1
ϵ^+	5	10.4
ξ	5	11.2
α^-	9	20.1
δ^+	6	14.5
Σ	65	147.6

Table 3.3: Relative and absolute domain wall sizes

The final facet analysis yields 65% of the total surface area of the examined facets were assigned to distinct domain walls, i.e. 35% of the total surface area is unfaceted (rendered grey in Fig. 3.17). Tab. 3.3 lists the relative and absolute domain wall sizes obtained from the analysis. It shows, for example, that the domain wall direction α^+ is of similar size as the opposite direction α^-. This corresponds well to the expectation Fig. 3.16 induces. However, γ^- is nearly two times larger than γ^+. This unbalance between opposite domain wall directions can be explained by constructs like the domain marked by a circle[24)] in the bottom left image of Fig. 3.16, where γ^- is reduced compared to γ^+ by the protruding corner of another domain. Another reason for unbalance can also be the extent of unfaceted regions.

[24)] This particular example would suggest $\gamma^- < \gamma^+$, but that is just the impression from a slice which can be different from the actual 3D property.

Chapter 4

Procedures: From the sample to the tomogram

In this chapter, I describe the sample production, the preparations necessary to obtain a sample suitable for TEM tomography and concepts of the acquisition of tilt series. This comprises a few measurements/estimations of device-specific conditions and a quantification of the performance of automatic focus and position tracking (xy-z-tracking). This information can be used to improve the automatic acquisition of tilt series and thereby the quality of the resulting tomograms. General acquisition parameters used for the acquisition of tilt series are given as well. Finally, important digital processing steps of the tilt series on the way to tomogram analysis are outlined, ranging from the use of the software IMOD[1] over different reconstruction algorithms/programs to tomogram filtering and analysis with ITK[2] and VTK[3].

4.1 Sample preparation

The investigated carbon black supported ruthenium nanoparticles were designed and created by colleagues at HZB, for detailed description see Ref. [191; 45; 192; 65; 130; 94; 186; 190]. Commercially available carbon black was used as starting material. $RuCl_3 \cdot xH_2O$ (Sigma-Aldrich®, metal content 35 wt%) was used as Ru precursor for catalyst preparation. All solvents were dried over molecular sieves before precursor solutions of appropriate Ru concentration were prepared. $RuCl_3$ was dissolved in water that had been purged with argon before. The precursor solutions were placed in a round-bottom flask at the end of a quartz tube which was inserted into a split hinge tube furnace. The resultant suspensions were agitated by ultrasound, after which the solvent was removed by rotary evaporation and the dried catalyst powder was heated under hydrogen at a temperature of 200°C. The resultant material was rinsed with water to remove all chlorine-containing residues. Finally, it was dried in a desiccator yielding a cloddish powder.

For the preparation of samples suitable for electron tomography, I dispersed the powder in butanol[1)] by ultrasound. The dispersion was then dropped onto a copper grid with a thin carbon foil containing fiducial gold markers (see e.g. Fig. 5.11).

Finally, the samples were heated in a furnace (90 min at 145°C) to remove any possible remnants (e.g. water or butanol) of the preparation procedure. The time and temperature was obtained from thermogravimetry.[2)]

I prepared the carbon foil by evaporation of carbon onto mica sheets, lifting it off in water and then settling it directly on the copper grids. The parameters for the preparation with devices at the HZB were optimized in the frame of a student project, see Ref. [174] for details.

Fiducial markers are needed for the fine alignment of the tilt series images. A suitable number are about 40 markers per image. The ruthenium nanoparticles could not be used as markers because they were to small or to densely packed. Therefore, gold particles were applied to the carbon foil. These must not agglomerate and should have a diameter of about 10 to 20 pixels in the image of the untilted sample. So the required number density and size of the gold particles depends on the desired magnification in the acquisition of the tilt series.

The gold particles were applied by sputtering (5 s to 10 s) to one or both sides of the carbon foil. Size and coverage of the gold particles were examined in each batch (TEM) because these properties cannot be controlled directly by the sputter parameters (see [174; 4]). In another project, replacements with higher transparency were sought to reduce the streak artefacts introduced by Au markers, see Ref. [4] for details. However, these did not form markers suitable for tomography.

4.2 Data acquisition

TEM tomography experiments were performed with a Zeiss LIBRA 200FE® transmission electron microscope (TEM) at the Helmholtz Centre Berlin for Materials and Energy (HZB) [193; 195]. With the available sample holder for tomography [46] the sample could be tilted at maximum from 75° to −75°. The actual limits depend on the displacement of the holder from the centre position in the goniometer and also on the extension of the shadows from the holder and grid bars of the sample. BF, ZL and STEM images were taken at 200 keV.

A tilt series is the base for the reconstruction of a tomogram [55; 52; 29; 146]. Therefore, it is important to acquire each image of the tilt series as well as possible. This means that the focus should be optimized and image distortion and noise minimized. A few important aspects of TEM concerning the image acquisition of predominantly

[1)] Before butanol, water was used as a dispersant to lower the contamination rate in the TEM since it does not introduce any hydrocarbons. However, the water lead to tightly agglomerated catalyst particles on the foil not suitable for tomography.

[2)] Measurements were performed with the help of G. Zehl (HZB).

amorphous samples are outlined below. These can be found in much more detail in the TEM literature, e.g. [146; 185; 2; 52; 145; 40].

The object needs to be appropriately focused. In transmission electron microscopy, the object is most often not in the Gaussian focal plane but in underfocus. The defocus Δf from the Gaussian focal plane is chosen depending on the sample type and which contrast type should dominate the image (e.g. phase or scattering contrast (i.e. thickness contrast)). In underfocus the defocus value is negative. The Scherzer defocus Δf_S ($\Delta f_S \approx -55$ nm, for a spherical-aberration coefficient $C_s = 1.2$ mm and a wavelength $\lambda \approx 2.5$ pm at 200 kV acceleration voltage) yields maximum positive phase contrast. For magnifications up to about 100 kX and mass thickness as contrast mechanism negative defocus values of a few microns are used (e.g. [90]).

Typical TEM image distortions are either optical (e.g. axial astigmatism, none-axial astigmatism (caused by a beam tilted relative to the optical axis of the lens), image rotation, magnification change) or mechanical (e.g. specimen drift, either caused by holder vibrations or by changes in sample charging, or by beam damage). Effects like Bragg reflections and channelling dislocations can be regarded as 'sample region dependent image distortions', as they also depend on optical settings (e.g. defocus and apertures). The specimen drift can also be sample region dependent.

The signal to noise ratio (SNR) is another aspect of image quality. It depends on the illumination intensity, the acquisition time and the intensity loss caused by the optical set-up (e.g. apertures). The optimization of the SNR is often restricted by the sensitivity of the sample to beam damage and relates to the electron dose. This is also the case for most samples of this work.

For the acquisition of a tilt series, the acquisition time of each image is chosen such that the sample does not change significantly by the overall dose of the whole tilt series acquisition. The TEM is adjusted to minimize image distortions before the start of the acquisition. Generally, I did these adjustments on a sample region not meant for tomography to keep the sample damage of the region for tomography (region of interest, ROI) at a minimum. However, 'sample region dependent image distortions' have to be corrected on the actual ROI and as quickly as possible to minimize the dose.

Since generally the studied samples suffered quickly from beam damage, only automatic acquisition enabled me to record tilt series at sufficient image quality within the range of total dose the samples would stand. A manual acquisition of each tilt series image (as it is still practised) increases the total dose on the sample because manual detail tracking (xy-tracking) and focussing (z-tracking) is only possible with a continuous irradiation until all adjustments are made. This needs about 10 s to 20 s per image whereas automatic tracking needs less than 1 s and less illumination intensity (see also e.g. [198]). Therefore, I had to use automatic acquisition on the used TEM. However, this comes with the need for further adjustments and additional limitations as will be discussed in the following text.

Cooling with liquid nitrogen improves the pressure reported for the sample chamber but the rate of sample contamination was unaffected by cooling. Also the use of

the additional ion-getter-pump (IGP) did not lead to a noticeable reduction of the contamination rate.

Automated acquisition of tilt series

Additional adjustments needed for the automated acquisition (e.g. eucentric hight, illumination- and image-shift) have to be adjusted on the actual ROI since they depend on the specimen drive for the used TEM (i.e. mechanical sample position set by the goniometer). Other adjustments such as the digital image pre-filters for the digital tracking procedures depend on the spacial frequencies of the actual ROI. It should be noted that I generally mean the eucentric height defined by the position of the rotation axis. There is another eucentric height defined by the focal distance at standard excitation of the objective lens to which the optic system is calibrated. The difference between these two eucentric heights is around a few micrometers for the used TEM. This discrepancy causes standard calibrations of the optical system to be inappropriate for acquisition of tilt series.

During acquisition, the defocus (z-tracking) and the sample position (xy-tracking) have to be adjusted for every tilt increment. The cumulative tracking curves are shown in Fig. 4.1 and the xy-tracking trace as would be seen on the viewing screen in Fig. 4.2. Z-tracking in the TEM-mode uses the beam-tilt-induced-image-shift (BTIS) method [84; 85; 86; 199].[3)] The image shift is analysed by a cross correlation. This is accomplished by the tracking software (Tomography module of DigitalMicrograph™ (DMG) of the Gatan Microscopy Suite (GMS)[26]). The adjustment for every tilt increment is necessary due to the significant mechanical misalignment of the rotation axis of the goniometer and the optical axis of the TEM (described in Fig. 4.5 and discussed in Sec. 6.1). This misalignment is probably also the reason why the pre-calibration curves of the goniometer for tracking depend on the applied specimen drive. Therefore, tracking could not be optimized by pre-calibration curves (as described by e.g. Ziese et al. [198]) or movement predictions [112], which would reduce the total dose and acquisition time.

It is rarely possible to position the region in which no manual intervention is necessary (grey area in Fig. 4.2) such that the whole trace lies within this region since the actual trace is not known before the tilt series is fully acquired. This trackable region varies in shape and size depending on the magnification used. The size decreases with increasing magnification making acquisitions above 63 kX very cumbersome. Its actual centre and the border depends on the pre-image-shift already used by the service for the default user settings.

The time delay (Δt), between successive tilt increments to let the holder and its vibration settle (settling time), has sometimes to be adjusted during acquisition. This is because the damping of vibrations after each tilt increment depends on the tilt angle. I

[3)] This method is not applicable for STEM tomography. STEM auto-focussing is based on a search for a focus that maximizes a function that measures the contrast (e.g. image variance or autocorrelation difference), see e.g. [175]. This methods needs more than two images as the BTIS method for TEM.

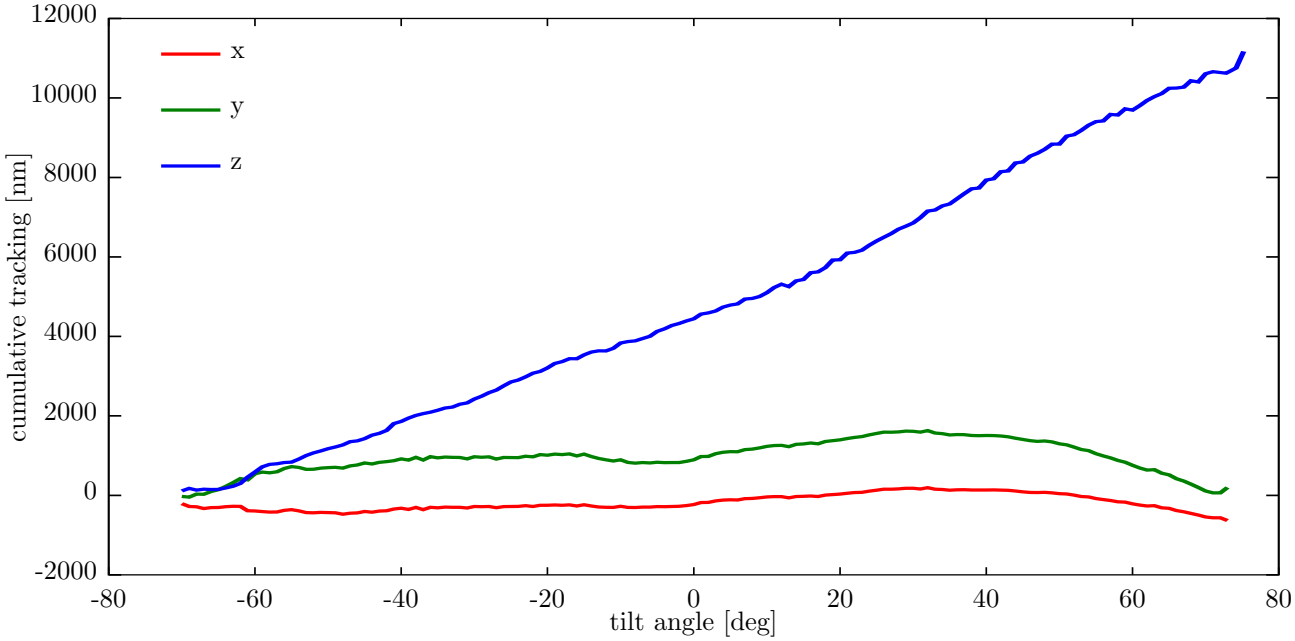

Figure 4.1: Cumulative xy-z-tracking curves

The cumulative xy-z-tracking curves belong to trace c in Fig. 4.2 and to the second tilt series acquired for the tomogram in Fig. 5.3. The total defocus needed for z-tracking was around $\Delta_z \approx$ 11 µm.

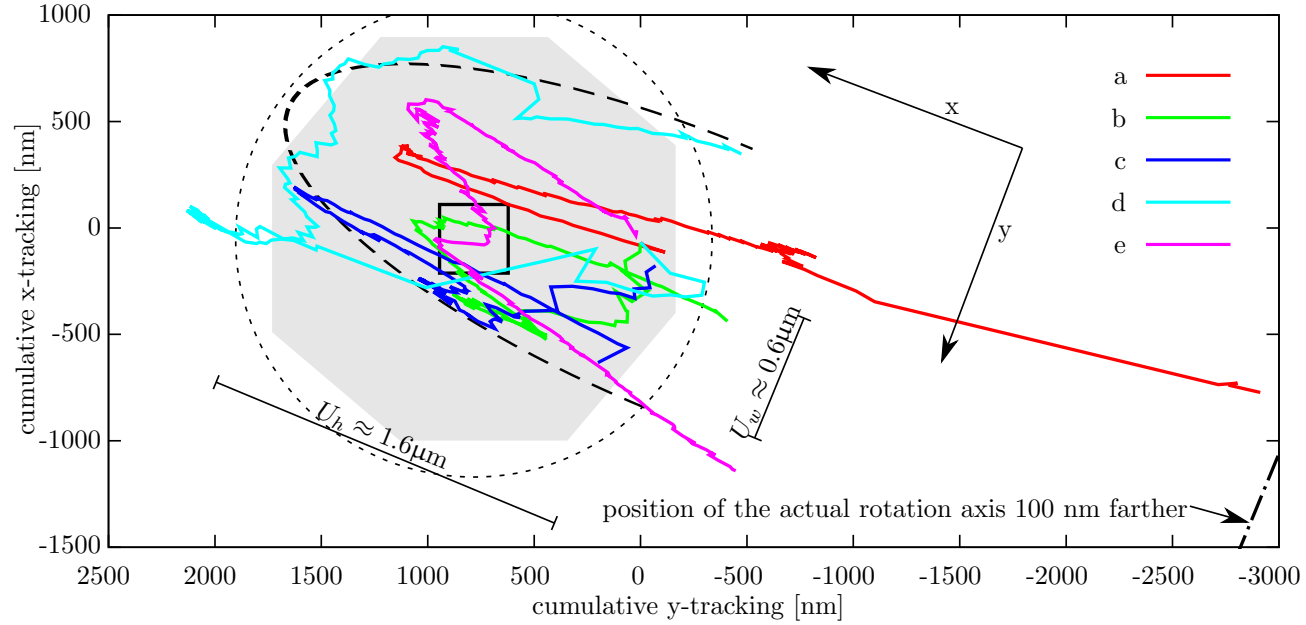

Figure 4.2: xy-tracking traces

The plot shows multiple xy-tracking traces and demonstrate how much the traces of tilt series can differ. The traces tend to follow the path of a partial ellipse, i.e. they have a distorted U-shape. The x- and y-axis correspond approximately to the coordinate system of the tilt series, i.e. the y-axis is parallel to the rotation axis. It can be seen that in most cases a total image shift between 1500 nm and 2500 nm is needed. The traces differ significantly so that no pre-calibration can be used to predict the trace of the next acquisition. The position of the traces relative to each other might vary. The traces belong to tomograms in Figures: a: 5.11, b+c: 5.3, d: 5.6

The square indicates the region imaged by the CCD at 63 kX (as was used for b and c). The dashed circle represents the viewing screen that the image-shift-limits are given to [193]. The grey region marks the area that was actually reachable by the image shift. In the case of trace c it was just about possible to avoid the need for manual intervention.

often did not use a fixed Δt for the whole acquisition since the necessary settling times normally range from 10 s to 100 s during a tilt series at 68 kX or higher. Together with the alignments, just one tilt series could generally be acquired during a day. The possible need for manual adjustments during the automated acquisition did not allow unsupervised acquisitions that could run over night or multiple days.

The total dose on the sample during acquisition of the tilt series ranged from $D_t \approx 400 \cdot 10^3$ e^-/nm^2 to $D_t \approx 8000 \cdot 10^3$ e^-/nm^2. In some cases, acquisition suffered from significant sample drift caused by sample charging. This charging depends on the conductivity of the sample. The conductivity of the samples studied depends on the local thickness of the support foil and apparently also on the density and size of the gold markers. Charging occurs when the beam is unblanked above the sample for acquisition of an image. Blanking the beam above the sample (pre specimen-blanking) reduces the dose on the sample drastically since the sample is not irradiated during the change of tilt and the time delay Δt for mechanical settling. However, images acquired of a sample that drifted up to 10 nm because of charging during the acquisition are of no use. At times when the contamination of the samples in the TEM was less, blanking of the beam behind/below the sample (post specimen-blanking) was feasible. The idea to use both pre and post specimen blanking together with a time delay has not been implemented for the combination of DMG with the TEM used but is available e.g. with SerialEM[24] for other TEMs [112]. Pre specimen-blanking would reduce the dose on the sample. After some time delay, post specimen-blanking would be used for acquisition. The time delay would be chosen such that the sample drift caused by charging has settled.

Although according to the eq. 2.1 (p. 11) the resolution of the tomogram depends on the tilt increment, only 1° to 3° are typically used (e.g. [55; 90; 11]) to reduce the total dose or due to limited resolution of the tilt series images [52]. Below 1°, the resolution of TEM tomograms is additionally limited by other factors (e.g. image misalignment, missing wedge and projection violations). In contrast, in X-ray and neutron tomography tilt increments below 0.5° are generally used. A further reduction of tilt increment might become important for newly developed reconstruction algorithms such as DIRECTT and for 180°/360° TEM tomography. Then, an unsupervised automated acquisition would be essential. The general problem that sample thicknesses are too large concerning transmission at very hight tilt angles ($\alpha > 60$) is not so problematic for the samples studied since particles can be chosen that have an approximate rotational symmetry along the goniometer rotation axis. The increase of projection thickness of the carbon foil is insignificant since it is very thin (below 10 nm).

As mentioned above, the digital evaluation of recorded image shifts is accomplished with 2D cross correlation (CC) which is based on a Fourier transformation (see e.g. [27]). Therefore, CC depends on the spatial frequencies of the actual ROI. Image pre-filters such as the Hanning window and band-pass-filter (see e.g. [27; 29]) have to be adjusted to emphasize the contrast of spatial frequencies characteristic for the ROI to make the CC sensitive for these frequencies. Otherwise the correct image shifts will not be determined causing automatic tracking to fail. Although generally the contrast of the

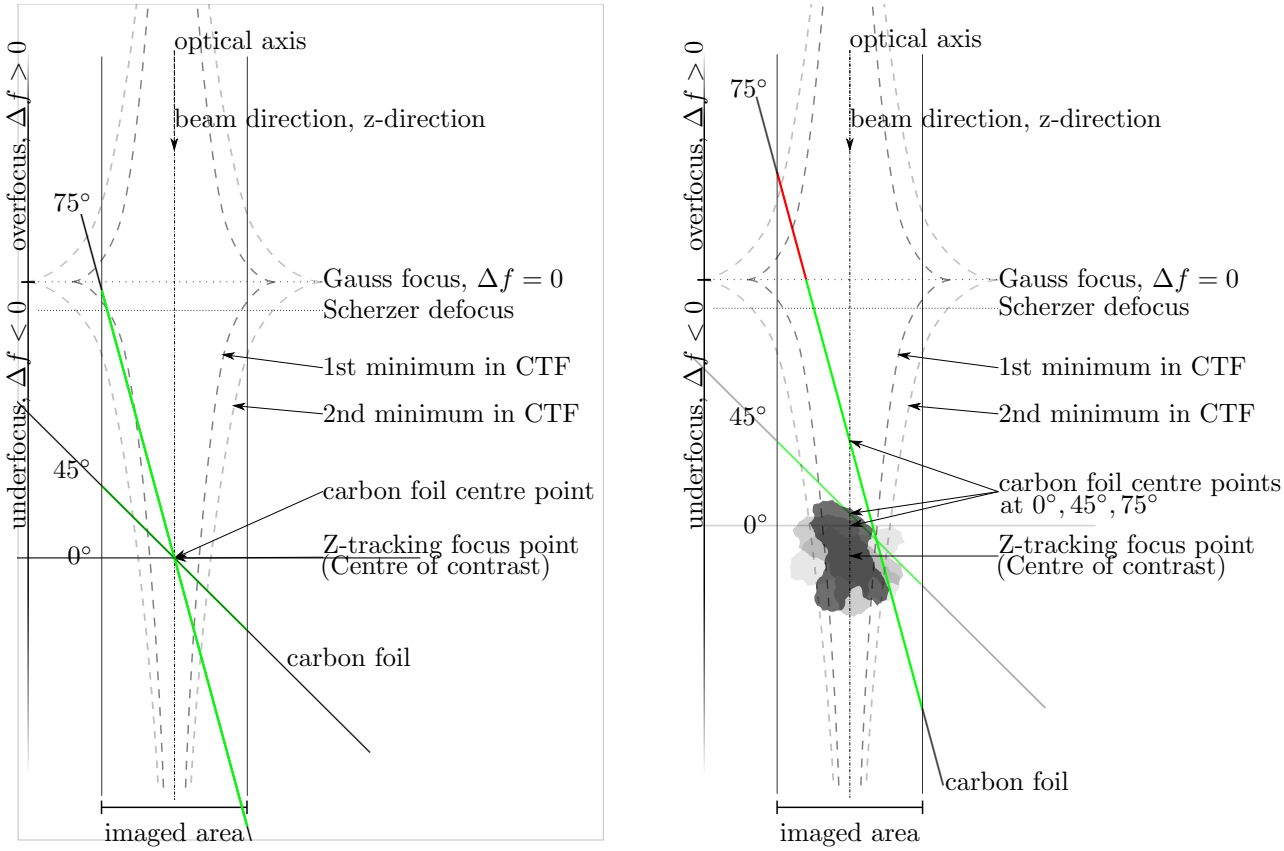

Figure 4.3: Schematic z-tracking and z-dependent CTF

The left image shows z-tracking of only a carbon foil with marker (or a comparable sample of neglectable thickness) in underfocus. In this case, the centre of contrast (CoC) is the centre of the carbon foil (CoF). For ideal z-tracking, the distance of the CoF to the Gauss focus (GF) is constant because the cross correlation z-tracking is tracking the CoC and the imaged region is all in underfocus, green.

The dashed lines mark schematically the position/radius of the first and second minimum of the z-dependent contrast transfer function (CTF, see e.g. [157]) as seen in the FFT of the untilted carbon foil at the corresponding defocus, i.e. z-position (see also Fig. 4.4 and Fig. 2.1).

In the right image, a particle is attached below the carbon foil. Now, the main contrast in the image originates from the particle and so the CoC is close to the centre of the particle (CoP). The displacement between the CoF and the CoP increases with increasing tilt and therefore parts of the imaged carbon foil can be in overfocus (red) while the particle still resides fully in underfocus. This condition corresponds to that imaged in Fig. 2.1.

carbon foil can be neglected when tracking a particle, the contrast contributed by gold markers to the CC can be significant.

The contrast transfer function (CTF) of the TEM depends on the defocus chosen for acquisition, implied in Fig. 4.3. If the focal length of the objective lens is kept fixed but the untilted sample is translated in z-direction by the goniometer, the image is nearly the same as if the sample was kept stationary and the focal length of the objective lens, i.e. the defocus Δf, was changed (by changing the current through the lens coils). Only 'nearly' the same, because the changed focal length causes a change in magnification. However, the change in magnification, even for a defocus range of 10 µm, is less than 1% for the TEM used (according to fine alignment results from IMOD, see Sec. 4.3). The described conditions lead me to an idea enabling to check the quality of the z-

tracking of a whole tilt series. I call it the arc-integration-image method. It is outlined in Fig. 4.4.

If the goniometer tilts to 75° the sample covers a very wide range of z-positions throughout the image, see Fig. 4.3. Now the FFT of the image of the tilted sample shows the effective CTF (eCTF) the combination of all CTFs in the z-range covered by the sample. Hence, the FFTs of images at high tilt angles do not show the distinct first minimum circle as FFTs of images at lower tilt do. This is also visible in the arc-integration-image created of the stack of FFTs of a tilt series as shown in Fig. 4.4b. For this reason, the evaluation outlined in Fig. 4.4 used the gradient image, which caused the border of the region of the 0th maximum to extend up to the maximum gradient of the arc-integration-image, Fig. 4.4bc. Basically, this border is better defined in the arc-integration-image for high tilt angles than the border defined by the position of the first minimum. The error in the actual position of the border increases with the tilt angle magnitude. Therefore, it is unsure if the actual border turns towards lower or higher spatial frequencies for tilt angles above 45°. However, the turn towards lower values fits to the impression of mean defocus values that images above 45° tend to have with automatic z-tracking. Therefore, the FFT stack and its arc-integration-image evaluation seem to give a reasonable measure for the quality of the z-tracking of the whole tilt series. By relating the found border to the first minimum of the eCTF it is possible to estimate the actual mean defocus for each image in the tilt series (see e.g. [169]).

If the image region the FFTs are calculated from is reduced, this arc-integration-image method can be related to the local FFT evaluation described in Fig. 2.1. As evaluated in Fig. 4.4d, the resolution of the individual images is at least 11 Å. This is very close to the 3D resolution of 12 Å evaluated by FSC (see App. A.2) and might be the integral 3D resolution limit achievable with the used TEM in conjunction with WBP reconstructions.

For the calculation of the tracking parameters transferred to the TEM, it is crucial that the calibration of the DMG tomography module is exact, i.e. that the corresponding DAC (digital-to-analog converter) values lead to a re-centring of the image. These calibrations are specific for each magnification and due to changes (caused by different use of the TEM) had to be redone for each tomography session (a specific problem of the combination of DMG with the used TEM).

Typical tracking curves and traces are shown in Fig. 4.1 and 4.2. Z-tracking and other differences to automatic acquisition in the STEM-mode will not be explained further because no usable STEM tilt series could be acquired with the TEM used due to increased contamination caused by the focused beam (see Fig. A.4).

Apart from the acquisition problems mentioned before (i.e. beam damage and drift problems caused by sample holder vibrations or sample charging), the misalignment between the rotational and optical axis lead to multiple problems:

- Pre-calibration curves could not be used. Thus, the need for xy-z-tracking after each tilt increment increased the total dose on the sample.

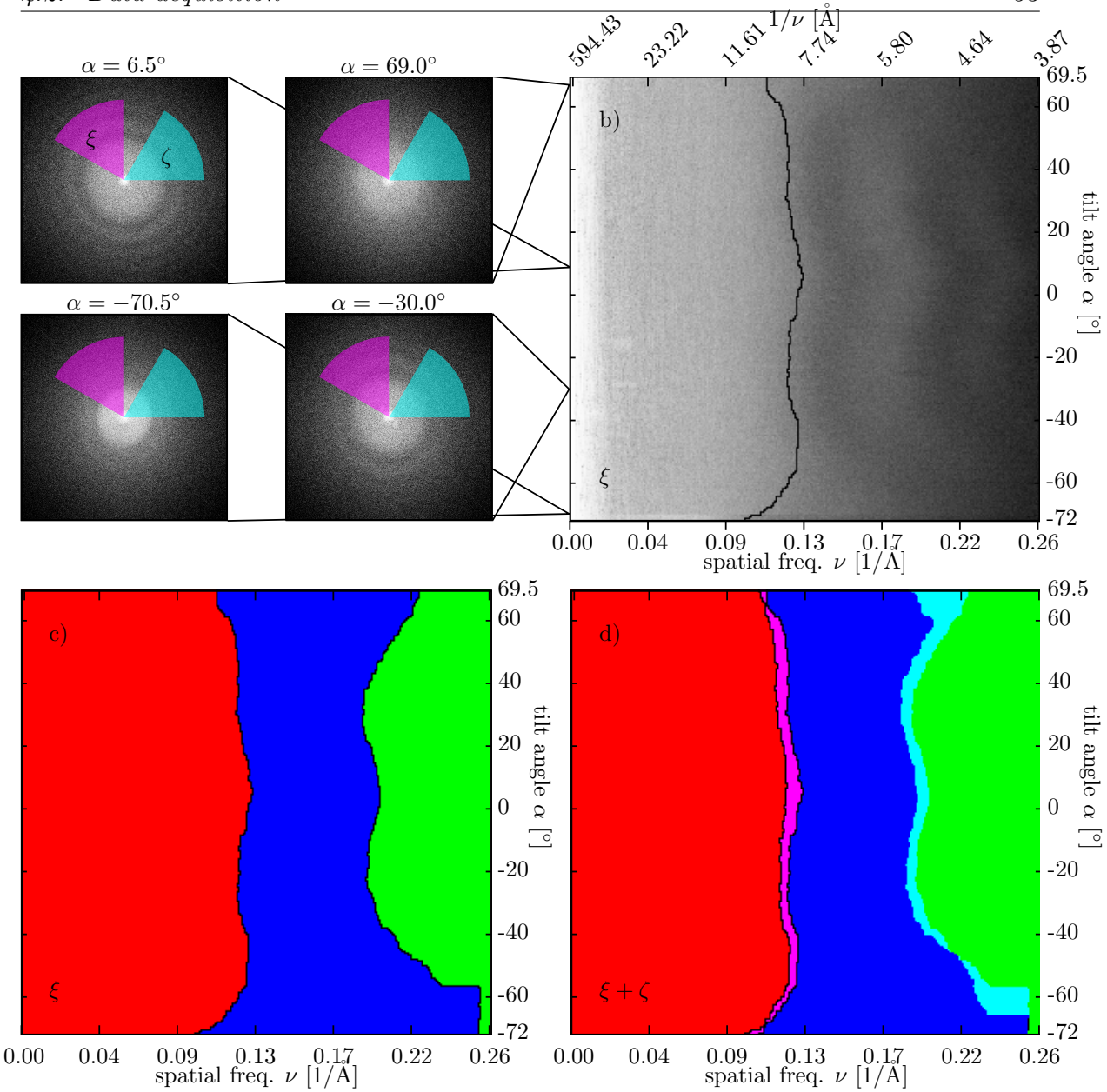

Figure 4.4: Quality check of the z-tracking by the arc-integration-image method

Four exemplary images of a tilt series acquired at four different tilt angles α were selected. The FFTs of these images are shown in the top left images. The minima of the eCTF can be seen, up to the third in the upper left. Each FFT of the stack was pixel wise averaged along fixed radii [7;19] within the magenta coloured sectors ξ to reduce noise. The resulting line profile was interpreted as a 1-D image. All 1-D images stacked yield the image b), the arc-integration-image. Therefore, the x-axis of image b) corresponds to the radial position starting from the centre of the FFT (i.e. spatial frequency ν) and the y-axis to the tilt angle α. The corresponding positions of the four exemplary FFTs in the stack is indicated by the lines.

As explained in the text, not the position of the first minimum was marked by the image analysis but the position of maximum gradient. The image analysis is based on the watershed transformation applied to the gradient image of b) evaluated in x-direction, image c) (for details see Sec. 3.4.1 **7.)**). The resulting border line towards the FFT centre is also drawn into b).

To also analyse the change of astigmatism, a second arc-integration-image was created from the cyan coloured integration sector ζ which is 90° rotated to the magenta sector. The rgb-overlay of image c) and the corresponding one from the second evaluation result in image d). Therefore, the magenta and the cyan regions in d) mark the difference between the found borders which corresponds to the amount of astigmatism.

Image d) shows that astigmatism and its variations are small in this tilt series. The variations in z-tracking are slightly more pronounced. Therefore, the resolution of the individual images of the tilt series (determined by the first minimum as explained in Fig. 2.1) varies. Using the marking lines in d) instead of the actual first minimum, the resolution varies between about 7.7 Å and 11 Å.

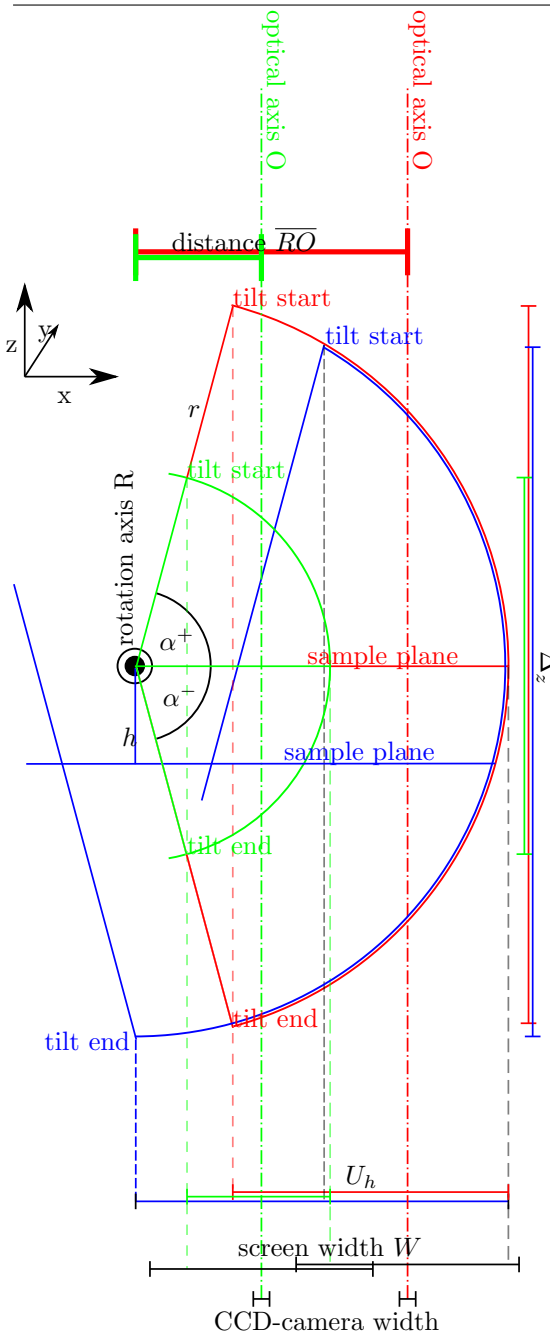

Schematic drawing showing the geometric relations arising from the displacement between rotation axis R (y-axis) of the goniometer and the optical axis O of the TEM (z-axis). The axis R points out of the paper. For simplification, R is perpendicular to O, i.e. U_w would be 0 in Fig. 4.2. The sample detail moves along the circular paths (with radius r) when tiled from α^- to α^+ during acquisition of the tilt series. For simplification, the magnification M was ignored (set to unity, $M = 1$). Otherwise the real track width (U_h, a few µm, see Fig. 4.2) is much smaller than the effective track width on the screen (U_{h_s}, around 15 cm). Under symmetric conditions ($|\alpha^-| = |\alpha^+|$): $U_{h_s} = M \cdot U_h$ and $U_h = r(1-\cos(\alpha))$.
Blue: General case where the sample plane is not in the eucentric height, i.e. $h \neq 0$. Although $|\alpha^-| = |\alpha^+| = 75°$, the tracking trace will not be symmetric and U_h will be given by $|\alpha^-|$ if the sample plane is below the rotation axis R.
Red: The sample plane is now at the eucentric height, i.e. $h = 0$. However, the distance $\overline{RO}$ is so large that U_h does not fully fit within the screen width W. The sample cannot be continuously tracked over the whole tilt range.
Green: A smaller distance $\overline{RO}$ allows U_h to fully fit within the screen, i.e. $U_h \leq W$. This is drawn here as if the optical axis was shifted towards R. Such a shift can be achieved by the use of image- and illumination-shift. If $\overline{RO}$ does not lie within the limits of the optical shift, mechanical alignment of the goniometer axis to the optics is necessary to reduce $\overline{RO}$.

Figure 4.5: Displacement between rotation axis and optical axis

- The need for a wider range of optical image shift (its limits become more restrictive with higher magnifications) introduced variations in the illumination intensity profile and changes in the beam tilt (in relation to the optical axis).

- The wide range of z-tracking introduced optical problems such as changing astigmatism and aperture shadows entering the image region.

The resulting need for manual interventions during automatic acquisition increased the total dose on the sample drastically. If the mechanical specimen drive has to be used for manual xy-tracking, the mechanical backlash generally causes an additional displacement of the rotation axis of the goniometer. Thereby, further manual interventions during the remaining acquisition are more likely.

Figure 4.5 shows a schematic drawing of the geometry of rotation axis R of the goniometer and the optical axis O of the TEM. Additionally to the displacement of R and O as outlined in Fig. 4.5, R and O are not perpendicular to each other in the TEM used. This causes the spreading of the tracking traces in y-direction, which results in the U-shape of the tracking traces as visible in Fig. 4.2.

DMG does not offer the feature to calculate the displacement as other acquisition software does (e.g. SerialEM[24] [112]). However, the misalignment can be estimated, e.g. by the tracking characteristics of a sample detail throughout a tilt series if the tracking limits were just about reached, because then the centre of the screen can be regarded as the approximate position of the optical axis and $W \approx U_h$. This was the case for e.g. the second tilt series of the tomogram in Fig. 5.3 with $\alpha = 70°$. The tracking curves and trace are shown in Fig. 4.1 and 4.2. With the geometry of Fig. 4.5: $\overline{RO} \approx r - W/2 \approx r - U_h/2$ and $\Delta_z \approx 11$ µm, $U_h \approx 1.6$ µm (see Fig. 4.2). There are two ways to estimate r: Firstly, $r_1 = \Delta_z/2/\sin(\alpha) \approx 2.4$ µm, secondly $r_2 = U_h/(1-\cos(\alpha)) \approx 5.9$ µm. There is a large discrepancy between the two estimates of r. However, the estimate given by r_2 is very sensitive to the height h, i.e. the distance between the sample plane and the rotation axis R. If $h \neq 0$ (blue in Fig. 4.5) the approximation of r by r_2 is no longer appropriate. The estimate given by r_1 is quite insensitive to the eucentric height h, and therefore $r \approx r_1 \approx 5.9$ µm should be used. Hence, the displacement distance $\overline{RO} \approx \Delta_z/2/\sin(\alpha) - U_h/2 \approx 5$ µm. The approximate position of the actual rotation axis is therefore 100 nm farther than indicated by the dot-and-dashed line in Fig. 4.2. The tilt around the x-axis (referred to as x-tilt) away from perpendicular alignment of R and O is about $\beta \approx \arcsin(U_w/\Delta_z \cdot sin(\alpha)) \approx 3°$ estimated by $U_w \approx 0.6$ µm (see Fig. 4.2). This estimation assumes an angle-invariant x-tilt. However, when looking at the shape of the traces, some significant deviations from a U-shaped path can be seen for various traces. These deviations can be caused by angle dependent x-tilts, e.g. when the actual tilt axis follows a cone. This can be caused by the mechanical lever that holds and moves the holder in y-direction (x-direction of the TEM coordinate system, i.e. direction of the rotation axis, see e.g. [193, Fig. 3-17]). The x-tilt can be measured (and compensated) by IMOD. The IMOD estimation for β is only about half of what was estimated by the tracking trace. A more robust estimation of $\overline{RO}$ could be achieved by fitting a circle/ellipse to all tracking points in 3D.

An automatic acquisition without manual intervention is only possible if the sample trace can be positioned such that it stays within the trackable region, grey in Fig. 4.2. As a rule of thumb, the trackable region is about seven times the width of the CCD chip. Therefore, at 68 kX the sample displacement during acquisition, U_h, has to be below 2 µm and the sample ROI may only be as big as about 300 nm. Depending on the available initial image shift, the sample ROI is then 4 µm to 6 µm away from the rotation axis of the goniometer (R). This means, the sample ROI is displaced from the rotation axis R by about a factor of 16 of the width of the ROI. At e.g. 160 kX, U_h has to be below 1 µm.

4.2.1 Acquisition parameters

The meaning of the parameters I used for acquisition are as follows and were taken either from the TEM control (WinTEM[27]) or from DigitalMicrograph™ (DMG) and generally are approximates. Generally, no errors are given by the software or the manual. Therefore, stated errors were evaluated through an estimation of the variation for repeated measurements of same conditions. Acquisition was always done with a constant angle increment and generally with illumination tracking. For the acquisition of the tilt series no objective aperture could be used because it would have limited the tilt range to ±45°. Important values that differed from those reported here are given in Chap. 5 for each presented measurement:

- TEM acquisition mode: BF-TEM, ZL-TEM, STEM (the large energy filter entrance aperture was used in ZL-mode);
- Magnification M (WinTEM);
- Tilt range (WinTEM);
- Illumination collection angle $\xi = 25$ µrad (WinTEM);
- Acquisition times: $t = 1$ s for the tilt series image, xy-tracking $t_{xy} = 0.1$ s and z-tracking $t_z = 0.25$ s, (WinTEM));
- Average number of electrons collected per nm^2 $\#_e$ (DMG);
- Pixel size s_p (DMG);
- Average time delay $\Delta t \approx 50$ s between successive tilt increments (DMG);
- The diameter of the condenser aperture $\varnothing_C = 200$ µm (WinTEM);
- The width of the slit aperture of the energy filter when in ZL-mode $\Delta E \approx 16$ eV (measured with DMG, centred at about 0 eV);
- The eucentric hight ΔZ generally lay between 25 µm and 35 µm (WinTEM);
- The displacement of the maximum of the cross correlation from the image centre for z-tracking $\Delta d_z \approx 20\%$ (i.e. 450 pixel of 2048 pixel achieved with a beamt tilt of 25 mrad, DMG);
- Blanker used (generally pre specimen-blander, e.g. Gun-Bl or C1-Bl, WinTEM);
- The fixed defocus Δf_f, that DMG was set to maintain, generally lay between -1 µm to -2 µm (DMG);
- The initial image shift generally lay between 25% and 50% off the user centre (WinTEM, the direction of the offset is dependent on M);
- Average pressure reported for the sample chamber P (WinTEM);
- Liquid nitrogen (lN_2) used or not for cooling of the anti contamination cryoshields;

The illumination current density J can be estimated by ξ and the brightness of the electron source or by t and $\#_e$ (see Sec. 5.1). The total dose can be estimated with the

illumination current density J and the acquisition times per tilt series frame ($t+2\cdot t_{xy}+2\cdot t_z$). The generally used beam tilt of 25 mrad for z-tracking leads to a displacement of $\Delta d_z \approx 20\%$ which yields a reliable nearly constant defocus (see Fig 4.4). The defocus the TEM control reported Δf_Z (WinTEM) and that measured by DMG Δf_G generally had a ratio of $\Delta f_Z/\Delta f_G \approx 0.65$.

4.3 Tilt series, reconstruction and 3D processing

After acquisition of a tilt series, it has to be digitally aligned because even with an optimal xy-z-tracking, the alignment between successive images in the tilt series can vary by up to about 500 pixel, i.e. 25% of the image width. A grey scale normalization of the stack images containing a constant gradient should be done before the alignment because the alignment would translate the gradient profile.

Alignment of the tilt series images

The quality of the alignment of the tilt series images has a high impact on the resolution and the depression of artefacts in the tomographic reconstruction. Therefore, the alignment of the images should be done carefully and manual alignment[4)] taken only as the last resort. Generally, the best alignments are achieved with fiducial marker tracking although new markerless methods like trifocal geometry [25; 52] show promising alternatives. Most of the tilt series I aligned by fiducial marker tracking using the software package IMOD[1] (described in Ref. Kremer et al. [88]; Mastronarde et al. [115]). IMOD offers an alignment by filtered CC (called coarse alignment) and an alignment by fiducial marker tracking (called fine alignment). For both methods it is possible to compute a local alignment of patches of the images. This allows to compensate for image distortions caused by the optics (e.g. changes in illumination tilt, magnification, image rotation) as well as those caused by a change of the sample (e.g. sample shrinkage). Those distortions that cannot be compensated in the 2D images are compensated during reconstruction/reprojection. This kind of correction is based on local deformations of the ray path within the sample.[5)] This creates a dependence between the alignment result and the reconstruction. The fine alignment reveals that the tilt angles can vary by $\pm 0.5°$ and the image rotation by around 0.5°. The change in magnification, even for a defocus range of $\Delta f \approx \pm 5\mu m$, is less than 1% for the TEM used.

[4)] E.g. with `midas` of IMOD[1]

[5)] This is the basic difference between the programs `tilt` and `xyzproject` of IMOD[1].

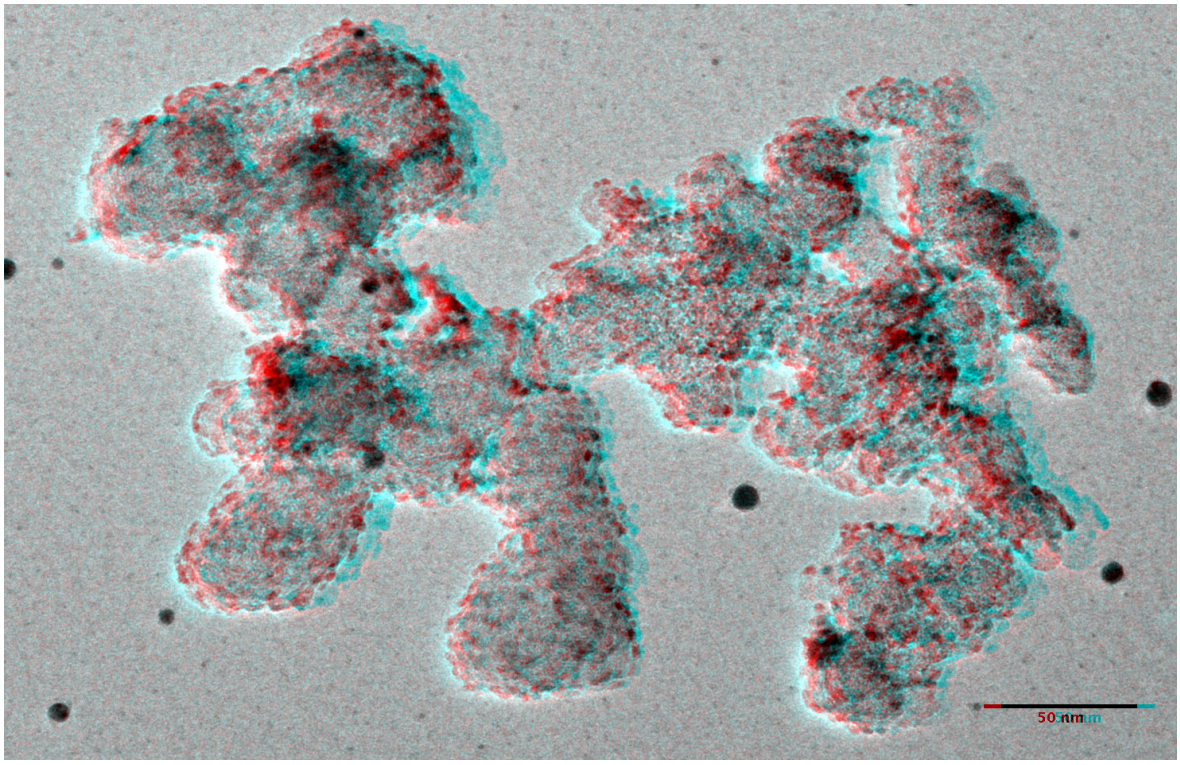

Figure 4.6: Anaglyph (red-cyan overlay) of a catalyst particle
The figure shows an anaglyph of the catalyst particle from Fig. 5.11. The anaglyph was constructed from two images of the tilt series which are 5° apart at around 0° tilt, i.e. the carbon support foil in the anaglyph lies in the plane of the paper. When viewed with red-cyan glasses the extent of the sample in the third dimension (the z-direction) can be perceived. The apparent depth varies depending on the distance to the anaglyph when viewed. The larger the distance the more pronounced is the depth effect.

Videos and anaglyphs from tilt series

Rotation of the sample visible in a video of the aligned tilt series already gives a 3D impression. In regard to the samples studied, the rough positions of the ruthenium particles could already be determined and the question whether they are situated within or on the surface of the support answered. The structure of the carbon support, which significantly suffers from noise, can be seen best in videos of tilt series. The advantage here is: There are no misleading artefacts from reconstruction. Additionally, the human brain is able to compensate the noise of a single image by the 3D impression and the imaginary relation to a rotating object which is still hardly achievable by digital filters. However, the impression from tilt series videos is not easily accessible to quantitative evaluation by software but possible [165]. Furthermore, the view is restricted to the tilt range and axis that was chosen at acquisition time. A reduction to only two images in the tilt series leads to stereo microscopy (see e.g. [40, sec. 1.6, p. 18]) or generalized to stereoscopy including anaglyphs as in Fig. 4.6. Another analysis method for 3D properties is stereology [179] which is based on at least two images of successive sections.

3D reconstruction of the sample from the tilt series images

In addition to the significant image distortions (partially compensated by the alignment), various other limitations (i.e. deviations from ideal complete tomographic data) have to be dealt with in the reconstruction of the tomogram:

1. Limited range of view (i.e. 'missing wedge'),
2. Non-equidistant angle increments
3. Tilt around the x-axis, i.e. optical (beam) tilt or a tilt away from perpendicular alignment of R and O in Fig. 4.5 (mechanical tilt).
4. Too few projections considering the image size of generally 2048x2048 pixels
5. Influence of object parts outside the 3D region-of-interest (ROI), entering at higher tilt angles (e.g. gold markers on the support foil or other parts of the sample)

Conventional reconstruction software does not account well for all these restrictions. Therefore, IMOD offers reconstruction programs based on WBP (Weighted Back Projection) or SIRT (Simultaneous Iterative Reconstruction Technique), i.e. called IMOD-WBP and IMOD-SIRT, that take these specific TEM tomography limitations into account (except point 5). IMODs reconstruction programs can even compensate for a varying tilt around the x-axis, e.g. when the rotation axis follows a cone during tilt series acquisition. However, some distortions can only be measured (and compensated) if the sample is section-like (e.g. from serial sectioning of the sample with a microtome) containing fiducial markers on both sides of the sample section.

The DIRECTT algorithm (Direct Iterative Reconstruction of Computed Tomography Trajectories [97; 96; 98]) represents a promising alternative for the reconstruction of TEM tomograms. DIRECTT can take the limitations mentioned above into account except point 3 [95; 65]. Instead of back-projecting all sinogram values at once, DIRECTT traces single sinusoidal trajectories in Radon space which are selected from the set of all possible trajectories by criteria such as their angular averaged (filtered) weight or contrast to adjacent trajectories. These reconstruction elements are only partially added to an intermediate reconstruction. The reprojection (Radon transform) of this reconstruction is then subtracted from the original (i.e. measured) data set. The obtained residual sinogram is treated in the same way in the subsequent iteration steps until a pre-selected criterion of convergence is reached. Careful data pre-processing combined with the advantages of DIRECTT, in particular extending the range of reconstruction beyond the input image size (point 5, [68]), proved to effectively eliminate disturbing streak artefacts. However, the reprojection in DIRECTT does not account for local deformations of the ray paths as IMOD-WBP and IMOD-SIRT do (as mentioned above). Extending DIRECTT to do so could lead to a further improvement of the DIRECTT reconstructions of TEM tilt series. There are many other reconstruction algorithms that can also be used to reconstruct TEM tomograms. Due to limited availability of

reconstruction programs and insufficient time for the creation of own implementations, only IMOD-WBP, IMOD-SIRT and DIRECTT were used in this work. For details about the individual reconstruction algorithms/programs the reader is referred to the literature (see e.g. [14; 52; 29; 16; 176; 63; 11; 167])

A dual tilt series reconstruction consists of two combined tomograms which reduces the 'missing wedge' and increases the SNR [111]: For a dual tilt series reconstruction the sample is rotated by 90° in the sample plane for a second tilt series acquisition (for details see Ref. [46]). Two tomograms are reconstructed from each tilt series. One of the tomograms is deformed according to local 3D cross correlations with the other tomogram. This process is called matching. It is necessary because of different image deformations between the two tilt series, caused e.g. by different magnification changes due to other defocus values during xy-z-tracking. After matching, the two reconstructions of each tilt series are combined in Fourier space [111]. This reduces the 'missing wedge' to a 'missing pyramid'.

Despite these advantages, it was only possible once to acquire a usable second tilt series of the same sample detail. The acquisition of a second tilt series makes only sense if beam damage during the acquisition of the first series did not change the sample detail significantly. For the samples studied, it is also problematic not to loose the sample detail during the 90° rotation. The translation of the detail is normally quite large (up to 1 mm). Therefore, only a very low magnification of 100 X allows to keep track of at least the grid square of the sample detail. Due to the large translation, the sample detail may end up at a position where the acquisition tilt range is insufficient.

Figure 4.7 shows slices of the same regions of a catalyst sample created by IMOD-WBP, IMOD-SIRT and DIRECTT. It can be seen that the DIRECTT reconstruction show significant less dominant artefacts and an improved spatial resolution. A quantification of the suppression of streak and missing wedge artefacts is presented in Sec. 5.3.4.5. The background gradient in the SIRT reconstruction is assumed to originate from iteration fluctuations caused by a too low SNR or x-tilt-correction as often observed for low dose cryro data.[6)]

Processing of tomograms

Generally, the tomogram resulting from reconstruction has to be filtered to reduce noise and/or to enhance some structures in regard to others. Various grey scale filters exist for these purposes, e.g. median filter; non-linear diffusion filter; mean, Gauss and other convolution filter; filter based on weight functions of the Fourier space like band-pass filter (except for discrepancies due to discretization equivalent to convolution filter), morphological image filters to list just a few. The reader is referred to the literature for more details about digital image filters and their use (see e.g. [76; 162; 189; 27; 115; 144; 53]). In contrast to the tilt series stack, the tomogram should in most cases be filtered in 3D. Various programs exist to process 3D datasets with 3D filters. However, the

[6)] Personal communication with D. Mastronarde, see also [115, `sirtsetup`].

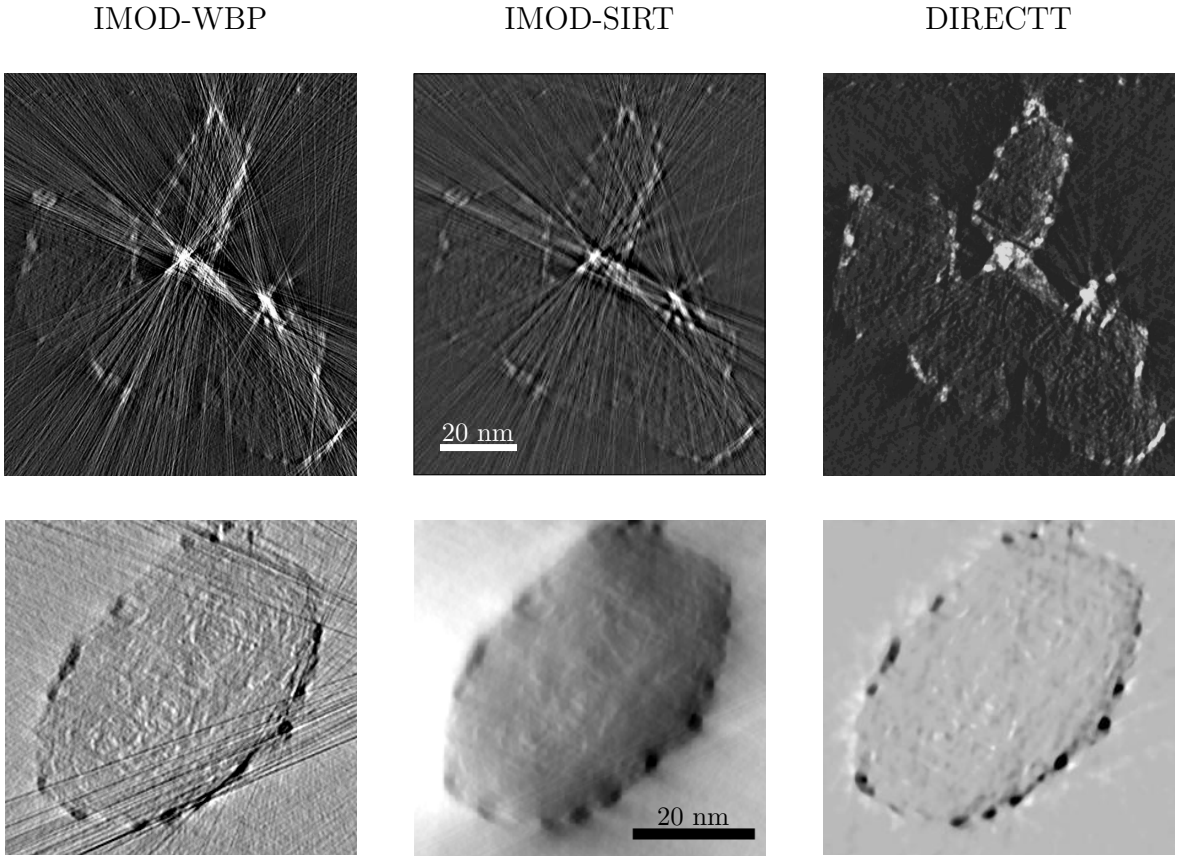

Figure 4.7: IMOD-WBP, IMOD-SIRT and DIRECTT reconstruction
The top row shows contrast inverted reconstruction slices (xz-plane) to make the streak artefacts better visible. The influence of the artefacts reduces from left to right and the spatial resolution increases.
The bottom row demonstrates the difference between carbon support and empty space in the reconstructions. Whereas SIRT exhibits the highest contrast difference, it also has the strongest background gradient. The detail seems highest in the WBP reconstruction.

execution time and accuracy varies and care must be taken to document introduced modifications to the data that might influence later analyses. For most automated quantitative analyses the 3D data has to be segmented or binarized by thresholding filters such as global thresholds or sophisticated algorithms as listed in App. A.1. There are many binary filters that can be applied to the binary datasets then (see literature listed for grey scale filters). Many depend on a (voxel) structuring-element or on the definition of the neighbourhood. Two common neighbourhoods in 2D are either the 4 directly connected pixels (4-connectivity) or additionally those only connected by a corner (8-connectivity, $3^2 - 1$). In 3D the corresponding neighbourhoods either have 6 or 26 ($3^3 - 1$) connectivity (for depictions and other neighbourhoods see e.g. [53]).

There are two common types of visualization of 3D data: Either voxel rendering or surface rendering (see e.g. the program `Paraview` [1]). They are based on two different data representations, i.e. voxel representations or mesh representations. These are further described in App. A.1 and in the literature (e.g. [76; 155; 12]). Different algorithms exist to generate mesh representations from voxel representations (see e.g. [106; 127]). Various different analysis methods are possible depending on the type

of data representation (see Chap. 3 and 5). The generation of mesh representations and their analysis is time consuming and was therefore parallelized with python [116] in this work. Concerning analyses of mesh representations it is important to be aware of (closed) manifolds and their creation or preservation by mesh filters.

The presented image analyses are mainly based on the following programs:

- Filtering and analysis: ITK[2], VTK[3], VTKBlender[15], Blender[4], Octave[5], ImageJ[7] and awk[16]
- Visualization[7)8)]: Blender[4], Paraview[8], ImageJ[7], gnuplot[6], Inkscape[9], Gimp[10] and LaTeX[11]
- Programming was mainly done in C/C++[12], Python[13] and Java[14]

Linux[17] was the operating system used but most programs are also available for other operating systems. Apart from these free/open-source programs, MAVI[25], VGStudiomax[28] and Avizo/Amira[29] were used as well.

7) In this work, data is plotted with lines connecting data points if lines make it easier to follow successive data points and/or if it helps to distinguish data points from multiple plots within the same figure. Using different point styles to avoid the need for connecting lines was often much more difficult to read.

8) The colours were chosen such that they are easily distinguishable. The images in this document are displayed correctly with e.g. xpdf, Evince and SumatraPDF but some PDF-viewers display some of the images badly, i.e. in modified colours.

Chapter 5

Tomographic characterization of ruthenium-based catalysts

The ruthenium nanoparticle samples investigated were deposited on two different types of carbon support, namely Vulcan® XC-72R (from CABOT Corp [30], denoted by 'VC') and Black Pearls 2000 (from CABOT Corp [31], denoted by 'BP'). The carbon support was either pretreated with CO_2 (denoted by 'CO_2') to increase the surface and the porosity, or used unmodified (denoted by 'um').[1)] I prepared the TEM-samples and reconstructed TEM tomograms as described in Chap. 4. The four types of samples are referred to as $RuVC_{um}$, $RuVC_{CO_2}$, $RuBP_{um}$ and $RuBP_{CO_2}$. Furthermore, I created tomograms of four carbon samples without ruthenium (VC_{um}, VC_{CO_2}, BP_{um} and BP_{CO_2}) to investigate if the ruthenium treatment changes the carbon support. This might influence catalytic activity of the material.

In the following sections, the tomographic results of the samples without ruthenium are presented first, followed by the results of the samples with ruthenium. The tomographic datasets are examined and characterized. The detailed quantification by means of the developed analysis tools discussed in Chap. 3 will be demonstrated on $RuVC_{um}$. The tomograms of the other samples could not be studied in such detail because either the resolution was insufficient concerning the sizes of the ruthenium particles and the carbon structure or significant contamination during image acquisition in the TEM made any evaluation dependent on the actual position of the carbon surface impossible (e.g. the uncovered ruthenium surface). Some preliminary discussions are given if they relate directly to the presented results. Discussions spanning multiple results are given in Chap. 6.

5.1 Support particles without ruthenium

The support particles consist of different synthetic partially graphitized carbon black (see e.g. [187], [40, sec. A12.2, p. 31]). The differences observable in TEM images are: particle size, particle shape and the degree of graphitization.

[1)] The samples were designed and created by colleagues at HZB, for detailed description see e.g. [191; 45; 192; 65; 130; 94; 186; 190].

The degree of graphitization is the least quantifiable of the support characteristics. Most carbon particles are polycrystalline. The degree of graphitization can be regarded as the size and amount of graphitic regions in a carbon particle [187]. According to Wissler [187], the structural properties of graphitic crystals are described adequately by: crystallite size, L_c (crystallite dimension in the c-axis direction), L_a (crystallite dimension in the a-axis direction) and the interlayer spacing, $c/2$ (half the hexagonal lattice c-axis). Although the model in Fig. 5.1 shows well-defined mono crystalline regions, the transition from graphitic to amorphous carbon is continuous (see e.g. [82; 187], Fig. 5.1). Therefore, the listed properties are not easily determined. Hence, I use the terms 'more amorphous' and 'more graphitic' to express the tendency of the local carbon structure.

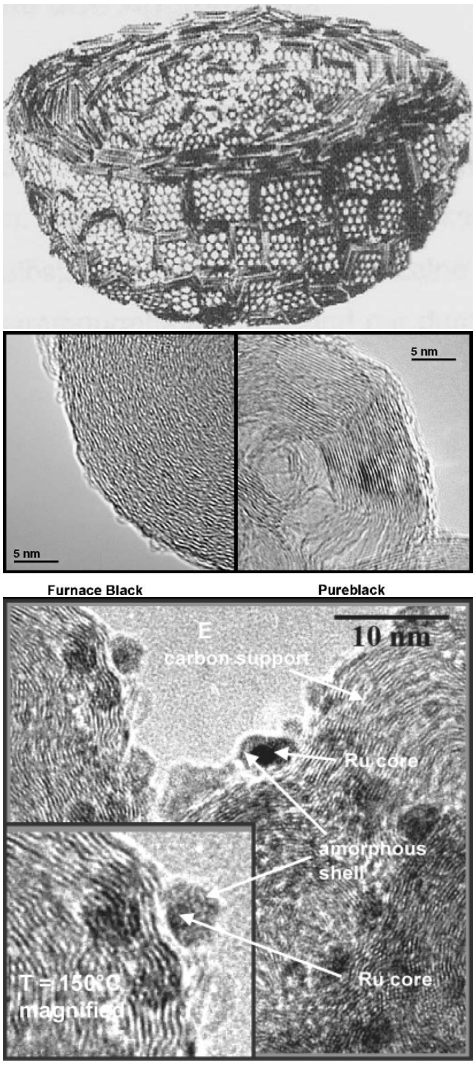

Figure 5.1: Graphitization

The top image shows a model of a partially graphitized carbon ball (Fig. 2 of [187]), the middle image different degrees of graphitization (Fig. 3 of [187]) and the bottom image ruthenium particles on partially graphitized carbon (Fig. 3 of [45]).

The tendency towards more graphitic carbon structure is expressed by a higher ordering of the graphene sheets and a more ball-shaped structure. It is observed that the ordering of graphene sheets is visible in some TEM images but much better in tilt series videos. The reason for a better recognition in tilt videos is probably due to the human skill to reduce the SNR between successive images by following the details of the 3D structure for frame rates below about 5 fps (frames per second, see also Sec. 4.3).

Most particles I observed in the TEM, showed either a branched structure (as visible in e.g. Fig. 5.3) or a structure made up of grouped balls (e.g. Fig. 5.5). The ball-shaped structure shows graphene layers whereas the branched structure does not. Therefore, the shape can be regarded as an indirect indicator of more graphitic regions even if the resolution of the images or the tomogram is not sufficient to reveal graphene layers. Inspired by the impressions from the TEM images and Fig. 2 of [187] (Fig. 5.1) I would expect the formation of the ball-shaped structures to originate from fullerenes (buckyballs) on which further graphene sheets grow. The term 'onion layer' structure is used to express this property which is even visible in some tomograms (e.g. Fig. 5.5). As reported by Wissler [187] and as visible in tomograms (e.g. Fig. 5.5), the innermost part ($\varnothing \approx 10$ nm) of a ball is less ordered which might be due to tension caused by the outer shells crunching the inner fullerene.

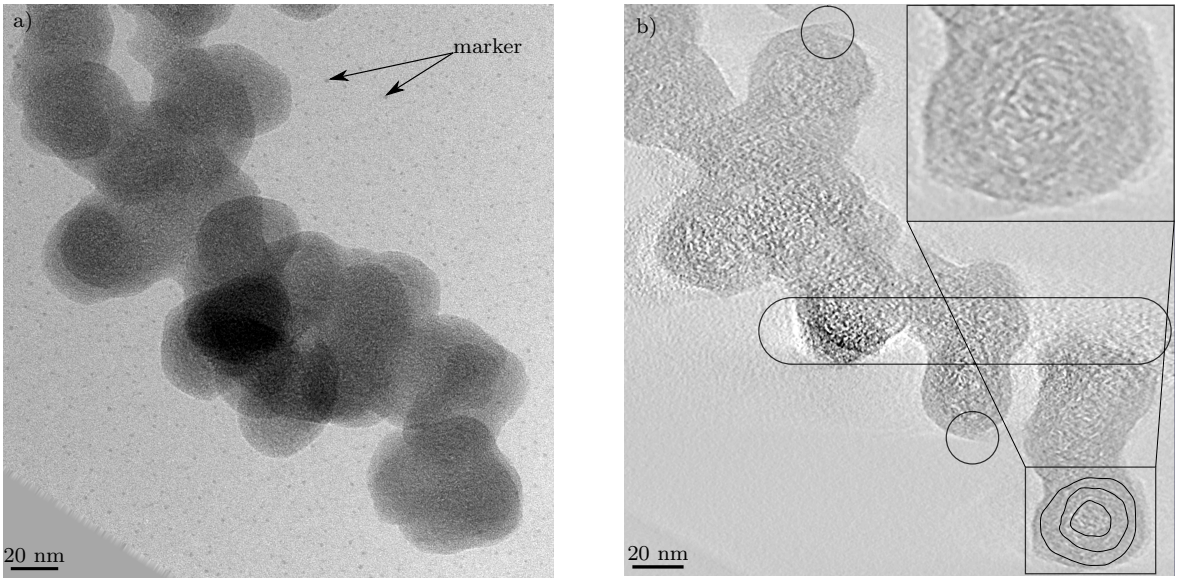

Figure 5.2: Sample type VC_{um}

Image a) shows a ZL-TEM image of a part of a VC_{um} particle. It sticks to a carbon foil with Au marker ($\varnothing \approx 2$ nm). The homogeneous grey area around the scale bar originates from the alignment of the image for the reconstruction. Image b) shows a slice of the WBP reconstruction. The circles mark the artefacts originating from contamination during acquisition of the tilt series. The oval marks a region that suffers from streak artefacts originating from the region of the sample where the thickness is larger than 100 nm (dark region in image a)). The thin lines indicate the slightly visible 'onion layer' structure.
ZL; $M = 63$ kX; 73° -> -66.5° @ 0.5°; $t = 8$ s; $\#_e \approx 16000$ e^-/nm^2; $s_p = 1.64$ Å; $P \approx 5 \cdot 10^{-8}$ mBar; no lN_2 used;

The overall sizes of the carbon particles vary from around 50 nm up to a few micrometer. However, most carbon particles would be characterized more precisely if instead of the overall extent, the width of a branch or a ball was regarded. Branches seem to range from 10 nm to 30 nm while balls are slightly larger, 40 nm to 60 nm. These sizes also match the ASAXS measurements of $\varnothing \approx 26$ nm [192] much better. Furthermore, the range corresponds to the most dominant image frequency of TEM images of these carbon particles, which is important for the optimization of the automated xy-z-tracking (see Chap. 4) during acquisition of tilt series of these samples.

The TEM images and tomographic slices I created of the different carbon support samples are presented in the following paragraphs. Some qualitative estimations and remarks are given as well.

VC_{um} The VC_{um} particle in Fig 5.2 exhibits the structure I refer to as the ball structure. In the tilt series video the 'onion layers' are also visible in other regions of the particle than indicated in Fig 5.2b by lines along the layers. No obvious impurities can be found. The circles mark the type of artefact that arises from contamination during acquisition of the tilt series (see Sec. 2). The thickness of the contamination can be estimated at around 3 nm to 5 nm between the first and the last image of the tilt series. Other particles of this type also contain parts that can be attributed to the branch structure (see e.g. Fig 5.5).

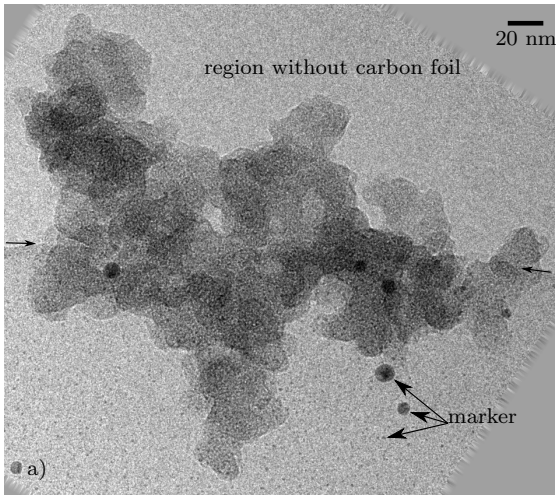

A ZL-TEM image of a BP_{um} particle is shown in a). The particle resides on a rim of the carbon foil with the Au marker. The rim of the foil is indicated by the arrows on the left and right side. Image b) shows a slice of a WBP dual tilt reconstruction. Image c) shows a slice of the DIRECTT reconstruction of a single tilt series. The circles mark impurities in the carbon particle. Although the pores are more distinct in b), the borders of the carbon particle are more distinct in c) This is obvious when the regions in the rectangles are compared.

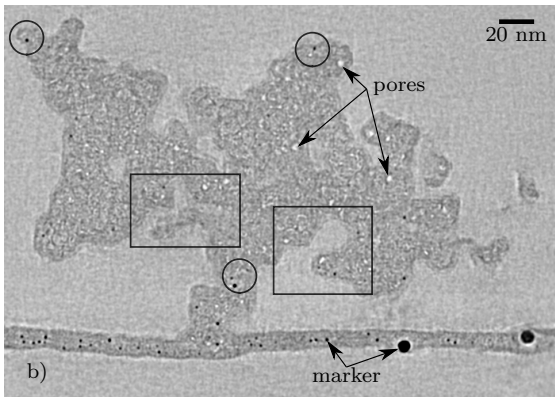

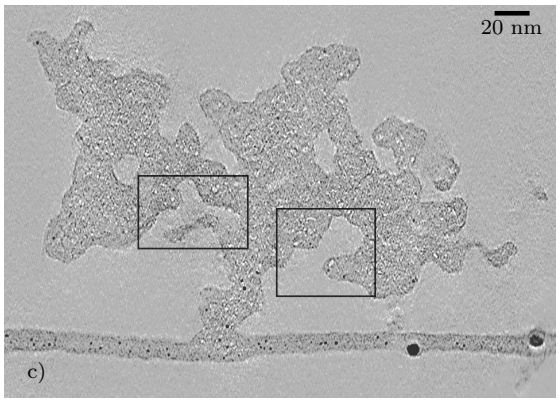

Figure 5.3: Sample type BP_{um}
ZL; $M = 63$ kX; -70° -> 74° and -71° -> 73° @ 1°; $t = 0.5$ s; $t_{xy} = 0.1$ s; $t_z = 0.25$ s $\#_e \approx 1200\,e^-/nm^2$; $s_p = 1.64$ Å; $\Delta f_f \approx$ -1.9 µm; $P \approx 1.1 \cdot 10^{-7}$ mBar; lN_2 used;

BP_{um} The BP_{um} particle in Fig 5.3 exhibits the structure I refer to as the branch structure. No 'onion layers' can be recognized not even in the tilt series video. Instead, it contains pores and impurities marked by arrows and circles in Fig 5.3b. Two tilt series could be acquired for this particle allowing for a dual tilt reconstruction (procedure explained in 4.3) with IMOD.
The contamination during acquisition of the tilt series is insignificant. However, a contamination layer of around 1 nm thickness originates from the electron dose during the alignment of the particle for the acquisition of the second tilt series. This change of the outer surface of the particle is probably the reason for the outer surface to be less distinct than the inner surface of the pores (Fig 5.3b).

Figure 5.3c shows the DIRECTT reconstruction of a single tilt series. It exhibits less noise/artefacts than the WBP dual tilt reconstruction but small particles are less round. Furthermore, the outer surface is much more distinct than in Fig 5.3c. However, this does not apply to the inner surface. The two DIRECTT reconstructions could not be matched (procedure explained in Sec. 4.3) to each other. Therefore, they could not be combined to yield a better base for the comparison with Fig 5.3b. Nevertheless, a DIRECTT reconstruction of a single tilt series already yields sharper borders than a WBP dual tilt reconstruction.

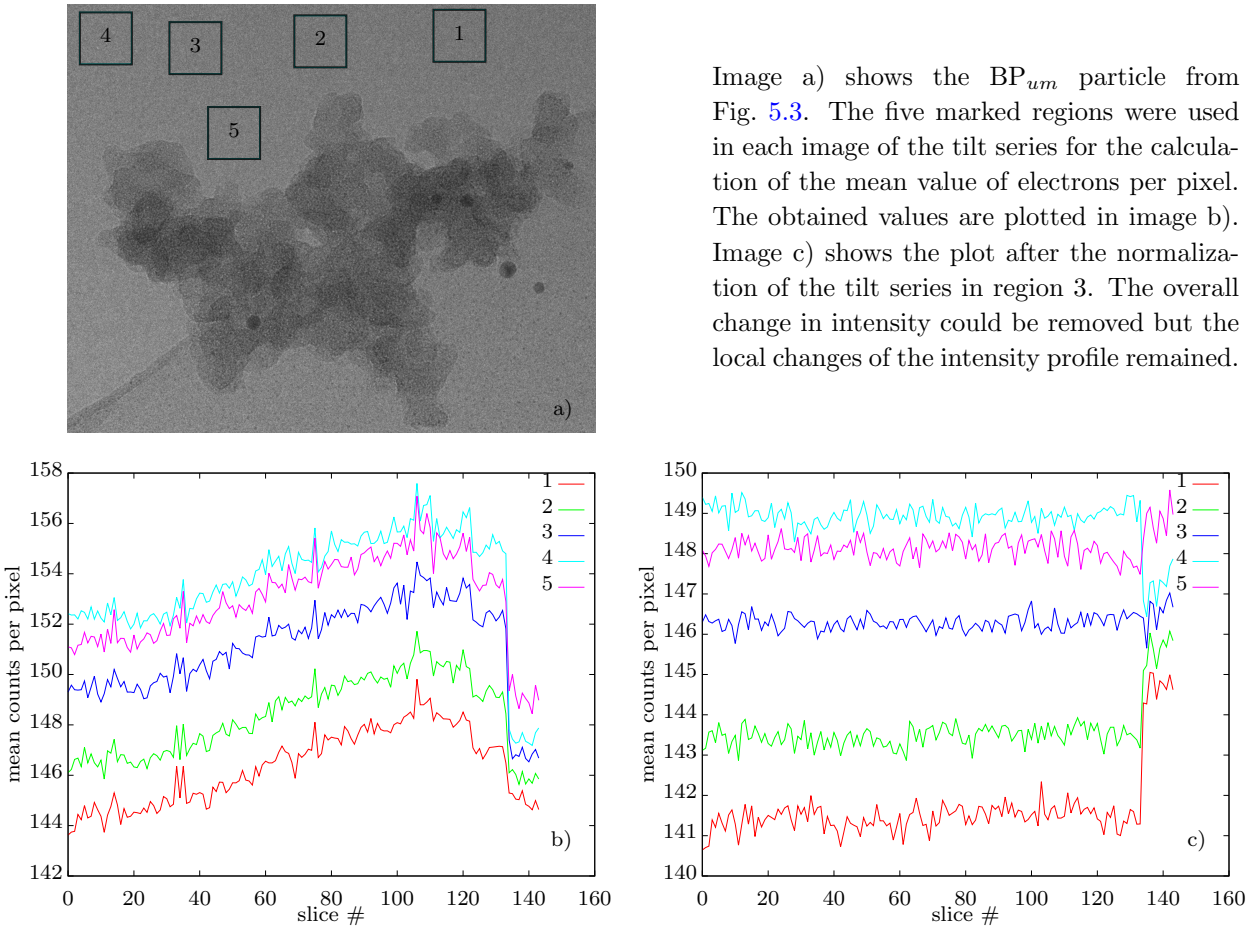

Image a) shows the BP_{um} particle from Fig. 5.3. The five marked regions were used in each image of the tilt series for the calculation of the mean value of electrons per pixel. The obtained values are plotted in image b). Image c) shows the plot after the normalization of the tilt series in region 3. The overall change in intensity could be removed but the local changes of the intensity profile remained.

Figure 5.4: Intensity profile and normalization

The particle resides on a rim of a broken carbon support film. This enabled me to check how the average beam intensity (i.e. current density J) and the intensity profile changed during acquisition of the tilt series. The measured mean intensities of five positions for each image of the tilt series are shown in Fig. 5.4. They vary slightly (up to 4 counts per pixel, i.e. about 3%) over the period of acquisition of the series up to the point of a manual intervention (at image # 134), which was necessary because the condenser aperture shadow entered the image due to illumination tracking. Illumination tracking corresponds to the displacement of the optical axis above the sample. It is synchronized with and governed by the displacement of the optical axis below the sample, i.e. the image-shift needed for xy-tracking (see Sec. 4.2). However, synchronization is controlled by DMG and can only be maintained for the tracking region in which both shifts are proportional to each other. When the applied image shift comes close to its limits (around 2 µm at 63 kX Fig. 4.2) the proportionality is not given any more, leading to the described desynchronization of the illumination and the image shift. Although no manual xy-tracking was necessary the intervention changed the average beam intensity. The illumination profile was influenced as well which can be concluded from the different order and spacing of the five measurement positions.

Figure Fig 5.4c shows the mean intensities of five positions after normalization of the tilt series images in region 3. Normalization means an adjustment of the brightness of the TEM images to a mean value. Thereby, the global change in brightness between

successive images is removed which is caused by intensity fluctuations of the electron beam. However, the local changes in brightness cannot be removed that are caused by a brightness gradient that is constant throughout series acquisition until manual interaction. The change of the beam intensity profile during acquisition, i.e. the fluctuations in each region can be neglected. The brightness gradient that is constant throughout acquisition could be removed by an image without the sample. However, the removal of the sample out of the imaged region can only be accomplished mechanically. Since this introduces significant backlash, it can only be done after the acquisition of the whole series. As described above, manual intervention causes a change in the brightness gradient such that a gradient correction is only possible if no manual intervention was necessary during acquisition of the tilt series. However, the measurement shows that the fluctuations in the intensity profile are sufficiently small, in regard to the present noise, to be ignored concerning binarization and image analysis of the resulting tomogram.

The current density $J \approx 2400$ e$^-$/nm^2/s is not constant over the profile of the electron beam. It varies by about 160 e$^-$/nm^2/s (7%). The approximate electron dose on the sample per image is $D_i \approx 1200$ e$^-$/nm^2 and lies in the range reported by Kübel et al. [90]. These are no low-dose conditions. However, the noise of the images was already high for the reconstruction by DIRECTT.[2)] The total dose on the sample over the acquisition of one tilt series (145 images) is therefore $D_t \approx 2400 \cdot (2 \cdot 0.1 + 2 \cdot 0.25 + 0.5) \cdot 145$ e$^-$/nm^2 $\approx 418 \cdot 10^3$ e$^-$/nm^2 of which 58% are from the additional images needed for the tracking. The TEM tomogram example of Reimer and Kohl [146, Fig. 6.37, p. 261] only lead to a total dose of 2000 e$^-$/nm^2 but was reconstructed only from 19 projections and refined by single-particle reconstruction (see e.g. [35; 114]).

In App. A.2 the resolution of the dual tilt reconstruction is estimated by means of the Fourier Shell Correlation (FSC) and the 2σ-threshold curve is found to be approximately 12 Å. To what extend this is an appropriate resolution estimate and that the resolution might be underestimated is discussed in Sec. 6.3 and in full detail in the literature, e.g. [177; 104; 52; 33].

VC$_{CO_2}$ The VC$_{CO_2}$ particle in Fig 5.5a exhibits both the ball and the branch structure. A slight difference in contrast and structure pattern between ball and branch structure can be seen in Fig 5.2b. It seems as if the ball structure originates from seven buckyballs. The 'onion layers' are visible in Fig 5.2c. Only the branch structure contains impurities. The sample became contaminated during acquisition which caused contamination artefacts. The thickness of the contamination varies between 1 nm and 10 nm over the particle. The CO_2 treatment seems not to have had any obvious effect. Other particles of this type show a difference to VC$_{um}$, possibly caused by the CO_2 treatment. However, only the branch structure seems to be effected.

BP$_{CO_2}$ The BP$_{CO_2}$ particle in Fig 5.6a exhibits only the branch structure as it is typical for BP carbon. The CO_2 treatment seems to have had an effect since the surface of the particle is less even than it usually is for BP$_{um}$. Impurities are found mainly on the outer surface.

[2)] According to A. Lange (BAM) DIRECTT expert.

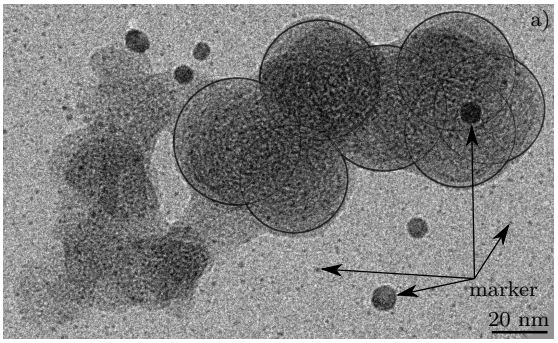

A ZL-TEM image of a VC_{CO_2} particle is shown in a). The right part consists of the ball structure (marked by seven circles) and the left part of the branch structure. There are Au marker with different sizes on the carbon foil. Two slices of a WBP reconstruction are shown in b) and c). Impurities can be found in the branch structure. The onion layer are best visible in c). The rectangles mark contamination artefacts. The black lines in c) indicate the surface of the particle before contamination.

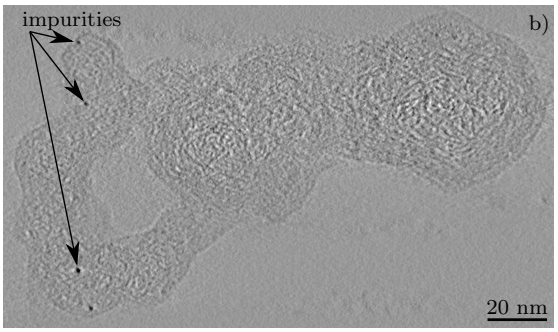

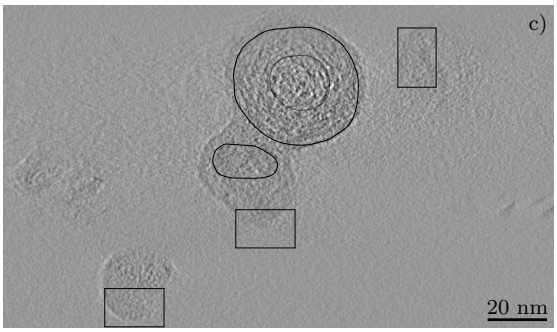

Figure 5.5: Sample type VC_{CO_2}
ZL; M = 80 kX; -72.0° -> 69.5° @ 0.5°; t = 1 s; $\#_e \approx$ 1700 e$^-$/nm^2; s_p = 1.16 Å; $\Delta f_f \approx$ -2 µm;

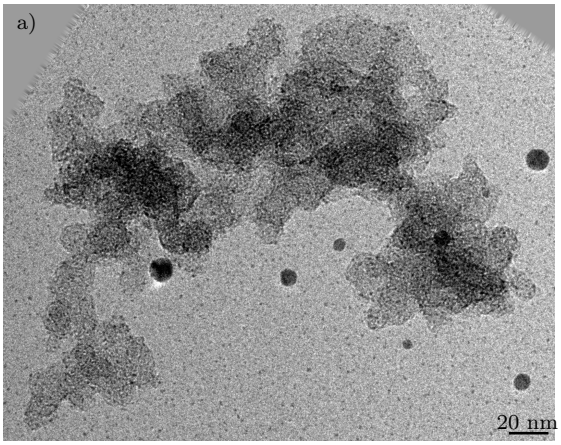

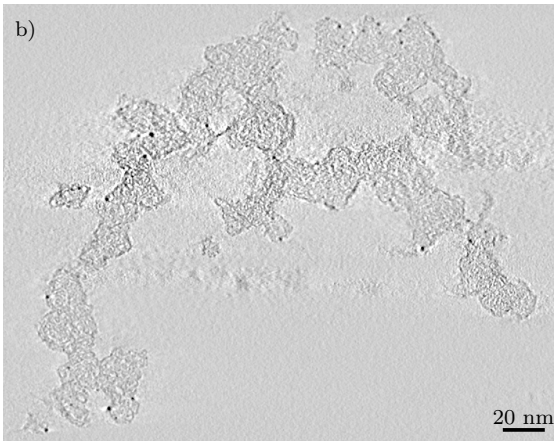

Figure 5.6: Sample type BP_{CO_2}
A ZL-TEM image of a BP_{CO_2} particle is shown in a). The surface of its branch structure is less even than for BP_{um}. This is also visible in the tomographic slice of the WBP reconstruction, b). Impurities are found mainly on the outer surface.
ZL; M = 63 kX; -68° -> 67° @ 1°; t = 1 s; $\#_e \approx$ 2400 e$^-$/nm^2; s_p = 1.64 Å; $\Delta f_f \approx$ -2.4 µm;

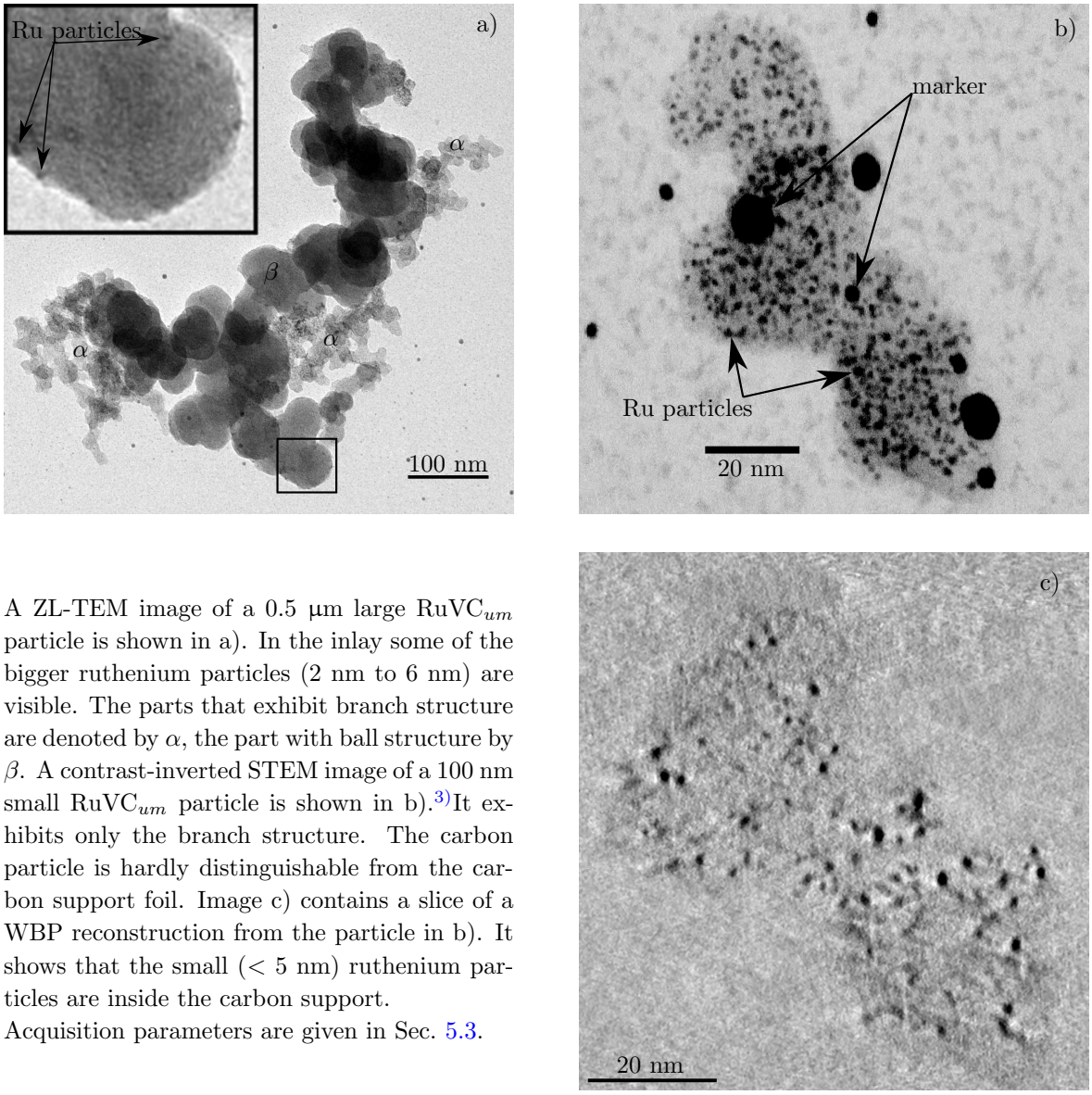

A ZL-TEM image of a 0.5 µm large $RuVC_{um}$ particle is shown in a). In the inlay some of the bigger ruthenium particles (2 nm to 6 nm) are visible. The parts that exhibit branch structure are denoted by α, the part with ball structure by β. A contrast-inverted STEM image of a 100 nm small $RuVC_{um}$ particle is shown in b).[3)] It exhibits only the branch structure. The carbon particle is hardly distinguishable from the carbon support foil. Image c) contains a slice of a WBP reconstruction from the particle in b). It shows that the small (< 5 nm) ruthenium particles are inside the carbon support.
Acquisition parameters are given in Sec. 5.3.

Figure 5.7: Sample type $RuVC_{um}$

5.2 Sample particles with ruthenium

In the following paragraphs, the different carbon support samples containing ruthenium are presented by TEM images and tomographic slices. Some qualitative estimations and comparisons are given.

$RuVC_{um}$ The $RuVC_{um}$ particle in Fig. 5.7a exhibits both the ball and the branch structure whereas the $RuVC_{um}$ particle in Fig. 5.7b only exhibits the branch structure. In the reconstruction slice (Fig. 5.7c) the carbon can hardly be distinguished from empty space. This shows that STEM is not well suited to image the carbon particle.

[3)] This STEM data set was acquired with a FEI Tecnai F20-G2 TEM at the Electron Microscopy Group in the Department of Materials Science & Metallurgy, University of Cambridgein with the help of J.C. Hernandez-Garrido.

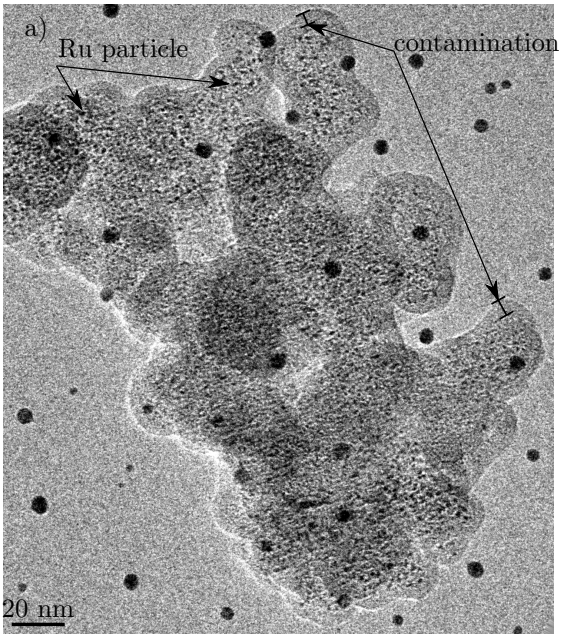

ZL-TEM images of RuBP$_{um}$ particles are shown in a) and b). The branch structure of the carbon seems unaffected by the ruthenium treatment (compare with Fig. 5.3). Many ruthenium particles can be seen in a). The thickness of the contamination during the acquisition was between 5 nm and 10 nm. Image c) shows a WBP reconstruction slice of the particle in b). The ruthenium particles are mostly inside the carbon support. The rectangle marks the region of a contamination artefact.

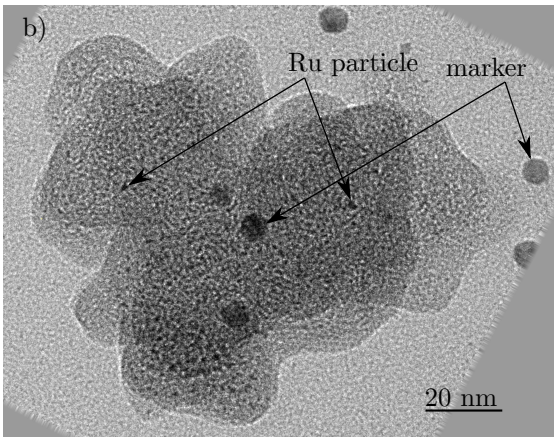

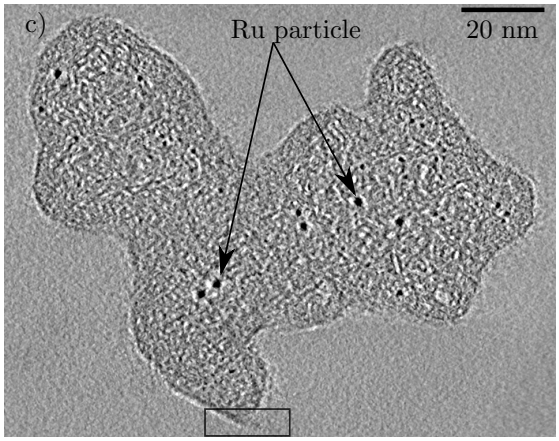

Figure 5.8: Sample type RuBP$_{um}$
ZL; M = 160 kX; 67.0° -> -70.5° @ 0.5°; $\#_e \approx$ 17000 e$^-$/nm^2; s_p = 0.7 Å; $P \approx 8.8 \cdot 10^{-8}$ mBar

However, the contrast difference between empty space and carbon suffices to conclude that the ruthenium particles are mostly inside the support of the branch structure. The sizes of the ruthenium particles range from 1 nm to 4 nm.

The particles shown in Fig. 2.3 and Fig. 5.11 also belong to this sample type. They also exhibit both the ball and the branch structure which is typical for VC particles. RuVC$_{um}$ is therefore analysed in more detail in Sec. 5.3.

RuBP$_{um}$ The RuBP$_{um}$ particles in Fig. 5.8a and Fig. 5.8b exhibit only the branch structure. They contain many ruthenium particles inside the carbon support. The sizes of the ruthenium particles range from 1 nm to 4 nm. The contamination layer is between 5 nm and 10 nm thick. This creates the impression in Fig. 5.8a that ruthenium particles are only found a few nanometres away from the carbon surface. However, the ruthenium particles reach up to the surface of the carbon support before contamination has built up during acquisition.

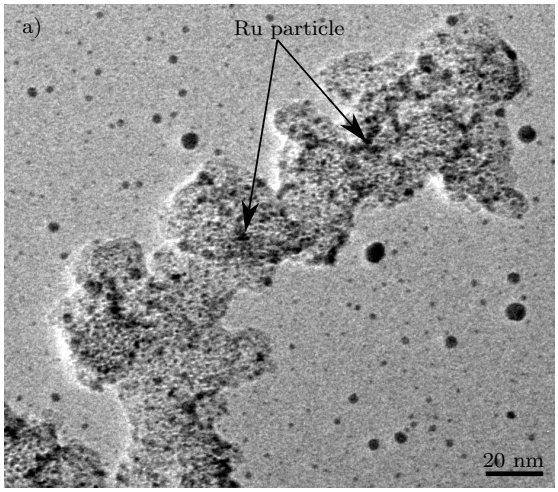

A ZL-TEM image of a part from a $RuVC_{CO_2}$ particle is shown in a). It only exhibits the branch structure. The WBP reconstruction slice in b) shows less and smaller ruthenium particles than the DIRECTT reconstruction slice in c). There are many ruthenium particles inside but also on the support. The sizes of the ruthenium particles inside range from 1 nm to 5 nm, whereas those on the support range from 5 nm to 15 nm.

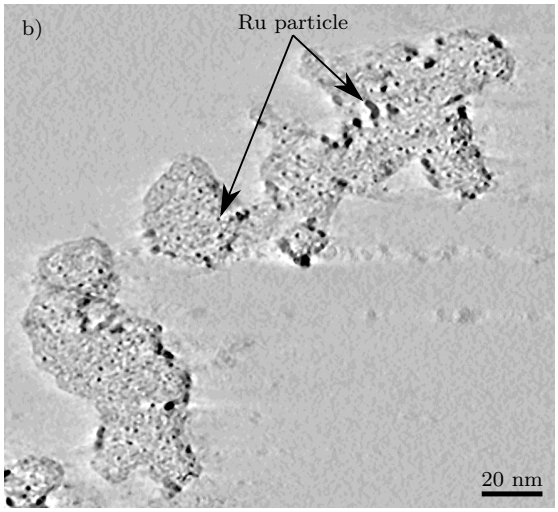

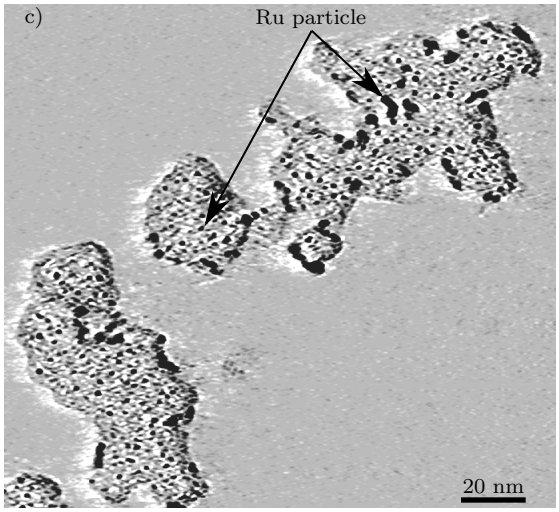

Figure 5.9: Sample type $RuVC_{CO_2}$
BF; M = 50 kX; -67° -> 73° @ 1°; t = 4 s; $\#_e \approx$ 13000 e^-/nm^2; s_p = 2.07 Å; $\Delta f_f \approx$ -1.5 µm;

$RuVC_{CO_2}$ The $RuVC_{CO_2}$ particle in Fig. 5.9a exhibits only the branch structure. The carbon is not obviously affected by the ruthenium treatment. The support particle contains many ruthenium particles not only inside but also on the carbon support. The WBP reconstruction slice in Fig. 5.9b shows less and smaller ruthenium particles than the DIRECTT reconstruction slice Fig. 5.9c. The sizes of the ruthenium particles inside range from 1 nm to 5 nm, whereas those on the support range from 5 nm to 15 nm. The maximum size of ruthenium particles on $RuVC_{um}$ particles seems lower than the maximum size of ruthenium particles on this CO_2-treated support particle.

Kübel et al. [92] found that the grey values in WBP reconstructions depend on the particle size. However, this seems not to be the case for DIRECTT reconstructions (see App. A.3). This is an explanation for the additional particles found in the DIRECTT reconstruction which are all very small ($\varnothing < 4$ nm). If the dependence found by Kübel et al. [92] also leads to a less steep transition in the intensity profile between particle and its surrounding this would also explain the increase in size of the particles in the DIRECTT reconstruction. However, the qualitative comparison here would not suffice to validate this.

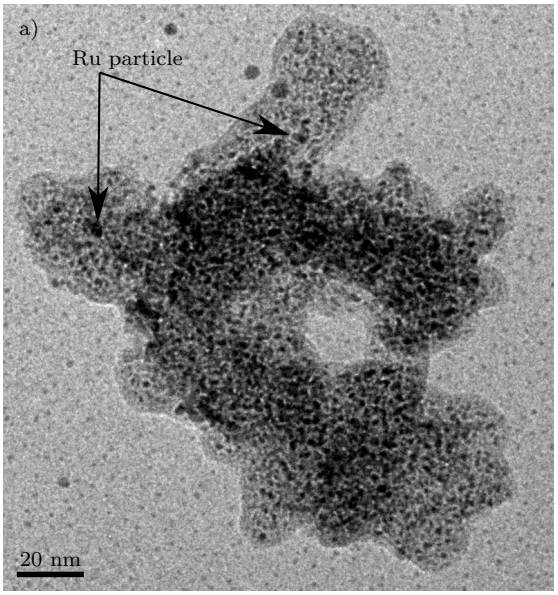

A ZL-TEM image of a $RuBp_{CO_2}$ particle is shown in a). It only exhibits the branch structure. The WBP reconstruction slice in b) shows smaller ruthenium particles than the DIRECTT reconstruction slice in c). Most ruthenium particles are inside the support. The sizes of the ruthenium particles range from 1 nm to 10 nm.

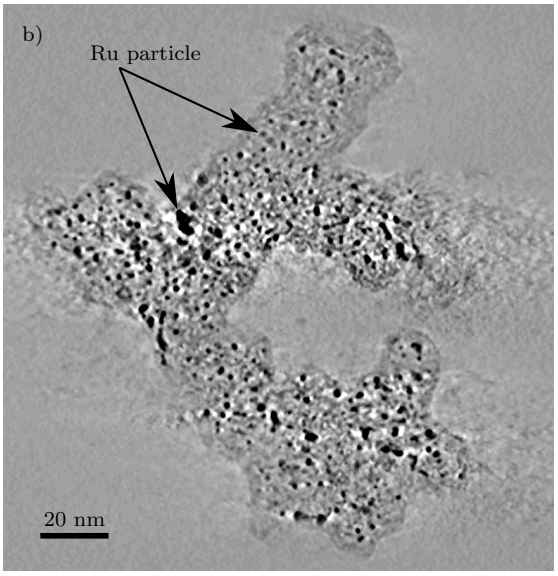

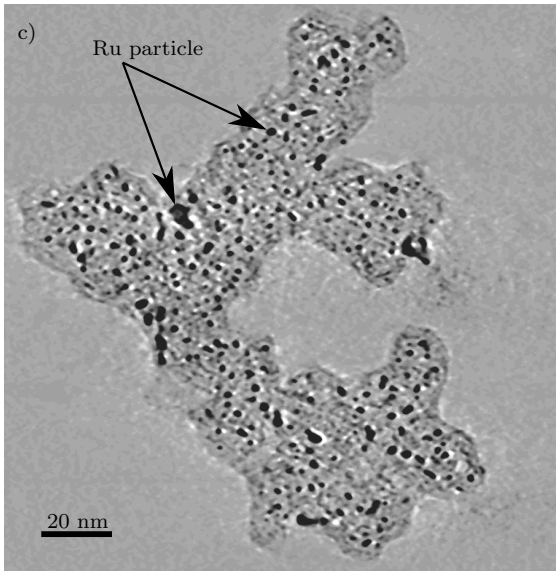

Figure 5.10: Sample type $RuBP_{CO_2}$
ZL; $M = 50$ kX; 62° -> -70° @ 1°; $t = 2$ s; $\#_e \approx 3900$ e$^-$/nm^2; $s_p = 2.07$ Å;

$RuBP_{CO_2}$ The $RuBP_{CO_2}$ particle in Fig. 5.10a exhibits only the branch structure. Neither the ruthenium treatment nor the CO_2 treatment had an obvious effect on the carbon support. The surface is not as rough as the surface of the BP_{CO_2} particle in Fig. 5.6. However, as it is the case with $RuVC_{CO_2}$, bigger ruthenium particles exist compared to $RuBP_{um}$ (Fig. 5.8). The sizes of the ruthenium particles range from 1 nm to 10 nm.

The WBP reconstruction slice in Fig. 5.10b shows again less and smaller ruthenium particles than the DIRECTT reconstruction slice in Fig. 5.10c. However, the difference is not as pronounced as in Fig. 5.9.

5.3 Detailed analysis of $RuVC_{um}$

The sample $RuVC_{um}$ has a high amount of ruthenium particles on the outer surface of the support. The structure of $RuVC_{um}$ turned out to be unique within the set of the sample types studied and is expected to have a strong influence on the catalytic effectiveness compared to the other samples. Therefore, the details of the tomographic analysis are explained on this sample.

First, the properties of the ruthenium and the carbon segments without any structural dependence are characterized. My analysis of the structures follows. It is divided into three parts: Evaluation of the particles of the ruthenium segment, the structure of the carbon segment and the relation between ruthenium particles and carbon support.

Figure 5.11 shows an image from the tilt series of the $RuVC_{um}$ particle, referred to as 'the poodle'[4)]. The TEM Bright Field (BF) images were taken at 200 keV while the sample was tilted from -69° to 74° with an angular increment of 1°. The total dose on the sample during the acquisition was $D_t \approx 4000 \cdot 10^3$ e^-/nm^2. Although the additional dose before acquisition was around $15000 \cdot 10^3$ e^-/nm^2, no contamination or any other beam damage could be observed. Automated tracking during acquisition, image alignment with IMOD and reconstruction were done as described in Chap. 4. The DIRECTT reconstruction shows a significant improvement concerning the spatial resolution and the suppression of streak artefacts (see Fig. 4.7). A reliable analysis of the IMOD-WPB or IMOD-SIRT reconstructions was not possible (see Sec. 5.3.4.5 and Fig. A.8). Computer analysis of the binarized tomogram segments enables global measurements concerning ruthenium and carbon and also measurements of each individual ruthenium particle. The digital analysis was carried out with the Insight Toolkit[2] (ITK), the Visualization Toolkit[3] (VTK), octave[5], gnuplot[6] and rendered with Blender[4].

5.3.1 Visual Assessment

Figure 5.11 shows a BF-TEM image of ruthenium catalyst nanoparticles (small dark spots) distributed over an agglomerate of Vulcan® XC-72 carbon black support (marked by arrow A) deposited on carbon foil with fiducial markers. The carbon particle in Fig. 5.11 consists mainly of two fractions which differ by their appearance and degree of graphitization. Larger branches of onion-like structure with diameters of around 50 nm (mostly on the left side of arrow A) are combined with smaller amorphous-like constituents forming irregular aggregates varying from 10 nm to 30 nm in width (mostly on the right side of arrow A). The much smaller ruthenium particles range from 1 nm to 5 nm in size (see arrows B and inset) and are spread over the surface of the carbon support. Fiducial gold markers are visible as separate spherical dots on the support foil (marked by arrow C) and were used for image alignment.

[4)] I use the association with a poodle since it allows not only to refer to this particular particle but also to specify parts of the particle.

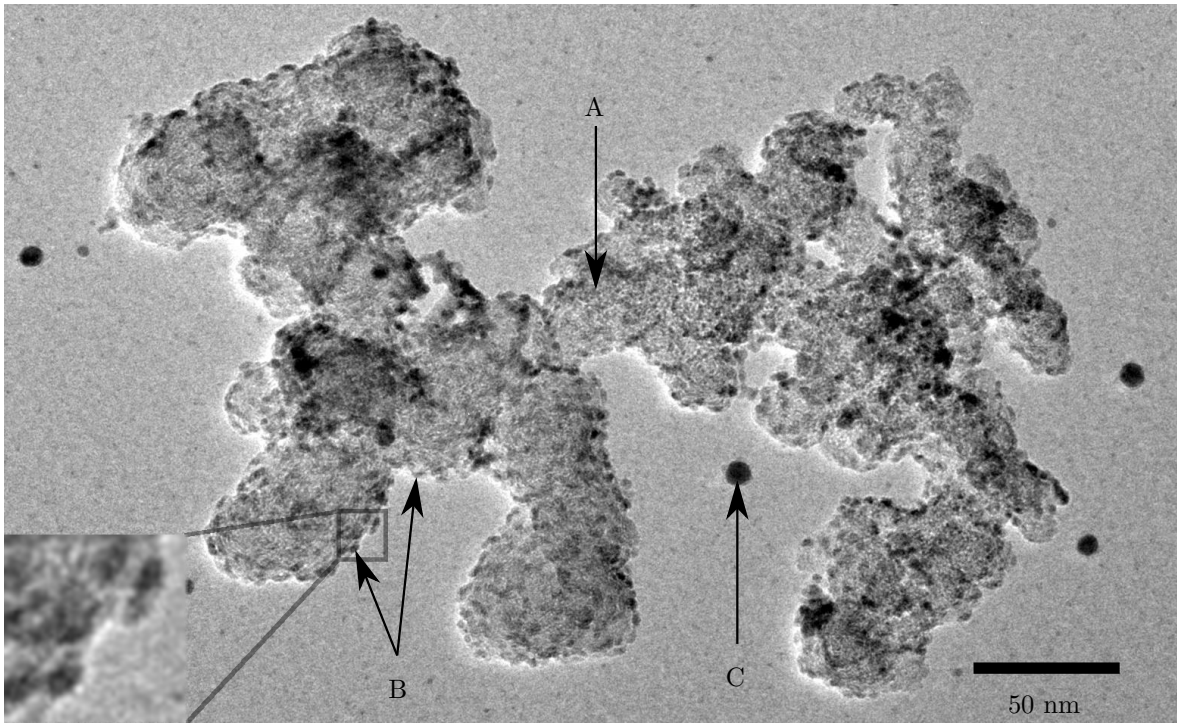

Figure 5.11: Bright field image of a $RuVC_{um}$ particle

Bright field TEM image of a $RuVC_{um}$ catalyst particle (named the poodle) showing ruthenium nanoparticles as dark spots (marked by arrows B) supported by a Vulcan® XC-72R carbon black agglomerate (marked by arrow A). Many ruthenium particles are situated on the outer surface of the carbon particle. To the right of arrow A the C-particle is more amorphous while to the left it has a more graphitic character. Arrow C points at a fiducial gold marker for the image alignment.

Figure 5.12 shows a cross section through the median-filtered tomogram and segments of the sample presented. A 3D median filter (with a kernel of 5x5x5) was needed to reduce noise. Most of the ruthenium particles are located on the outer surface of the carbon support and are partially embedded. This is typical for onion-like structured carbon regions. Some ruthenium particles can also be found inside the carbon matrix (see images on the right in Fig. 5.12). These particles are much smaller than those on the surface. However, they can only be found at some locations. This observation is further evaluated in Sec. 5.3.5.1. The carbon support foil is about (8 ± 1) nm thick, measured from the tomogram.

Figure 5.12: Cross section through the reconstructed tomogram

The upper image shows a cross section through the whole tomogram (contrast inverted, scale bar 60 nm); red marks the regions that have a more amorphous-like carbon structure, the other carbon possibly has a more graphitic character. The middle images show the framed regions of the two different structures in magnification. The result of segmentation is shown in the bottom images. Carbon segment (black), ruthenium segment (green), the pore segment (diameter less than 5 nm, grey, needed in sec. 5.3.5.1) and the surrounding empty space (white) of the tomogram.
BF; $M = 40$ kX; 74° -> -69° @ 1°; $\xi = 310$ µrad; $t = 0.5$ s; $\#_e \approx 25000$ e^-/nm^2; $s_p = 2.6$ Å; no lN_2 used;

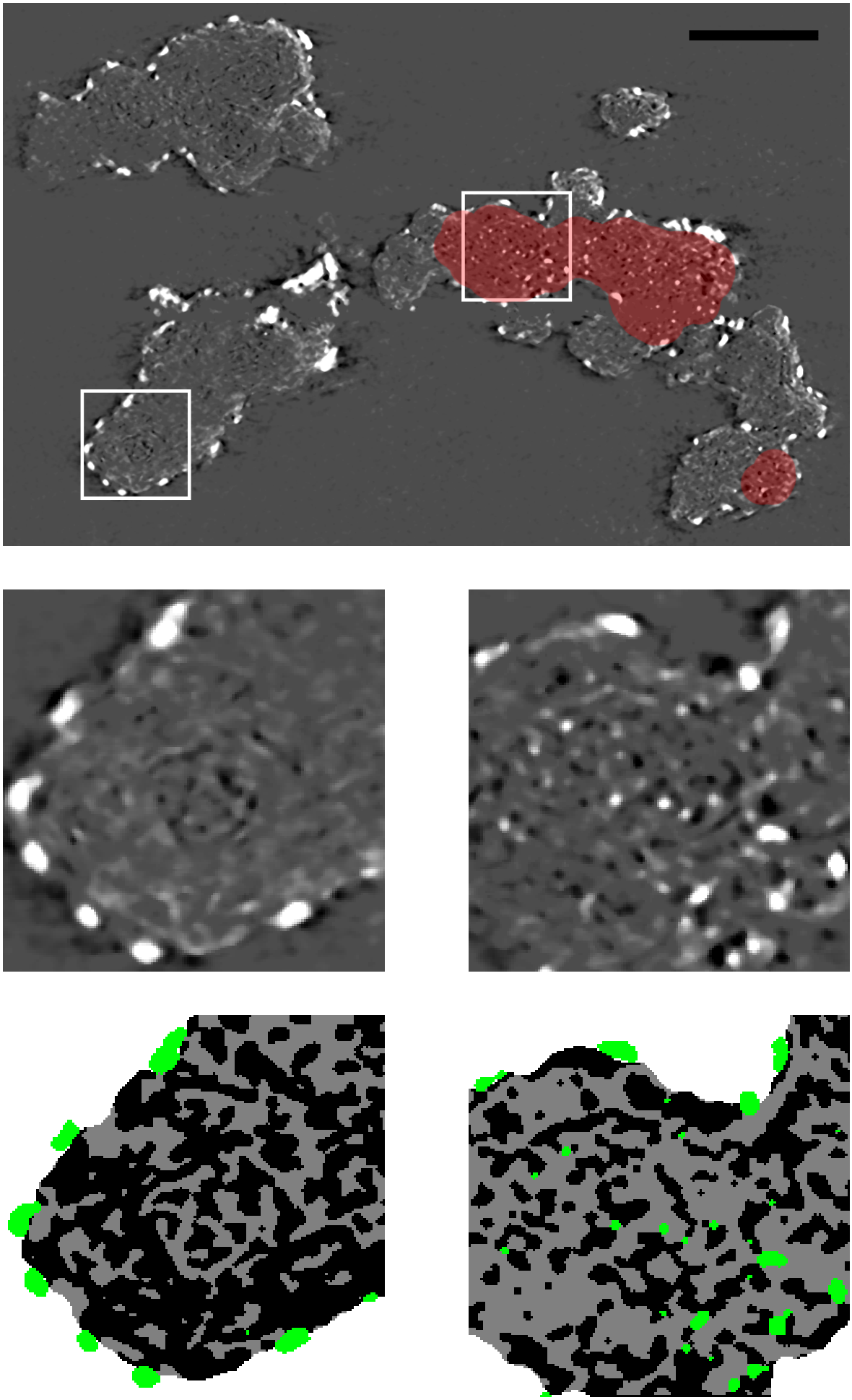

Figure caption on the opposite page

5.3.2 Creation of the ruthenium and carbon segments

The ruthenium segment in the DIRECTT reconstruction can be determined by the Otsu threshold criterion [135], which yields the lower threshold for the ruthenium segment. There is no need for an upper threshold. This way the segmentation of the ruthenium does not depend on operator decisions but is rather based on objective criteria. An adaptive threshold depending on the feature size, as described in Ref. [92], was not used because a dependence of the grey values on the feature size could not be observed in the DIRECTT reconstruction (see App. A.3). This is probably due to the nature of the reconstruction method of DIRECTT. However, the median filter introduced such a dependence for particles sizes below the kernel size (Fig. A.3). Therefore, more small particles (⌀ below ≈ 1 nm) should be expected in the sample than were actually accounted for in the following evaluations. The presented results are only valid for particles above about 1 nm. The small particles that are prone to error concerning shape were disregarded in any evaluation after Sec. 5.3.4.2 because they lack a sufficient resolution.

Although the DIRECTT reconstruction has fewer artefacts, some ruthenium particles that are very close to each other are probably connected because of limited spatial resolution. Therefore, the particles were separated by a filter chain consisting of two distance map evaluations and a watershed transformation as described in Sec. 3.2.[5)] The watershed algorithm used did not introduce walls [18; 20] so that the overall ruthenium segment was not changed. The second distance map filter was inserted to control over- and under-segmentation by an edge error of 2 voxels and a separation error of 6 voxels Sec. 3.2.1 and 3.2.2. The result of this filter chain is more realistic concerning amount, size and shape of the ruthenium particles in regard to the impression given by the original TEM images. Except for the watershed separation, which neither moved nor removed nor added voxels to the ruthenium segment, no further filtering was needed. The difference between the labels created by a mere interconnectivity criterion and those resulting from the watershed separation can be seen in Fig. A.6.

The upper threshold for the empty space was determined from the histogram of the tomogram. The carbon segment was created from the grey values between the vacuum segment and the ruthenium segment. However, this unmodified segment was significantly influenced by streak artefacts. A manual selection of the regions assigned to the carbon segment –as it is still common practice for electron tomograms [73; 52; 14; 189; 16]– would have been inappropriate for two reasons: It would have introduced strong personal bias and would have been very time-consuming considering the fine structure of the support and the size of the data set (1350x950x660 voxels). Therefore, I decided to remove the artefacts by fine adjusted selective filtering, still time-consuming but by far less prone to personal bias. The main idea of my filter chain is to create a mask, originating from a smaller range of grey values, that is modified before it is used for the removal of the artefacts of the actual carbon segment.

[5)] The whole dataset had to be cropped/trimmed as much as possible to reduce the size of the dataset down to 1350x950x660 voxel since otherwise the virtual memory of already about 120 GB would not have been sufficient for the computation of the Danielson distance map.

A morphological closing filter [162] followed by an opening filter [162] was applied to the mask to extend it by the regions of actual carbon that were missing because of the reduced grey value range. The significance of the filter order is demonstrated in Fig. A.1.

Most ruthenium particles are surrounded by a very thin layer of carbon grey values. This could originate from a very faint contamination before or during acquisition of the tilt series in the TEM. Another source could be remnants of the solvent from the TEM sample preparation or even from production. However, the layers could also be reconstruction artefacts. The layer was removed (see Fig. 5.13) where it is only up to two voxels (about 0.5 nm) thick since contamination definitely contributed. A cross section through the tomogram segments after the removal of reconstruction artefacts is shown at the bottom of Fig. 5.12.

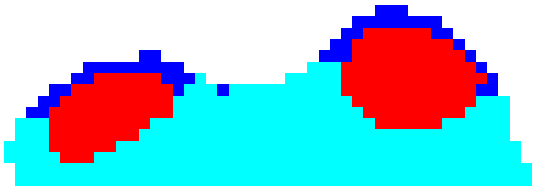

Figure 5.13: Removal of the carbon layer covering the ruthenium particles

The removal of the ruthenium cover is visualized by cross sections overlaid in RGB-channels. The red channel is used for the ruthenium segment, the blue channel shows the carbon support before local removal of thin carbon cover of ruthenium particles and the green channel contains the result after the local removal of the thin carbon cover. The unaffected regions of the carbon segment are therefore coloured in cyan. The removal is achieved by local opening of the carbon around the ruthenium particles (blue). For better visibility black was changed to white.

Although I was able to avoid manual segmentation, the fine adjusted filtering introduces personal judgement as well. This is caused either by the type and order of filter in the chain, or by the parameters chosen for the filters. A possible method to check how realistic the segmentations are is to re-project the final carbon and ruthenium segments and then to compare the obtained images with the original images of the tilt series. The binary segments have to be assigned an appropriate grey value before they are combined to form a discrete tomogram of just three values for empty space, carbon and ruthenium. This tomogram can then be projected in the directions of the original images and compared by their differences. The mean and variance of these difference images can be used as figure of merit for a quantitative evaluation of the overall influence of the many filters applied to the original tomogram. However, the evaluation would have to consider the contribution to the mean and variance of the difference images that are already present for the reprojections of the unmodified tomogram (as used in the SIRT reconstruction algorithm).[6)]

5.3.3 Measurements of the carbon and ruthenium segments

The carbon segment

The carbon soot usually used as a conductive and inert support for catalytically active metallic nanoparticles is a highly porous material. Since the contrast between carbon and the surrounding empty space is not high and the pores within the carbon matrix can

[6)] Although a program for such an evaluation was created, it could not be applied because the filtered segments were cropped and rotated manually prior to filtering, making it impossible to find the exact original position in the dataset corresponding to the tilt series.

be very small, the representation of the pores is less accurate than the representation of the overall contour of the carbon support.

Voids inside the carbon matrix with wall distances of less than 5 nm were regarded as 'pores'. A morphological closing operation [162] was applied to the carbon segment to create a carbon representation without pores. After the closing operation three small voids inside the carbon are left. Yet, more important is that the outer surface remains largely unchanged. These two representations enable me to discriminate between outer and inner surface of the carbon structure. Based on this, the carbon support particle from Fig. 5.11 has a volume of $V_{op} \approx 10.8 \cdot 10^5$ nm^3 (volume with open pores) and a total surface area of $S_{op} \approx 12.3 \cdot 10^5$ nm^2. Through the closing operation, the volume increases by 52% to $V_{cp} \approx 16.4 \cdot 10^5$ nm^3 (volume with closed pores) while the surface decreases to $S_{cp} \approx 2.69 \cdot 10^5$ nm^2. The pore volume then is: $V_p = V_{cp} - V_{op} \approx 5.6 \cdot 10^5$ nm^3; and the corresponding pore surface: $S_p = S_{op} - S_{cp} \approx 9.61 \cdot 10^5$ nm^2. The ratio of the inner surface to the outer surface is $S_p/S_{cp} \approx 3.6$, and the surface-to-volume ratios are $S_{op}/V_{op} \approx 1.14$ nm^{-1}; $S_{cp}/V_{cp} \approx 0.16$ nm^{-1}. These values are a measure of the surface roughness of the carbon support. The larger the roughness, the more sites/surfaces there are for ruthenium particles to grow. The less carbon volume necessary for this, the better is the packing of the whole structure with ruthenium particles. However, a very high packing would be counter-productive since then the ruthenium particles will be less likely reached by the reactants during catalysis. In the extreme case the ruthenium particles would grow together starting to form a film causing a loss in surface area.

The ruthenium segment

Before separation (see Sec. 5.3.2, denoted by 'bs') there are about 2600 ruthenium particles with a particle volume of at least 64 voxel ≈ 1.12 nm^3. The total Ru volume is $V_{bs} \approx 1.1 \cdot 10^5$ nm^3 and the surface $S_{bs} \approx 2.03 \cdot 10^5$ nm^2.

The ruthenium surface not covered by carbon (denoted by 'ubs': uncovered, before separation, evaluation described in Sec. 5.3.6.1) computes to $S_{ubs} \approx 0.74 \cdot 10^5$ nm^2, which is about 36% of the total ruthenium surface S_{bs}. This ratio of uncovered ruthenium surface to the total ruthenium surface (named Σ) is the key quantity for the effectiveness of the catalyst and will be further discussed in section 6.2.

After separation (denoted by 'as'), there are about 5700 ruthenium particles (again V > 64 voxel ≈ 1.12 nm^3) and a total ruthenium volume of $V_{as} \approx 1.1 \cdot 10^5$ nm^3. Since no voxels are removed by the watershed algorithm chosen, the overall ruthenium volume is not changed. The surface, however, is increased by 11% to $S_{as} \approx 2.25 \cdot 10^5$ nm^2 due to the boundary surface introduced. It is unclear, though, if this additional surface area is realistic. Even if, its contribution to catalysis would probably be insignificant because the distance to the nearby particles is too small to allow for good accessibility of this additional surface by the reactants. Therefore, in addition to Σ, I use S_{bs} and S_{ubs} for the calculation of the following values, which I think are important for a comparison with other catalysts of similar type:

- Γ: The amount of uncovered ruthenium surface per unit support surface characterizes the degree of utilization of available support surface,
- Θ: The amount of uncovered ruthenium surface per unit Ru/C catalyst volume can be used for the evaluation of space needed when loading the cathode up to a specific catalytic active surface,
- Ξ: The amount of uncovered ruthenium surface related to the mass of the Ru/C catalyst is a more convenient measure when preparing materials for catalyst production.[7)]

For the $RuVC_{um}$ sample these quantities evaluate to:
$\Sigma = S_{ubs}/S_{bs} = 36\%$,
$\Gamma = S_{ubs}/S_{op} = 6\%$,
$\Theta = S_{ubs}/(V_{cp} + V_{bs}) = 0.04\ \mathrm{nm}^{-1}$ and
$\Xi = S_{ubs}/(\rho_C V_{op} + \rho_{Ru} V_{bs}) = 0.02\ \mathrm{nm}^2/\mathrm{g}$.

I use V_{cp} for these calculations since the volume in the pores has to be regarded as occupied in macroscopic considerations. For macroscopic estimations, Θ still needs to be related to the volume between particles (characteristic for the used carbon soot powder). I used the density of Ru: $\rho_{Ru} = 12.37\ \mathrm{g/cm^3}$ and a density of graphite: $\rho_C = 2.25\ \mathrm{g/cm^3}$ [187]. V_{op} and the density of graphite are used because the density of graphite varies less than that of amorphous carbon which would be needed with V_{cp}.

5.3.4 Characterization of the ruthenium particles

Since the ruthenium segment represents a composition of many particles, these particle representations, referred to as labels after the watershed separation, are studied in more detail.

The evaluation of the sphericity c_p of the ruthenium particles (Sec. 5.3.4.1) gauges the extent to which a size distribution makes sense under the assumption of spherical symmetry (Sec. 5.3.4.2). The result motivates analyses of shape by fitting of ellipsoids (Sec. 5.3.4.3).
The size distribution –although the particles are mostly non-spherical (see Fig. 5.11 and 5.12)– allows for a comparison with the results obtained by other methods such as X-ray diffraction (XRD) and anomalous small-angle X-ray scattering (ASAXS) (Sec. 6.2) which were based on spherical approximations.
The actual deviation from spherical symmetry motivates further evaluation of the local and global orientation of the particles (Sec. 5.3.6.2 and Sec. 5.3.4.5) which is made possible through the ellipsoidal analysis developed in Sec. 3.1. This is useful because the spatial distribution discussed in Sec. 5.3.4.7 of the different shape types identified by the ellipsoidal analysis can be related to the morphology of the carbon support particle (Sec. 5.3.5.1).

[7)] This is a different quantity than the 'local catalyst loading' as reported by e.g. Midgley et al. [125] where the mass of catalyst per support surface area is evaluated. There is no distinction between total and uncovered catalyst surface in the 'local catalyst loading'.

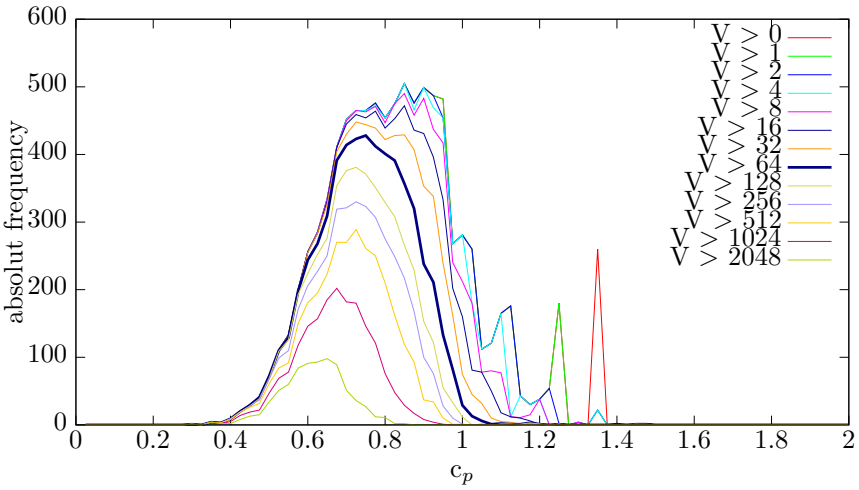

Figure 5.14: Sphericity of the ruthenium particles
Histogram plots of the sphericity c_p (see Sec. 3.1) of the ruthenium particles. Only particles whose volume (in voxel) was bigger than the chosen threshold were considered in the corresponding histogram.

5.3.4.1 Deviation from spherical symmetry

Most ruthenium particles deviate from spherical shape (see inset in Fig. 5.11 and Fig. 5.12). The sphericity $c_p = 6\sqrt{\pi} \quad V/S^{3/2}$ (see Sec. 3.1) of the ruthenium particles was investigated to quantify the deviation. Figure 5.14 shows multiple histograms of the sphericity. The histograms differ by their minimum volume threshold. Particles with volumes below this threshold are not included in the corresponding histogram. Values of c_p above 1 in the histograms in Fig. 5.14 are caused by errors in the surface estimation of the voxel representations of the small particles (see A.1). These particles have to be neglected. Therefore, the further analyses are restricted to particle volumes greater than 64 voxels ($\approx 1.1\ \mathrm{nm}^3$), although shape evaluations of particles with as few as 6 voxels have been reported [24].

Any histogram in Fig. 5.14, with a minimum volume threshold of at least 64 voxels, has very few particles that are actually spherical ($c_p = 1$). The degree of deviation from spherical shape is much more pronounced than expected from conventional 2D TEM images and as commonly assumed for such metallic nano crystallites [191]. This motivates fitting ellipsoids to the ruthenium particles rather than simple spheres. Generally, it can be assumed that the particles have the form of truncated hexagonal bipyramids because Ru metal crystallizes in a hexagonal closed packed structure [45; 131]. However, the truncated bipyramids are expected to resemble shapes close to ellipsoids if the resolution of the tomographic dataset is insufficient to reveal facets. The shape of the resulting particle representations can range from prolate (cigar-shaped) to oblate (lentil-shaped) depending on the position of the truncation or preferential growth directions. The additional information from the ellipsoid fitting provides an estimate of the significance of these influences.

5.3.4.2 Size distribution

The size distribution of ruthenium particles shown in Fig. 5.15 is given as a function of the radius of a sphere with the same volume as the corresponding particle. The normal-

[8] These estimated separation values for the two modes seem sufficient in this case, but many separation algorithms exist for bimodal histograms (e.g. [20]).)

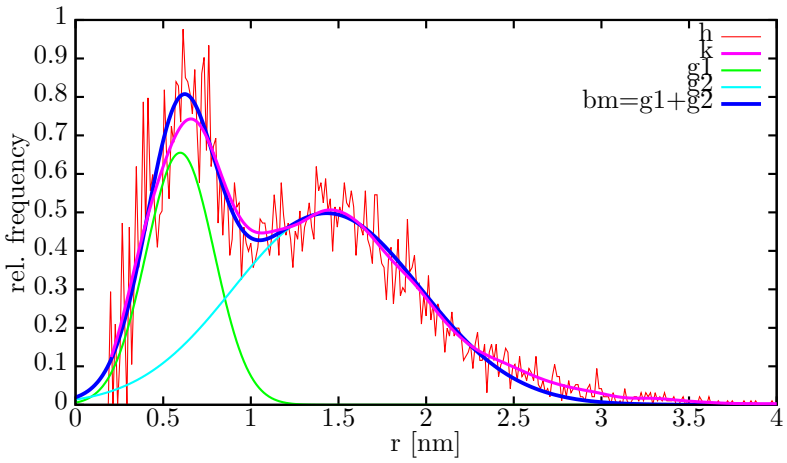

Figure 5.15:
Particle size distribution
Histogram showing the distribution of the radii of all representative ruthenium particles considering spherical approximation (h). The bimodal distribution can be fitted by the sum (bm) of two Gaussian distributions (g1 and g2). The fitted function nearly matches the kernel density plot (k). The local minimum of the distribution lies around 1 nm and the intersection of the two Gaussian functions at around 0.8 nm.[8)]

ized histogram[9)] (h) has 300 bins and shows a noisy but distinct bimodal distribution of the particle radii (particles with $c_p > 1$ were excluded). A kernel density distribution plot (k, see page 28) accounts for the uncertainty of the representation of ruthenium particles. This also reduces the noise and the bimodal distribution becomes more obvious. The distribution was decomposed into two Gaussian functions. Therefore, the sum (bm) of two Gaussian functions (g1 and g2) was fitted by non-linear least-squares (NLLS, Marquardt-Levenberg algorithm [6, sec. 57, p. 58]) to the histogram (h). The fitted function has a very good correlation (root mean square (RMS) of residuals: 0.07) and only differs slightly from the kernel density plot (k). The fitting function is:

$$f(r) = a\exp(-(r-k)^2/(2s^2) + b\exp(-(r-l)^2/(2t^2))$$

and the result is:

$$a = 0.7, k = 0.6, s = 0.2; b = 0.5, l = 1.4, t = 0.5$$

The two mean radii of the bimodal distribution are therefore: $r_1 = 0.6$ nm (variance 0.2 nm) and $r_2 = 1.4$ nm (variance 0.5 nm). In reality, there are probably more small particles ($r < 0.5$ nm) because of the influence of the median filter on the grey values as explained previously in Sec. 5.3.2. This would affect the smaller mode by increasing the value of a and possibly decreasing r_1. However, the result that there are two modes should not be affected because the maximum of the bigger mode lies at $r_2 = 1.4$ nm which is about three times larger than the range of the median kernel ($r \approx 0.5$ nm).

[9)] The terminology is not consistent in this case. I refer to a normalized histogram when its overall integral equals unity [79, sec. 13.2.1, p. 257].

5.3.4.3 Shape analysis

Shape analysis is done by fitting an ellipsoid to each particle after watershed separation.[10)] The parameters of the ellipsoid, namely axes lengths, axes orientations and position in space, are determined from the binary image moments of first and second order (see Sec. 3.1). Scaling of the fit-ellipsoids (to make them have the same volume as the corresponding particles) does not change the ratio of the lengths of the main axes: a:b:c (referred to as a:b:c-ratio from now on). Contrary to other work containing shape analysis based on binary image moments [24; 26; 140], my evaluation is based on LWPDs introduced in Sec. 3.3 allowing to introduce shape categories.

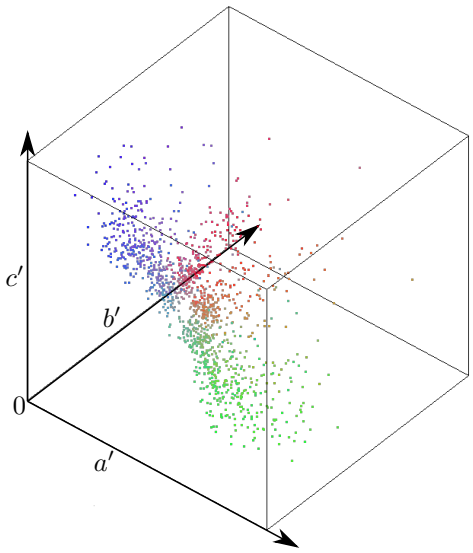

Figure 5.16: Distribution of the a:b:c-ratios in 3D

Visualization of the a:b:c-ratios as point vectors for all ruthenium particles extracted from the tomogram. The points are mapped into the rgb colour space to preserve 3D information in the projection, i.e. points close to the a'-axis contain more green, those close to the b'-axis more red and to the c'-axis more blue.

For an evaluation of these ratios I interpreted the actual lengths of the axes a', b' and c' as components of point vectors in 3D space as shown in Fig. 5.16. They reside within the positive quadrant because a', b' and c' are always positive. In this representation the distance of each data point from the origin is proportional to the size of the particle. However, for the evaluation of the shape of each particle, its actual size, i.e. the actual length of the point vector, is of no importance. Therefore, all data points of Fig. 5.16 were radially projected onto the unit sphere, as displayed in Fig. 5.17 which is further explained below. This projection maps $a' \Rightarrow a$, $b' \Rightarrow b$ and $c' \Rightarrow c$ changing the individual axes lengths but not the a:b:c-ratios.

The axes were sorted by their lengths $a < b < c$. This causes the points to be restricted to a rectangular spherical triangle on 1/48 ($1/8 \cdot 1/6$, concluded form underlying symmetry) of the surface of the unit sphere. The points on the triangle arcs correspond to special ellipsoids:

The prolate arc:	$a = b < c \Leftrightarrow 1 = a/b < c/b$
The oblate arc:	$a < b = c \Leftrightarrow a/b < c/b = 1$
The ellipse arc:	$a = 0$

The naming of the axes does not correspond to the common naming in hexagonal systems. The mathematical category of prolate ellipsoids (cigar shape) have a rotational symmetry about the long axis (c), whereas the oblate ellipsoids (lentil shape) have a rotational symmetry about the small axis (a). The corner points of the spherical triangle in Fig. 5.17 correspond to even more special conditions of the ellipsoids:

[10)] This can only be done in 3D because an unambiguous evaluation of the shape of particles that resemble arbitrarily shaped ellipsoids is not possible in 2D projections or cross sections, i.e. stereology [133, sec. 8.1.1, p. 242].

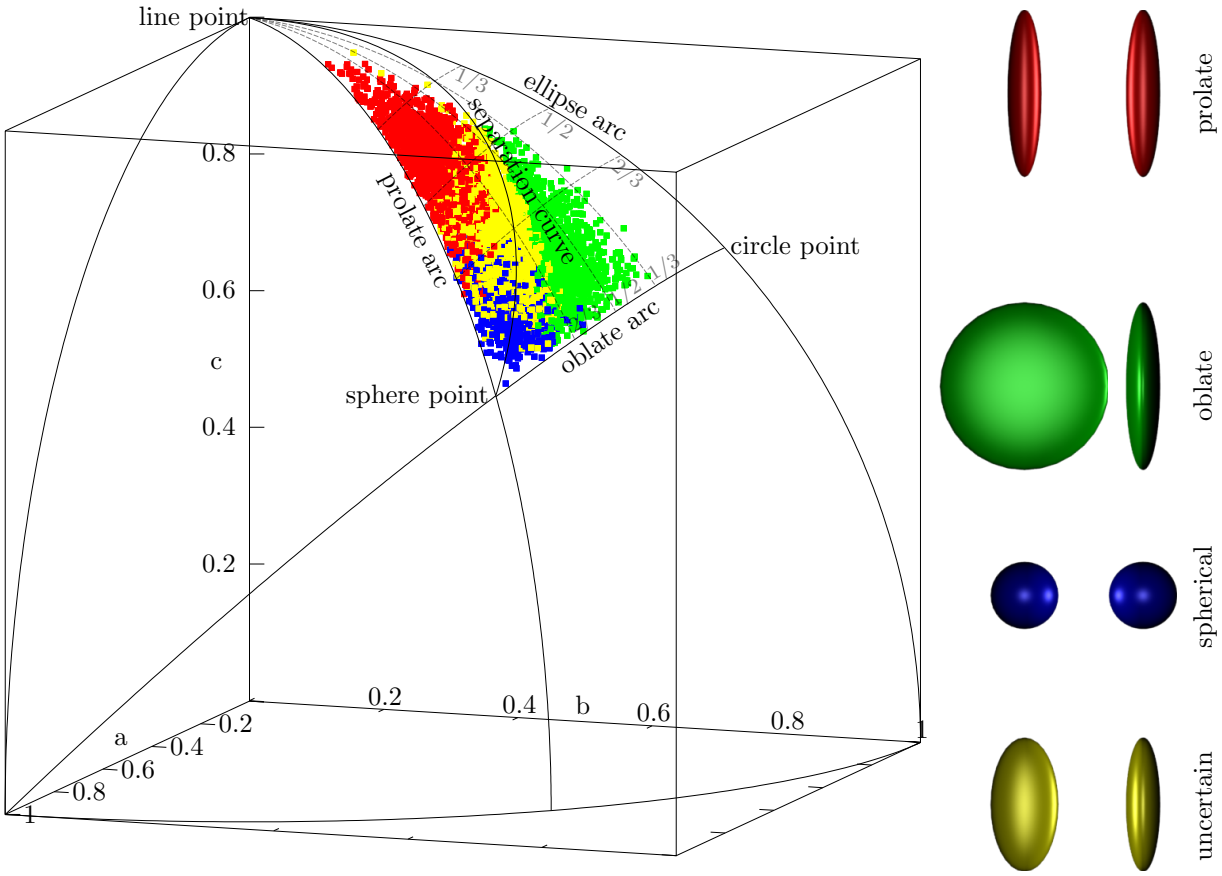

Figure 5.17: Radial projection of a:b:c-ratios

Radial projection of the a:b:c-ratio point vectors onto the unit sphere. Due to sorting, $a < b < c$, all the points lie within a rectangular spherical triangle. The special lines are explained in the text. The broken lines ending at the oblate arc mark the corresponding a/b ratios; those ending on the ellipse arc mark the corresponding b/c ratios. The colour of each point corresponds to its ellipsoid type: prolate: red (# 1783); oblate: green (# 983); spherical (within error limits, # 676): blue; uncertain (within error limits, # 2257): yellow. The ellipsoids on the side represent the four different types (second column: view rotated by 90°) in their extremes.

The sphere point:	$a = b = c$
The circle point:	$a = 0 \wedge b = c$
The line point:	$a = b = 0$

The ranges of the a, b and c values are:

$$a \in [0; \sqrt{1/3}], b \in [0; \sqrt{1/2}], c \in [\sqrt{1/3}; 1]$$

Perfectly prolate, oblate or spherical ellipsoids, i.e. with rotational symmetry, represent extreme geometrical cases that are unlikely to appear in the distribution (indicated by the unpopulated prolate and oblate arcs in Fig. 5.17). Nevertheless, a large fraction of data points are a significant distance away from the sphere point, indicating that the majority of particles are non-spherical in accordance to the result of Sec. 5.3.4.1.

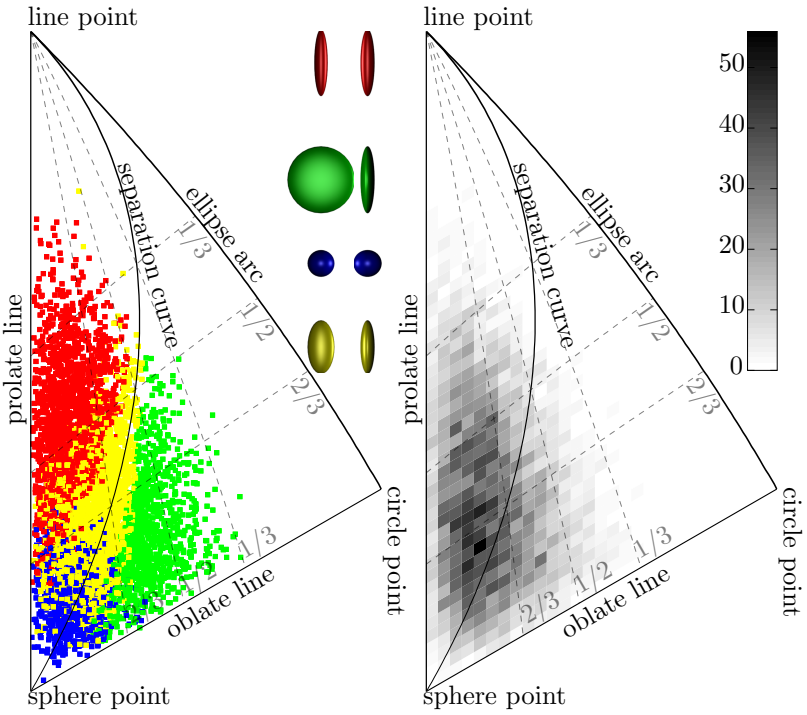

Figure 5.18: Stereographic projection of a:b:c ratios and 2D-histogram
a) The stereographic projection of Fig. 5.17. The chosen origin of projection on the sphere is $(\sqrt{1/3}, \sqrt{1/3}, \sqrt{1/3})$, the 'sphere point'. The colour of each point and the labels corresponds to those in Fig. 5.17.
b) 2D-histogram showing the distribution of the ratios of fit-ellipsoid axes. Each histogram field is coloured according to the number of ellipsoids with a:b:c lying within the area of the field. The fields are parallelograms to avoid under estimation along the 'oblate line'.

A way to partition all possible ellipsoids into two definite classes is to define the separation condition $a/b = b/c$. Ellipsoids with $a/b < b/c$ are oblate-like, whereas those with $a/b > b/c$ are prolate-like. The condition $a/b = b/c$ corresponds to the case where the eccentricity of the ellipse in the ab-plane equals the eccentricity of the ellipse in the bc-plane. This defines the separation curve in Fig. 5.17.

This separation line condition combined with the unit sphere condition leads to:

$$ac = b^2 \wedge a^2 + b^2 + c^2 = 1 \Rightarrow a^2 + ac + c^2 = 1$$

This cannot be resolved for any of the variables so I parametrized with $c = \frac{a}{x}$:

$$a = \frac{1}{\sqrt{\frac{1}{x^2} + \frac{1}{x} + 1}}, b = \frac{1}{\sqrt{\frac{1}{x^2} + \frac{1}{x} + 1}} \frac{1}{\sqrt{x}}, c = \frac{1}{\sqrt{\frac{1}{x^2} + \frac{1}{x} + 1}} \frac{1}{x}$$

For $x \in]0; 1]$ the value ranges of a, b, c are:

$$a \in]0; \sqrt{1/3}], b \in]0; \sqrt{1/3}], c \in]1; \sqrt{1/3}]$$

This means that the resulting separation line runs from the 'line point' to the 'sphere point' and does not split the area of the spherical triangle into two equal parts.

Each a:b:c-ratio has an error because of the uncertainty in the particle representation. This can be regarded as an error box (not shown, $\pm$ 0.5 nm $\widehat{=}$ $\pm$ 2 voxels) around each point in Fig. 5.16 and also in Fig. 5.17. If the error permits the shape to be either prolate or oblate, i.e. the error box intersects with the separation curve, the shape is uncertain within the error limits. If, however, the error box includes the sphere point, the ellipsoid can be regarded as spherical within the error limits.

This spherical triangle is stereographically projected, see Fig. 5.18a. The origin of projection was chosen to be the 'sphere point' such that the prolate and the oblate arcs are projected onto straight lines.[11)] However, the true point density cannot be read from Fig. 5.18a due to coincidence/overlap of points. The 2D histogram in Fig. 5.18b visualizes the actual point density distribution of a:b:c-ratios. The grey scale indicates the amount of a:b:c-ratio-points within a field, i.e. the number of particles whose a:b:c-ratios are similar. The fields are not rectangular to avoid underestimation along the 'oblate line'. It is visible that the prolate-like ellipsoids dominate over the oblate-like ones, since the densities in Fig. 5.18b are higher in the prolate region (red points in Fig. 5.18a) than in the oblate region (green points in Fig. 5.18a). It should be noted that it is possible to plot a 2D-histogram of a/b- and b/c-ratios. However, this 'projection' causes additional distortion and the resulting point density could not be interpreted directly.

5.3.4.4 Degree of resemblance between particle and fit-ellipsoid

In order to quantify the degree of resemblance between a given particle and its corresponding fit-ellipsoid, I introduced the concept of ellipsoidity in Sec. 3.1. Figure 5.19 shows histograms for the comparison of the distributions of ellipsoidity of the ruthenium particles in different datasets of the 'poodle' particle. The evaluation of the ellipsoidity $\eta = A_e/A_p$ should yield values of $\eta \leq 1$. However, there are values above unity because the volume V_p and surface area A_p of the particles are based on estimates of the voxel representation (discussed in App. A.1).[12)]

The histograms show how much the ellipsoidity of the particles differs between the SIRT and the DIRECTT reconstructions (compare the normalized histograms 'SIRT norm.', blue and 'DIRECTT bs norm.', green)[13)]. This can be interpreted as a significant decrease of the influence of streak artefacts in the DIRECTT reconstruction since streak artefacts cause false connections, i.e. virtual 'glueing' as defined in Sec. 3.2, of in reality separated particles. The more particles are 'glued' together the more 'ginger like' the

[11)] A stereographic projection yields less distortion in the point density than an orthographic projection. Both the stereographic and the orthographic projections project the prolate arc and the oblate arc onto straight lines if $(\sqrt{1/3}, \sqrt{1/3}, \sqrt{1/3})$ is chosen as the projection centre. However, the stereographic projection yields less area distortion in this case: The angle between $(0, 0, 1)$ and $(\sqrt{1/3}, \sqrt{1/3}, \sqrt{1/3})$ is about 55°. The ratio of the actual length of the prolate arc and the length of the projected line is about 0.85 (15% less) for the orthographic projection and about 1.08 (8% more) for the stereographic projection.
A specially tailored projection with additional radial scaling could project even the ellipse arc on a straight line. However, this effort is not necessary here since there are no points close to the ellipse arc nor is its curvature of any significance after stereographic projection.

[12)] It would be possible to calculate A_p and V_p from the mesh representation of each particle to avoid this discrepancy but it leads to a significant increase in computation time. Considering the introduction of further uncertainties by the conversion from voxel to mesh representation and the additional programming effort I decided not to do so since the gain in accuracy is not necessary for the presented comparison.

[13)] Only the comparison of normalized histograms makes sense in this case since the difference in the number of particles between the SIRT and the DIRECTT reconstruction is not directly related.

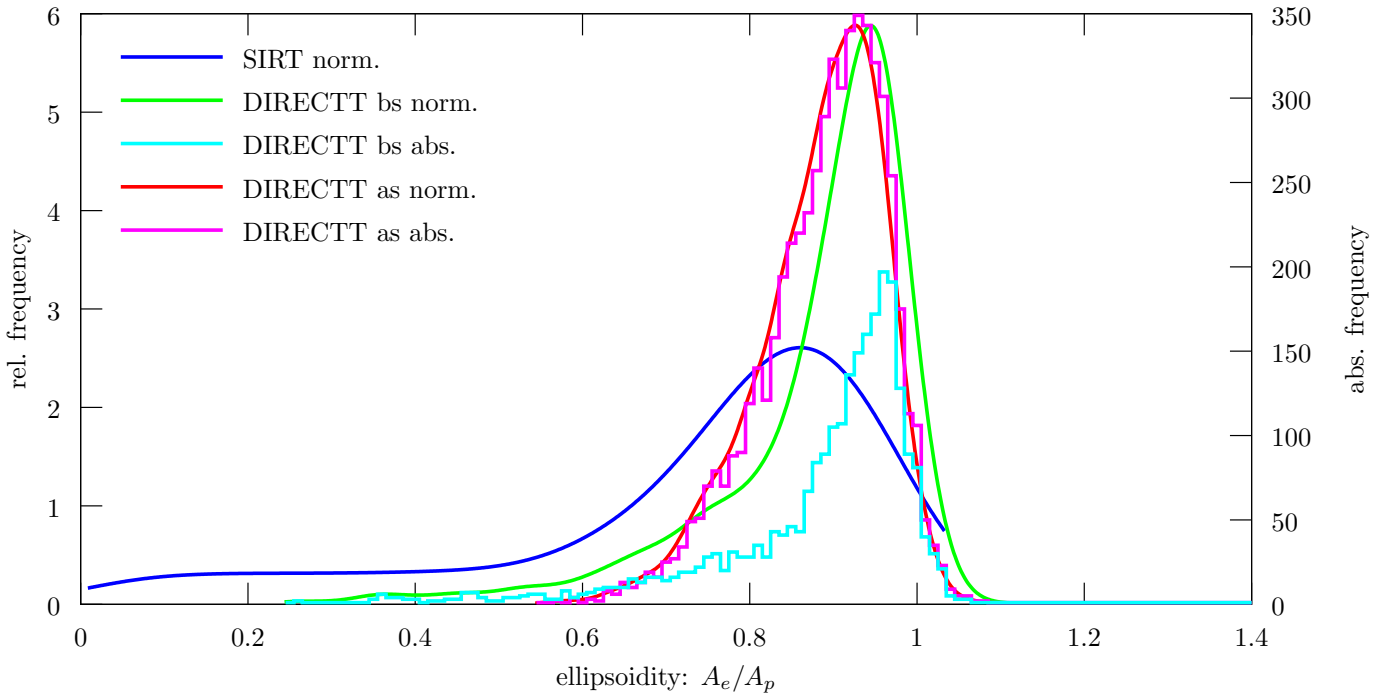

Figure 5.19: Histograms of the ellipsoidity of the ruthenium particles

Histograms showing the distribution of the ellipsoidity $\eta = A_e/A_p$ of the reconstructed ruthenium particles. The correspondence between a particle and its fit-ellipsoid is best at $\eta \approx 1$. The normalized histograms are kernel density plots (see Sec. 3.4.1) of relative frequency. They allow a comparison of the ellipsoidity distribution of the SIRT and DIRECTT reconstructions. The deviation from ellipsoidal shape is reduced in the DIRECTT reconstruction. This is described further in the text.

objects appear (see e.g. Fig. 3.1) and the larger the deviation from ellipsoidal shape. Since the ruthenium particles are expected to be of ellipsoidal shape (see Sec. 5.3.4.1) under the given spatial resolution, a significant deviation from ellipsoidal shape can be regarded as a significant influence of artefacts on the quality of the reconstruction (for an extreme example see right image of Fig. 3.1).

Since the watershed separation (see Sec. 3.2) of the particles is a counter-measure against the virtual gluing by artefacts, the overall deviation from ellipsoidal shape is expected to be reduced for the dataset of separated particles. The histograms of this dataset ('DIRECTT as') confirm this expectation. The amount of particles with low ellipsoidity ($\eta < 0.65$) is particularly reduced (compare 'DIRECTT bs' and 'DIRECTT as') which leads to an increase of particles in the region between $\eta \approx 0.7$ and $\eta \approx 0.95$. This is the only reason for the shift of the maximum from $\eta \approx 0.95$ (green histogram, 'DIRECTT bs norm.') to $\eta \approx 0.9$ (red histogram, 'DIRECTT as norm.'). No significant amount of particles that initially had a very high ellipsoidity ($\eta > 0.95$) are degraded to shapes of less ellipsoidity by the watershed separation. This can be seen by comparing the absolute histograms before and after separation ('DIRECTT bs abs.', cyan and 'DIRECTT as abs.' magenta). The magenta histogram fully contains the cyan histogram from $\eta \approx 0.65$ on. The comparison of the absolute histograms also shows that the few particles with $\eta < 0.65$ were split up into many more particles (see Fig. 3.2) since the difference between the histograms is much bigger in the range between $\eta \approx 0.7$ and $\eta \approx 0.95$ than the difference for $\eta < 0.65$.

5.3.4.5 Anisotropy in the global orientations

The particles that deviate from spherical symmetry have a distinct orientation. This orientation can be represented by the directions of the fit-ellipsoid axes (according to the fit procedure from Sec. 3.1). Therefore, the directions of the fit-ellipsoid axes can be used to reveal anisotropy in the global orientation distribution of the particle representations, i.e. the orientation relative to the axes of the tomogram.

The production conditions for the catalyst particles investigated suggest an isotropic orientation distribution. Anisotropy can be caused by ion irradiation [159; 158]. However, it is unlikely that the electron irradiation of the sample during acquisition of TEM images resulted in a significant elongation of the ruthenium particles because of the huge difference in mass between electrons and ruthenium atoms. The partially directional growth of carbonaceous contamination is more likely to have an influence but is also thought to be negligible because of the high contrast difference between ruthenium particles and the contamination. Most likely the elongations of the particle representations in the tomogram are not real but are caused by reconstruction artefacts. The 'missing wedge' (as mentioned in Chap. 2) causes unidirectional elongations along the wedge direction while the 'gluing' of particles by streak artefacts (see Chap. 2) can lead to elongations along the projection directions of the tilt series (see e.g. Fig. A.8).

I analysed the three axes of each fit-ellipsoids separately to evaluate these effects. As before, I represent the orientation vectors as points on the unit sphere. Due to the mirror symmetry of ellipsoids the sign of the direction vector is meaningless. Therefore, all points on the unit sphere are restricted to a hemisphere to define a main direction, which in this work is the positive x-axis of the tomogram. Any anisotropy leads to a variation in the Local Weighted Point Densities (LWPD). For the local number density the weights are set to unity.

The evaluation of LWPDs of points (the general problem is described in Sec. 3.3) restricted to a hemisphere is problematic because there is a boundary (i.e. a hemisphere is an open manifold [80]) and the distortions of a projected hemisphere are significant: The Projection of the Points into a Plane (PPP, as used in Sec. 5.3.4.3, see also Sec. 3.3) either leads to projection boundaries that the fields of a 2D histogram can not be aligned to (if an area-preserving projection is used, e.g. sinusoidal projection), or the projection introduces distortions that significantly influence the point densities within histogram fields (if a projection is used that projects a hemisphere into a parallelogram, e.g. equirectangular projection). The evaluation of points restricted to a hemisphere by Local Sphere Sampling (LSS, see also Sec. 3.3) also suffers from undersampling along the boundary of the hemisphere. However, in this particular condition, the problem can be circumvented by mirroring each point onto the opposite position on the sphere. This creates a point distribution over the whole sphere. The redundancy that is introduced is removed by only displaying the calculated LWPD values for the points that reside within the unambiguous region of a hemisphere.

The idea of LSS is to evaluate the point density within a solid angle centred on a point P. A small sphere ($r < 1$) is positioned with its centre at the point position P

(see Fig. 3.4). The sum of the weights of all the points that lie within the small local sphere is then assigned as the Local Weighted Point Density (LWPD) to the point P. This procedure is done for all points such that finally each point has its LWPD computed. For the calculation of the LWPD of a single point, all other points have to be checked if they reside within the local sphere. This causes the computation time to be proportional to N^2, but for the amount of particles present in the dataset this is not a restricting factor since each particle only leads to a single point in the evaluation (in contrast to the facet analysis). The variation in the LWPDs can then be visualized by a field depiction (explained in Fig. 3.4) that *averages* the LWPDs of points lying in the same field after an equirectangular projection, Fig. 5.20. Since only the points on a hemisphere (i.e. only points with an x-coordinate ≥ 0) are regarded, ϑ and φ are in the range $\pm 90°$. The middle axis b and the longest axis c are processed in the same manner and yield their own distributions.

Figure 5.20 visualizes the anisotropy in the distribution of the global orientations of ruthenium particle axes in IMOD-WBP, IMOD-SIRT (20 iterations) and DIRECTT (10 iterations, without watershed separation) reconstructions of the poodle sample (Fig. 5.11). The orientations are regarded in the coordinate system of the tomogram which does not exactly correspond to the acquisition coordinate system because the tomogram was rotated to eliminate the support foil with the gold markers. The overall rotation between the two coordinate systems was less than 5°.

The diagrams for axis c and c_w in Fig. 5.20 show that all reconstructions have a higher LWPD close to the poles of the z-axis. This effect is probably caused by the 'missing wedge' whose centre is slightly displaced from the z-axis because of the asymmetric tilt range of the dataset (-69° to 74°). However, the effect is most pronounced for SIRT and significantly less for DIRECTT. If the degree of elongation of the individual particles is

Figure 5.20: Global orientation of the axes

The figure table visualizes the anisotropy in the distribution of the global orientations of the axes of ruthenium particles in IMOD-WBP, IMOD-SIRT and DIRECTT reconstructions of the 'poodle' particle (Fig. 5.11).

The local weighted point densities (LWPDs) were evaluated by local sphere sampling (LSS), then projected by an equirectangular projection, averaged and visualized by a field depiction (with a resolution of 30x30 fields) as described in the text.

The projection used the standard mathematical relationship between orthogonal coordinates (x,y,z) and spherical coordinates $(\vartheta, \varphi, r = 1)$. Therefore, the intersection of the x-axis with the unit sphere lies at $[\vartheta = 0°, \varphi = 0°]$, the intersection of the y-axis at $[\vartheta = 0°, \varphi = \pm 90°]$ and the intersection of the z-axis at $[\vartheta = \pm 90°]$.

The sampling radius ϱ of LSS was chosen to correspond to $\varrho = 10°$ such that the solid angle is $\Omega = 2\pi(1 - \cos\varrho) \approx 0.1$. For the first three rows (a,b,c) the weight W was chosen to be $W = 1/2N$, N being the number of particles in the evaluation, WBP: $N = 3991$; SIRT: $N = 1852$; DIRECTT: $N = 2565$. In the last row, c_w, the weight was set to $W = c/\sqrt{ab}/2N$ to account for the degree of elongation of the individual particles. The scale of the first three rows (a,b,c) was chosen such that the maximum value in the c-row (about 0.1) is red. However, the maximum value in SIRT-a is 1.6. The scale for the last row was chosen such that the maximum value (SIRT-c_w, about 0.3) is red. The white fields contain no points. This is either due to an actual low LWPD or due to a reduction in point density (not LWPD) because of the projection distortion (e.g. around $\vartheta \approx \pm 90°$).

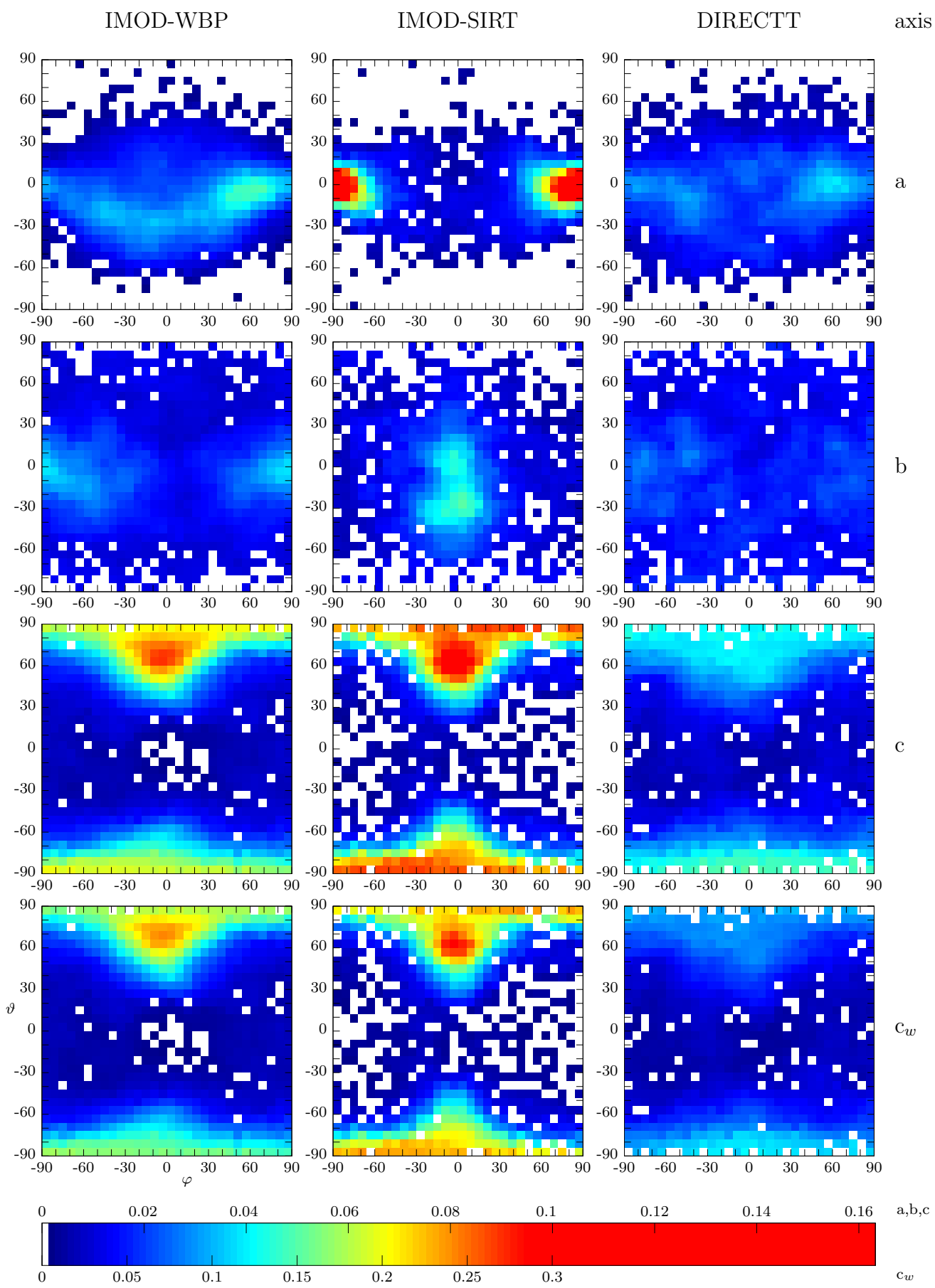

Figure caption on the opposite page

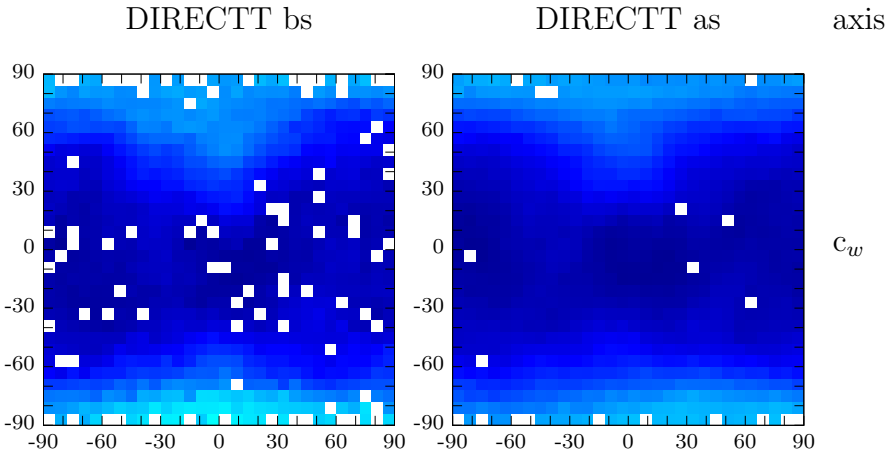

Weighted global orientation distribution of the DIRECTT dataset before (bs, same plot as Fig. 5.20c_w) and after watershed separation (as). The scale is the same as for c_w in Fig. 5.20. A reduction of the tendency to form a 'belt' can be seen in 'DIRECTT as'. The belt originates from particles connected by streak artefacts.

Figure 5.21: Global orientation of the axes for DIRECTT bs and DIRECTT as

regarded (row c_w) the maximum of the LWPD is less broad for all reconstructions but that of DIRECTT is even less pronounced than in row c. This means firstly that fewer particles have their longest axis pointing in the direction of the missing wedge in the DIRECTT reconstruction and secondly that the elongation of particle representations caused by the missing wedge is less than in the WBP or SIRT reconstructions.

The DIRECTT reconstruction also exhibits a more isotropic distribution of the a- and b-axes of the particles than the WBP and SIRT reconstructions. The WBP reconstruction shows the expected distribution of a- and b-axes. These have to lie around the 'equator' if the c-axes are mainly aligned along the z-direction. Since the missing wedge is slightly displaced from the z-axis, the 'equator' of the missing wedge follows a sine curve in the projection as in WBP-a of Fig. 5.20.

The SIRT reconstruction shows an extreme pole (more pronounced than the missing wedge) of the a-axis in the direction of the y-axis of the tomogram. This might be a result of a not (sufficiently) converged IMOD-SIRT reconstruction [60; 59]. Although it is common practice to use only 20 to 30 iterations [11; 120], it has been shown that the convergence rate depends on the relaxation parameter [63; 176]. However, IMOD-SIRT seems to have a fixed relaxation parameter [115, `sirtsetup`] which might not lead to convergence within 20 to 30 iterations.

Streak artefacts can cause false connections (virtual 'gluing') of particles along streaks. The directions of the streaks are along the directions of the projections of the tilt series. There seems to be no influence of the particle gluing by streak artefacts in the DIRECTT reconstruction since any such influence would lead to increased LWPDs in the plane (approximately x-z-plane) perpendicular to the rotation axis (approximately the y-axis) in Fig. 5.20c. Depending on the resolution of the field depiction, these punctual increased LWPDs (for this tomogram 144 corresponding to the number of images in the tilt series) smear out and form a 'belt'. A tendency to form such a belt can be seen in row c and c_w (Fig. 5.20) of the WBP and SIRT reconstructions as a vertical extension of the missing wedge.

Comparing the results of the weighted c-axis evaluation of the DIRECTT reconstruction without (c_w in Fig. 5.20) and with watershed separation, Fig. 5.21, shows a slight reduction of the tendency to form this belt. However, this kind of evaluation is probably not as sensitive as the ellipsoidity evaluation (Sec. 5.3.4.4) concerning the answer to the question how well the watershed separation counteracted against the artefact gluing.

5.3.4.6 Degree of facettation

Many ruthenium particles show a tendency to be partially faceted but the resolution of the tomogram is in many cases insufficient for the particle representations to exhibit distinct facets. Since facettation of catalyst particles has a significant influence on their effectiveness, an automated facet analysis (as described in Sec. 3.4.1) was developed to investigate facettation statistically.

The result of the facet analysis for all 2600 ruthenium particles (of the dataset without watershed separation) does not show any particular angle distribution. However, if only the particles that have at least six facets with a minimum relative facet size of 4% are regarded, the interplanar angle frequency plot (Fig. 5.22, $\sigma = 4 \mathrel{\widehat{=}} \text{FWHM} \approx 10°$) shows four distinct peaks at about: 60°, 90°, 120° and 140°. Only 40 particles fulfil these two conditions but still yield 923 interplanar angles (see 3.4.1 **10.)**) for statistic analysis. The particles are shown in Fig. 6.3 and have diameters down to about 2.6 nm, i.e. 10 voxels.

I created a program to relate the interplanar angles of the hexagonal system of ruthenium with the interplanar angles that the facet analysis yields. It is based on the article of Hogan and Dyson [69] and has the advantage (in regard to other such programs, e.g. [168]) that it calculates *all* possible interplanar angles α between any two facet normals for a set of Miller indices and reports those angles lying within a specified range. For example, ruthenium with lattice constants $a = 2.704$ Å and $c = 4.282$ Å [188] has in the range of $140° \pm 1°$ (i.e. $139° \leq \alpha < 141°$) 8 possible facet combinations with angles of $\alpha \approx 139.4°$ for h,k,l $\in [-1, 0, 1]$ (e.g. $\measuredangle\,(1\,1\,0)(0\,\bar{1}\,1) \approx 139.4°$) However, plotting the facet indices on a Wulff net (see Fig. A.9 and Fig. A.10) reveals that the angle of $\alpha \approx 139.4°$ is formed between one of the additional facets of a prism with 12 faces and a facet of a hexagonal bipyramid. These shapes are known to exist and are further described in e.g. [83, p. 72 ff] [143, p. 46 f]. The plots also show that for symmetry reasons e.g. $\measuredangle\,(2\,\bar{1}\,0)(\bar{1}\,0\,1)$ and $\measuredangle\,(2\,\bar{1}\,0)(\bar{1}\,1\,1)$ have to be regarded as well. This yields in total 24 facet pairs of $\alpha \approx 139.4°$ for a hexagonal bipyramid and a prism with 12 faces. If any combination of h,k,l $\in [-2, -1, 0, 1, 2]$ is allowed then 166 facet pairs can be found in the range of $140° \pm 1°$.

According to the literature, ruthenium crystallizes in a hexagonal structure [45; 131] and therefore the angles 60°, 90° and 120° appear between the facet normals of a hexagonal prism. However, the crystals are assumed to form hexagonal bipyramids or bipyramids elongated by hexagonal prisms [131], see Fig. 5.24. The facets are expected to have only low Miller indices.

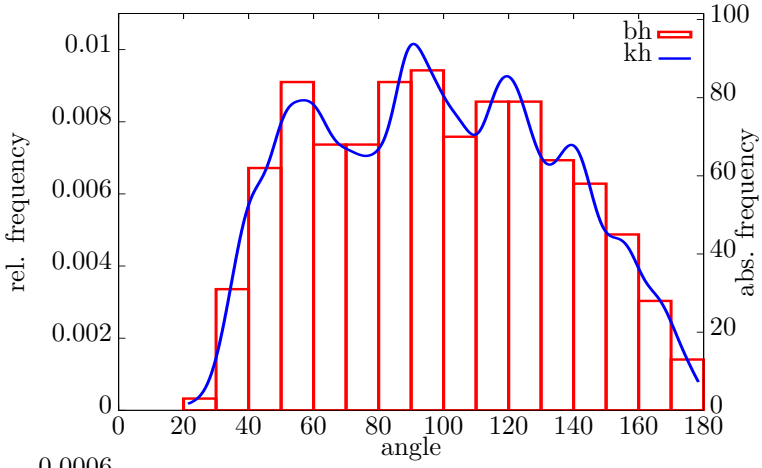

Figure 5.22: Interplanar angle frequency plot of ruthenium particles
The plot shows the frequency of the interplanar angles of 40 ruthenium particles which have at least six facets with a minimum relative facet size of 4%. The distinct peaks of the kernel density plot (kh, $\sigma = 4$) at 60°, 90°, 120° and 140° are discussed in the text.

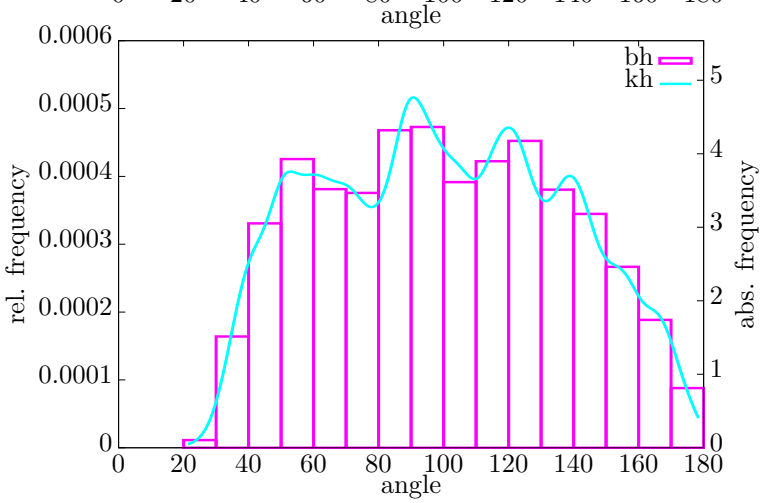

Figure 5.23: Weighted interplanar angle frequency plot of ruthenium particles
The plot shows the weighted (harmonic mean of the corresponding two relative facet sizes) frequency of the interplanar angles of 40 ruthenium particles which have at least six facets with a minimum relative facet size of 4%. The peak at 60° of the kernel density plot (kh, $\sigma = 4$) is less pronounced than those at 90°, 120° and 140° which are similar in shape compared to Fig. 5.22.

Table 5.1 lists the frequencies of interplanar angles for any combination of ruthenium facets with h,k,l $\in [-1, 0, 1]$. This consideration does not take any crystallographic conditions (e.g. $(2\,\bar{1}\,0)$ as mentioned above) into account and, therefore, the absolute frequencies from the bar histogram in Fig. 5.22 cannot be directly related to the calculated facet-combination-ratios of the dominant angles (as it was possible in Sec. 3.4.2.1 and Sec. 3.4.2.2). However, the frequencies of Tab. 5.1 provide a base for the interpretation of the interplanar angle frequency plot: 90° are most frequent while 60° and 120° are less but nearly equally frequent, 140° is possibly less popular because of the dependence on the additional facets of a prism with 12 facets. The detected facets statistically fit the expected crystal angles for ruthenium even though no simple, distinct crystal geometry, e.g. hexagonal prism or bipyramid, is dominant in the dataset.

range of α	α measured	# calc. comb.	# measured	example
$60° \pm 1°$	56°	6	155	$\measuredangle\,(1\,0\,0)(1\,\bar{1}\,0)$
$90° \pm 1°$	90°	36	165	$\measuredangle\,(1\,1\,1)(1\,\bar{1}\,0)$
$120° \pm 1°$	120°	6	160	$\measuredangle\,(1\,0\,0)(0\,\bar{1}\,0)$
$140° \pm 1°$	140°	8	120	$\measuredangle\,(1\,1\,0)(0\,\bar{1}\,1)$

Table 5.1: Frequencies of interplanar angles for ruthenium facets with h,k,l $\in [-1, 0, 1]$ (measured values are approx.)

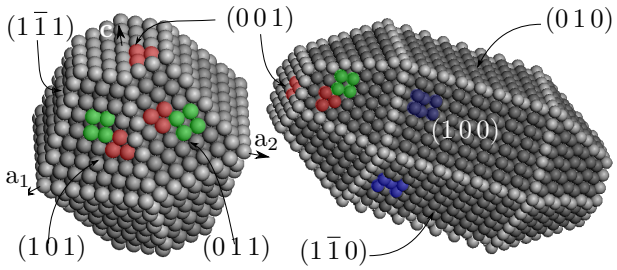

Figure 5.24: Ruthenium crystal geometries
Example geometries for a ruthenium nano cluster crystal: Simple hexagonal bipyramid and a possible elongation by a hexagonal prism. Some positions with threefold (red), fourfold (green) and higher coordination (blue) are marked. Figure based on images created by G. Zehl (Materials Studio[30]).

The weighted angle frequency plot, shown in Fig. 5.23, reveals that the facets forming an angle of 60° are not as balanced in their facet sizes as the facets corresponding to the other dominant angles (90°, 120° and 140°). Therefore, it can be concluded that the regarded particles mostly do not form, e.g, a complete hexagonal prism.

The angle frequency plots with a lower angle uncertainty (e.g. $\sigma = 2$) contain more peaks that also fit other interplanar angles of ruthenium crystals. For example the peak at about 56° splits up into two peaks at around 51° and 60°. Fig. A.10 shows that the interplanar angle between adjacent facets of the hexagonal pyramid (e.g. $\measuredangle\,(0\,1\,1)(\bar{1}\,1\,1)$) is about 52°.

5.3.4.7 Spatial distribution of the different shape types

To investigated how the studied particles of different shape are distributed in space, each ellipsoid is displayed at the centroid (barycentre or centre of 'mass') of the corresponding particle, see Fig. 5.25. Most of the spherical ellipsoids (blue) are small (Fig. 5.25) and are located inside (Fig. 5.26) the carbon support particle where the carbon seems to be more amorphous-like (see Fig. 5.11 and 5.12). Limited spatial resolution can be a reason for some small particles to appear spherical. However, many other particles, especially those located on the surface of the carbon support, have a distinctly ellipsoidal shape despite their small volume.

This was further evaluated by removing the ellipsoids that are bigger than 128 voxel (2.2 nm^3), which corresponds to a radius exceeding ca. 3 voxels ($\approx$ 0.8 nm). Thus, close to the intersection of the two Gaussian functions in Fig. 5.15. Additionally, the ellipsoids within a 5 nm (20 voxels) vicinity of the non-porous representation of the carbon (grey surface in Fig. 5.26) particle were removed as well. Figure. 5.26 shows clearly that the remaining ellipsoids dominate the right part of the carbon particle which is also the part that seems more amorphous-like in the TEM images (Fig. 5.11).

[14] The more the colour of an ellipsoid is saturated the better it fits its particle, i.e. the saturation of the colour corresponds to the ellipsoidity of the particle. However, this additional colouring dependence is not very pronounced after the watershed separation (as discussed in Sec. 5.3.4.4, compared with Fig. A.7 prior to watershed separation).

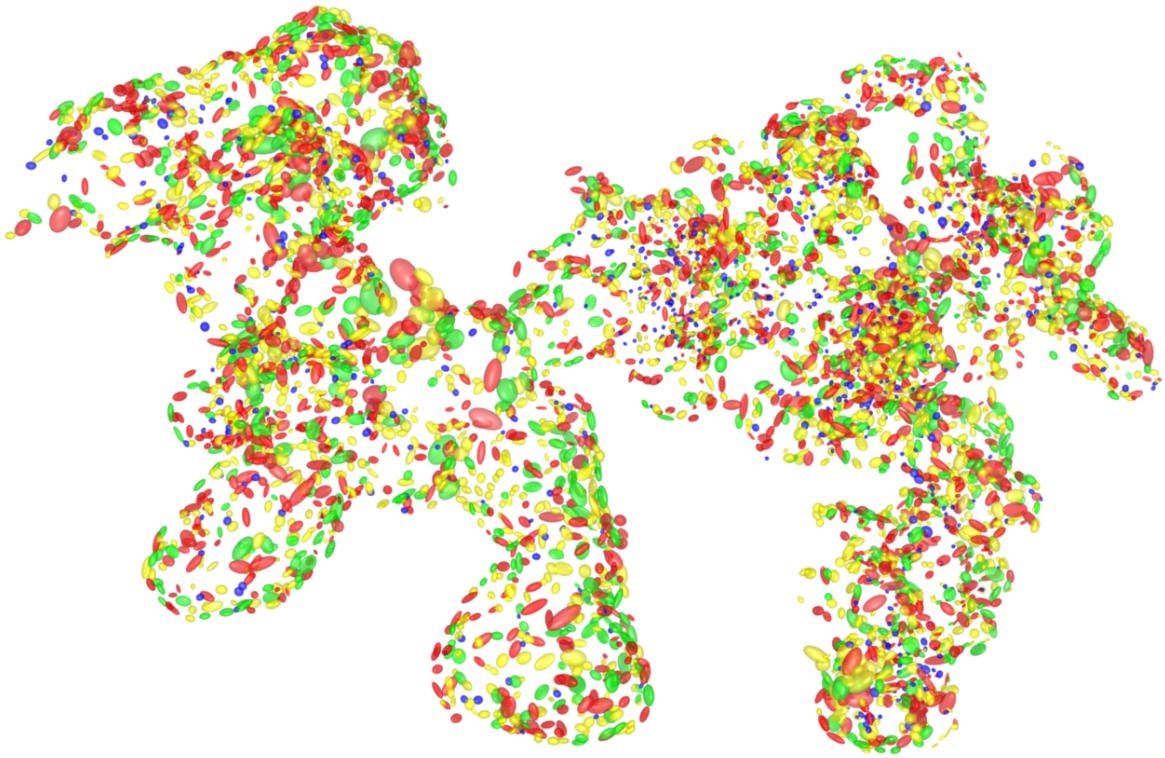

Figure 5.25: Spatial distribution of fit-ellipsoids

Spatial distribution of the fit-ellipsoids without the carbon support. Green: oblate, red: prolate, yellow: undistinguishable, blue: spherical within the error limits. The particle density is obviously higher on the right side. Figure A.7 shows the fit-ellipsoids prior to watershed separation.[14)]

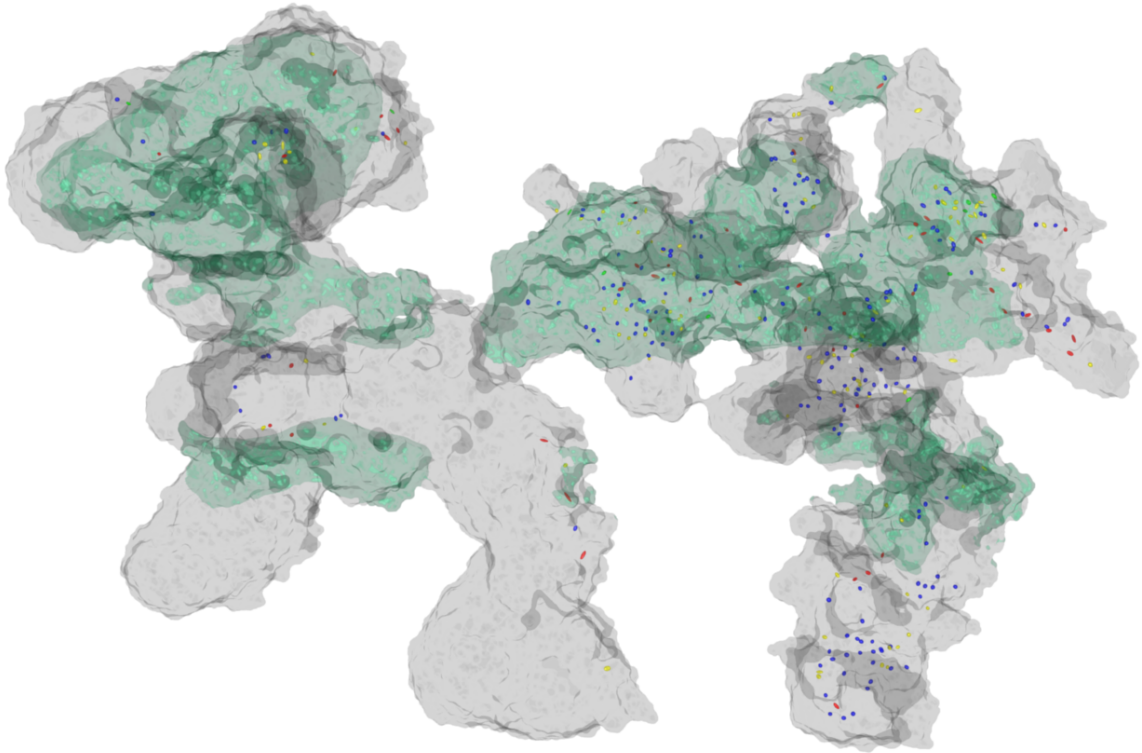

Figure 5.26: Relation of the inner particles to the morphology of the carbon support

The image shows only the small ellipsoids that are inside the outer carbon surface (grey). Most of the small inner ellipsoids are spherical (blue) and are located in the right side of the support. The light green surfaces enclose the regions of the carbon particle with a higher local pore density. These surfaces originate from the thresholded results of the local pore density filter (lpd_{16}) described in Sec. 5.3.5.1).

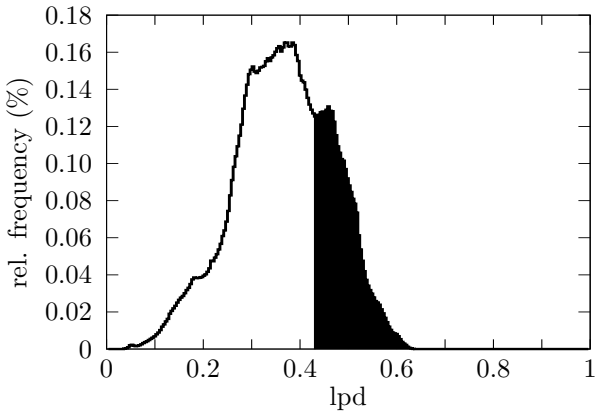

Figure 5.27: Histogram of the local pore density (lpd_{16})
This lpd_{16} is the local ratio (within a spherical vicinity of 16 nm radius) of the pore volume (pores below 5 nm diameter) to the sum of the pore volume and the carbon volume. Under the assumption of a bimodal distribution only the regions in the tomogram with $lpd_{16} > 0.43$ (black histogram part) where enclosed by a green surface mesh in Fig. 5.26.

5.3.5 Characterization of the morphology of the carbon support

The representation of the carbon support suffers from reconstruction artefacts, mainly streak artefacts originating from ruthenium particles. Therefore, the carbon representation is more uncertain than the ruthenium representation and should only be analysed by integral or statistical methods that incorporate larger regions ($\varnothing \approx 30$ nm) than the sizes of the ruthenium particles. In the following section, such an evaluation about the local pore density is given which allows for conclusions of local changes in morphology of the carbon support. However, a more thorough evaluation would be needed to complete the characterization of the carbon support. Since these evaluations would need a more exact carbon representation, they are listed in the outlook (Sec. 7).

5.3.5.1 Distinction of graphitic and amorphous regions by the local pore density

I analysed the correlation between ruthenium particle density inside the carbon support and the apparent carbon structure (crystalline/amorphous) more quantitatively. The more graphitic-like parts cannot be distinguished from the more amorphous-like parts based on contrast because the difference in contrast (if existent in the tomogram) is lost in the present noise (discussion in Sec. 6.1). Therefore, my approach to distinguish between the two forms makes use of their visibly different porous structure. For each voxel, the local pore density (lpd), which is the ratio in a vicinity sphere of radius R_v around the voxel of the pore volume (pores below 5.2 nm diameter, see bottom images of Fig. 5.12) to the sum of the pore volume and the carbon volume (disregarding the outside space), was calculated.

For a vicinity of $R_v \approx 16$ nm, the lpd_{16} shows a slight bimodal distribution (Fig. 5.27). The regions in the tomogram with $lpd_{16} > 0.43$ (black histogram part) were enclosed by a green surface mesh in Fig. 5.26. These are the regions which correspond to highly porous parts of the carbon particle.

The regions on the right can be assigned to the more amorphous-like parts which have been identified in Sec. 5.3.1. However, the left part has a region with a high lpd_{16} too. An explanation for this is that also the more graphite-like carbon parts contain voids

in the shape of bent plates between 'onion layers' which dominate the left side of the carbon particle (Fig. 5.12).

To distinguish between pores in the amorphous-like carbon and pores in the graphitic-like carbon (independent of the *lpd*), a filter is needed that takes the shape of the pores into account, since the cavities between the onion layers have the shape of bent plates and the pores in the amorphous-like carbon are more tube-like.[15)]

5.3.6 Relationship between ruthenium particles and carbon support

Figure 5.28: Extension of the carbon segment into the ruthenium segment
The preparation of the carbon segment for the evaluation of the uncovered ruthenium surface is visualized by cross sections overlaid in RGB-channels. The red channel is used for the ruthenium segment, the green channel shows the carbon support prior to local dilation. After local dilation of the carbon support around the ruthenium particles, the carbon support (blue channel) extends into the ruthenium particles yielding the magenta coloured regions. This overlap of the segments is essential for the evaluation of the 'uncovered ruthenium surface'. Most of the carbon support is unaffected by the procedure (cyan).

The relationship between the ruthenium particles and their carbon support (e.g. uncovered catalyst surface and local alignment to the support) is also important for the understanding of the catalytic activity and the processes during production. In contrast to previous evaluations, the following ones depend on both the carbon and the ruthenium representations. Therefore, the results suffer from uncertainties of the carbon representation and can only be taken as an estimate. However, the influence of uncertainties is less for the presented evaluations than for those mentioned in the outlook (Sec. 7) because these here are based on integral measures instead of punctual measures. Anyhow, the representations are suitable to outline the ideas of the analyses and their results make sense and allow further interpretations.

5.3.6.1 Ruthenium surface not covered by carbon support

An important quantity for heterogeneous catalysts is the amount of catalyst surface that is not covered or screened by the support material. Only the uncovered catalyst surface can be contacted by the reactants and therefore leads to catalysis. However, the surface of the catalyst that is in contact with the support material is equally important because this interface enables conduction of electrons. The larger the interface surface is, the higher is the conductivity. The higher the conductivity the less energy is lost in the conduction of the electrons from the source to the electrical device. Therefore, an optimum ratio between covered and uncovered catalyst surface is expected.

The evaluation of the ruthenium surface that is not covered by the carbon is not straight-forward because the voxel representations of the ruthenium and the carbon segment do not intersect in the way they were created. Even if an intersection is

[15)] An objectness enhancement filter [8] might enable to distinguish these different regions. However, this was not evaluated further because a more exact pore representation would be needed.

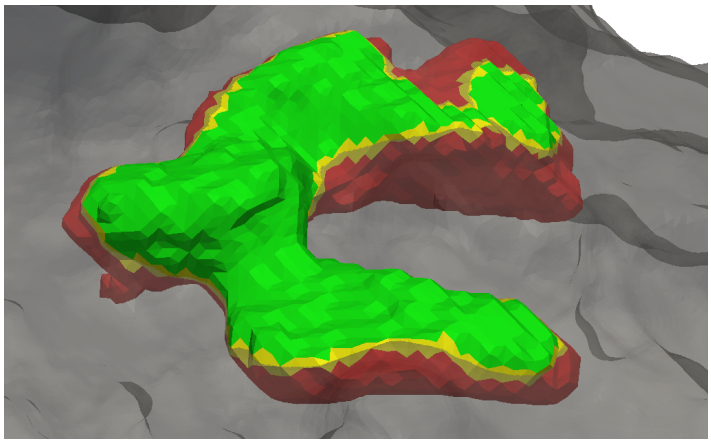

Figure 5.29:
Determination of the uncovered ruthenium surface

Schematic visualization showing the carbon mesh (transparent grey) intersecting with the mesh of a ruthenium particle. The triangles of the ruthenium mesh which reside completely outside the carbon mesh are coloured green, the triangles that reside completely inside are coloured red and the remaining triangles yellow.

created, a voxel representation is not suited for the calculation of the uncovered surface. Therefore, the ruthenium segment[16)] has to be converted into a mesh representation:

First, the carbon voxel representation is dilated by a kernel with a radius of one voxel but only in the vicinity of the ruthenium, Fig. 5.28. Then the mesh representations are created. Finally, the triangles of the ruthenium surface that do not reside inside the dilated carbon support are regarded as the uncovered ruthenium surface, see Fig. 5.29. Although each particle can be evaluated separately, only the total uncovered ruthenium surface was determined: $S_{ubs} \approx 0.74 \cdot 10^5$ nm^2, which is about 36% of the total ruthenium surface S_{bs} (see Sec. 5.3.3).

5.3.6.2 Orientation of ruthenium particles to the carbon surface

The fitted ellipsoids not only allow an evaluation of the particle shape but also for an analysis of the orientation of the ruthenium particles with respect to the carbon support. This can be quantified through the orientation of the mean local surface normal of the carbon support relative to the ellipsoid axes. The voxel representation of the carbon support particle has to be converted into a surface mesh to derive a mean local surface normal. The discrete-marching-cubes algorithm [106] in combination with a windowed-sinc-smoothing filter [12] of VTK[3] was used to create such a mesh representation of the carbon support surface. Figure 5.30 demonstrates this approach. For the estimation of the local mean normal the vector sum of triangle normals weighted by their triangle area is calculated. The summation is over all surface triangles of the carbon support within the ellipsoid.[17)] The triangles of the carbon mesh inside the ellipsoid are highlighted in Fig. 5.30. The direction of the mean surface normal is indicated by the line originating from the centre of the ellipsoid. Note that triangles not visible in the view of Fig. 5.30 also contribute to the normal calculation.

The upper image in Fig. 5.30 shows that this estimation can be inappropriate if the ellipsoid only encloses very few triangles of the carbon surface. To improve this the

[16)] The carbon segment was transformed into a mesh representation as well because this enables the use of VTK-functions for the evaluation.

[17)] The ratio of the length of the resulting vicinity to the enclosed surface area of the carbon within the vicinity yields a measure for the unevenness of the local surface.

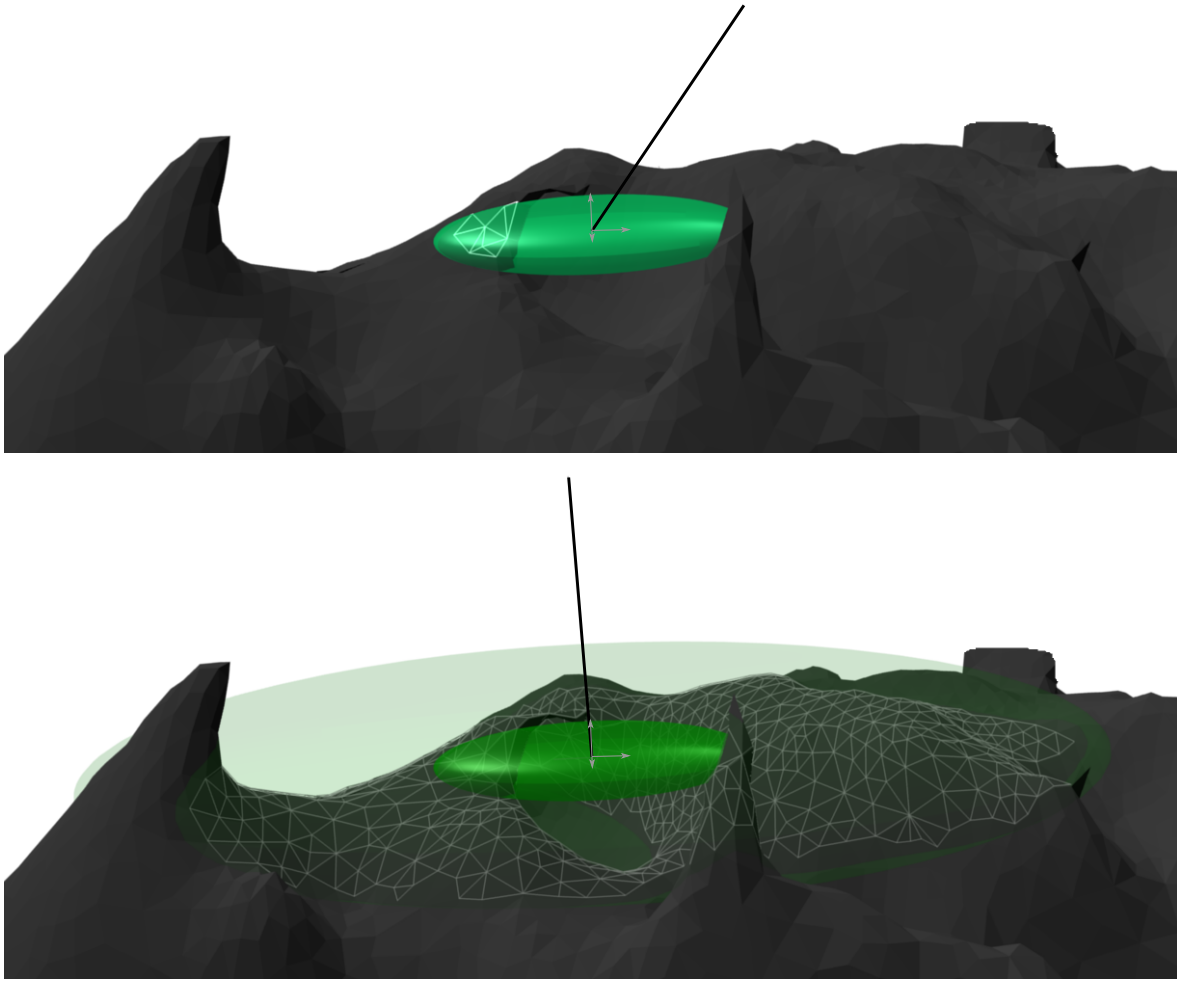

Figure 5.30: Calculation of the local carbon surface normal

Schematic images to explain the calculation of the local average surface normal. The top image shows an ellipsoid that touches the supporting surface only at its left end. Only the few highlighted faces of the support mesh are used for the calculation of the local average normal (black). However, in the overall view the ellipsoid lies flat on the supporting carbon (which e.g. got displaced by previous filtering). The extension technique (described in the text) allows to account for this. The transparent ellipsoid in the bottom image is the extension of the actual one. The amount of triangles contributing to the local carbon surface normal calculation increased significantly yielding a more appropriate estimate of the average surface normal.

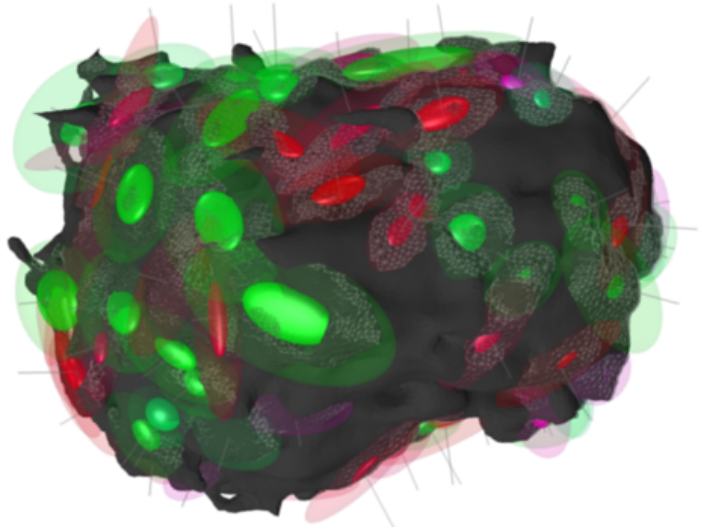

Schematic image of the process that evaluates the local orientation of the ruthenium particles to their carbon support. The support particle (grey) is rendered together with the fit-ellipsoids. The transparent ellipsoids are the extensions of the actual ones (opaque). The outlined triangles of the support inside the extended ellipsoids are used for the calculation of the average local normals. The prolate-like ellipsoids are coloured in red whereas the oblate-like ellipsoids are coloured in green.

Figure 5.31: Carbon support, local surface normals and fit-ellipsoids

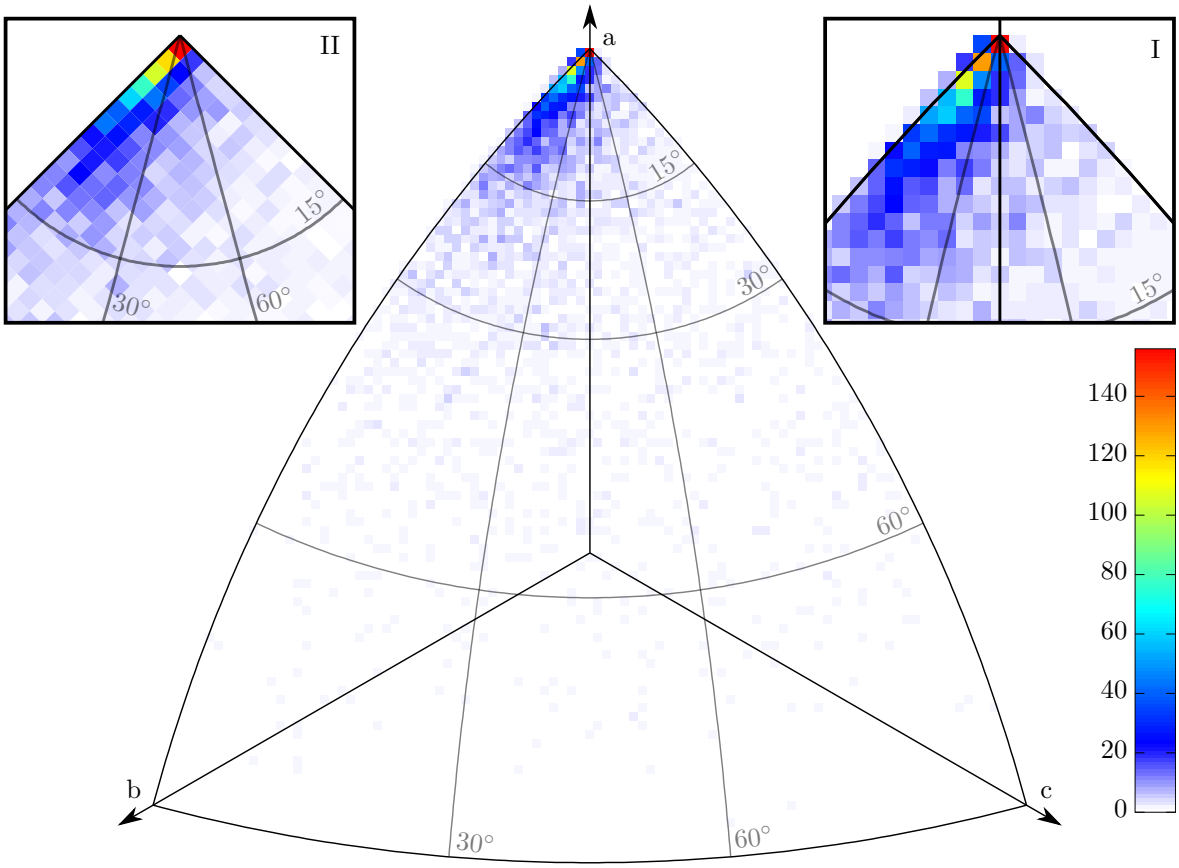

Figure 5.32: orientation tendency of the ellipsoids to the local support surface
The histogram visualizes the orientation tendency of the ellipsoids to their local support surface. Each local surface normal is expressed by the coordinate system of the corresponding axes of the ellipsoid (a,b,c). The direction of a,b,c are defined such that all normal vectors lie within the positive quadrant. The intersection points of these normal vectors with the unit sphere are stereographically projected. The projection direction along [111] causes least distortion for this part of the unit sphere.
Inlay I and II show the region around the a-axis magnified by two. As most points are close (up to 15°) to the a-axis [100] it is reasonable to project stereographically along [100] direction (a-axis). This allows to circumvent the under sampling of the histogram fields along the edges (inlay II).

ellipsoid was inflated by about 1 nm (see lower image in Fig. 5.30). After this extension, much more triangles are considered in the calculation of the mean local carbon surface normal. It only makes sense to consider ellipsoids near the carbon surface, i.e. that intersect with the mesh of the carbon surface. Finally, the orientations of the mean local surface normals relative to the axes of their fit-ellipsoids can be evaluated for all particles (Fig. 5.31).

A graphical visualisation of these results can be obtained by regarding the orientation of the local surface normal as a point on the unit sphere. The coordinate system implied by the ellipsoid's axes can be chosen such that all angles are $\leq 90°$. This makes the points of all local normals lie within the spherical triangle of the first quadrant and allows to combine the data in a single plot. Fig. 5.32 shows the stereographic projection of this quadrant along [111] direction. As before, the point density is visualized by a 2D-histogram. The corners of the projected spherical triangle correspond to the directions

of the ellipsoid axes (a,b and c).

Most particles are oriented in such a way that the local surface normals of the carbon points along the a-axis which is by definition the smallest of the ellipsoids axes. As a preliminary discussion, this means that most particles stick to the carbon in such a way that they are in a potential minimum of the attractive forces of the carbon surface, i.e. they stick to the carbon support with their least curved ('flattest') side.[18)] For a nearly even surface this also means that the contact area of the slightly embedded particles to the carbon surface is maximized, as generally expected. Therefore, the 'flattest' side can be regarded as the 'largest' side.

However, the 2D-histogram in Fig. 5.32 shows a significant deviation from the expected radial distribution around the a-axis point in the top corner. A larger fraction of particles can be found along the arc connecting a-axis and b-axis (see Inlay II in Fig. 5.32). This suggests that a statistically significant number of particles seems to not contact only the carbon support with their largest side but also with the next smaller side. Such cases can be explained by particles aligned along steps of graphene layers on the outer surface of the carbon support (as in Fig. 6.2).

[18)] Strictly speaking, ellipsoids do not have 'sides', only e.g. the smallest enclosing box or the corresponding particle of a fit-ellipsoid.

Chapter 6

Discussion

An interpretation of the results obtained are given in this chapter. Additionally, ideas are outlined how these results can be used to improve production and catalytic activity of the investigated samples. The following sections are divided into discussions concerning data acquisition (Chap. 4), the actual results (Chap. 3 and 5) and issues of artefacts and resolution.

6.1 Acquisition limitations

Apart from problems with the acquisition software (WinTEM, DMG), the two major problems limiting the quality of the acquired tilt series were beam damage in conjunction with a mechanically misaligned TEM.

A higher SNR would improve the resolution of the tomograms and reduce the need for filtering. However, any method increasing the SNR (by increasing the illumination intensity or by longer acquisition times) leads to a higher total dose on the sample. This in turn causes more beam damage to the sample, either by contamination or by etching (see Sec. 2). Beam damage originates from hydrocarbon (contamination) or H_2O, O_2 or N_2 (etching) on the sample or in the sample chamber. Prior to TEM investigations, the samples were heated in a furnace to remove any possible remnants of the TEM sample preparation procedure (see Sec. 4.1). Since in other TEMs[1)] beam damage to the same samples was barely observable, it is likely that the beam damage is not caused by molecules introduced into the chamber by the sample. Over the three years time of studies, a general increase in the contamination rate (apart from the usual 'daily variations') could be noticed which might originate from successive service operations affecting the sample chamber.

The thickness of contamination coatings can be estimated in the sinograms of the tilt series after the fine alignment with markers, see Fig. 6.1. The accuracy of fine alignment is not influenced directly by the change caused by contamination because the contrast difference between gold and contamination is sufficiently high. As with etching, contamination also causes local tension, resulting in bending and contraction

[1)] FEI Tecnai F20-G2 TEM at the Electron Microscopy Group in the Department of Materials Science & Metallurgy, University of Cambridge and CM30 at HZB

of the carbon support foil. This changes the positions of the markers with respect to each other and in relation to the catalyst particle. The estimation by tomogram slices or TEM images is less reliable since the difference in contrast and structure between the contamination carbon and the support carbon is very faint. In some cases the original extent of the carbon can be estimated indirectly by the region containing ruthenium particles (see e.g. Fig. A.4).

The dependence of some adjustments and the tracking characteristics on the position of the chosen ROI (as described in Sec. 4.2) is probably due to mechanical misalignment of the rotation axis of the goniometer and the optical axis of the objective lens/TEM. The rotation axis appears to be significantly tilted out of the plane normal to the optical axis. Additionally, the optical axis and the rotation axis are displaced (as described by Fig. 4.5). The mechanical adjustment of the goniometer to reduce this misalignment can only be done by service personnel. However, the available space for mechanical adjustment of the goniometer to the TEM column is not sufficient to achieve an alignment such that the eucentric height, illumination- and image-shift would be independent of the chosen ROI. This would reduce image distortions (e.g. magnification changes) and the need for manual interaction (e.g. needed when tracking limits are reached or changes between successive tilts are too large for automated tracking) and would allow the use of pre-calibration curves [198]. Tracking with pre-calibration curves and without manual interactions would in turn reduce the overall dose on the sample.

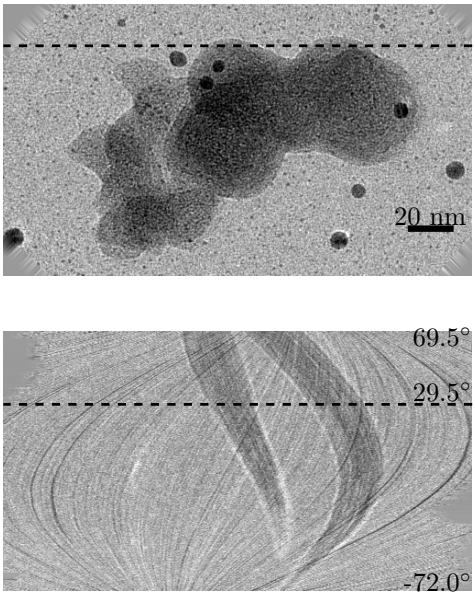

Figure 6.1: Contamination thickness estimation in sinogram

The top image shows the VC_{CO_2} particle from Fig. 5.5 at a tilt angle of 29.5° (xy-view). The dashed line indicates the position of the sinogram shown in the bottom image. The sinogram corresponds to the x-z-view of the tilt series stack. The z-coordinate corresponds to the tilt angle and therefore ranges from -72.0° to 69.5° for this tilt series. While the sine-traces of the small gold marker are nearly constant in width the traces of the support particle increase in width with increasing angle. Together with the radius of the local curvature of the support particle the contamination rate and thickness can be estimated.

A test done with the On-Axis Rotation Tomography Holder [47] and a cropped grid sample, as shown in Fig. A.5, showed an improved tracking behaviour, see Fig. A.12. The acquisition of the tilt series for the tomogram in Fig. 5.8 only had a $U_h \approx 800$ nm, i.e. about 80% of the trackable area at 160 kX. This improvement suggests that the Dual-Axis Tomography Holder generally used for tilt series acquisition might be bent or improperly held by the goniometer. Even with the On-Axis Rotation Tomography Holder, a misalignment of the goniometer is still present.

While the described misalignment is a general problem for TEM tomography due to the high magnifications available and a limit to the precision of the mechanics in the

goniometer, the misalignment of the TEM used is unusually hight. For example the displacement of the rotation axis and the optical axis $\overline{RO}$ is around 5 µm for the TEM used (see Sec. 4.2). Ziese et al. [198] report a displacement of just 1 µm. A more direct comparison is possible with the absolute/cumulative tracking curves. Under optimal conditions, i.e. sample at eucentric height of the goniometer and $\overline{RO}$ minimized by an initial image shift, the x- and z-tracking curves of Ziese et al. stay within about ±500 nm [198] whereas the best z-tracking curve achieved with the TEM used and the On-Axis Rotation Tomography Holder stays within $\Delta_z \approx 1600$ nm and $U_h \approx 800$ nm (see Fig. A.12). The z-tracking curves for the TEM used and the usual Dual-Axis Tomography Holder (which was the only tomography holder available for most of the studies) are far worse with $\Delta_z \approx 11000$ nm (Fig. 4.1). However, the xy-tracking curves ($U_h \approx 1600$ nm, $U_w \approx 600$ nm) are comparable with others [112; 52; 196]. The specifications for a different ZEISS TEM (ZEISS Libra 200 Kryo [194]) optimized for tomography with a piezo specimen drive are a $U_h \leq 200$ nm. In general, the distance $\overline{RO}$ can be reduced by a displacement of the optical axis achieved with an initial image and illumination shift [112; 198; 196]. However, the limits of the image shifts for the TEM used are reached when $\overline{RO}$ is still about 3 µm to 4 µm. In that case a mechanical alignment is necessary, but for the TEM used the limits of mechanical alignment are also already reached.

Motivation to reconstruct complete catalytic particles

In general, I tried to reconstruct complete catalytic particles. This avoids that any parts of the particles outside the ROI obscure the ROI at higher tilt angles (which leads to reconstruction artefacts, ROI problem). Additionally, this allows analysis of changes over the whole particle and avoids truncation problems (which is a common problem of FIB slicing datasets, see e.g. [129]). As $RuVC_{um}$ in Fig. 5.7 shows, there can be significant differences in the structure of a single catalytic particle.

In some cases, the reconstruction of the whole catalytic particle is not reasonable (e.g. in Fig. 5.2, 5.8a and 5.9). This is, for example, the case when the carbon support particle is so large that the low magnification necessary to image it completely results in a voxel/grain size too large to resolve the pores or the ruthenium particles. This problem is generally referred to as field of view [52].

It is possible to acquire multiple tilt series whose reconstructions cover the whole object if combined. These tomograms are sometimes called montage tomograms and are often used for biological samples [113; 110]. Combinations in all three directions are possible with IMOD[1]. For combinations in x- or y-direction the tilt series are combined and then reconstructed (montaged tilt series). For a combination in the z-direction, serial sections of the sample are necessary (e.g. created with a microtome) whose individual tomograms are then combined. The ROI problem can be reduced with serial sectioned samples. However, the creation of montage tilt series was not possible with the catalyst samples because of their sensitivity to beam damage. Serial sectioning was not done because the contrast difference between resin and carbon is even less than

the contrast between carbon and empty space. For biological samples, this problem can be circumvented by selected staining possible due to metabolism.

6.2 Discussion of the tomographic characterization of the catalysts

The presented methods provide a very detailed insight into the morphology of the samples studied and allow to draw conclusions about important processes taking place during production but also during catalysis. The methods of digital image analysis developed are not bound to electron tomography but could be applied to any 3D tomographic dataset.

Simplification of the sample system

Carbon-supported ruthenium nanoparticles investigated within this work may be used as electro-catalysts for the oxygen reduction reaction at the cathode side of fuel cells. However, their catalytic activity for this reaction can be significantly enhanced by decorating the surface of the ruthenium particles with Se to yield a catalyst with commercial significance [45; 191]. As the structure predetermined by Ru/C can be analysed unambiguously by TEM tomography, the results should also be valid for $RuSe_x$/C catalysts since selenization does not alter the morphology of the material above the resolution limit of TEM tomography [191; 192]. Thus, a selenium-free Ru/C intermediate was used which represents the final morphology despite the simplification.[2)].

Relation of the carbon support structure to the ruthenium particles

TEM tomography shows that most ruthenium particles are formed on the outer surface of the carbon support particles. The carbon support has different structures within it, one is more amorphous and the other more graphitic in character. These two carbon structures affect the formation of the ruthenium particles. The ruthenium particles have a preference to grow on the outer surface, but in the amorphous parts small ruthenium particles also exist inside the support.

Most ruthenium particles are found on the outer surface although the inner surface is about 3.6 times larger than the outer surface. This is due to the limited or restricted

[2)] If Se were present, the analysis would be complicated because Ru and Se could not be distinguished in the tomogram. Even energy filtered (EF) tomography would not allow to distinguish Ru and Se sufficiently because their spectra are very similar and their content in the sample is much lower than that of carbon, whose spectrum dominates. The spectra of Ru and Se [147; 56] only differ at A: Se-$M_{2,3}$, a very broad (FWHM of stripped edge ranges from 90 eV to 210 eV) and weak signal compared to the background, situated between Ru-$N_{2,3}$ and Ru-$M_{4,5}$, and B: Se-$L_{2,3}$ at about 1500 eV where the signal would be lost in the noise for this kind of sample.

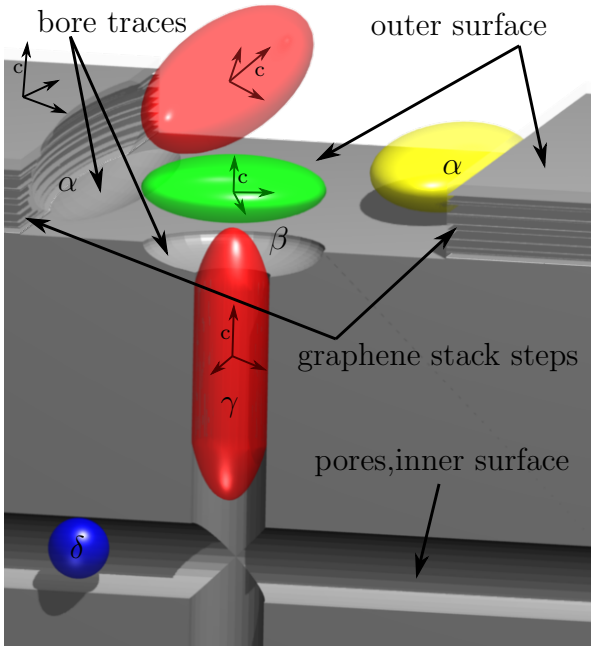

Figure 6.2: Schematic image of the ruthenium particle positions
Schematic cut-out of the structure to visualize the idealized positions of ruthenium particles related to features of the carbon support. Ruthenium particles are represented by their most likely type of fit-ellipsoid coloured according to Fig. 5.18. The particle positions at a step of a stack of graphene layers is marked by α. Pores can be closed (position β) by oblate or prolate particles or a combination of the two types. Particles inside pores close to the outer surface (position γ) can grow until their shape is restricted by the pore. Particle positions deep inside the pore system are denoted by δ. Two ellipsoids are slightly lifted from the surface to reveal their embedding/bore traces in the carbon. Local *crystallographic* coordinate systems are drawn for some ruthenium particles and graphite.

supply of RuCl during the formation process of the ruthenium particles: RuCl solution can penetrate deep into the pore system of the amorphous carbon because it has shorter and more direct connections to the outer surface (see Fig. 5.12). The pores found in this regions are comparable with types (c) (d) (e), sketched in the schematic cross section in Fig. 1 of [152, p. 1743]. The pores or cavities (like type (a) in [152, p. 1743]) in the more graphitic regions –the regions that are like layers of onions– have little or no direct connections to the outer surface which prevents the RuCl solution from penetrating deep into this pore system.

Supply of RuCl solution is important in the formation step of the ruthenium particles. If the supply in the pores is limited or even ceases, because the connection to the RuCl solution is blocked by condensation of the liquid close to the entries of micropores, the number of ruthenium particles formed after hydrogen treatment is limited and the particle shape defined by the size and the geometry of the micropore (see Fig. 6.2). Therefore, the particles that form inside the pore system (blue ellipsoid in Fig. 6.2) cannot grow as much as the particles on the outer surface. Furthermore, only very few particles can grow in the more graphitic regions since the pore system here has even fewer connections to the outer RuCl supply. This explains why only very few ruthenium particles are inside the part left of arrow A (Fig. 5.11) despite the high *lpd*, but also why the ruthenium particles in the more amorphous part on the right are small.

Hence, the large inner surface of the carbon support contains fewer ruthenium particles than the outer surface and therefore the inner surface and its ruthenium particles contribute less to the overall catalytic effectiveness of the material. In other words, the increase of the surface-to-volume ratio through the inner surface (from 0.16 nm^{-1} to 1.14 nm^{-1}) has less effect than an increase of the ratio by additional outer surface would have. Space in the pores is too restricted (i.e. the pore volume is too small) for the pore system to have the same importance on catalysis as the outer structure. This

holds with respect to the amount of catalytic sites but also regarding the accessibility of these sites by the reactants.

One third of the total ruthenium surface has no interface with the carbon support. One explanation for this low amount is the confinement of the particles inside the pores and the partial embedding of the outer particles into the carbon support (see Fig. 6.2). This means that only one third of the total surface of the ruthenium particles present in the investigated sample can contribute to the catalytic active surface in the process of the oxygen reduction reaction at the cathode side in a fuel cell. This result can tentatively be explained by particle formation as a result of the interaction of the RuCl precursor adsorbed on the carbon surface and the subsequent reduction of it by hydrogen under formation of ruthenium nanoparticles. The probability of nucleation of metal particles is highest in pores and along steps/kink sites of graphene layers at the outer surface of the carbon support. Homogeneous nucleation can be expected in amorphous cavities of the carbon support. Formation of (0 0 1), (1 0 0), (0 1 1) and facets of equivalent symmetry is most likely due to their low surface energies [131]. These crystallites have the shape of truncated hexagonal bipyramids occasionally combined with the facets of a hexagonal prism. Most projections of such nanoparticles are nearly spherical under limited resolution as reported by Nielsen et al. [131]. The elongated particles are expected to exhibit a preferential growth in the direction of the hcp c-axis of the metallic ruthenium. They are assumed to either grow along micropores (position γ in Fig. 6.2, generally oriented in the [0 0 1] direction of the graphite, i.e. perpendicular to graphene layers) or along steps of graphene stacks on top of the graphite substrate (position α in Fig. 6.2, c-axis of the metallic ruthenium perpendicular to the [0 0 1] direction of the graphene layers). Particles at position α in Fig. 6.2 would explain the spread towards the b-axis in Fig. 5.32. Not only the 'flattest' side touches the carbon support but also the 'next flattest' side, which sticks to the step of a stack of graphene layers. Particles which nucleate on top of micropore entries (position β in Fig. 6.2) presumably form tabular ellipsoids by interaction of the (0 0 1) ruthenium facet with the graphene surface (epitaxial orientation). It can further be assumed that catalytic effects occur on e.g. (1 0 0) and (0 1 1) facets of ruthenium rather than on (0 0 1) facets because of the higher surface roughness and a higher coordination of absorbed gas molecules (see Fig. 5.24). The higher reactivity of those centres compensates for the decreased catalytic active surface of the Ru particles due to their embedding.

Another possible reason for the embedding is that ruthenium particles catalyse carbon oxidation in the annealing process, causing them to bore themselves into the carbon support.[3)] This effect is more pronounced in amorphous regions. In more graphitic regions they remain on the surface, catalysing the steps/kink sites of graphene layers which causes them to move along these steps at kink sites on the surface. This behaviour would also explain the spread towards the b-axis in Fig. 5.32.

[3)] A publication about this effect is in progress (G. Zehl and others).

The importance of covered and uncovered ruthenium surface

The two thirds of the ruthenium surface that touch the carbon support are also important since the electrons have to be conducted from the carbon support to the ruthenium particle during the catalytic process in the fuel cell. The larger the contact area of the ruthenium particles to the carbon support, the higher is the conductance. Therefore, the quantity Σ (the ratio of uncovered to total ruthenium surface) is expected to possess an optimal value. If Σ is close to 0, the amount of uncovered ruthenium surface is low and limits catalytic activity, if Σ is close to 1, catalytic activity is limited due to insufficient conduction of electrons.

Comparison with 2D-TEM, XRD and ASAXS results

The ruthenium particle size distribution (Sec. 5.3.4.2), assuming spherical symmetry, yields two radii of which the bigger radius $r_2 = 1.4$ nm corresponds to a diameter of 2.8 nm with a variance of 1 nm. This result is comparable to the diameters evaluated by other methods: ASAXS [192]: 2.5 nm; XRD [192]: 2.2 nm; BF-TEM: 3±1 nm. If only one Gaussian function (as for ASAXS and XRD) is fitted to the radius distribution in Fig. 5.3.4.2 the resulting mean diameter is about 2.5 nm. We explain the slightly higher estimate from TEM images by the actual deviation from spherical symmetry and the fact that isotropically oriented ellipsoidal particles generally appear bigger in a projection than the radius estimated by an equal volume approach (as in Fig. 5.3.4.2). Also, smaller particles are more easily overlooked since these are manual measurements.

I expect the deviation of the particles from spherical shape to lead to a broadening of the peaks in the XRD and ASAXS measurements since the deviation from spherical shape creates orientation-dependent changes of the diameter. An ideal, i.e. error-free, but orientation-independent measurement of the diameter of a single non-spherical particle would yield a mean diameter that would already have a variance. Therefore, a distinction between spherical particles with varying diameter and isotropically oriented but identical, non-spherical particles is difficult with integral measurement methods.

This restriction of integral measurements also explains the different results for the sizes of the carbon support particles. As the images of the various sample particles at the beginning of Chap. 5 show, the most common spatial frequency, that can be regarded as a ‘size’ measure, is in the range of 10 nm to 60 nm. The result from the ASAXS measurement of the carbon particle diameter $\varnothing \approx 26$ nm [192] lies in this range. However, TEM images reveal that this is by far not the ‘size’ a sieve would have to have to let these particles pass through the mesh of the sieve. TEM images also show that the carbon particles deviate from spherical shape more than the average ruthenium particle.

Comparison with NAA result

Neutron activation analysis (NAA) yields a mass ratio of ruthenium to carbon of $m_{Ru}/m_C = 20.6\%$. This is equivalent to a volume ratio[4)] of V_{Ru}/V_C ranging from 3.3% to 4.2%; the same ratio evaluated from tomograms is about 4.3%. This is a good agreement taking into account that NAA is based on a much bigger volume than TEM tomography.

Comparison with electrochemical CO stripping result

There has been an attempt to determine the fraction of the total ruthenium surface of the presented samples that is available for the catalytic reactions by electrochemical CO stripping.[5)] My calculation to relate the result of the CO stripping (surface area per mass) to the uncovered surface evaluated by tomography (described in Sec. 5.3.6.1) can be found in App. A.5. CO stripping yields a value of $S_{Ru} \approx 50$ nm^2 for the 'poodle' particle of RuVC$_{um}$, while the tomographic analysis yields a value of $S_{ubs} \approx 74000$ nm^2 (Sec. 5.3.3). An explanation for the high discrepancy can be a significant difference in the *active* and the *uncovered* ruthenium surface. The two quantities do not have to be equal because different ruthenium facets have different coordination numbers for absorbed gas molecules. This means that the amount of actually absorbed gas molecules per uncovered surface area varies depending on the exposed facet type.

Another explanation for the discrepancy can be the actual existence of a thin film covering the ruthenium particles which is visible in the tomogram. It was removed under the assumption that it is a reconstruction artefact, which might be inappropriate. If at least some fraction of the removed film was actually existent, the discrepancy would be less. If the covering film is not removed in the tomogram, there is no uncovered ruthenium surface at all. This shows, that the tomographic evaluation is completely dependent on digital filtering and does not yield a reliable result. However, the method gives an estimation of the maximum available ruthenium surface (ranging from $S_{bs} \approx 2.03 \cdot 10^5$ nm^2 to $S_{as} \approx 2.25 \cdot 10^5$ nm^2 for about 2000 to 6000 particles, see Sec. 5.3.3) and suggests that an actual removal of the cover would increase the uncovered ruthenium surface significantly. The method also shows that, at least for RuVC$_{um}$, only a very thin layer (about 1 nm) has to be removed to achieve an increase of the uncovered ruthenium surface of about 30%. If the layer consists mostly of carbon, the removal can possibly be realized e.g. by an additional CO_2 treatment (as it was done on the raw carbon support) after the application of the ruthenium or after the application of the selenium if this does not chemically modify the catalytic (Ru or RuSe$_x$) particles. The removal would have to be done very carefully not to loosen the catalytic particles from the support completely.

[4)] Using the density of Ru: $\rho_{Ru} = 12.37$g/cm^3 and the density of graphite ρ_C ranging from 2.0 g/cm^3 to 2.5 g/cm^3 [93]. The density of graphite is used because the pore volume is not included in the ratio calculation from the tomogram measurements.

[5)] The measurements were performed by I. Dorbandt (HZB).

Another reason for the discrepancy could be an underestimation of the active ruthenium surface determined by CO stripping. According to Wippermann et al. [186], there is no suitable method available to determine the active surface of $RuSe_x$ catalysts because $RuSe_x$ does not adsorb methanol or CO. Therefore, methods like methanol/CO stripping or CO adsorption in the gas phase cannot be applied. However, CO stripping was not done on $RuSe_x$ but on Ru/C. If the absorption of CO was not as much as expected for the method, the active surface would be underestimated.

The divergence from spherical shape

As any deviation of the ruthenium particles from spherical shape increases their surface-to-volume-ratio, more surface is available for catalysis without an increase in material. The result is a more effective catalyst at the same material costs.

The analysis of the shape of the particles (approximated by ellipsoids) shows that most particles (about 40% of 5699) have an undefined shape, i.e. neither prolate nor oblate nor spherical. However, there are about twice as many prolate particles as oblate particles (prolate:oblate = 2:1). This ratio is not affected much by the separation procedure (without separation it is 936:422) nor is the number of spherical particles increased significantly (412 before and 676 after separation). The shape of the ruthenium particles can be an indicator for preferential growth directions that can lead to differently sized and differently oriented facets. These preferential growth directions can be along steps of graphene layers on the outer surface or along pores of the support material, see Fig. 6.2. Metallic hcp-Ru nanoparticles usually expose surfaces with different crystallographic orientation to the chemical reactants, likely featuring different catalytic activity depending on the size and orientation of the facets. Therefore, the ratio between prolate and oblate nanoparticles should be considered as one factor influencing the overall catalytic activity.

Facet analysis

Although the facet analysis in Sec. 5.3.4.6 already proves that the dataset contains particles with facets of the hexagonal crystal system, a dataset with a higher resolution is necessary to draw conclusions about the ratio of faceted and unfaceted particles. This ratio would be of particular interest for the interpretation of the catalytic activity, since the different coordination numbers of reactants on different facets (see Fig. 5.24) are expected to influence the catalytic activity due to 'facet dependent fractal dimensions' [41; 23]. For example[6)], adsorbed oxygen is threefold coordinated on (0 0 1) facets (red in Fig. 5.24). On (1 0 1) facets, both threefold and fourfold coordination sites can be found (red and green in Fig. 5.24). Atomically rough surfaces are represented by (1 0 0) facets and are responsible for complex reactions of O_2 molecules (blue in Fig. 5.24).

[6)] Examples are based on discussions with S. Fiechter.

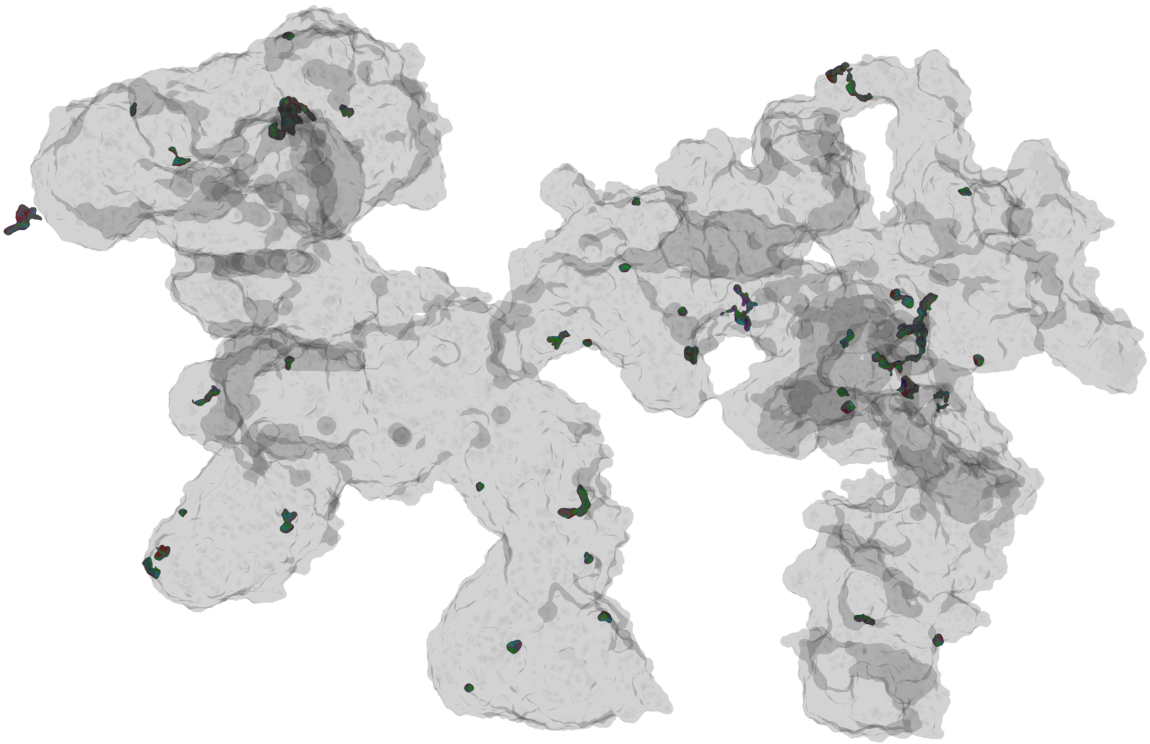

Figure 6.3: 'Highly' facetted ruthenium particles
The image shows the spatial distribution (corresponding to the view of Fig. A.6) of only the ruthenium particles with at least 6 facets with a minimum relative facet size of 4% (see Sec. 5.3.4.6). The particles are not restricted to any particular region.

It should be kept in mind that seemingly 'unfaceted' regions might consist of very small facets not resolved (see Sec. 3.4.2.1). Small facets would lead to a high number of edges. Since it is unclear how significant the contribution of edges to the catalytic activity is [41], seemingly 'unfaceted' regions might be important as well. In general, not only the type of facet (i.e. the individual Miller indices) but also the relative facet size and the ratio of faceted to unfaceted regions influence catalysis. The developed facet analysis can give access to all three characteristics.

Despite the 40 'highly' faceted particles used for the facet statistics (see Fig. 6.3), there are many more particles that show facettation, i.e. that have facets but not as many and/or as big as demanded by the selection criterion used (at least 6 facets of at least 4% relative facet size). Considering a low resolution of these additional particles, the variations introduced by the increased number of interplanar angles smear out distinct peaks in the angle frequency plot. Additionally it should be noted that the smaller the interplanar angle, the higher the resolution has to be for the detection of the corresponding facets. Therefore, no peaks can be expected below about 20°.

Discretization of real space into voxels naturally leads to facettation of any object owing to the triangles introduced by the algorithm which creates the mesh representation whose orientations are based on a cubic system, i.e. voxels. For example, a simple

'lego-surface'[7] only contains up to six different face orientations, whereas the marching-cubes-surface contains up to 26 different face orientations (see Sec. 3.4.1). Therefore, the mesh has to be smoothed to adjust the orientations of the triangles (which make up the surface) such that not only the orientations of the adjacent, neighbouring voxels are taken into account as done by the meshing algorithm, i.e. 6-connectivity for a 'lego-surface' and 26-connectivity for a marching-cubes-surface. Only smoothing leads to facet orientations other than those created by the meshing algorithm. Smoothing adjusts triangle orientations according to an average orientation within a radius of influence of a smoothing kernel, i.e. it extends the radius of influence from the nearest neighbours (6|26-connectivity) to neighbours farther away. The degree of smoothing can be regarded as the length of a chosen radius of influence. If the radius of influence is chosen too small, the influence of orientations characteristic for the discretization is still present. If the radius of influence is too large, edges become round and in the extreme the mesh approximates a sphere. The fact that only angles typical for a hexagonal system are found, leads to the conclusion that the degree of smoothing was sufficient to actually remove the distinct facettation of the raw marching-cubes-surface, which is cubic. The actual detection of facets shows that the degree of smoothing was not too large.

If particles with facets of a cubic system are represented in the tomogram (as presented in Sec. 3.4.2) the simple conclusion from above for a sufficient degree of smoothing cannot be used. However, the 26 orientations of a marching-cubes-surface are globally fixed to the coordinate system of the voxel representation. Therefore, if particles with facets typical for the marching-cubes-surface actually exist in the dataset (e.g. octahedra as in Sec. 3.4.2.2 and Sec. 3.4.2.1) a different orientation of these facets to the global coordinate system allows conclusion about a sufficient degree of smoothing. This is, for example, visible in Fig. 3.4 where the maxima of the LWPDs do not lie on the 26 symmetry points of the global coordinate system, compared with Fig. A.11 which shows the facet analysis result without smoothing.

Impurities

In general it is not possible to distinguish between impurity particles already present in the carbon support without ruthenium and the ruthenium particles added. Neither do the grey values of impurities or ruthenium differ significantly in the reconstructions nor is it possible to completely rule out either type depending on the positions on/in the support, because either type can be found in as well as on the support. However, there are many more particles in/on the support after ruthenium application than before. Also, XRD and ASAXS measurements showed that ruthenium is definitely present [192] and impurity particles seem to be distributed within the support quite homogeneously and therefore are rarely on the surface of the support. No impurities

[7] The term 'lego-surface' is used for the unmodified surface of a voxel representation, i.e. the 'lego-surface' only consists of voxel faces (squares) that can have one of only six different orientations.

were observed in the ball structure characteristic for the VC samples (see VC_{um} and VC_{CO_2} in Sec. 5.1).

A significant influence of the impurities on catalysis cannot be expected since the impurity particles are few and mainly inside the support. Sulphur is expected as an impurity of the carbon particles [30]. However, the attenuation coefficients of the impurities in the tomograms are found to be closer to that of ruthenium and gold than to carbon, but the atomic number Z (on which contrast depends, see Chap. 2) of sulphur ($Z = 16$) is much closer to carbon ($Z = 6$) than to ruthenium ($Z = 44$) or gold ($Z = 79$). Therefore, another explanation for the presence of impurities could be that some gold from the markers on the carbon foil may have been washed from the foil by the butanol when the dispersed catalyst particles were dropped on the sample grid during the TEM sample preparation (see Sec. 4.1). This would only explain particles on the surface of the carbon support. The impurity particles that reside deep inside the carbon support particles might therefore originate from diffusion of the gold nanoclusters from the carbon foil [103].

6.3 Artefacts and resolution

The 'quality' of tomographic reconstructions depends on the degree of reconstruction artefacts present and on the resolution of the tomogram. Depending on the definition of resolution, this term may already incorporate the loss of quality of a tomogram by artefacts. This is not the case for the resolution estimate by FSC because the artefacts represent mutual correlations between the two half-datasets evaluated by the FSC [177; 33]. For example, as shown by Mastronarde [111], the reduction of the 'missing wedge' artefact by dual-tilt reconstructions depends on how the two tomograms were combined. The reduction of the artefact is better if the datasets are combined in Fourier space than by averaging in real space. However, the FSC resolution estimate is only based on the two individual datasets before combination and therefore cannot account for the improvement in quality by the combination method used.

In the end, the definition of the resolution limit depends on what is analysed. For example, the resolution needed for the mere distinction of two separated objects is less than the resolution needed to analyse facets of these two objects. Therefore, it can be concluded that the influences of resolution limit and reconstruction artefacts on a result must be discussed with respect to the applied evaluation.

Influences of artefacts

The ruthenium particle representations are expected to be affected by the missing wedge which causes an elongation of the ruthenium particle representation. This will result in a tendency towards prolate ellipsoids in the shape analysis. Therefore, the actual ratio of prolate to oblate shaped particles will be more balanced than 2:1 (result from Sec. 5.3.4.3). However, an actual deviation from spherical symmetry is definitely

present due to the significant number of oblate particles. The effect of the missing wedge on spherical particles would only lead to prolate particle representations, i.e. a ratio of prolate to oblate of 1:0.

The fact that in most cases the a-axis of the ellipsoid is aligned with the local surface normal (see Sec. 5.3.6.2), rules out a significant effect of the missing wedge in the DIRECTT reconstruction. An elongation of the particles caused by the missing wedge would not be isotropic but only along one global axis. This would not permit a result as obtained by the local alignment analysis (Sec. 5.3.6.2) since the orientation of the local carbon surface normal can be expected to be isotropic.

Also the fact that the elongation caused by the missing wedge has a global orientation allows to regard the evaluation in Sec. 5.3.4.5 as a measure of how pronounced the missing wedge artefacts are. Figure 5.20 visualizes the significant differences of this effect between the evaluated reconstruction algorithms. This method, together with the ellipsoidity evaluation (Sec. 5.3.4.4), should also allow evaluation of how pronounced the 'gluing' of particles by streak artefacts is (as in Fig. A.8) as well as the effectiveness of the watershed separation as a counter measure.

Resolution

The two independent reconstructions with 1° tilt increments as described in Sec. 5.1 were used to estimate the resolution by FSC and the 2σ-criterion. The resolution estimate is taken at the intersection point of the FSC and the threshold curve, as demonstrated in App. A.2. This evaluation yields a resolution of about 1.2 nm which is close to the limit of 1 nm that is generally reported to be achievable [90; 122]. According to Cardone et al. [33, sec. 4.6], the actual resolution will be underestimated by the use of tomograms from dual tilt reconstructions because the second tilt series depicts a specimen that has been subjected to more radiation. The resolution estimate should improve further if the dependence of the resolution on the combination method (see beginning of Sec. 6.3) is taken into account. Although the FSC evaluation is often regarded as a resolution estimate [33; 177; 104] it is actually a figure of merit (FOM) [25; 52]. Figures of merit are generally used to compare different tomograms of the same object [25; 52; 107]. The difference originates from changes in the creation procedure of the tomograms, e.g. from different reconstruction techniques [52, chap. 7] or different alignment techniques [25]. FOMs allow an evaluation of quality based on the criterion used to define the individual FOM [107]. The FSC measures the normalised cross-correlation coefficient between two 3D volumes over corresponding shells in Fourier space [177]. In other words, the FSC measures the SNR as a function of spatial frequency. There is no simple relationship between the FSC and the resolution concept used in optics, where the wavelength and the point-spread function (PSF) of the imaging system are regarded [52, chap. 7]. The modulation transfer function (MTF) resolution estimate used for tomograms obtained by other methods (e.g. X-ray or neutron tomography) is based on a minimal contrast difference as a function of spatial frequency [29, sec. 9.2] and can be related to the PSF. In my opinion an

ultimate resolution estimation should regard both the SNR and the MTF. However, a method for such a resolution estimate is not yet known.

The FSC, the MTF and other methods like (e.g. DPR and SSNR see App. A.2) depend on a threshold criterion for the determination of the actual resolution. Many different criteria are proposed and discussed [177; 104; 52; 33] but lead to very different resolution estimates. It seems reasonable to only use threshold curves for the FSC evaluation (based on e.g. '1/2-bit'- and σ-criterion) that depend on the spacial frequency and that take important properties of the individual tomogram into account (e.g. symmetry, fraction of the object to the reconstructed space) [177].

Samples containing a variety of differently sized structures but a low variance in shape and size of the individual structure are ideal to estimate an object determined resolution (ODR, as mentioned in Sec. 2). Biological samples often fulfil this condition because cell constructs, macro molecules and their substructure down to atom spacings are already known (see e.g. [35; 120]). The studied samples are not ideal for an ODR estimation. Nevertheless, the studied samples can be used to some extent for an ODR estimation since 2D-TEM, XRD and ASAXS measurements are available. It can be concluded from the agreement of the ruthenium particle size measurements that the resolution of the tomogram is at least 2 nm. This can only be regarded as a rough estimate because the variance of the ruthenium particles is large. It should be noted, that this resolution estimation results in a better resolution than that given by the Crowther criterion (eq. 2.1). The direction dependent resolution estimation by eq. 2.1 and eq. 2.2 for the poodle particle with $D \approx 250$ nm, $N = 144$, $\delta_y \approx 1$ nm (see Fig. 2.1) yields $\delta_x \approx$ 5.5 nm, $\delta_z \approx 7.0$ nm

The resolution limit concerning resolving shape can be estimated with the result of the facet analysis (Sec. 5.3.4.6). The result shows that particle shapes are resolved sufficiently to exhibit the expected facettation down to a particle size of 2.6 nm (10 voxels). This coincides with the estimation of Sec. 3.4.2.1 that a particle representation needs at least a diameter of about 10 voxels to exhibit actual facets. Under this consideration, the resolution here is limited by the voxel size and not yet by the device. These might only be local resolutions, since only few particles showed a high degree of facettation. However, the particles fulfilling the restrictive criteria of the evaluation are not restricted to any particular region of the tomogram (see Fig. 6.3).

The estimation of the ODR limit set by the TEM and the reconstruction method used cannot be determined by the tomogram of the poodle particle because the voxel size limits the resolution. Although the TEM offers magnifications up to 1000 kX, the high magnifications could not be used for tomography because of the mentioned tracking/alignment problems. The highest magnification that lead to a usable tilt series was 160 kX (see Fig. 5.8). However, the directly interpretable resolution most images of the corresponding tilt series have is only about 9 Å (determined as in Fig. 2.1) due to the used defocus. The resolution limit of the corresponding tomogram could not yet be evaluated due to software problems.

Chapter 7

Summary, conclusions and outlook

The presented work demonstrates that electron tomography can provide a quantitative structure analysis of catalytically active ruthenium nanoparticles supported by carbon. The detailed analysis of $RuVC_{um}$ (see Fig. 5.7) shows that the size distribution of the ruthenium particles is bimodal. Particles from the smaller mode are formed preferentially within the more amorphous parts of the support, whereas larger particles are formed on the outer surface of the support. Fitting ellipsoids to the individual particles reveals that most particles are not spherical and the ratio of prolate to oblate particles numbers is about 2:1. The analysis of the alignment of the ruthenium particles with respect to the local support surface suggests that prolate particles form along the edges of graphene sheets on the support or grow along pores. One factor influencing the overall catalytic activity is the ratio between prolate and oblate nanoparticles since it can indicate preferential growth directions which lead to differently sized facets. The analysis of the facets of ruthenium particles indicates that not only facets of hexagonal prisms and pyramids are formed but also facets of twelve-fold symmetry. The catalytic activity is expected to vary between different facets due to different coordination numbers.
It could be quantified how pronounced the missing wedge artefact is depending on the reconstruction algorithm used concerning assessment of the shape. The reconstruction of the DIRECTT algorithm exhibits an insignificant effect of the missing wedge enabling a reliable interpretation of the shape of the ruthenium particles.

My studies enabled me to characterize the given catalysts and to suggest further procedures during production to improve the catalytic properties of the investigated catalysts. For example, the use of a carbon support with less micro porosity might be better since ruthenium particles that form deep inside these pores are barely accessible by the reactants and therefore probably contribute little to the overall catalytic activity. Furthermore, an additional processes that removes a possibly existent but actually very thin cover over the ruthenium particles would increase the uncovered ruthenium surface. Thus, electron tomography has proven to yield valuable general information about the distinct nanostructure of different classes of catalytically active particles. Their individual contribution to the overall catalytic activity should be con-

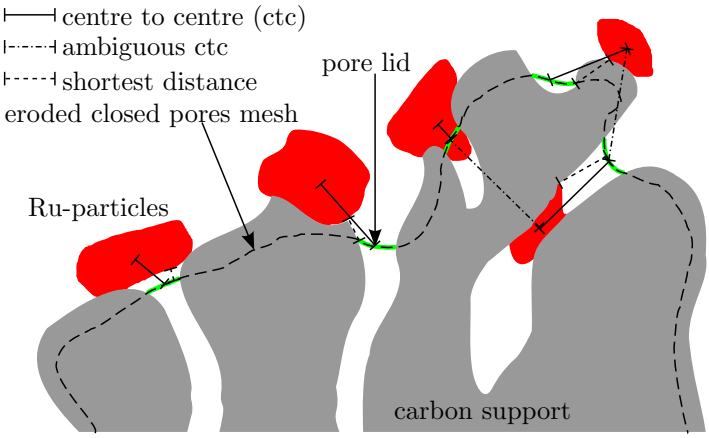

Figure 7.1: Relation of the pore entries to the ruthenium particles
Schematic drawing to demonstrate the evaluation of the relation of pore entries ('pore lids', green lines) of the carbon support to the ruthenium particles (red). The meaning of the labels is explained in App. A.4.

sidered in further investigations to optimise the oxygen reduction performance e.g. of carbon-supported selenium-modified ruthenium catalysts ($RuSe_x/C$).

For a more detailed characterization of the carbon support particles (in addition to that in Sec. 5.3.5) the following methods for analysis should be considered: A characterization of the pore size distribution by digital 3D granulometry [150; 162; 14; 39] or 3D-FFT-band-pass-filter, a shape analysis based on the Hessian-matrix [8], a percolation [134] and tortuosity [55; 53] estimation of the more graphitic and more amorphous parts, an individual pore analysis achievable by skeletonization [162; 39; 14]. A fractal characterization of the support (as done in e.g. [92; 181]) would be interesting as well. These properties are mentioned by Rouquerol et al. [152] as descriptions of complex pore systems and would enable a deeper understanding and possibly lead to improvements in production (e.g. concerning the discussion about the penetration of the RuCl solution in Sec. 6.2). However, the application of these methods to tomographic data is complicated and would need a carbon representation with a higher resolution than currently achievable with the available TEM because most pores are smaller than 2 nm. Although Rouquerol et al. [152] did not mention tomography as a characterization technique at that time, it should now be considered as well. Results obtained by tomography can be compared with other methods such as XRD and ASAXS but also with the Brunauer-Emmett-Teller (BET) physisorption method or capillary condensation (see e.g. [152]).

Apart from the analyses presented of the uncovered ruthenium surface (Sec. 5.3.6.1) and the local alignment of the particles to the support (Sec. 5.3.6.2), it would be interesting to also analyse the relative position of ruthenium particles in regard to the pore openings (see Fig. 7.1), and, the local curvature of the support in the vicinity of the ruthenium particles (as done by Ward et al. [181]). However, these properties were not probed because of uncertainties in the carbon representation, which would have had a strong influence on the results. The influence of the uncertainties is lower for the presented studies because they are based on integral measures instead of punctual measures such as the positions of pore entries and support curvature. Measurement of the support curvature can be done with standard methods (as described by e.g. Meyer et al. [119]) which are already implemented in (e.g. ITK[2] DiscreteGradientMagnitudeGaussianImageFunction and VTK[3] vtkCurvatures). The quantitative analysis of

the relation of particle positions to pore entries would be new and is described in short in App. A.4.

It would be interesting to use the (noise-compensated) leave-one-out method ((N)LOO) instead of FSC to estimate the resolution of tomograms. NLOO is a method based on the idea of comparing a single projection with the corresponding reprojection of a tomogram calculated from all the other projections with the exception of the projection in question (see e.g. [33]). Such an analysis would show the dependence of resolution on tilt angle. However, to apply this method software is needed that performs this evaluation.

In the future it might be possible to gain further insight into dimensions higher than our restricted three-dimensional world of experience with the help of digital reconstructions of 4D or higher dimensional space based on 3D 'projections' that make up our world. The difficulty will be to realize how something in 4D is projected to make an alignment of the 3D images possible as needed for reconstruction. With reprojections, slices and digital analyses of these 4D reconstructions, new insights might be gained to understand how our world is built. An example: Possibly, the evolution of the solar system can be explained and predicted in higher detail and accuracy with the idea that the solar system represents a 3D projection of a 'simpler' 4D rotating object. Thereby relating back to Goethe's Faust, the poodle and the wish to know: „ ... was die Welt im Innersten zusammenhält."

Bibliography

[1] J. Ahrens, B. Geveci, and C. Law. ParaView: An End-User Tool for Large Data Visualization. In C. Hansen and C. Johnson, editors, *In the Visualization Handbook*, chapter 36, pages 717–733. Elsevier, 2005.

[2] H. Alexander. *Physikalische Grundlagen der Elektronenmikroskopie*. 1997.

[3] R. M. Alijev and N. S. Jevsikova. Eine strukturgeometrische Analyse der Kristallflächen von Spinellen (am Beispiel von Magnetit). *Kristall und Technik*, 4(2):265–278, 1969. doi:10.1002/crat.19690040210.

[4] S. P. Alonso. Fiducial markers of different materials for electron tomography. Technical report, Helmholtz Zentrum Berlin für Materialien und Energie (HZB), 2009.

[5] N. Alonso-Vante. Carbonyl Tailored Electrocatalysts. *Fuel Cells*, 6(3-4):182–189, 2006.

[6] N. Alonso-Vante, H. Tributsch, and O. Solorza-Feria. Kinetics Studies of Oxygen Reduction in Acid Medium on Novel Semiconducting Transition Metal Chalcogenides. *Electrochimica Acta*, 40(5):567–576, 1995.

[7] A. M. Alyassin, J. L. Lancaster, J. H. D. III, and P. T. Fox. Evaluation of new algorithms for the interactive measurement of surface area and volume. *Medical Physics*, 21(6):741–752, 1994. doi:10.1118/1.597333.

[8] L. Antiga. Generalizing vesselness with respect to dimensionality and shape. *Insight Journal*, July 2007. URL http://hdl.handle.net/1926/576.

[9] K. Appel and W. Haken. Every planar map is four colorable. *Bulletin of the American Mathematical Society*, 82:711–712, 1976. URL http://projecteuclid.org/euclid.bams/1183538218.

[10] K. Appel and W. Haken. Every planar map is four colorable. Part I: Discharging. *Illinois Journal of Mathematics*, 21(3):429–490, 1977. URL http://projecteuclid.org/euclid.ijm/1256049011.

[11] M. Aronova, Y. Kim, R. Harmon, A. Sousa, G. Zhang, and R. Leapman. Three-dimensional elemental mapping of phosphorus by quantitative electron spectroscopic tomography (QuEST). *Journal of Structural Biology*, 160(1):35 – 48, 2007. doi:10.1016/j.jsb.2007.06.008.

[12] L. S. Avila, U. Ayachit, S. Barre, J. Baumes, F. Beitel, R. Blue, D. C. D. DeMarie, B. Geveci, W. A. Hoffman, B. King, K. Krishnan, C. C. Law, K. M. Martin, W. McLendon, P. Pebay, N. Russell, W. J. Schroeder, T. Shead, J. Shepherd, A. Wilson, and B. Wylie. *The VTK User's Guide*. Kitware, Inc., 11th edition, 2010. URL http://kitware.com/products/books/vtkbook.html.

[13] S. Bals, K. J. Batenburg, D. D. Liang, O. Lebedev, G. Van Tendeloo, A. Aerts, J. A. Martens, and C. E. A. Kirschhock. Quantitative Three-Dimensional Modeling of Zeotile Through Discrete Electron Tomography. *Journal Of The American Chemical Society*, 131(13):4769–4773, Apr. 2009. doi:10.1021/ja8089125.

[14] J. Banhart, P. Midgley, K. Schladitz, J. Ohser, N. Kardjilov, M. Weyland, et al. *Advanced Tomographic Methods in Materials Research and Engineering*. Oxford University Press, May 2008.

[15] J. Barthel and A. Thust. Quantification of the Information Limit of Transmission Electron Microscopes. *Phys. Rev. Lett.*, 101(20):200801–1 – 100801–4, Nov. 2008. doi:10.1103/PhysRevLett.101.200801.

[16] K. J. Batenburg, S. Bals, J. Sijbers, C. Kübel, P. A. Midgley, J. C. Hernandez, U. Kaiser, E. R. Encina, E. A. Coronado, and G. Van Tendeloo. 3D imaging of nanomaterials by discrete tomography. *Ultramicroscopy*, 109(6):730–740, May 2009. doi:10.1016/j.ultramic.2009.01.009.

[17] R. Beare. Morphology with parabolic structuring elements. *Insight Journal*, (228), Dec. 2008. doi:http://hdl.handle.net/1926/1370.

[18] R. Beare and G. Lehmann. The watershed transform in ITK - discussion and new developments. *Insight Journal*, (92), June 2006. URL http://hdl.handle.net/1926/202.

[19] S. Beucher and C. Lantuejoul. Use of Watersheds in Contour Detection. page 12, 1979.

[20] S. Beucher and F. Meyer. The Morphological Approach to Segmentation: The Watershed Transformation. In E. R. Dougherty, editor, *Mathematical Morphology in Image Processing*, volume 34 of *Optical Engeneering*, pages 433–482. Marcel Decker, Inc., Rochester, New York, 1993.

[21] J. Biskupek, A. Chuvilin, J. R. Jinschek, and U. Kaiser. Quantitative Investigations of the Depth of Field in a Corrected High Resolution Transmission Electron Microscope. In M. Luysberg, K. Tillmann, and T. Weirich, editors, *EMC 2008 14th European Microscopy Congress 1-5 September 2008, Aachen, Germany*, pages 101–102. Springer Berlin Heidelberg, 2008. doi:10.1007/978-3-540-85156-1_51.

[22] J. Biskupek, J. Leschner, P. Walther, and U. Kaiser. Optimization of STEM tomography acquisition – A comparison of convergent beam and parallel beam STEM tomography. *Ultramicroscopy*, 110(9):1231 – 1237, 2010. doi:DOI: 10.1016/j.ultramic.2010.05.008.

[23] P. Bogdanoff, I. Herrmann, M. Hilgendorff, I. Dorbandt, S. Fiechter, and H. Tributsch. Probing Structural Effects of Pyrolysed CoTMPP-based Electrocatalysts for Oxygen Reduction via New Preparation Strategies. *Journal of New Materials for Electrochemical Systems*, 7:85–92, 2004.

[24] A. Borbély, F. F. Csikor, S. Zabler, P. Cloetens, and H. Biermann. Three-dimensional characterization of the microstructure of a metal-matrix composite by holotomography. *Materials Science and Engineering A*, 367(1-2):40 – 50, 2004. doi:10.1016/j.msea.2003.09.068.

[25] S. S. Brandt and U. Ziese. Automatic TEM image alignment by trifocal geometry. *Journal of Microscopy*, 222(1):1–14, 2006. doi:10.1111/j.1365-2818.2006.01545.x.

[26] O. Brunke, S. Odenbach, and F. Beckmann. Quantitative methods for the analysis of synchrotron-µCT datasets of metallic foams. *Eur. Phys. J. Appl. Phys.*, 29(1): 73–81, 2005. doi:10.1051/epjap:2004203.

[27] T. Butz. *Fouriertransformation für Fußgänger*. Vieweg+Teubner Verlag, 6th edition, 2009.

[28] C. Buzea, I. I. Pacheco, and K. Robbie. Nanomaterials and nanoparticles: Sources and toxicity. *Biointerphases*, 2(4):MR17–MR71, 2007. doi:10.1116/1.2815690.

[29] T. M. Buzug. *Computed Tomography: From Photon Statistics to Modern Cone-Beam CT*. Jul 2008.

[30] Cabot. *Vulcan XC-72R*. Cabot Corporation, 2002. URL http://www.cabot-corp.com/wcm/download/en-us/sb/VULCAN_XC72R1.pdf.

[31] Cabot. *BLACK PEARLS 2000*. Cabot Corporation, 2004. URL http://www.cabot-corp.com/wcm/download/en-us/rb/BLACK_PEARLS_2000.pdf.

[32] D. Cao, A. Wieckowski, J. Inukai, and N. Alonso-Vante. Oxygen Reduction Reaction on Ruthenium and Rhodium Nanoparticles Modified with Selenium and Sulfur. *Journal of the Electrochemical Society*, 153(5):A869–A874, 2006.

[33] G. Cardone, K. Grünewald, and A. C. Steven. A resolution criterion for electron tomography based on cross-validation. *Journal of Structural Biology*, 151(2):117 – 129, 2005. doi:10.1016/j.jsb.2005.04.006.

[34] A. E. Comyns. Mixed reactant fuel cells. *Focus on Catalysts*, (5):10.1016/S1351–4180(07)70248–9, 2007. doi:10.1016/S1351-4180(07)70248-9.

[35] J. Cope, S. Gilbert, I. Rayment, D. Mastronarde, and A. Hoenger. Cryo-electron tomography of microtubule-kinesin motor complexes. *Journal of Structural Biology*, 170(2):257 – 265, 2010. doi:DOI: 10.1016/j.jsb.2009.12.004.

[36] R. A. Crowther, D. J. DeRosier, and A. Klug. The Reconstruction of a Three-Dimensional Structure from Projections and its Application to Electron Microscopy. *Proceedings of the Royal Society of London. A. Mathematical and Physical Sciences*, 317(1530):319–340, 1970. doi:10.1098/rspa.1970.0119.

[37] C. Dalitz, G. Michalakis, and C. Pranzas. Optical recognition of psaltic Byzantine chant notation. *International Journal on Document Analysis and Recognition*, 11: 143–158, 2008. doi:10.1007/s10032-008-0074-4.

[38] D. M. T. Dekker, R. Wagner, R. Blaauwgeers, J. Bueno, and R. Jochemsen. Analysis of ^{3}He Crystal Images Using a Computer-Generated Wire-Frame. *Journal of Low Temperature Physics*, 139:509–513, 2005. doi:10.1007/s10909-005-5434-6.

[39] E. R. Dougherty. *Mathematical Morphology in Image Processing*, volume 34 of *Optical Engeneering*. Marcel Decker, Inc., University of Rochester, New York, 1993.

[40] J. W. Edington. *The operation and calibration of the electron microscope*, volume 1 of *Monographs in practical electron microscopy in materials science*. Macmillan (Philips technical library), 1974.

[41] D. Farin and D. Avnir. The reaction dimension in catalysis on dispersed metals. *Journal of the American Chemical Society*, 110(7):2039–2045, 1988. doi:10.1021/ja00215a004.

[42] S. Fiechter. Materialien für Solar- und Brennstoffzellen: Präparation und physikalisch-chemische Charakterisierung. lecture, Oct.-Feb. 2008/2009.

[43] S. Fiechter. Photoelektrische und Photoelektrochemische Energieumwandlung - Materialien, Messmethoden und Konzepte. lecture, Oct.-Feb. 2009/2010.

[44] S. Fiechter. Solare Brennstoffe und Energiespeicher: Materialien, Messmethoden und Konzepte. lecture, Oct.-Feb. 2010/2011.

[45] S. Fiechter, I. Dorbandt, P. Bogdanoff, G. Zehl, H. Schulenburg, and H. Tributsch. Surface modified ruthenium nanoparticles: Structural investigation and surface analysis of a novel catalyst for oxygen reduction. *Journal of Physical Chemistry C*, 111(1):477–487, Jan. 2007. doi:10.1021/jp0618431.

[46] Fischione. *Dual-Axis Tomography Holder (Model 2040, LIBRA-design)*. Fischione Instruments, Inc., 9003 Corporate Circle Export, PA 15632 USA.

[47] Fischione. *On-Axis Rotation Tomography Holder (Model 2050, LIBRA-design)*. Fischione Instruments, Inc., 9003 Corporate Circle Export, PA 15632 USA, 035-1299 Rev 00.

[48] J. Flusser. On the independence of rotation moment invariants. *Pattern Recognition*, 33(9):1405 – 1410, 2000. doi:10.1016/S0031-3203(99)00127-2.

[49] A. Frangi, W. Niessen, K. Vincken, and M. Viergever. Multiscale vessel enhancement filtering. In W. Wells, A. Colchester, and S. Delp, editors, *Medical Image Computing and Computer-Assisted Interventation – MICCAI'98*, volume 1496 of *Lecture Notes in Computer Science*, pages 130–137. Springer Berlin / Heidelberg, 1998. doi:10.1007/BFb0056195.

[50] J. Frank. A Practical Resolution Criterion In Optics and Electron-microscopy. *Optik*, 43(1):25–34, 1975.

[51] J. Frank. Determination of Source Size and Energy Spread From Electron-micrographs Using Method of Youngs Fringes. *Optik*, 44(4):379–391, 1976.

[52] J. Frank. *Electron Tomography: Methods for Three-Dimensional Visualization of Structures in the Cell*. Springer, Berlin, 2nd edition, 2006. doi:10.1007/978-0-387-69008-7.

[53] Fraunhofer ITWM. MAVI - Modular Algorithms for Volume Images documentation. commercial, 1.3.1. URL http://www.itwm.fraunhofer.de/bv/projects/MAVI/Documents/MaviHandbook.pdf.

[54] B. Freitag and C. Kisielowski. Determining resolution in the transmission electron microscope: object-defined resolution below 0.5 Å. In M. Luysberg, K. Tillmann, and T. Weirich, editors, *EMC 2008 14th European Microscopy Congress 1-5 September 2008, Aachen, Germany*, pages 21–22. Springer Berlin Heidelberg, 2008. ISBN 978-3-540-85156-1. doi:10.1007/978-3-540-85156-1_11.

[55] H. Friedrich, P. E. de Jongh, A. J. Verkleij, and K. P. de Jong. Electron Tomography for Heterogeneous Catalysts and Related Nanostructured Materials. *Chemical Reviews*, 109(5):1613–1629, May 2009. doi:10.1021/cr800434t.

[56] Gatan, Inc. EELS Atlas. part of DigitalMicrograph™ of the Gatan Microscopy Suite (GMS), 2008.

[57] Gatan, Inc. *ultrascan*, 2011. URL http://www.gatan.com/products/digital_imaging/products/ultrascan_specs.php.

[58] A. Gelas, A. Gouaillard, and S. Megason. Surface Mesh Normals Filter. *Insight Journal*, (303):2, Sep. 2008. doi:http://hdl.handle.net/1926/1495.

[59] P. Gilbert. Iterative methods for the three-dimensional reconstruction of an object from projections. *Journal of Theoretical Biology*, 36(1):105 – 117, 1972. doi:10.1016/0022-5193(72)90180-4.

[60] M. Goitein. Three-dimensional density reconstruction from a series of two-dimensional projections. *Nuclear Instruments and Methods*, 101(3):509 – 518, 1972. doi:10.1016/0029-554X(72)90039-0.

[61] U. Golla and H. Kohl. Theoretical and experimental investigations of resolution and detection limits in energy-filtering electron microscopy. *Micron*, 28(5):397 – 406, 1997. doi:DOI: 10.1016/S0968-4328(97)00048-6.

[62] L. C. Gontard, R. E. Dunin-Borkowski, R. K. K. Chong, D. Ozkaya, and P. A. Midgley. Electron tomography of Pt nanocatalyst particles and their carbon support. *Journal of Physics: Conference Series*, 26:203–206, 2006. doi:10.1088/1742-6596/26/1/048.

[63] J. Gregor and T. Benson. Computational Analysis and Improvement of SIRT. *Medical Imaging*, 27(7):918–924, 2008. doi:10.1109/TMI.2008.923696.

[64] R. Grothausmann. In-Situ Elektronenstrahldeposition von Leiterbahnen im Transmissionselektronenmikroskop. Diplomarbeit, Universität Regensburg, Nov. 2007.

[65] R. Grothausmann, I. Manke, G. Zehl, I. Dorbandt, P. Bogdanoff, S. Fiechter, M. P. Hentschel, A. Lange, A. Kupsch, A. Hilger, and J. Banhart. Characterisation of fuel cell catalyst materials using electron tomography. *MP Materials Testing*, 52 (10):706–711, 2010. URL http://www.materialstesting.de/directlink.asp?MP110174.

[66] S. Hata, K. Kimura, H. Gao, S. Matsumura, M. Doi, T. Moritani, J. S. Barnard, J. R. Tong, J. H. Sharp, and P. A. Midgley. Electron Tomography Imaging and Analysis of γ' and γ Domains in Ni-based Superalloys. *Advanced Materials*, 20(10): 1905–1909, 2008. doi:10.1002/adma.200702461.

[67] P. W. Hawkes. The Electron Microscope as a Structure Projector. In J. Frank, editor, *Electron Tomography: Methods for Three-Dimensional Visualization of Structures in the Cell*, pages 83–111. Springer, Berlin, 2nd edition, 2006. doi:10.1007/978-0-387-69008-7.

[68] M. P. Hentschel, A. Lange, A. Kupsch, and B. R. Müller. Reconstruction of incomplete model data sets in computed tomography by DIRECTT algorithm. *MP Materials Testing*, 52(10):668–675, 2010. URL http://www.materialstesting.de/directlink.asp?MP110175.

[69] D. Hogan and D. Dyson. Angles between planes in the hexagonal and tetragonal crystal systems. *Micron (1969)*, 2(1):59 – 61, 1970. doi:10.1016/0047-7206(70)90045-2.

[70] M. F. Hohmann-Marriott, A. A. Sousa, A. A. Azari, S. Glushakova, G. Zhang, J. Zimmerberg, and R. D. Leapman. Nanoscale 3D cellular imaging by axial scanning transmission electron tomography. *Nat Meth*, 6(10):729–731, Oct. 2009. doi:10.1038/nmeth.1367.

[71] W. J. Huang, R. Sun, J. Tao, L. D. Menard, R. G. Nuzzo, and J. M. Zuo. Coordination-dependent surface atomic contraction in nanocrystals revealed by coherent diffraction. *Nature Mater*, 7(4):308–313, Apr. 2008. doi:10.1038/nmat2132.

[72] S. W. Hughes, T. J. DArcy, D. J. Maxwell, J. E. Saunders, C. F. Ruff, W. S. C. Chiu, and R. J. Sheppard. Application of a new discreet form of Gauss' theorem for measuring volume. *Physics In Medicine And Biology*, 41(9):1809–1821, Sept. 1996. doi:10.1088/0031-9155/41/9/016.

[73] A. Hungria, D. Eder, A. Windle, and P. Midgley. Visualization of the three-dimensional microstructure of TiO2 nanotubes by electron tomography. *Catalysis Today*, In Press, Corrected Proof:–, 2008. doi:DOI: 10.1016/j.cattod.2008.09.014.

[74] J. Höög and C. Antony. Whole[hyphen (true graphic)]Cell Investigation of Microtubule Cytoskeleton Architecture by Electron Tomography. In J. R. McIntosh, editor, *Cellular Electron Microscopy*, volume 79 of *Methods in Cell Biology*, pages 145 – 167. Academic Press, 2007. doi:10.1016/S0091-679X(06)79006-9.

[75] J. L. Höög, C. Schwartz, A. T. Noon, E. T. O'Toole, D. N. Mastronarde, J. R. McIntosh, and C. Antony. Organization of Interphase Microtubules in Fission Yeast Analyzed by Electron Tomography. *Developmental Cell*, 12(3):349 – 361, 2007. doi:10.1016/j.devcel.2007.01.020.

[76] L. Ibáñez, W. Schroeder, L. Ng, J. Cates, and "the Insight Software Consortium". *The ITK Software Guide*. Kitware, Inc, 2nd edition, November 2005. URL http://www.itk.org/ItkSoftwareGuide.pdf.

[77] A. Immirzi. TRY, a new computer program for crystal structure analysis from diffraction data based on internal coordinates and on a molecular modelling procedure free of redundant coordinates. *J. Appl. Cryst.*, 40(6):1044–1049, 2007. doi:10.1107/S0021889807048339.

[78] International union of crystallography. *International tables for X-ray crystallography: Mathematical tables*, volume II. Kynoch Press, Birmingham, Eng., 1972. URL http://openlibrary.org/books/OL16397366M/International_tables_for_X-ray_crystallography.

[79] P. K. Janert. *Gnuplot in Action Understanding Data with Graphs*. Manning Publications, 2009. URL http://www.manning.com/janert/.

[80] K. Jänich. *Vektoranalysis*. Springer, 5 edition, 2005. doi:10.1007/b138936.

[81] K. Kimura, S. Hata, S. Matsumura, and T. Horiuchi. Dark-field transmission electron microscopy for a tilt series of ordering alloys: toward electron tomography. *Journal of Electron Microscopy*, 54(4):373–377, 2005. doi:10.1093/jmicro/dfi060.

[82] K. Kinoshita. *Carbon: Electrochemical and Physicochemical Properties*. Wiley & Sons, 1988. ISBN 978-0-471-84802-8.

[83] F. Klockmann. *Lehrbuch der Mineralogie*. Ferdinand Enke, 1903. URL http://www.archive.org/details/lehrbuchdermine00klocgoog.

[84] A. Koster, A. V. den Bos, and K. van der Mast. An autofocus method for a TEM. *Ultramicroscopy*, 21(3):209 – 222, 1987. doi:10.1016/0304-3991(87)90146-X.

[85] A. Koster, W. de Ruijter, A. V. D. Bos, and K. V. D. Mast. Autotuning of a TEM using minimum electron dose. *Ultramicroscopy*, 27(3):251 – 272, 1989. doi:10.1016/0304-3991(89)90018-1.

[86] A. Koster, H. Chen, J. Sedat, and D. Agard. Automated microscopy for electron tomography. *Ultramicroscopy*, 46(1-4):207 – 227, 1992. doi:10.1016/0304-3991(92)90016-D.

[87] L. Kovacik, J. M. Plitzko, M. Grote, and R. Reichelt. Electron tomography of structures in the wall of hazel pollen grains. *Journal of Structural Biology*, 166(3): 263 – 271, 2009. doi:10.1016/j.jsb.2009.03.008.

[88] J. R. Kremer, D. N. Mastronarde, and J. R. McIntosh. Computer Visualization of Three-Dimensional Image Data Using IMOD. *Journal of Structural Biology*, 116 (1):71–76, Jan. 1996. doi:10.1006/jsbi.1996.0013.

[89] C. Kübel and A. Thust. TrueImage: Introduction to Focal-Series Reconstruction. In T. Weirich, J. Labar, and X. Zou, editors, *Nato Science Series E*, pages 373–391. Kluwer Academic Publishers, 2005.

[90] C. Kübel, A. Voigt, R. Schoenmakers, M. Otten, D. Su, T.-C. Lee, A. Carlsson, and J. Bradley. Recent Advances in Electron Tomography: TEM and HAADF-STEM Tomography for Materials Science and Semiconductor Applications. *Microscopy and Microanalysis*, 11(05):378–400, 2005. doi:10.1017/S1431927605050361.

[91] C. Kübel, M. Godehardt, R. Cieslinski, and S. Rozeveld. Towards a Quantitative Understanding in Electron Tomography. *Microscopy and Microanalysis*, 15:602–603, 2009. doi:10.1017/S1431927609092812.

[92] C. Kübel, D. Niemeyer, R. Cieslinski, and S. Rozeveld. Electron Tomography of Nanostructured Materials - Towards a Quantitative 3D Analysis with Nanometer Resolution. In T. Chandra, N. Wanderka, W. Reimers, and M. Ionescu, editors, *THERMEC 2009*, volume Volumes 638-642, pages 2517–2522. Materials Science Forum, Jan. 2010. doi:10.4028/www.scientific.net/MSF.638-642.2517.

[93] H. Kuchling. *Taschenbuch der Physik*. Fachbuchverlag Leipzig, Leipzig, 16 edition, 1996.

[94] P. J. Kulesza, K. Miecznikowski, B. Baranowska, M. Skunik, A. Kolary-Zurowska, A. Lewera, K. Karnicka, M. Chojak, I. Rutkowska, S. Fiechter, P. Bogdanoff, I. Dorbandt, G. Zehl, R. Hiesgen, E. Dirk, K. S. Nagabhushana, and H. Boennemann. Electroreduction of oxygen at tungsten oxide modified carbon-supported RuSex nanoparticles. *Journal Of Applied Electrochemistry*, 37(12):1439–1446, Dec. 2007. doi:10.1007/s10800-007-9349-6.

[95] A. Kupsch, A. Lange, M. P. Hentschel, I. Manke, N. Kardjilov, T. Arlt, and R. Grothausmann. Reconstruction of limited experimental CT data of fuel cell components by Directt. *MP Materials Testing*, pages 676–683, 2010. URL http://www.materialstesting.de/directlink.asp?MP110174.

[96] A. Kupsch, A. Lange, M. P. Hentschel, and B. R. Müller. Improved Computed Tomography by Variable Desmearing. *MP Materials Testing*, 52(6):394–400, 2010. URL http://www.materialstesting.de/directlink.asp?MP110141.

[97] A. Lange, M. P. Hentschel, and A. Kupsch. Computed tomography reconstructions by DIRECTT-2D model calculations compared to filtered backprojection. *MP Materials Testing*, 50(5):272–277, 2008. URL http://www.materialstesting.de/directlink.asp?MP100885.

[98] A. Lange, A. Kupsch, M. P. Hentschel, I. Manke, N. Kardjilov, T. Arlt, and R. Grothausmann. Reconstruction of limited computed tomography data of fuel cell components using Direct Iterative Reconstruction of Computed Tomography Trajectories. *Journal of Power Sources*, 196(12):5293 – 5298, 2011. doi:10.1016/j.jpowsour.2010.10.106. Selected papers presented at the 12th Ulm ElectroChemical Talks (UECT):2015 Technologies on Batteries and Fuel Cells.

[99] F. Lasagni, A. Lasagni, E. Marks, C. Holzapfel, F. Mücklich, and H. Degischer. Three-dimensional characterization of 'as-cast' and solution-treated AlSi12(Sr) alloys by high-resolution FIB tomography. *Acta Materialia*, 55(11):3875 – 3882, 2007. doi:DOI: 10.1016/j.actamat.2007.03.004.

[100] G. Lehmann. Component tree: an efficient representation of grayscale connected components. *Insight Journal*, (176), Dec. 2007. doi:http://hdl.handle.net/1926/1328.

[101] G. Lehmann. Label object representation and manipulation with ITK. *Insight Journal*, (176), Aug 2008. URL http://hdl.handle.net/1926/584.

[102] M. Lentzen, B. Jahnen, C. L. Jia, A. Thust, K. Tillmann, and K. Urban. High-resolution imaging with an aberration-corrected transmission electron microscope. *Ultramicroscopy*, 92(3-4):233 – 242, 2002. doi:10.1016/S0304-3991(02)00139-0.

[103] L. J. Lewis, P. Jensen, N. Combe, and J.-L. Barrat. Diffusion of gold nanoclusters on graphite. *Phys. Rev. B*, 61(23):16084–16090, June 2000. doi:10.1103/PhysRevB.61.16084.

[104] H. Y. Liao and J. Frank. Definition and Estimation of Resolution in Single-Particle Reconstructions. *Structure*, 18(7):768 – 775, 2010. doi:DOI: 10.1016/j.str.2010.05.008.

[105] P. S. Liao, T. S. Chew, and P. C. Chung. A fast algorithm for multilevel thresholding. *Journal of Information Science and Engineering*, 17(5):713–727, Sept. 2001.

[106] W. E. Lorensen and H. E. Cline. Marching cubes: A high resolution 3D surface construction algorithm. *Computer Graphics*, 21:163–169, July 1987. doi:10.1145/37402.37422.

[107] S. Lueck, A. Kupsch, A. Lange, M. Hentschel, and V. Schmidt. Statistical analysis of tomographic reconstruction algorithms by morphological image characteristics. *Image Analysis and Stereology*, 29(2):61–77, 2011. URL http://www.ias-iss.org/ojs/IAS/article/view/870.

[108] I. Manke, N. Kardjilov, R. Schäfer, A. Hilger, M. Strobl, M. Dawson, C. Grünzweig, G. Behr, M. Hentschel, C. David, A. Kupsch, A. Lange, and J. Banhart. Three-dimensional imaging of magnetic domains. *Nature Communications*, 1(8):125–, Nov. 2010. doi:10.1038/ncomms1125.

[109] I. Manke, H. Markötter, C. Tötzke, N. Kardjilov, R. Grothausmann, M. Dawson, C. Hartnig, S. Haas, D. Thomas, A. Hoell, C. Genzel, and J. Banhart. Investigation of Energy-Relevant Materials with Synchrotron X-Rays and Neutrons. *Advanced Engineering Materials*, 2011. doi:10.1002/adem.201000284.

[110] B. J. Marsh, D. N. Mastronarde, K. F. Buttle, K. E. Howell, and J. R. McIntosh. Organellar relationships in the Golgi region of the pancreatic beta cell line, HIT-T15, visualized by high resolution electron tomography. *Proceedings of the National Academy of Sciences of the United States of America*, 98(5):2399–2406, 2001. doi:10.1073/pnas.051631998.

[111] D. N. Mastronarde. Dual-Axis Tomography: An Approach with Alignment Methods That Preserve Resolution. *Journal of Structural Biology*, 120(3):343–352, Dec. 1997. doi:10.1006/jsbi.1997.3919.

[112] D. N. Mastronarde. Automated electron microscope tomography using robust prediction of specimen movements. *Journal of Structural Biology*, 152(1):36 – 51, 2005. doi:10.1016/j.jsb.2005.07.007.

[113] D. N. Mastronarde, K. L. McDonald, R. Ding, and J. R. McIntosh. Interpolar spindle microtubules in PTK cells. *The Journal of Cell Biology*, 123(6):1475–1489, 1993. doi:10.1083/jcb.123.6.1475.

[114] D. N. Mastronarde et al. Particle Estimation for Electron Tomography (PEET) documentation. open source, 1.5.1. URL `ftp://bio3d.colorado.edu/pub/PEET`.

[115] D. N. Mastronarde et al. IMOD documentation. open source, 4.1. URL `http://bio3d.colorado.edu/imod/doc/tomoguide.html`.

[116] N. Matloff and F. Hsu. Tutorial on Threads Programming with Python. PDF-file, 2009. URL `http://heather.cs.ucdavis.edu/~matloff/Python/PyThreads.pdf`. now a chapter in the open-source text-book on parallel programming (`http://heather.cs.ucdavis.edu/~matloff/158/PLN/ParProcBook.pdf`).

[117] M. McCormick. Higher Order Accurate Derivative and Gradient Calculation in ITK. *Insight Journal*, (775):5, Nov. 2010. doi:http://hdl.handle.net/10380/3231.

[118] F. Meyer. Topographic distance and watershed lines. *Signal Processing*, 38(1): 113 – 125, 1994. doi:10.1016/0165-1684(94)90060-4.

[119] N. Meyer, M. Desbrun, P. Schröder, and A. H. Barr. Discrete differential-geometry operators for triangulated 2-manifolds. In H.-C. Hege and K. Polthier, editors, *Visualization and Mathematics III*, pages 35–57. Springer, Berlin, 2003.

[120] P. Midgley and M. Weyland. Fundamentals of electron tomography. In J. Banhart, editor, *Advanced Tomographic Methods in Materials Research and Engineering*, pages 305–334. Oxford University Press, May 2008.

[121] P. Midgley, M. Weyland, and H. Stegmann. Applications of electron tomography. In J. Banhart, editor, *Advanced Tomographic Methods in Materials Research and Engineering*, pages 335–372. Oxford University Press, May 2008.

[122] P. A. Midgley and R. R. Dunin-Borkowski. Electron tomography and holography in materials science. *nature materials*, pages 271–280, march 2009. doi:10.1038/nmat2406.

[123] P. A. Midgley and M. Weyland. 3D electron microscopy in the physical sciences: the development of Z-contrast and EFTEM tomography. *Ultramicroscopy*, 96 (3-4):413 – 431, 2003. doi:10.1016/S0304-3991(03)00105-0. Proceedings of the International Workshop on Strategies and Advances in Atomic Level Spectroscopy and Analysis.

[124] P. A. Midgley, M. Weyland, J. M. Thomas, P. L. Gai, and E. D. Boyes. Probing the Spatial Distribution and Morphology of Supported Nanoparticles Using Rutherford-Scattered Electron Imaging. *Angewandte Chemie*, 114(20):3804–3807, 2002. doi:10.1002/1521-3757(20021018)114:20<3958::AID-ANGE3958>3.0.CO;2-P.

[125] P. A. Midgley, J. M. Thomas, L. Laffont, M. Weyland, R. Raja, B. F. G. Johnson, and T. Khimyak. High-Resolution Scanning Transmission Electron Tomography and Elemental Analysis of Zeptogram Quantities of Heterogeneous Catalyst. In *Journal of Physical Chemistry B* Weyland et al. [184], pages 4590–4592. doi:10.1021/jp049750b.

[126] K. Mosaliganti, A. Gelas, and S. Megason. An Adaptive Thresholding Image Filter. *Insight Journal*, (702), Oct. 2009. URL `http://www.insight-journal.org/browse/publication/702`.

[127] D. Mueller. Cuberille Implicit Surface Polygonization for ITK. *Insight Journal*, (740), Jul. 2010. doi:http://hdl.handle.net/10380/3186.

[128] C. Muhlfeld, B. Rothen-Rutishauser, F. Blank, D. Vanhecke, M. Ochs, and P. Gehr. Interactions of nanoparticles with pulmonary structures and cellular responses. *American Journal of Physiology-lung Cellular and Molecular Physiology*, 294(5):L817–L829, May 2008. doi:10.1152/ajplung.00442.2007.

[129] B. Münch, P. Gasser, L. Holzer, and R. Flatt. FIB-nanotomography of particulate systems - Part II: Particle recognition and effect of boundary truncation. *Journal of the American Ceramic Society*, 89(8):2586–2595, Aug. 2006. doi:10.1111/j.1551-2916.2006.01121.x.

[130] K. S. Nagabhushana, E. Dinjus, H. Bonnemann, V. Zaikovskii, C. Hartnig, G. Zehl, I. Dorbandt, S. Fiechter, and P. Bogdanoff. Reductive annealing for generating Se doped 20 wt% Ru/C cathode catalysts for the oxygen reduction reaction. *Journal of Applied Electrochemistry*, 37(12):1515–1522, Dec. 2007. doi:10.1007/s10800-007-9423-0.

[131] R. M. Nielsen, S. Murphy, C. Strebel, M. Johansson, I. Chorkendorff, and J. H. Nielsen. The morphology of mass selected ruthenium nanoparticles from a magnetron-sputter gas-aggregation source. *Journal of Nanoparticle Research*, 12 (4):1249–1262, May 2010. doi:10.1007/s11051-009-9830-8.

[132] W. Nolting. *Grundkurs Theoretisch Physik 1*. Springer, 6th edition, 2002. doi:10.1007/978-3-540-34833-7.

[133] J. Ohser and F. Mücklich. *Statistical Analysis of Microstructures in Materials Science*. John Wiley & Sons, Ltd., 2000.

[134] J. Ohser and K. Schladitz. *3D Images of Materials Structures: Processing and Analysis*. Wiley-VCH, Nov 2009.

[135] N. Otsu. A threshold selection method from gray-level histograms. *IEEE Transactions on Systems, Man and Cybernetics*, 9(1):62–66, Jan 1979. doi:10.1109/TSMC.1979.4310076.

[136] D. Padfield and J. Miller. A Label Geometry Image Filter for Multiple Object Measurement. *Insight Journal*, (301), Sep 2008. URL http://hdl.handle.net/1926/1493.

[137] D. C. Papageorgopoulos, F. Liu, and O. Conrad. A study of Rh_xS_y/C and $RuSe_x$/C as methanol-tolerant oxygen reduction catalysts for mixed-reactant fuel cell applications. *Electrochimica Acta*, 52(15):4982 – 4986, 2007. doi:10.1016/j.electacta.2007.01.076.

[138] J. Perry. An Infinitely Colorable Set of 3D Regions. WWW, 2010.10.23. URL http://demonstrations.wolfram.com/AnInfinitelyColorableSetOf3DRegions/. The Wolfram Demonstrations Project.

[139] L. Pugin, J. Hockman, J. A. Burgoyne, and I. Fujinaga. Gamera Versus Aruspix: Two Optical Music Recognition Approaches. In J. P. Bello, E. Chew, and D. Turnbull, editors, *ISMIR*, pages 419–424, 2008.

[140] A. Rack. *Untersuchung komplexer Materialsysteme mittels Synchrotron-Tomographie und 3D-Bildanalyse*. PhD thesis, Fakultät III Prozesswissenschaften, Technische Universität Berlin, 2006. URL http://opus.kobv.de/tuberlin/volltexte/2006/1370/.

[141] M. Radermacher. Three-Dimensional reconstruction of single particles from random and nonrandom tilt series. *Journal of Electron Microscopy Technique*, 9 (4):359–394, 1988. doi:10.1002/jemt.1060090405.

[142] J. Radon. Über die Bestimmung von Funktionen durch ihre Integralwerte längs gewisser Mannigfaltigkeiten. *Berichte Sächsische Akademie der Wissenschaften, Leipzig*, 69:262–277, 1917. nachgedruckt in: P. Gruber et al. (Ed.) Radon, Johann: Gesammelte Abhandlungen. Verlag der Österreichischen Akademie der Wissenschaften, Wien; Birkhäuser, 1987.

[143] P. Ramdohr and H. Strunz. *Klockmanns Lehrbuch der Mineralogie*. Ferdinand Enke, 16th edition, 1978.

[144] W. Rasband. ImageJ documentation. open source, 1.43u. URL http://rsbweb.nih.gov/ij/docs/guide/index.html.

[145] L. Reimer. *Elektronenmikroskopische Untersuchungs- und Präparationsmethoden*. Springer, 2th edition, 1967.

[146] L. Reimer and H. Kohl. *Transmission Electron Microscopy: Physics of Image Formation*. Springer, 5th edition, 2008. URL http://www.springer.com/materials/book/978-0-387-40093-8.

[147] L. Reimer, U. Zepke, J. Moesch, S. Schulze-Hillert, M. Ross-Messemer, W. Probst, and E. Weimer. EELS Atlas. Carl Zeiss, Electron Optics Division, Oberkochen, 1992.

[148] G. F. Rempfer, K. K. Nadakavukaren, and O. H. Griffith. Depth of field in emission microscopy. *Ultramicroscopy*, 5(1-3):449 – 457, 1980. doi:DOI: 10.1016/0304-3991(80)90045-5.

[149] F. J. Rodríguez, P. J. Sebastian, O. Solorza, and R. Pérez. Mo-Ru-W chalcogenide electrodes prepared by chemical synthesis and screen printing for fuel cell applications. *International Journal of Hydrogen Energy*, 23(11):1031–1035, 1998.

[150] H. Rösner, S. Parida, D. Kramer, C. A. Volkert, and J. Weissmuller. Reconstructing a nanoporous metal in three dimensions: An electron tomography study of dealloyed gold leaf. *Advanced Engineering Materials*, 9(7):535–541, July 2007. doi:10.1002/adem.200700063.

[151] H. Rösner, T. Scherer, and G. Wilde. Electron tomography of lead nano-inclusions in aluminium. *Scripta Materialia*, 60(3):168–170, Feb. 2009. doi:10.1016/j.scriptamat.2008.09.025.

[152] J. Rouquerol, D. Avnir, C. W. Fairbridge, D. H. Everett, J. M. Haynes, N. Pernicone, J. D. F. Ramsay, K. S. W. Sing, and K. K. Unger. Recommendations for the characterization of porous solids (Technical Report). *Pure and Applied Chemistry*, 66(8):1739 – 1758, 1994. doi:10.1351/pac199466081739.

[153] H. Sawada, T. Tomita, M. Naruse, T. Honda, P. Hambridge, P. Hartel, M. Haider, C. Hetherington, R. Doole, A. Kirkland, J. Hutchison, J. Titchmarsh, and D. Cockayne. Experimental evaluation of a spherical aberration-corrected

TEM and STEM. *Journal of Electron Microscopy*, 54(2):119–121, Apr. 2005. doi:10.1093/jmicro/dfi001.

[154] P. Schlossmacher, A. Thesen, and G. Benner. Picture perfect. *european semiconductor*, 27(3):4, Mar 2005.

[155] W. Schroeder, K. Martin, and B. Lorensen. *The Visualization Toolkit: An Object-Oriented Approach to 3D Graphics*. Kitware, Inc., 4th edition, December 2006. URL http://www.kitware.com/products/books/vtkbook.html.

[156] T. S. Sheu and H. H. Chien. Computer aided analysis on twinning plane of InSb single crystal. *Materials Letters*, 24(4):225 – 229, 1995. doi:10.1016/0167-577X(95)00111-5.

[157] D. Shindo and K. Hiraga. *High-resolution Electron Microscopy For Materials Science*. Springer-Verlag Tokyo, Inc., 1998. doi:ISBN: 4431702342.

[158] M. Shirai, T. Horiuchi, A. Horiguchi, S. Matsumura, K. Yasuda, M. Watanabe, and T. Masumoto. Morphological change in FePt nanogranular thin films induced by irradiation with 2.4 MeV Cu2+ ions: Electron tomography observation. *Materials Transactions*, 47(1):52–58, Jan. 2006. URL http://www.jim.or.jp/journal/e/47/01/52.html.

[159] M. Shirai, K. Tsumori, M. Kutsuwada, K. Yasuda, and S. Matsumura. Morphological change in FePt nanogranular thin films induced by swift heavy ion irradiation. *Nuclear Instruments and Methods in Physics Research Section B: Beam Interactions with Materials and Atoms*, 267(10):1787 – 1791, 2009. doi:10.1016/j.nimb.2009.03.079.

[160] M. K. Singh, E. Titus, G. Goncalves, P. A. A. P. Marques, I. Bdikin, A. L. Kholkin, and J. J. A. Gracio. Atomic-scale observation of rotational misorientation in suspended few-layer graphene sheets. *Nanoscale*, 2(5):700–708, 2010. doi:10.1039/B9NR00256A.

[161] R. Smith, D. Antonova, and D.-S. Lee. Adapting the Tesseract open source OCR engine for multilingual OCR. In *Proceedings of the International Workshop on Multilingual OCR*, pages 1–8, Barcelona, Spain, 2009. ACM. doi:http://doi.acm.org/10.1145/1577802.1577804.

[162] P. Soille. *Morphological Image Analysis: Principles and Applications*. Springer, 2nd edition, 2004.

[163] A. Spadaccini and V. G. Rizzo. A Multiple-Choice Test Recognition System based on the Gamera Framework. In C. Dalitz, editor, *Document Image Analysis with the Gamera Framework*, volume 8, pages 5–15. Shaker Verlag, 2009. URL http://gamera.informatik.hsnr.de/publications/spadaccini_multiplechoice_09.pdf.

[164] S. Srinivasan, E. Ticianelli, C. Derouin, and A. Redondo. Advances in solid polymer electrolyte fuel cell technology with low platinum loading electrodes. *Journal of Power Sources*, 22(3-4):359 – 375, 1988. doi:10.1016/0378-7753(88)80030-2. Proceedings of the Space Electrochemical Research and Technology Conference.

[165] J. Starink, B. Humbel, and A. Verkleij. Three-dimensional localization of immunogold markers using two tilted electron microscope recordings. *Biophysical Journal*, 68(5):2171–2180, May 1995. doi:10.1016/S0006-3495(95)80399-1.

[166] O. Stiller and N. Combé. Nanotechnologie - Die zweite industrielle Revolution. April 2005. Theodor Heuss Akademie, Gummersbach.

[167] P. M. V. Subbarao, P. Munshi, and K. Muralidhar. Performance of iterative tomographic algorithms applied to non-destructive evaluation with limited data. *NDT & E International*, 30(6):359 – 370, 1997. doi:DOI: 10.1016/S0963-8695(97)00005-4.

[168] T. Suh, S. O. Kang, and I.-H. Suh. InterplanarA: A Computer Program for the Calculation of the Crystallographic Interplanar Angles. *Korean Journal of Crystallography*, 20(1):15–18, 2009. URL http://koixra1.kisti.re.kr/ra_resolution.jsp?koi=KISTI1.1003/JNL.JAKO200919038643925.

[169] K. Tani, H. Sasabe, and C. Toyoshima. A set of computer programs for determining defocus and astigmatism in electron images. *Ultramicroscopy*, 65(1-2):31 – 44, 1996. doi:10.1016/S0304-3991(96)00052-6.

[170] G. Taubin, T. Zhang, and G. Golub. Optimal surface smoothing as filter design. In B. Buxton and R. Cipolla, editors, *Computer Vision – ECCV '96*, volume 1064 of *Lecture Notes in Computer Science*, pages 283–292. Springer Berlin / Heidelberg, 1996. doi:10.1007/BFb0015544.

[171] V. Trapp, P. Christensen, and A. Hamnett. New catalysts for oxygen reduction based on transition-metal sulfides. *Journal of the Chemical Society, Faraday Transactions*, 92(21):4311–4319, 1996.

[172] B. A. Turlach. Bandwidth Selection in Kernel Density Estimation: A Review. In *CORE and Institut de Statistique*, pages 23–493, 1993.

[173] N. Tustison, P. Yushkevich, Z. Song, and J. Gee. Graph Cuts, Caveat Utilitor, and Euler's Bridges of Königsberg. *Insight Journal*, (306):13, Jul. 2008. URL http://www.insight-journal.org/browse/publication/306.

[174] K. Vaideeswaran. Optimization of Preparation Process of Carbon Support Films for Tomographical Analysis. Technical report, Helmholtz Zentrum Berlin für Materialien und Energie (HZB), 2008.

[175] W. Van den Broek. *Advanced Focus Methods in Electron Microscopy: Tomographic Reconstruction of the EELS Data Cube, Autofocus of HAADF-STEM Images*. PhD thesis, Universiteit Antwerpen (Faculteit Wetenschappen, Departement Fysica), 2007.

[176] A. van der Sluis and H. van der Vorst. SIRT- and CG-type methods for the iterative solution of sparse linear least-squares problems. *Linear Algebra and its Applications*, 130:257 – 303, 1990. doi:10.1016/0024-3795(90)90215-X.

[177] M. van Heel and M. Schatz. Fourier shell correlation threshold criteria. *Journal of Structural Biology*, 151(3):250–262, Sept. 2005. doi:10.1016/j.jsb.2005.05.009.

[178] R. van Liere and W. de Leeuw. GraphSplatting: Visualizing graphs as continuous fields. *Ieee Transactions On Visualization And Computer Graphics*, 9(2):206–212, Apr. 2003. doi:10.1109/TVCG.2003.1196007.

[179] D. Vanhecke, D. Studer, and M. Ochs. Reprint of "Stereology meets electron tomography: towards quantitative 3D electron microscopy" [J. Struct. Biol. 159 (2007) 443-450]. *Journal of Structural Biology*, 161(3):314–321, Mar. 2008. doi:10.1016/S1047-8477(08)00061-0.

[180] H. Wadell. Volume, Shape, and Roundness of Quartz Particles. *Journal of Geology*, 43(3):250–280, 1935. doi:10.1086/624298.

[181] E. P. W. Ward, T. J. V. Yates, J. J. Fernandez, D. E. W. Vaughan, and P. A. Midgley. Three-dimensional nanoparticle distribution and local curvature of heterogeneous catalysts revealed by electron tomography. *Journal of Physical Chemistry C*, 111(31):11501–11505, Aug. 2007. doi:10.1021/jp072441b.

[182] E. W. Weisstein. Four-Color Theorem. WWW, 2010.10.23. URL `http://mathworld.wolfram.com/Four-ColorTheorem.html`. MathWorld–A Wolfram Web Resource.

[183] E. W. Weisstein. Map Coloring. WWW, 2010.10.23. URL `http://mathworld.wolfram.com/MapColoring.html`. MathWorld–A Wolfram Web Resource.

[184] M. Weyland, P. A. Midgley, and J. M. Thomas. Electron Tomography of Nanoparticle Catalysts on Porous Supports: A New Technique Based on Rutherford Scattering. *Journal of Physical Chemistry B*, 105(33):7882–7886, Aug. 2001. doi:10.1021/jp011566s.

[185] D. B. Williams and C. B. Carter. *Transmission Electron Microscopy: A Textbook for Materials Science*. Springer, 2nd edition, 2009.

[186] K. Wippermann, B. Richter, K. Klafki, J. Mergel, G. Zehl, I. Dorbandt, P. Bogdanoff, S. Fiechter, and S. Kaytakoglu. Carbon supported Ru-Se as methanol tolerant catalysts for DMFC cathodes. Part II: preparation and characterization of MEAs. *Journal of Applied Electrochemistry*, 37(12):1399–1411, Dec. 2007. doi:10.1007/s10800-007-9348-7.

[187] M. Wissler. Graphite and carbon powders for electrochemical applications. *Journal of Power Sources*, 156(2):142 – 150, 2006. doi:10.1016/j.jpowsour.2006.02.064.

[188] R. W. G. Wyckoff. *Crystal Structures*, volume I. John Wiley & Sons, 2nd edition, 1963.

[189] T. Yoo, E. Angelini, B. Avants, S. Aylward, T. Chen, J. Duda, J. Gee, L. Ibanez, C. Imielinska, Y. Jin, J. Kim, B. Lorensen, D. Metaxas, L. Ng, P. Saha, G. Stetten, T. Sundaram, J. Udupa, R. Whitaker, and Y. Zhuge. *Insight into Images: Principles and Practice for Segmentation, Registration, and Image Analysis*. A K Peters, Ltd., Jul 2004.

[190] G. Zehl, I. Dorbandt, G. Schmithals, J. Radnik, K. Wippermann, B. Richter, P. Bogdanoff, and S. Fiechter. Preparation of carbon supported Ru-Se based catalysts and their electrochemical performance in DMFC cathodes. *ECS Transactions*, 3(1):1261–1270, 2006.

[191] G. Zehl, P. Bogdanoff, I. Dorbandt, S. Fiechter, K. Wippermann, and C. Hartnig. Carbon supported Ru-Se as methanol tolerant catalysts for DMFC cathodes. Part I: preparation and characterization of catalysts. *Journal of Applied Electrochemistry*, 37(12):1475–1484, Dec. 2007. doi:10.1007/s10800-007-9375-4.

[192] G. Zehl, G. Schmithals, A. Hoell, S. Haas, C. Hartnig, I. Dorbandt, P. Bogdanoff, and S. Fiechter. On the structure of carbon-supported selenium-modified ruthenium nanoparticles as electrocatalysts for oxygen reduction in fuel cells. *Angewandte Chemie, International Edition*, 46(38):7311–7314, 2007. doi:10.1002/anie.200701473.

[193] Zeiss. *Benutzerhandbuch LIBRA 200*. Carl Zeiss NTS GmbH, Carl-Zeiss-Str. 56 73447 Oberkochen Germany, 1.30 edition, . 344000-0000-026.

[194] Zeiss. *Product Specification ZEISS Libra 200 Kryo*. Carl Zeiss SMT, Carl Zeiss NTS GmbH A Carl Zeiss SMT AG Company Carl-Zeiss-Str. 56 73447 Oberkochen Germany, .

[195] Zeiss. *Product Specification Zeiss LIBRA 200FE*. Carl Zeiss SMT, Carl Zeiss NTS GmbH A Carl Zeiss SMT AG Company Carl-Zeiss-Str. 56 73447 Oberkochen Germany, .

[196] Q. S. Zheng, M. B. Braunfeld, J. W. Sedat, and D. A. Agard. An improved strategy for automated electron microscopic tomography. *Journal of Structural Biology*, 147(2):91 – 101, 2004. doi:DOI: 10.1016/j.jsb.2004.02.005.

[197] J. Ziegel and M. Kiderlen. Estimation of surface area and surface area measure of three-dimensional sets from digitizations. *Image and Vision Computing*, 28(1): 64–77, Jan. 2010. doi:10.1016/j.imavis.2009.04.013.

[198] U. Ziese, A. H. Janssen, J. L. Murk, W. J. C. Geerts, T. Van der Krift, A. J. Verkleij, and A. J. Koster. Automated high-throughput electron tomography by pre-calibration of image shifts. *Journal Of Microscopy-Oxford*, 205:187–200, Feb. 2002. doi:10.1046/j.0022-2720.2001.00987.x.

[199] U. Ziese, W. J. C. Geerts, T. P. Van Der Krift, A. J. Verkleij, and A. J. Koster. Correction of autofocusing errors due to specimen tilt for automated electron tomography. *Journal of Microscopy*, 211(2):179–185, 2003. doi:10.1046/j.1365-2818.2003.01153.x.

Software

[1] David N. Mastronarde et al. IMOD. open source, 4.1. URL http://bio3d.colorado.edu/imod/.

[2] ITK development team. ITK. open source, 3.18. URL http://www.itk.org.

[3] VTK development team. VTK. open source, 5.4. URL http://www.vtk.org.

[4] Blender Foundation. Blender. open source, 2.49. URL http://www.blender.org.

[5] John W. Eaton et al. Octave. open source, 3.0.5. URL http://www.gnu.org/software/octave/.

[6] Thomas Williams, Colin Kelley, et al. gnuplot. open source, 4.4. URL http://gnuplot.sourceforge.net/docs_4.4/gnuplot.pdf.

[7] W.S. Rasband. ImageJ. open source, 1.43u. URL http://rsb.info.nih.gov/ij/.

[8] ParaView development team. ParaView. open source, 3.6.2. URL http://www.paraview.org.

[9] Inkscape-Team. Inkscape. open source, 0.48. URL http://www.inkscape.org/.

[10] GIMP-Team. gimp (GNU Image Manipulation Program). open source, 2.6.8. URL http://www.gimp.org/.

[11] Donald Ervin Knuth, Leslie Lamport, et al. LaTeX 2_ε. open source. URL http://www.tug.org/.

[12] Free Software Foundation. gcc (GNU Compiler Collection). open source, 4.x. URL http://gcc.gnu.org/.

[13] Python Software Foundation. Python. open source, 2.6.2. URL http://www.python.org.

[14] James Gosling et al. Java. open source, 1.6. URL http://www.java.com/.

[15] Chris Want and Fritz Mielert. VTKBlender Module. open source, 1.19. URL http://www.ualberta.ca/CNS/RESEARCH/Vis/VTKBlender/.

[16] Alfred V. Aho, Peter J. Weinberger, Brian W. Kernighan, Free Software Foundation, et al. awk (GNU Awk). open source, 3.1.3. URL http://www.gnu.org/software/gawk/gawk.html.

[17] Linus Torvalds, Free Software Foundation, et al. GNU-Linux. open source, 2.6. http://www.kernel.org/ and http://www.gnu.org/.

[18] Steffen Weber. JWulff - stereographic projections. careware, 1998. URL http://www.jcrystal.com/steffenweber/JAVA/JWULFF/JWULFF.zip.

[19] Philippe Carl. Radial Profile Plot. open source, 2006/08/18. URL http://rsbweb.nih.gov/ij/plugins/radial-profile-ext.html. imagej plugin.

[20] Gabriel Landini. Auto Threshold. open source, v1.10 (25 May 2010). URL http://pacific.mpi-cbg.de/wiki/index.php/Auto_Threshold.

[21] Gabriel Landini. Auto Local Threshold. open source, v1.2 (25 May 2010). URL http://pacific.mpi-cbg.de/wiki/index.php/Auto_Local_Threshold.

[22] Bernard Heymann et al. Bsoft. open source, 1.7.0. URL http://lsbr.niams.nih.gov/bsoft/.

[23] Image Science Software GmbH. FSC (foushell). closed source, 071217. URL http://www.imagescience.de/fsc/index.htm.

[24] David N. Mastronarde et al. SerialEM. open source, 3.0.1. URL http://bio3d.colorado.edu/SerialEM/index.html.

[25] Fraunhofer ITWM. MAVI - Modular Algorithms for Volume Images. commercial, 1.3.1. URL http://www.itwm.fraunhofer.de/bv/projects/MAVI/.

[26] Gatan, Inc. DigitalMicrograph™ of the Gatan Microscopy Suite (GMS). commercial. URL ftp://ftp.gatan.com/pub/software/PC/.

[27] Carl Zeiss NTS. WinTEM™. commercial. URL http://www.zeiss.de/nts.

[28] Volume Graphics. VGStudio MAX. commercial, 1.2. URL http://www.volumegraphics.com/.

[29] Mercury Computer Systems. Avizo (fire). commercial, 2009.

[30] Inc. Accelrys. Materials Studio. commercial. URL http://accelrys.com/products/materials-studio/.

List of publications

[1] Roman Grothausmann, Ingo Manke, Gerald Zehl, Iris Dorbandt, Peter Bogdanoff, Sebastian Fiechter, Manfred P. Hentschel, Axel Lange, Andreas Kupsch, André Hilger, and John Banhart. Characterisation of fuel cell catalyst materials using electron tomography. *MP Materials Testing*, 52(10):706–711, 2010. URL http://www.materialstesting.de/directlink.asp?MP110174.

[2] Roman Grothausmann, Gerald Zehl, Ingo Manke, Sebastian Fiechter, Peter Bogdanoff, Iris Dorbandt, Andreas Kupsch, Axel Lange, Manfred P. Hentschel, Gerhard Schumacher, and John Banhart. Quantitative structural assessment of heterogeneous catalysts by electron tomography. submitted, 2011.

[3] Roman Grothausmann. In-Situ Elektronenstrahldeposition von Leiterbahnen im Transmissionselektronenmikroskop. Diplomarbeit, Universität Regensburg, Nov. 2007.

[4] Hendrik Schulenburg, Bernhard Schwanitz, Julijana Krbanjevic, Nicolas Linse, Guenther G. Scherer, Alexander Wokaun, Roman Grothausmann, and Ingo Manke. 3D Imaging of Catalyst Support Corrosion in Polymer Electrolyte Fuel Cells. *The Journal of Physical Chemistry C*, 2011. doi:10.1021/jp203016u.

[5] Ingo Manke, Henning Markötter, Christian Tötzke, Nikolay Kardjilov, Roman Grothausmann, Martin Dawson, Christoph Hartnig, Sylvio Haas, Diana Thomas, Armin Hoell, Christoph Genzel, and John Banhart. Investigation of Energy-Relevant Materials with Synchrotron X-Rays and Neutrons. *Advanced Engineering Materials*, 2011. ISSN 1527-2648. doi:10.1002/adem.201000284.

[6] Axel Lange, Andreas Kupsch, Manfred P. Hentschel, Ingo Manke, Nikolay Kardjilov, Tobias Arlt, and Roman Grothausmann. Reconstruction of limited computed tomography data of fuel cell components using Direct Iterative Reconstruction of Computed Tomography Trajectories. *Journal of Power Sources*, 196(12):5293 – 5298, 2011. ISSN 0378-7753. doi:10.1016/j.jpowsour.2010.10.106. Selected papers presented at the 12th Ulm ElectroChemical Talks (UECT):2015 Technologies on Batteries and Fuel Cells.

[7] Andreas Kupsch, Axel Lange, Manfred P. Hentschel, Ingo Manke, Nikolay Kardjilov, Tobias Arlt, and Roman Grothausmann. Reconstruction of limited experimental CT data of fuel cell components by Directt. *MP Materials Testing*,

pages 676–683, 2010. URL http://www.materialstesting.de/directlink.asp?MP110174.

[8] Axel Lange, Manfred P. Hentschel, Andreas Kupsch, Ingo Manke, Nikolay Kardjilov, Tobias Arlt, and Roman Grothausmann. Rekonstruktion limitierter CT-Datensätze von Brennstoffzellen mit DIRECTT. pages 1–11. Carl Hanser Verlag, 2010.

[9] Markus Wollgarten, Roman Grothausmann, Peter Bogdanoff, Gerald Zehl, Iris Dorbandt, Sebastian Fiechter, and John Banhart. Ruthenium deposition on CO2-treated and untreated carbon black investigated by electron tomography. In Sivia Richter and Alexander Schwedt, editors, *EMC 2008, 14th European Microscopy Congress, 1–5 September 2008, Aachen, Germany*, volume 2, page 279280. Springer Berlin Heidelberg, 2008. doi:10.1007/978-3-540-85226-1_140.

List of Figures

List of Tables

Appendix A

Additions to the chapters

A.1 Additional aspects of image processing and analysis

In this chapter some additional aspects of digital image processing and analysis are described. The descriptions are far from complete but references are given for more detailed texts. Generally, the terminology of the ITK/VTK documentation (e.g. [76; 12]) is used.

Image and mesh representations

There a two common types of 3D data representation: images and meshes. Images are bitmaps in which data is represented by a regular grid. A cell is called pixel, in 3D often voxel. A (3D) mesh –comparable to 2D vector graphics– consists of points, edges (connected points) and flat polygons (connected edges, often triangles) that define a discrete surface not bound to a grid (contrary to the voxel image representation).

The image representation (or also called pixel/voxel representation) allows different pixel types to store different integers or floating point values. Generally they are referred to as either grey value representations, where each pixel value represents a measured or computed value (e.g. local absorption coefficient), or binary representations consisting only of a foreground and a background, or label images.

In a label image, different regions of the foreground of a binary dataset are assigned to different integer values. The regions are defined by a specific criterion, e.g. interconnectivity of foreground pixel or the result of a watershed transformation. This allows, for example, to store identified connected regions of a binary dataset, i.e. particles, together in a single dataset. In this case all pixels belonging to the same region have the same label. Labels are often visualized by a small amount of different colours (colour look up table, LUT) to ease the distinction by eye. When there are more labels than entries in the LUT the colours of the LUT are reused for different labels.

The colours are commonly not assigned by application of the four-colour theorem [182] and therefore identical colours can sometimes appear side by side.[1)]

Watershed transformation, segmentation and separation

The watershed transformation can be regarded as a flooding of a grey scale image. The grey values represent hights and the flooding starts filling valleys or basins on this hight map. The water for flooding originates from wells that are given in a second input image containing markers for these wells. When pools from different wells are about to merge a 'dam' or 'water shed' is created. This dam can have a width, e.g. 4|8 connectivity in 2D or 6|26 connectivity in 3D and is then called a wall. There are algorithms that do not create walls but label the water in each pool uniquely such that no wall is needed to distinguish the water from different pools [18; 20]. The shape of the dam depends on the algorithm used. For example, a dam can be build such that its size is minimal (e.g. for recreating pore walls of a foam which also try to minimize their size). Examples and more details can be found in [76, sec. 9.2, p. 524 ff], for images see [18, Fig. 1 and 10].

It is important to note that a *watershed transformation* refers to the basic flooding described above. This must not be mistaken with the term *watershed separation* which means separation of particles based on a distance map. The watershed separation is described in Sec. 3.2. Another term is *watershed segmentation* which is basically a watershed transformation based on labelled markers as mentioned above. Commonly, the result of a watershed transformation is expected to be labelled (a label image), i.e. each pool has a unique value assigned to all its pixel.

It is possible to identify particles that got separated by a watershed separation if no walls were introduced. In that case it is simply checking each label if it contains voxels whose neighbouring voxels (same connectivity as used by the watershed transformation) are of another label.

Estimation errors of digital representations

Estimation of surface areas of voxel representations is a complex problem [197; 7]. Usually surfaces are estimated by the Crofton formulae [14, chap. 3, p. 82 ff] [134] which is also the case for the surface estimation of the ITK label analyser from Lehmann [101]. There are multiple criteria that should be fulfilled to achieve sufficient exact estimations, e.g. the Euler numbers of 6, 14.I, 14.II and 26 connectivity should all be similar, other criteria are the surface fractal dimension and the integral of mean curvature fractal dimension [53]. Still, it is impossible to quantify the overall

[1)] The four-colour theorem (first proven by Appel and Haken [9, 10]) states that any map in a 2D plane can be coloured, using only four different colours, in such a way that regions sharing a common boundary (other than a single point) do not share the same colour. Contrary, in 3D the number of colours needed to assure the same criterion can be infinite [138].

measurement error [53]. The surface estimation never corresponds exactly to the surface actually enclosing the volume of the particle representation.

In contrast, surface areas of mesh representations are easily calculated but the conversion of voxel representations into mesh representations introduces further discrepancies in regard to the original objects represented. In addition, the computation of volumes of mesh representations is not as straight forward as it is for voxel representations. It is possible though to calculate the volume enclosed by a closed manifold mesh with the divergence theorem from Gauss (a special case of Stokes' Theorem) in a discrete form [7; 72].

List of some sophisticated thresholding algorithms

- Otsu (multiple thresholds) ([135; 105], ITK implementation available, also in ImageJ and MAVI)
- K-Means ([76, sec. 10.4.2, p. 679], ITK implementation available)
- Fuzzy Connectness [189]
- Markov Random Fields, MRF ([76, sec. 10.4.5, p. 691], ITK implementation available)
- Adaptive Otsu ([126], ITK implementation available)
- Graph Cuts ([173], ITK implementation available)
- Various other global and adaptive thresholds implemented for ImageJ[20;21]

A.2 Resolution estimation by FSC

The tool `bresove` from Bsoft[22] computes the FSC, DPR, SSNR and RA+B as well as the 2σ-threshold curve. The computation of the 2σ-threshold curve (by `bresove`) neither takes into account any dependence on the degree of filling of the tomogram by the object nor possible symmetry of the object. Although it is show by van Heel and Schatz [177] that these must be taken into account, their extended definition of the σ-threshold curve is such that it is identical to the standard definition in case of no symmetry (point group symmetry C1) and a degree of filling of 60% [177, sec. 2.3 and 2.4]. Since the tomograms of this study approximately fulfil these two conditions, the 2σ-threshold curve of `bresove` is applicable.

The two reconstructions of independent tilt series from Sec. 5.1 were used for an exemplary estimation of the resolution by FSC. According to Cardone et al. [33, sec. 4.6] the resolution will be underestimated by the use of tomograms from dual tilt reconstructions.

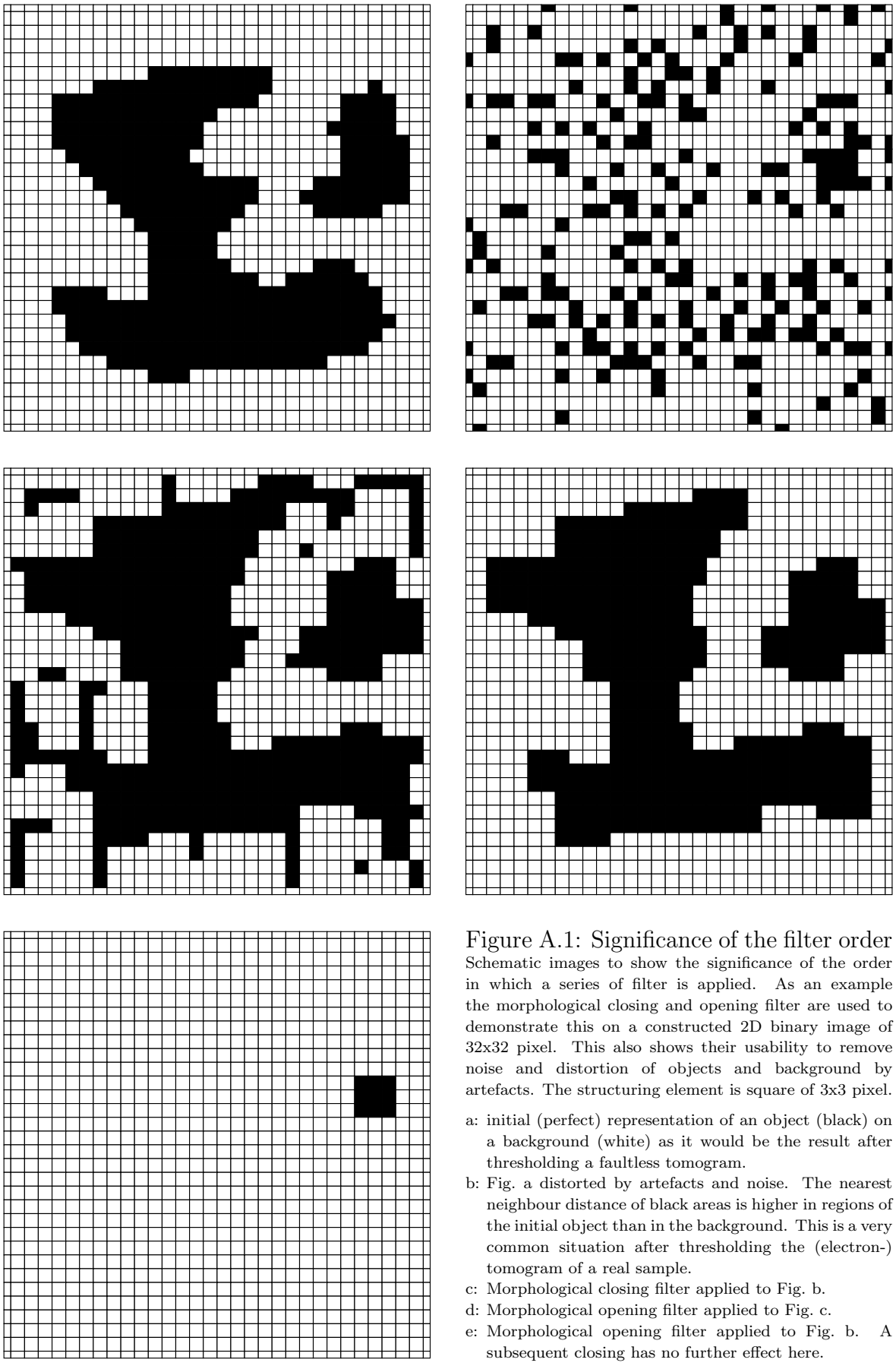

Figure A.1: Significance of the filter order
Schematic images to show the significance of the order in which a series of filter is applied. As an example the morphological closing and opening filter are used to demonstrate this on a constructed 2D binary image of 32x32 pixel. This also shows their usability to remove noise and distortion of objects and background by artefacts. The structuring element is square of 3x3 pixel.

a: initial (perfect) representation of an object (black) on a background (white) as it would be the result after thresholding a faultless tomogram.
b: Fig. a distorted by artefacts and noise. The nearest neighbour distance of black areas is higher in regions of the initial object than in the background. This is a very common situation after thresholding the (electron-) tomogram of a real sample.
c: Morphological closing filter applied to Fig. b.
d: Morphological opening filter applied to Fig. c.
e: Morphological opening filter applied to Fig. b. A subsequent closing has no further effect here.

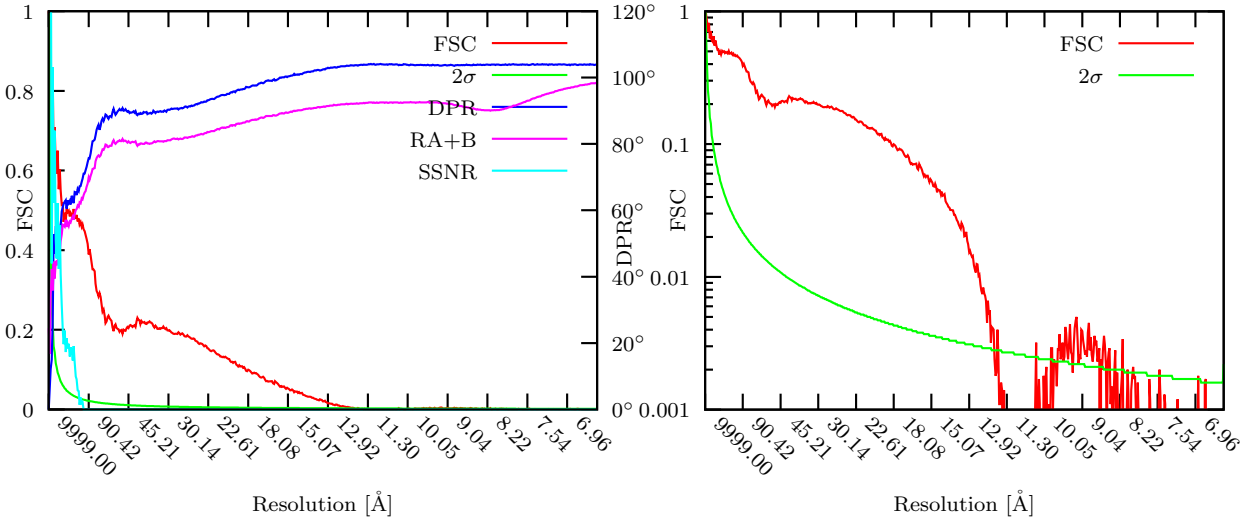

Figure A.2: FSC resolution estimates of BP_{um}

Plots of FSC, 2σ-threshold curve, DPR, SSNR and RA+B. The plot with the logarithmic y-axis allows to evaluate the intersection of the 2σ-threshold curve with the FSC at approximately 12 Å.

The FSC was calculated by `bresove` from the tomogram of the first tilt series and the matched tomogram of the second tilt series.[2)]. The resulting FSC and the corresponding 2σ-threshold curve are plotted in Fig. A.2. The fixed threshold of 0.5, which is often used as a resolution criterion [104; 33; 25; 52] but which is inappropriate according to van Heel and Schatz [177], yields a resolution of 144 Å. Instead of a fixed threshold, a threshold curve, e.g. 2σ-curve or the 1/2-bit curve, is more appropriate [177]. The 2σ-curve intersects with the FSC curve at approximately 12 Å which can be seen in the logarithmic plot (right plot in Fig. A.2). The region between 8 Å and 10 Å is above the 2σ-criterion but is disregarded because of the high noise and the small difference between the two functions. It shows, however, that the FSC values can increase again at higher spatial frequencies if parts of the sample exhibit repetitive structures of high contrast (e.g. lattice spacing in crystalline regions of the sample).

Other resolution estimations with fixed cut-offs yield the following values: DPR = 45° at 781 Å, SSNR = 1 at 1543 Å and RA+B = 0.5 at 134 Å. This shows how significantly the quantitative resolution estimates with fixed cut-offs can differ and how inappropriate they can be. For example the SSNR estimate yields a resolution of half the width of the whole tomogram (3366 Å). These resolution estimates are so conservative that no interpretation of the data would be possible. The 2σ-estimate of 12 Å seems quite reasonable. It corresponds to 3 to 4 voxels in the binned ($s_p \approx 3.3$ Å) tomogram.

The 1/2-bit information threshold curve could not be plotted because the only program available to calculate it (`foushell`[23]) did not work.

2) It is very important that the matched tomogram contains no information of the other tomogram. The execution of the command `submfg -t matchorwarp` in the directory of the corresponding etomo-project ensures that the unfilled space in the result (`*.mat`) is filled by the mean value of the tomogram.

A.3 Dependence of grey values on particle size in DIRECTT reconstructions

The effect particle size can have on grey values as reported by Kübel et al. [92] is evaluated in Fig. A.3. While the effect seems negligible in the unfiltered DIRECTT reconstruction, the median filtered tomogram exhibits a dependence for particles that are smaller than the kernel size. This influence of the median filter is expected. The small particles that are affected were excluded from the evaluations in Sec. 5.3.

Only a manual evaluation of the influence of particle size on grey values was possible because the filter needed for a global analysis is not yet available in MAVI. It would be interesting though to quantify the significance of this effect for different reconstruction algorithms and programs (e.g. IMOD-WBP, IMOD-SIRT, Inspec3D-SIRT and DIRECTT).

A.4 Relation between ruthenium particles and pore entries of the support

The preparation process and the fact that there are ruthenium particles inside and on the surface of the support motivate the growth interpretation of the ruthenium particles as described in Sec. 6.2. In that case, it is likely that ruthenium particles grow either inside a pore or on the outer surface of the support at a pore entry (Fig. 7.1, see also Sec. 5.3.6).

It is possible to analyse the position of ruthenium particles in regard to pore openings of the support by the following virtual procedure:

- Erosion of the voxel representation of the carbon support with its pores closed. This moves the carbon surface inwards by a distance d
- Creation of a mesh of the result, (the resulting mesh being called ECPm: Eroded Closed Pores Mesh, dashed line in Fig. 7.1)
- Evaluation of which parts of ECPm are outside the mesh of the carbon representation with pores (COPm). The algorithm from Sec. 5.3.6.1 can be used for this. The parts of ECPm that are outside COPm are the 'lids' of the carbon pore entries (green lines in Fig. 7.1) at a distance d away from the surface of the carbon segment without pores.
- With the program `mtk` from IMOD[1] it is now possible to evaluate the nearest ruthenium particle to each pore lid and their separation distance (labelled 'shortest distance' in Fig. 7.1). This can be refined by evaluating only the distance

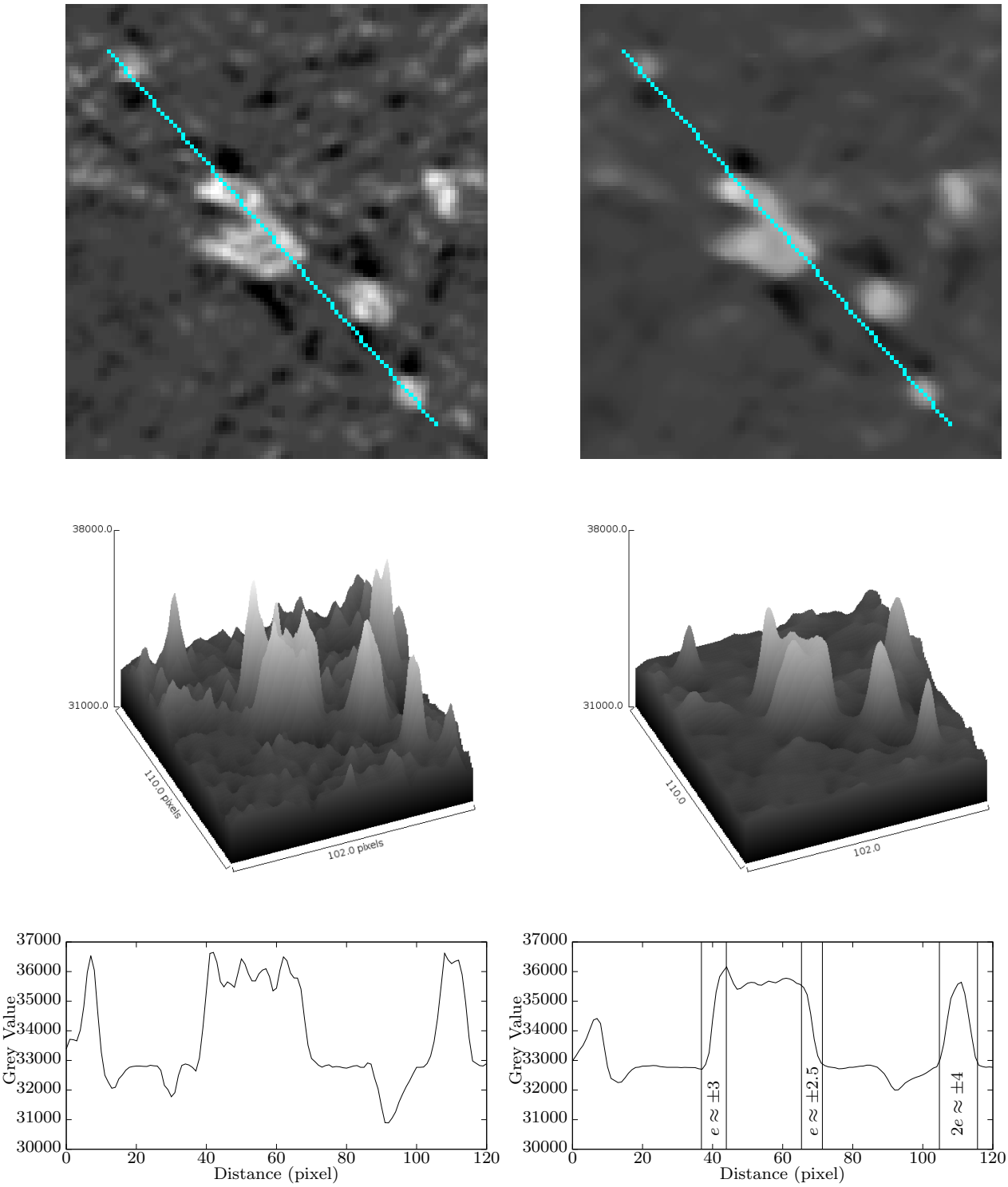

Figure A.3: Dependence of the grey values on the size of the particle

A magnification of a DIRECTT reconstruction slice is visible in the top images. The left image is unfiltered while the image on the right is filtered by a 3D median of 5x5x5. The middle images represent a surface plot of the region and the bottom images a profile plot along the cyan line of the upper images. The pixel size is 0.26 nm.

The left profile plot shows that the influence on the grey values depending on the size of the particle is insignificant in the DIRECTT reconstruction. However, the median filter introduces a dependence for particles below the kernel size. The edge-error lies between $e \approx \pm\ 2$ voxels and $e \approx \pm\ 3$ voxels.

of the centre of the pore lid[3] to the nearest ruthenium particle centre[4] (labelled 'centre to centre' (ctc) in Fig. 7.1). This simple procedure would not check if a particle-lid-pair is directly connected through a pore nor would it check if pore lids are already assigned to a particle.

A.5 Active ruthenium surface calculated from CO stripping result

This is the calculation for Sec. 6.2.
Result from electrochemical CO stripping of $RuVC_{um}$:

$$S_{r_{Ru/C}} = 3,7 \cdot 10^{-8}\ \mathrm{m^2}/5,15\ \mu\mathrm{g} \approx 7,18 \cdot 10^{-3}\ \mathrm{m^2/g}$$

NAA result:

$$20.6/100\ (m_{Ru}/m_C)$$

Therefore:

$$S_{r_{Ru}} = S_{r_{Ru/C}} \cdot 100/20.6 \approx 34.8 \cdot 10^{-3}\ \mathrm{m^2/g}$$

With $\rho = m/V$ and $\rho_{Ru} = 12,37\ \mathrm{g/cm^3} = 12,37 \cdot 10^6\ \mathrm{g/m^3}$ and the total ruthenium volume determined from the tomogram (Sec. 5.3.3):

$$V_{Ru} \approx 1.1 \cdot 10^5\ \mathrm{nm^3} = 1.1 \cdot 10^{-22}\ \mathrm{m^3}$$

$$S = S_r \cdot m = S_r \cdot \rho \cdot V$$

yields:

$$S_{Ru} = 34.8 \cdot 10^{-3}\ \mathrm{m^2/g} \cdot 12.37 \cdot 10^6\ \mathrm{g/m^3} \cdot 1.1 \cdot 10^{-22}\ \mathrm{m^3} \approx 47.5 \cdot 10^{-18}\ \mathrm{m^2}$$

Therefore:

$$S_{Ru} \approx 50\ \mathrm{nm^2}$$

[3] The centre of each lid can be calculated by the vector average of all vertices the lid consists of.
[4] This also drastically decreases the computational effort because only one distance per lid-particle pair has to be computed.

A.6 Additional figures

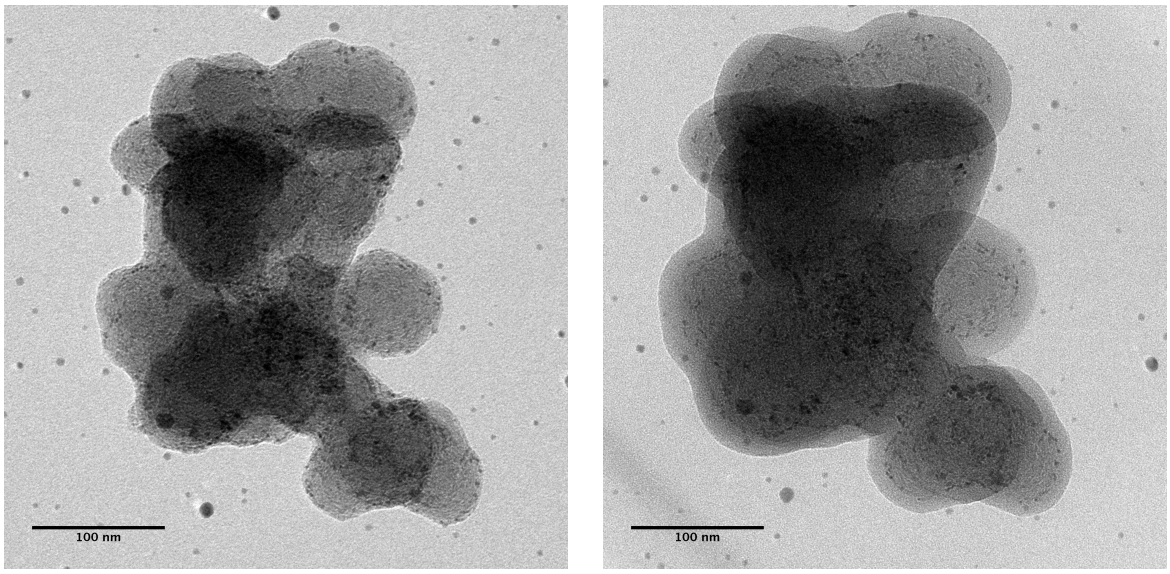

Figure A.4: Sample changes due to contamination
The images show a RuBP$_{um}$ particle before (left) and after (right) the application of an electron dose similar to acquisition of a STEM tilt series. The surface of the particle has obviously changed. The thickness of the contamination can be estimated to vary between 10 nm and 20 nm. This is possible due to the extent of the ruthenium particles. A difference in the carbon structure between the support particle and the contamination can also be seen. Since the particle was not rotated during the dose application the contamination layer is much more uniform than it usually is for STEM tilt series acquired in the TEM used.

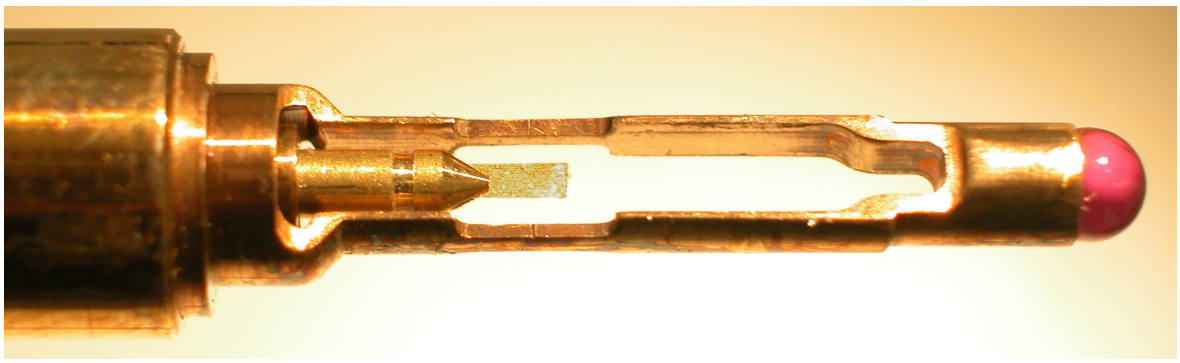

Figure A.5: On-Axis Rotation Tomography Holder with grid sample
Tip of the On-Axis Rotation Tomography Holder (for 360° rotations) with a grid sample. The grid was cropped to make it fit into the sample space.

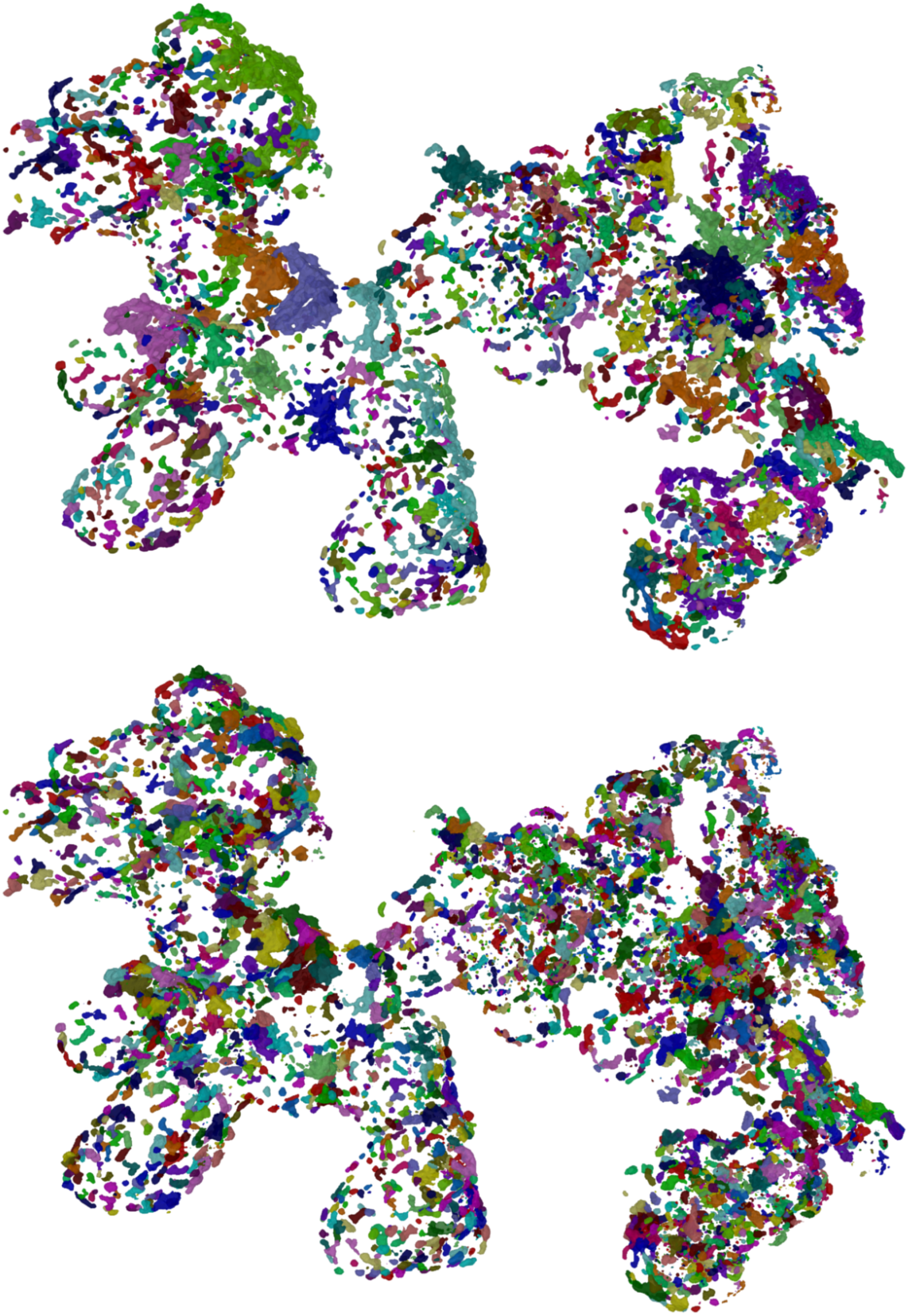

Figure A.6: Ruthenium particles before and after the watershed separation
The top image shows a surface render of the ruthenium particles labelled by an interconnectivity criterion while the bottom image shows the ruthenium particles after the labelling from a watershed separation. This visualizes how the big particles (e.g. at the neck and head) are split up. The bottom image shows all particles while the top image only contains the particles above 64 voxel (see also Fig. 3.1 and Fig. 3.2).

Figure A.7: Spacial distribution of fit-ellipsoids before the watershed separation
Spacial distribution of the fit-ellipsoids before the watershed separation (see also caption of Fig. 5.25).

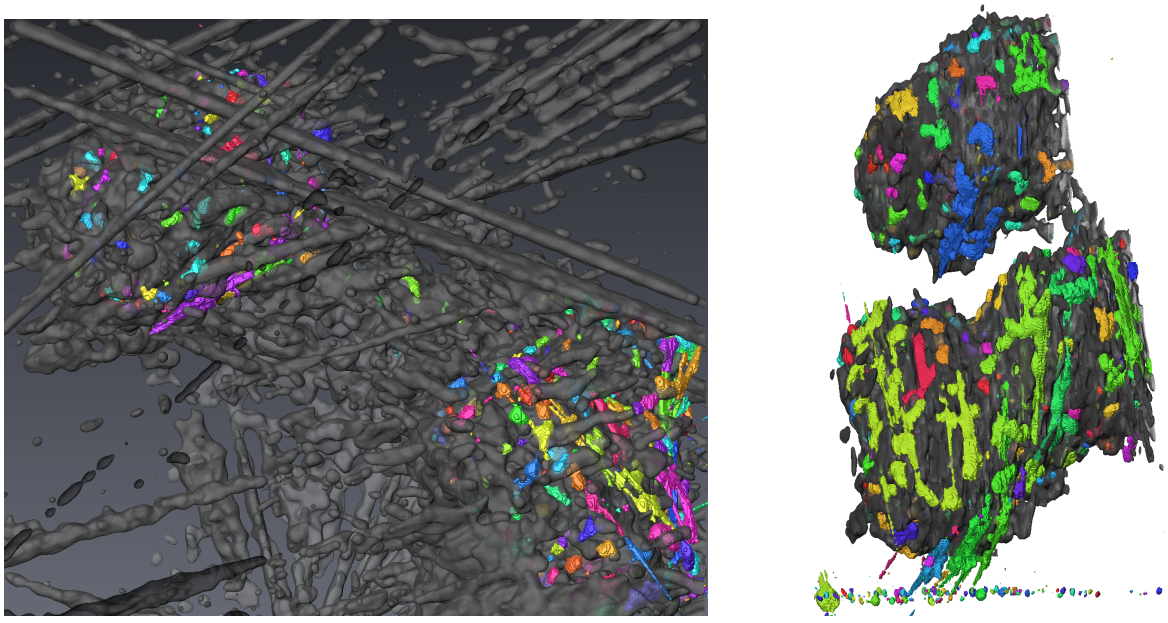

Figure A.8: SIRT reconstruction of the poodle particle
Images visualizing the carbon (grey) and the ruthenium particles (coloured) of a region from the SIRT reconstruction of the poodle ('the front legs'). The image on the left shows the carbon segment in a pre filtered stage where the ray artefacts originating from the ruthenium particles are still obvious. In the right image the 'gluing' of ruthenium particles by the ray artefacts is best visible. The region containing the other parts of the poodle was dominated by ray artefacts and could not be visualized meaningful, not even after excessive filtering. Obviously the ray artefacts dominate over the 'missing wedge' artefacts which are only visible on the small gold markers on the bottom.

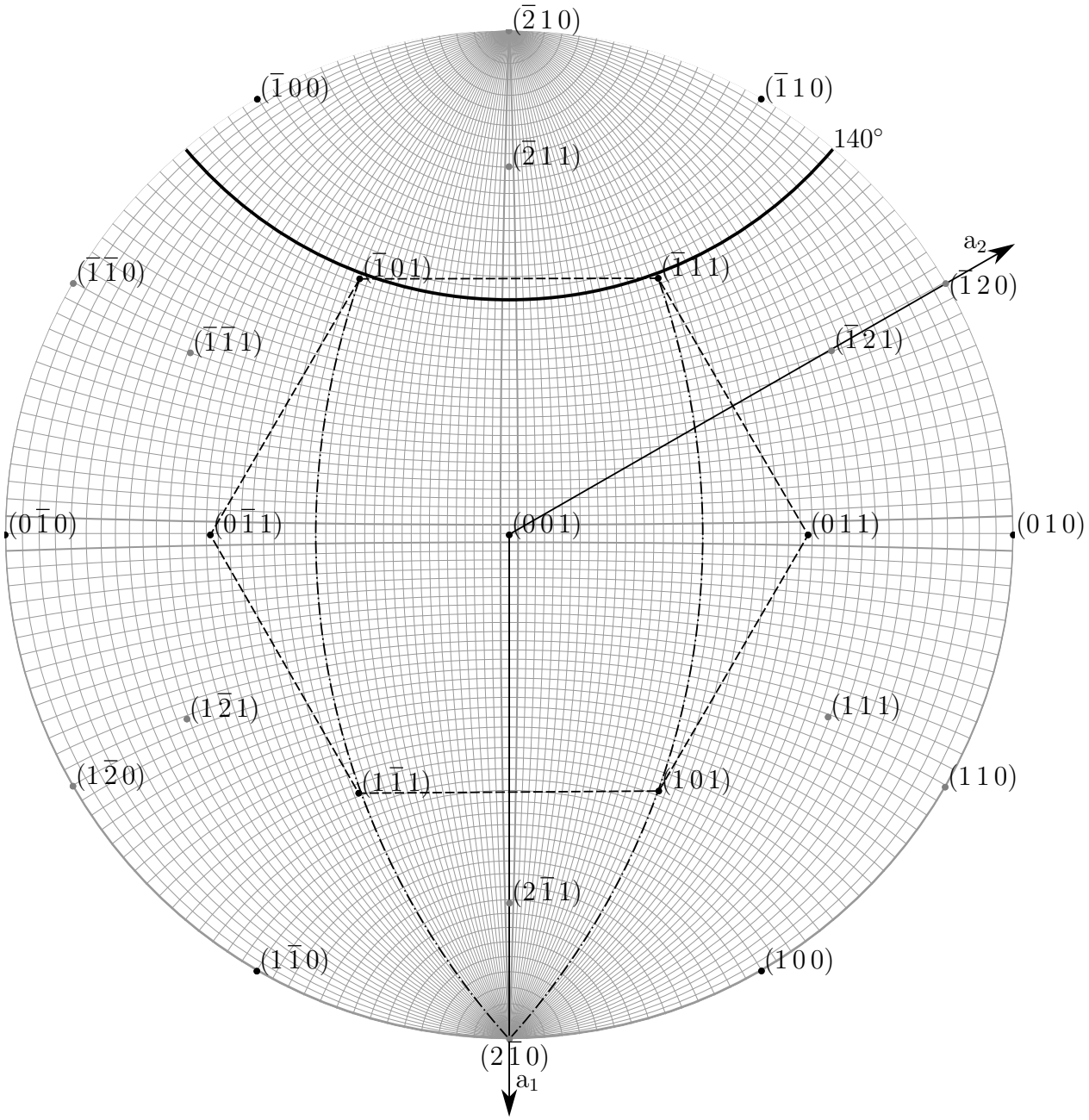

Figure A.9: Ru facet orientations on Wulff net, centred on $(2\,\bar{1}\,1)$

The facet indices for h,k,l $\in [-1, 0, 1]$ plus those needed to complete the symmetry on the upper hemisphere are plotted on a Wulff net, $(0\,0\,1)$ pointing out of the paper. The orientation of the facet indices is chosen such that the interplanar angle between $\measuredangle\,(2\,\bar{1}\,0)(\bar{1}\,0\,1)$ and $\measuredangle\,(2\,\bar{1}\,0)(\bar{1}\,1\,1)$ of $\alpha \approx 139.4°$ can be measured on the Wulff net. Due to the hexagonal symmetry this angle pair occurs six times for points on the dashed hexagon. The black points correspond to the facets of a hexagonal prism and a hexagonal pyramid. The grey points mark the additional facets of a prism and a pyramid with 12 faces. This shows that the angle of $\alpha \approx 139.4°$ can only occur between a black and a grey point. Created with JWulff[18] and modified with inkscape[9].

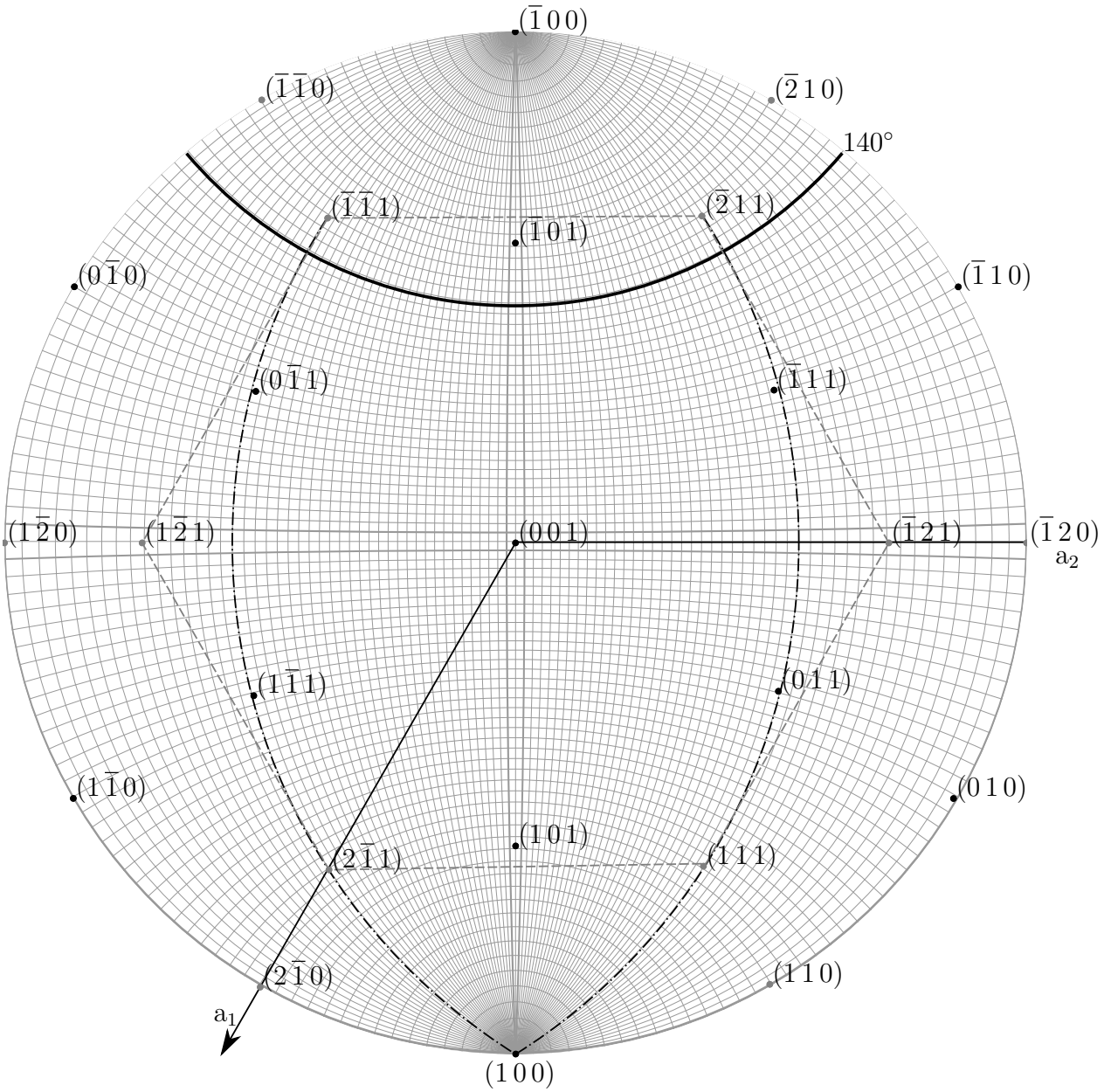

Figure A.10: Ru facet orientations on Wulff net, centred on (1 0 0)

The facet indices for h,k,l $\in [-1, 0, 1]$ plus those needed to complete the symmetry on the upper hemisphere are plotted on a Wulff net, (0 0 1) pointing out of the paper. The orientation of the facet indices is chosen such that the interplanar angle between $\measuredangle$ (1 0 0)($\bar{1}\,\bar{1}$ 1) and $\measuredangle$ (1 0 0)($\bar{2}$ 1 1) of $\alpha \approx 145.7°$ can be measured on the Wulff net. Due to the hexagonal symmetry this angle pair occurs six times for points on the dashed hexagon. The black points correspond to the facets of a hexagonal prism and a hexagonal pyramid. The grey points mark the additional facets of a prism and a pyramid with 12 faces. This shows that the angle of $\alpha \approx 145.7°$ can only occur between a black and a grey point. Created with JWulff[18] and modified with inkscape[9].

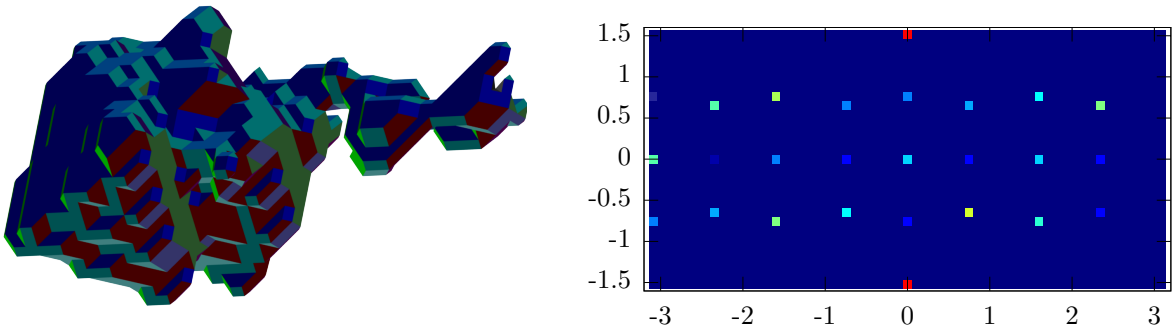

Figure A.11: Facet analysis of a marching-cubes-surface without smoothing

The left image shows the detected facets of the not smoothed (raw) marching-cubes-surface from Fig. 3.5. Since it was not smoothed, the facet analysis yields 26 distinct and globally fixed orientations as visible in the right image, which corresponds to and has the same scale as Fig. 3.4d of the smoothed version. Any raw marching-cubes-surface can only yield any of the 26 orientation fields. Only the field intensities would differ for any other object represented by a marching-cubes-surface.

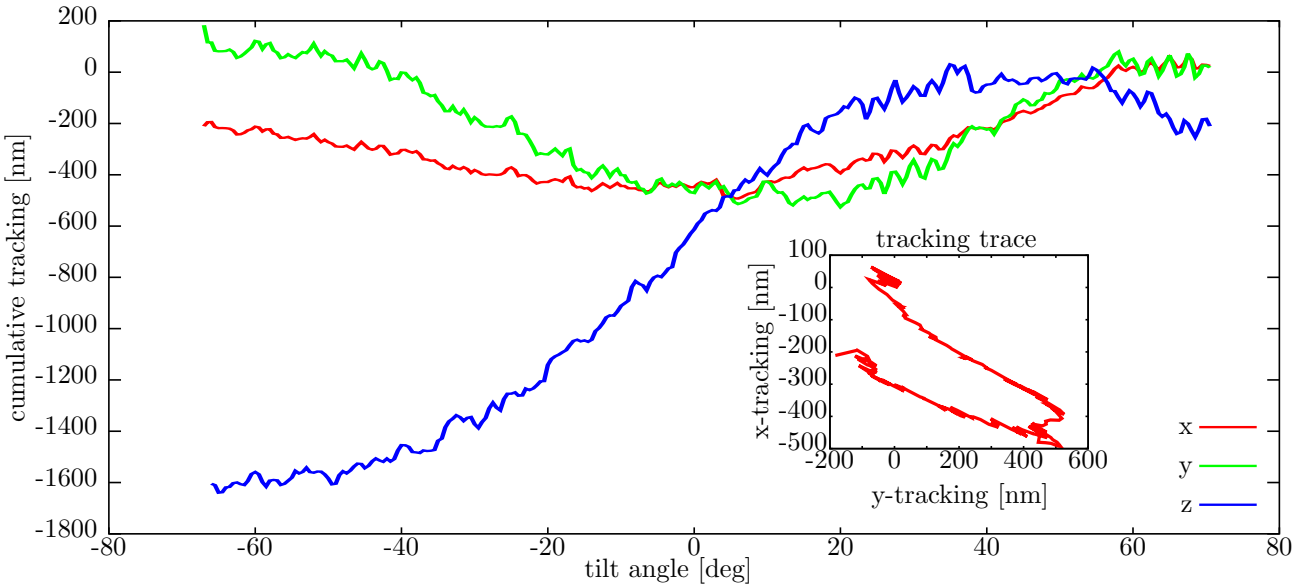

Figure A.12: Cumulative xy-z-tracking curves and trace

Cumulative xy-z-tracking curves belonging to the tomogram in Fig. 5.8. The tilt series was acquired with an On-Axis Rotation Tomography Holder and a cropped grid sample, as shown in Fig. A.5. The total defocus needed for z-tracking was $\Delta_z \approx$ 1.6 µm, $U_h \approx 800$ nm and $U_w \approx 300$ nm. The trace has a different orientation compared to those in Fig. 4.2 due to a change in image rotation of around 180° for 160 kX. An xy-z-tracking curve for a Dual-Axis Tomography Holder is shown in Fig. 4.1.

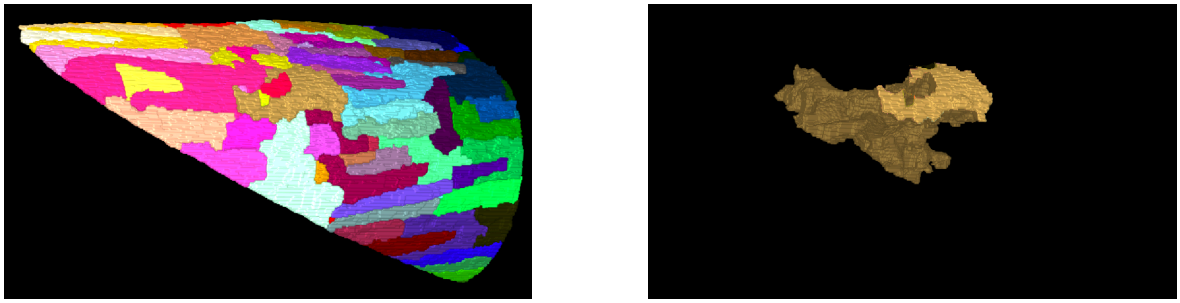

Figure A.13: 3D visualization of the FeSi wedge and its labelled domains

The left image shows the whole wedge and all its labelled domains whereas the right images shows only the brown domain referred to in Fig. 3.16. Its inner surface is rendered darker.

Danksagung

Mein Dank gilt Prof. Dr. John Banhart für die Chance, in seiner Arbeitsgruppe zu forschen und zu promovieren, für seine fachlichen Anleitungen und die wertvollen Anregungen zur Ausführung der Arbeit. Herrn Dr. Christian Kübel danke ich für die aufschlussreichen Gespräche über die Elektronentomographie und für seine Bereitschaft, Zweitgutachter zu sein.
Ich danke Dr. Ingo Manke für die Aufnahme in die Tomographiegruppe und die Anleitung, die wertvollen Anregungen und Unterstützung bei der Promotion. Ebenso danke ich Prof. Dr. S. Fiechter, Dr. Gerald Zehl, Dr. Peter Bogdanoff und Iris Dorbandt für die gute Kooperation, die Herstellung der Proben und die Anregungen und Unterstützung bei den Untersuchungen und Auswertungen. Mein weiterer Dank gilt den Kollegen des Instituts für Angewandte Materialforschung sowie Dr. Daniel Abou-Ras und Sebastian Schmidt für den regen wissenschaftlichen Austausch und die Unterstützung. Besonders möchte ich mich bei Dr. Nelia Wanderka, Dr. Christian Abromeit und Dr. Nikolay Kardjilov bedanken. Dr. Markus Wollgarten danke ich für die Einweisung in die Benutzung des TEM-Labors und die fachlichen Anregungen. Ich danke den Kollegen der BAM für die DIRECTT Rekonstruktionen, Ulrike Bloeck, Harald Stapel, Christiane Förster, Claudia Leistner und Holger Kropf für die Unterstützung bei der Probenpräparation und Jörg Bajorat und den Kollegen der DV für die Hilfe und Administration der Computersysteme. Des weiteren möchte ich mich bei Melanie Timpel, Dr. Elisa Wheeler, und Dr. Scott Williams für das gründliche Korrekturlesen und die Verbesserungsvorschläge zu dieser Arbeit bedanken. Mein Dank gilt auch Kaushik Vaideeswaran, Samuel P. Alonso, Julien Gout und den hilfreichen Mitgliedern der ITK-, VTK- und IMOD-Mailinglisten, insbesondere Dr. David N. Mastronarde, Gaëtan Lehmann, Dr. Richard Beare und Dr. Luis Ibáñez.
Mein ganz besonderer Dank gilt meinen Eltern, auf deren Unterstützung ich mich immer verlassen konnte.